



Swansea University  
Prifysgol Abertawe



## Swansea University E-Theses

---

# Resistance bonding of dissimilar alloys using a powder interlayer: A feasibility study.

Pleydell-Pearce, Cameron

### How to cite:

---

Pleydell-Pearce, Cameron (2008) *Resistance bonding of dissimilar alloys using a powder interlayer: A feasibility study.* thesis, Swansea University.

<http://cronfa.swan.ac.uk/Record/cronfa42467>

### Use policy:

---

This item is brought to you by Swansea University. Any person downloading material is agreeing to abide by the terms of the repository licence: copies of full text items may be used or reproduced in any format or medium, without prior permission for personal research or study, educational or non-commercial purposes only. The copyright for any work remains with the original author unless otherwise specified. The full-text must not be sold in any format or medium without the formal permission of the copyright holder. Permission for multiple reproductions should be obtained from the original author.

Authors are personally responsible for adhering to copyright and publisher restrictions when uploading content to the repository.

Please link to the metadata record in the Swansea University repository, Cronfa (link given in the citation reference above.)

<http://www.swansea.ac.uk/library/researchsupport/ris-support/>

**RESISTANCE BONDING OF DISSIMILAR ALLOYS  
USING A POWDER INTERLAYER:**

**A FEASIBILITY STUDY**

*Submitted to Swansea University in fulfilment of the requirements for the  
Degree of Doctor of Philosophy.*

**(PhD Thesis)**

*Cameron Pleydell-Pearce*

Materials Research Centre: Swansea University

2008



**Swansea University  
Prifysgol Abertawe**

ProQuest Number: 10798175

All rights reserved

INFORMATION TO ALL USERS

The quality of this reproduction is dependent upon the quality of the copy submitted.

In the unlikely event that the author did not send a complete manuscript and there are missing pages, these will be noted. Also, if material had to be removed, a note will indicate the deletion.



ProQuest 10798175

Published by ProQuest LLC (2018). Copyright of the Dissertation is held by the Author.

All rights reserved.

This work is protected against unauthorized copying under Title 17, United States Code  
Microform Edition © ProQuest LLC.

ProQuest LLC.  
789 East Eisenhower Parkway  
P.O. Box 1346  
Ann Arbor, MI 48106 – 1346



## ABSTRACT

An experimental framework has been developed that allows investigation of a novel resistance bonding technique incorporating a metal powder interlayer as a means of forming sound joints between dissimilar alloys. Bonds have been produced between Ti-6Al-4V, Inconel 718 and super CMV steel. Ti-6-4, BurTi and Inconel 718 powder interlayer layers have been trialed. The use of diffusion barrier coatings and transition layers have been explored with particular interest focussed on the effect of tantalum. These trials were then compared to analysis of corresponding bond chemistries produced by a conventional hot isostatic pressing technique. It was found that joints between Ti-6Al-4V and Inconel 718 and super CMV were prone to the formation of intermetallic films at the interface (NiTi, Ti<sub>2</sub>Ni, Fe<sub>2</sub>Ti), resulting in poor bond quality. Whilst the use of diffusion barrier layers reduced reaction zone size, tantalum layers in particular were found to severely degrade joint integrity. Bonds produced between Inconel 718 and super CMV performed more encouragingly; achieving around 70% of Inconel 718 parent metal properties in the optimum condition. Comparisons between conventional HIP procedures and resistance bonding elucidated far better powder consolidation in the former. This was shown to be due to a 'differential heating' effect under resistance heating. A quasi isostatic powder interlayer bonding technique (QUIP) has been developed that has shown to substantially improve joint integrity. This is under continuing development.

**DECLARATIONS AND STATEMENTS**

**DECLARATION**

This work has not previously been accepted in substance for any degree and is not being concurrently submitted in candidature for any degree.

Signed ..... (candidate)

Date 4/12/08 .....

**STATEMENT 1**

This thesis is the result of my own investigations, except where otherwise stated.

Other sources are acknowledged by footnotes giving explicit references. A bibliography is appended.

Signed ..... (candidate)

Date 4/12/08 .....

**STATEMENT 2**

I hereby give my consent for my thesis, if accepted, to be available for photocopying and for inter-library loan, and for the title and summary to be made available to outside organisations.

Signed ..... (candidate)

Date 4/12/08 .....

## TABLE OF CONTENTS

1	INTRODUCTION .....	1
2	LITERATURE REVIEW .....	3
2.1	Introduction to literature review .....	3
2.2	Titanium and titanium alloys .....	4
2.2.1	Pure titanium .....	4
2.2.2	Alloy classification .....	5
2.2.3	Commercial alloys [7].....	6
2.2.4	Heat treatment processes.....	6
2.2.5	Application of titanium alloys in the aerospace industry.....	9
2.3	Nickel base Superalloys and Inconel 718 .....	11
2.3.1	Metallurgy .....	15
2.3.2	Strengthening mechanisms .....	18
2.3.3	Processing Ni-Fe alloys .....	22
2.4	Cr-Mo-V Steels .....	23
2.4.1	Basic metallurgy .....	23
2.4.2	Structure / property control .....	28
2.4.3	Alloy development and application .....	35
2.5	Powder metallurgy .....	38
2.5.1	Production of powders .....	39
2.5.2	Compact consolidation – sintering.....	40
2.5.3	Microstructural features of consolidated PM materials .....	44
2.5.4	Metal Injection moulding (MIM).....	47
2.6	Fundamentals of welding .....	49
2.6.1	Common considerations.....	49
2.6.2	Weld microstructure and basic metallurgical factors.....	51
2.6.3	Standard heat treatment process.....	54
2.7	Established welding techniques .....	55
2.7.1	Metal inert gas (MIG) welding .....	55
2.7.2	Tungsten inert gas (TIG) welding.....	56
2.7.3	Plasma arc welding (PAW).....	57
2.7.4	Friction welding .....	58
2.7.5	Power beam Processes .....	60
2.7.6	Resistance welding.....	61
2.8	Solid state joining processes (diffusion bonding).....	63
2.8.1	Mechanisms of bonding .....	64
2.8.2	Effect of bonding conditions.....	67
2.8.3	Common diffusion bonding processes [81] .....	69
2.9	Existing techniques for solid-state joining with powders .....	70
2.10	Joining dissimilar alloys.....	75
2.10.1	Case studies on dissimilar alloy welds.....	76
2.11	Conclusions of literature review .....	81
3	EXPERIMENTAL PROCEDURE .....	85
3.1	Material .....	85
3.1.1	Ti -6Al – 4V (Ti-6-4).....	85

3.1.2	Inconel 718 (IN718).....	86
3.1.3	Super CMV steel (SCMV).....	87
3.1.4	Powder material .....	88
3.1.5	Powder paste .....	90
3.1.6	Coated material .....	90
3.1.7	Brazed material .....	91
3.2	Bonding Apparatus: The Gleeble 1500 thermo-mechanical simulator.....	91
3.2.1	Resistance heating.....	92
3.2.2	Specimen geometry.....	94
3.3	Bonding Procedure.....	95
3.3.1	Gleeble specimen preparation.....	95
3.3.2	Preparation of powder interlayer.....	95
3.3.3	Loading / unloading of specimens .....	96
3.4	Bonding trials.....	98
3.5	Production of HIPed bonds.....	99
3.5.1	Production route.....	99
3.5.2	Specimen preparation.....	101
3.6	Bond Characterisation.....	101
3.6.1	Sample preparation .....	101
3.6.2	Sectioning.....	101
3.6.3	Optical microscopy .....	104
3.6.4	Scanning electron microscopy (SEM) .....	105
3.6.5	Chemical analysis (EDX).....	105
3.6.6	Microhardness testing .....	105
3.7	Mechanical testing .....	105
4	RESULTS: Resistance bonded joints .....	107
4.1	Debinding procedures .....	107
4.2	Tantalum coated Inconel 718 to Ti-6-4 with Ti-6-4 powder interlayer.....	110
4.2.1	Surface analysis.....	110
4.2.2	Metallography .....	112
4.3	Nickel coated SCMV to Ti-6-4 with Ti-6-4 interlayer .....	114
4.3.1	Surface Analysis .....	116
4.3.2	Metallography .....	117
4.4	Differential Heating .....	119
4.4.1	Material compatibility.....	121
4.4.2	Experimental design modifications.....	122
4.5	Ti-6-4 to Nickel coated SCMV with Ti-6-4 / BurTi interlayer.....	124
4.6	Chemical compatibility .....	128
4.6.1	Comparisons to conventional HIP technique.....	128
4.6.2	Further modifications.....	129
4.7	Ti to Ni-Cr-V (triple) coated SCMV with BurTi interlayer.....	130
4.8	Tantalum coated SCMV to Inconel 718 with Inconel 718 powder .....	133
4.9	Quasi isostatic forces during resistance bonding (QUIP) .....	134
4.10	Tantalum coated Inconel 718 to Ti-6-4 with BurTi powder .....	138
4.11	Copper impregnated powder interlayers .....	140
4.12	Titanium substrate to IN718 substrate using a Copper braze interlayer .....	143



4.13	IN718 Vs SCMV using a Microbraz LM braze.....	144
4.13.1	Bond microscopy .....	146
4.13.2	Mechanical testing .....	150
4.14	Heat affected zones (HAZ) .....	158
4.14.1	IN718 / SCMV post weld heat treatment (PWHT).....	164
5	RESULTS: HIPed joints .....	169
5.1	Tantalum coated Inconel 718 to Ti-6-4 with Ti-6-4 powder interlayer .....	169
5.2	Ti-6-4 to SCMV with Ti-6-4 / BurTi Powder interlayer .....	172
5.3	Tantalum coated SCMV to IN718 with IN718 Powder interlayer .....	174
5.4	Tantalum coated IN718 to Ti-6-4 with BurTi interlayer .....	176
5.5	Ti-6-4 to copper brazed IN718 without powder interlayer .....	177
6	DISCUSSION .....	180
6.1	General considerations.....	180
6.1.1	Design of experiments .....	180
6.1.2	Resistance heating in the experimental and industrial fields .....	181
6.1.3	Considerations for the powder interlayer.....	181
6.1.4	Cleanliness and noise factors .....	183
6.2	Ti-6Al-4V to Inconel 718 .....	185
6.2.1	Effects of interlayers / brazes.....	186
6.2.2	Powder consolidation and chemistry .....	193
6.3	Ti-6Al-4V to Super CMV steel.....	195
6.3.1	Thermo-physical effects – Differential heating .....	196
6.3.2	Effects of interlayers / brazes for Ti-6-4 powder interlayer joints.....	197
6.3.3	Triple layer transition joints employing a BurTi powder interlayer ....	205
6.4	Inconel 718 to Super CMV steel.....	208
6.4.1	Quasi-isostatic powder interlayer bonding (QUIP) and continuing development.....	209
6.4.2	Effects of interlayers / brazes with IN718 powder .....	211
6.4.3	Mechanical integrity .....	220
6.5	HAZ and macro scale microstructural effects.....	221
6.6	Recommendations for Industrial Employment .....	225
	CONCLUSIONS.....	227
7	RECOMMENDATIONS .....	230
7.1	Further Experimental design and process optimisation .....	230
7.2	Further dissimilar bonding trials .....	232
7.3	Revisions for the resistance heating technique .....	232
7.4	Quasi isostatic powder interlayer bonding.....	233
8	REFERENCES.....	234
9	APPENDICES .....	243

## LIST OF FIGURES

Figure 2.2.2: Typical bi-modal structure observed in Ti-6242. ....	7
Figure 2.2.3: Three $\beta$ annealed microstructures showing the effect of cooling rate from the $\beta$ phase field, (a) 1°C /min (b) 100°C/min (c) 8000 °C/min. ....	8
Figure 2.3.1: Nickel alloy microstructure, 5000x [16]. ....	15
Figure 2.3.2: Common unwanted phases or structures, 5000x [16]. ....	15
Figure 2.4.1: The iron-carbon equilibrium phase diagram. ....	24
Figure 2.4.2: Relationship to Fe-C phase diagram (a) of IT diagrams of eutectoid steel (b) and steel containing 0.5% carbon (c) [21]. ....	25
Figure 2.4.3: Microstructures of (a) lath and (b) plate martensite [22]. ....	26
Figure 2.4.4: A section of the Fe-C phase diagram with temperature ranges for full annealing, normalizing and homogenisation indicated. ....	28
Figure 2.4.5: The effect of temperature and carbon content on plain carbon steels (hatched area denotes retained austenite as a result of high carbon content). ....	30
Figure 2.4.6: The effect of alloying elements on the quantitative hardenability of plain carbon steels [23]. ....	31
Figure 2.4.7: CCT diagram for a plain carbon steel containing 0.38%C and 0.7%Mn, transformations are plotted as a function of bar diameter [24]. ....	32
Figure 2.4.8: CCT diagram for an alloy steel containing 0.4%C, 1.5%Ni, 1.2%Cr and 0.3%Mo [24]. ....	32
Figure 2.4.9: The effect of alloying elements on the retardation of softening during tempering at 260°C [25]. ....	34
Figure 2.4.10: The effect of alloying elements in the retardation of softening during tempering at 540°C [25]. ....	34
Figure 2.4.11: The relationship between tempering temperature and UTS for the S/CMV alloy [30]. ....	37
Figure 2.5.1: A schematic representation of the gas atomization process [36]. ....	40
Figure 2.5.2: A schematic representation of the MIM process [50]. ....	48
Figure 2.5.3: Examples of the complex geometry components that can be produced by the MIM process [52]. ....	48
Figure 2.6.1: A summary of weld structures as presented by Szekeres <i>et al</i> [54]. ....	51
Figure 2.6.2: Effect of thermal gradient on the mode of solidification in welds for a constant growth rate (a) planar growth (b) intermediate or cellular growth (c) dendritic growth (d) solidification of the weld. ....	53
Figure 2.7.1: A schematic diagram of the TIG welding process. ....	57

Figure 2.7.2: A schematic diagram of the plasma arc welding process.....	58
Figure 2.7.3: An illustration of the friction stir welding technique. ....	60
Figure 2.7.4: A schematic diagram of the electron beam welding process. ....	61
Figure 2.7.5: A Schematic representation of the resistance spot welding technique.....	62
Figure 2.8.1: (a) Asperities created by machining (b) Initial oval voids formed by the two mating surfaces (above) and voids after deformation stages (below) (c) Three separate examples of bulk diffusion for final closure of the voids at the interface [67].	65
Figure 2.8.2: A Schematic illustration of the process of interfacial oxide break up [78]. .....	66
Figure 2.9.1: The powder interlayer arrangement used in bonds produced in [104]. (1/4) the solid substrates being joined, (2) the powder interlayer, (3) the protective shell, (5) a sealing joint, (6) gas absorbing tablets.....	71
Figure 2.9.2: The powder interlayer resistance butt weld technique adopted in [104]. (1/5) the solid substrate materials (2) non conducting sleeve (3) powder (4) slit (6/7) current conducting jaws. ....	72
Figure 2.9.3: A schematic representation of the liquid phase sintering process.....	73
Figure 2.9.4: Two joint designs employed for the LIPIB bonding technique. ....	74
Figure 2.10.1: A summary of microstructural effects on the creep and fatigue resistance of titanium alloys [115]......	75
Figure 2.10.2: The typical banding of intermetallics observed by Ohran <i>et al</i> in diffusion bonds between micro-duplex stainless steels and Ti-6-4 [126]......	78
Figure 3.1.1: The parent microstructure of the Ti-6Al-4V material (nominal gleeble specimen orientations indicated). ....	85
Figure 3.1.2: The parent microstructure of the IN718 material (nominal gleeble specimen orientations indicated)......	86
Figure 3.1.3: The parent microstructure of the SCM V material (nominal gleeble specimen orientations indicated)......	88
Figure 3.1.4: Powder morphology and microstructure for as received (a) BurTi powder (b) Ti-6-4 powder and (c) IN718 powder. ....	89
Figure 3.2.1: The Gleeble 1500 thermo-mechanical simulator. ....	92
Figure 3.2.2: The interior of the vacuum chamber during bonding. ....	92
Figure 3.2.3: The resistance heating profile as predicted by steady state heat transfer equations (adapted from [146])......	93
Figure 3.2.4: The dimensions of the Gleeble specimens used in the bonding processes. .....	94
Figure 3.2.5: An illustration of the location of spot welds on Gleeble specimens. ....	95
Figure 3.3.1: A schematic representation of the powder application equipment.....	96

Figure 3.3.2: A schematic illustration of the alignment jig assembly.....	97
Figure 4.1.1: The vacuum used during initial debinding trials. ....	107
Figure 4.1.2: Disintegration of the powder interlayer during vacuum debinding.....	108
Figure 4.1.3: SEM images of the debound brown powder compacts produced at high temperature over 14 hours.....	109
Figure 4.1.4: Results of EDX chemical analysis of the brown compacts debound at condition 3.....	109
Figure 4.2.1: Plan and transverse macros of Test 1. ....	110
Figure 4.2.2: (a) Ti-6-4 sintered to Ti-6-4 substrate (b) less consolidated Ti-6-4 powder on Ti-6-4 substrate (c) Ti-6-4 powder bonded to IN718 substrate. ....	111
Figure 4.2.3: EDX Surface maps for both fracture surfaces in Test 1.....	111
Figure 4.2.4: Sections through the bond line in Test 2 at (a) low and (b) high magnification. ....	112
Figure 4.2.5: Sections through the bond line in Test 3 in (a) normal secondary electron and (b) backscattered electron modes. ....	113
Figure 4.2.6: An EDX traverse matching a high magnification backscattered image of Test 3.....	114
Figure 4.3.1: A Macro of Test 4.....	115
Figure 4.3.2: An illustration of the differential heating effect observed in Tests 4 and 5 .....	115
Figure 4.3.3: SEM images of (a) Ti-6-4 powder on Ti-6-4 substrate and (b) a backscattered image of adhesion sites on SCMV substrate.....	116
Figure 4.3.4: A comparison between EDX chemical analyses of adhesion sites on the SCMV surface and the substrate SCMV.....	117
Figure 4.3.5: A metallographic section of Ti-6-4 powder on Ti-6-4 substrate in Test 4 with high magnification image inset.....	118
Figure 4.4.1: A schematic representation of the jaw / specimen configuration of the Gleeble 1500. ....	120
Figure 4.4.2: Temperature profiles for the standard copper jaw configuration. ....	122
Figure 4.4.3: Temperature profiles for the uniform hot jaw configuration.....	123
Figure 4.5.1: The effect of the hot jaw configuration on the visible temperature profile. ....	124
Figure 4.5.2: A macro of Test 9. ....	124
Figure 4.5.3: SEM fractography of Ti-6-4 powder on Ti-6-4 substrate. ....	125
Figure 4.5.4: Macros of initial BurTi interlayer trial, with a section illustrating the deformation in the Ti-6-4 material.....	126

Figure 4.5.5: Macros of Tests (a) 12 and (b) 13 .....	126
Figure 4.5.6: Consolidation at the BurTi to SCMV interface.....	127
Figure 4.6.1: A schematic diagram of the sleeve design. ....	129
Figure 4.7.1: A macro of Test 14. ....	130
Figure 4.7.2: A macro of Test 16 bonded at 970°C. ....	131
Figure 4.7.3: SEM fractography and corresponding EDX analysis of fractured specimen halves from Test 16.....	131
Figure 4.7.4: A metallographic section of BurTi powder on Ti-6-4 substrate in Test 16. ....	132
Figure 4.8.1: A macro of Test 17. ....	133
Figure 4.8.2: SCMV images of (a) IN718 powder on IN718 substrate and (b) adhesion sites on SCMV substrate with a corresponding backscattered image (c). ....	134
Figure 4.9.1: A macro of test 18. ....	135
Figure 4.9.2: SEM images of (a) IN718 powder on uncommon SCMV substrate and (b) well assimilated IN718 powder on IN718 substrate with a higher magnification image inset. ....	135
Figure 4.9.3: An optical micrograph of the IN718 powder - IN718 substrate interface viewed under polarized light.....	136
Figure 4.9.4: A macro of Test 20. ....	136
Figure 4.9.5: SEM analysis of (a) IN718 powder on IN718 substrate and (b) adhesion sites of SCMV substrate for Test 20. ....	137
Figure 4.9.6: A high magnification optical micrograph of the SCMV - IN718 powder interface.....	138
Figure 4.10.1: A macro of Test 19. ....	139
Figure 4.10.2: SEM images (a) BurTi powder on Ti-6-4 substrate and (b) an image of an adhesion site on the SCMV substrate with a high magnification image inset. ....	139
Figure 4.10.3: An optical micrograph of the BurTi powder interlayer on Ti-6-4 substrate with high magnification detail inset.....	139
Figure 4.10.4: A high magnification optical micrograph of the tantalum coated IN718 bond half. ....	140
Figure 4.11.1: An overview of bond 21 from (a) the Ti-6-4 side and (b) the IN718 Side.....	141
Figure 4.11.2: Detailed views of the microstructures of (a) the impregnated powder compact and (b) the powder to IN718 interface. ....	142
Figure 4.12.1: A macro of bond 26.....	143
Figure 4.12.2: (a) A high magnification SEM image typical of the faying surface condition post bonding (b) a corresponding backscattered image.....	143

Figure 4.12.3: (a) A medium and high (inset) magnification micrograph typical of the appearance of the Ti-6-4 side and (b) the interfacial microstructure of the IN718 side of bond 2\*..... 144

Figure: 4.13.1: Macro images for post bond appearance of various Nicrobraz brazed SCMV to IN718 joints. .... 146

Figure 4.13.2: A polarized light micrograph of the interface between SCMV and IN718 pairs using a NicroBraz braze. .... 147

Figure 4.13.3: An overview of the interfacial microstructure of a Nicrobraz brazed SCMV to IN718 bond with high magnification detailed image inset..... 148

Figure 4.13.4: An overview of the interfacial microstructure for a Nicrobraz Brazed bond between SCMV and IN718 employing a powder interlayer with high magnification detail inset. .... 149

Figure 4.13.5: An image of the representative pore size found within the powder interlayers..... 150

Figure 4.13.6: Engineering stress vs strain plots for all Nicrobraz brazed trial bonds produced..... 151

Figure 4.13.7: An SEM image typical of the fracture surface found in failed SCMV to IN718 Nicrobraz brazed joints (b), with evidence of non-fusion defects (a). .... 153

Figure 4.13.8: A high magnification image of an SEM image of the brazed powder interlayer trial (plan view of fracture surface). .... 154

Figure 4.13.9: The fracture surface of the Nicrobraz brazed fusion weld (plan view).155

Figure 4.13.10: A section through the failed Nicrobraz brazed fusion weld mechanical test piece..... 156

Figure 4.13.11: An area of non-fusion observed in the IN718 side of the melted trial bond..... 157

Figure 4.14.1: A full microstructural assessment of HAZ banding in a bond between SCMV and IN718 employing a powder interlayer. .... 160

Figure 4.14.2: A Vickers microhardness traverse across a bonded specimen displaying HAZ banding..... 161

Figure 4.14.3: Microstructural variations noted in the Ti-6-4 substrate of trials performed employing the ‘hot jaws’ configuration. .... 163

Figure 4.14.5: A microhardness traverse across the heat affected zone in Ti-6-4 substrate from Test 16..... 164

Figure 4.14.6: PWHT microstructure of SCMV closer to the bond line. .... 165

Figure 4.14.7: PWHT structure of SCMV remote of the bond line..... 166

Figure 4.14.8: A comparison of microhardness traverse for the as bonded and heat treated condition..... 166

Figure 4.14.9: A comparison of Engineering stress- strain behaviour between the as bonded and PWHT conditions. ....	167
Figure 5.1.1: Overview (a) and detailed interfacial microstructure (b) of bond 5b, HIPed, IN718 to Ti-6-4 with Ta interlayer. ....	171
Figure 5.1.2: Optical micrographs of (a) Test 16b with no tantalum interlayer and (b) Test 8b with a tantalum interlayer.....	172
Figure 5.2.1: An overview of Test 11b. ....	173
Figure 5.2.2: High magnification optical micrographs of (a) the Ti-6-4 substrate to BurTi powder interface and (b) the SCMV to BurTi powder interface. ....	174
Figure 5.3.1: High magnification optical micrographs of Test 19b at (a) the IN718 substrate to IN718 powder interface and (b) the IN718 powder to tantalum coated SCMV substrate. ....	175
Figure 5.3.2: A high magnification optical micrograph of Test 19b illustrating the typical pore size found in the powder interlayer. ....	175
Figure 5.4.1: An overview of the interfacial microstructure of Test 14b. ....	176
Figure 5.4.2: High magnification optical micrographs of the interface between (a) In718 substrate and BurTi powder and (b) BurTi powder and Ti-6-4 substrate. ....	177
Figure 5.5.1: An overview of the interfacial microstructure of Test 33b (IN718 to Ti-6-4 including Cu braze). ....	178
Figure 5.5.2: Optical micrographs of the interfacial microstructure of (a) the copper brazed Ti-6-4 substrate and (b) the IN718 substrate. ....	179
Figure 5.5.3: A high magnification optical micrograph showing evidence of primary $\alpha$ growth remote of the Ti-6-4 substrate material. ....	179
Figure 6.2.1: EDX traverses for minority and majority elements in Test 2.....	187
Figure 6.2.2: EDX traverses for minority and majority elements Test 16b.....	188
Figure 6.2.3: Spot EDX analysis on intermetallic films found in Test 2. ....	189
Figure 6.2.4: Spot EDX analysis on intermetallic films found in Test 8b. ....	189
Figure 6.2.5: Microhardness traverse across the interface of Test 16b.....	190
Figure 6.2.6: A minority element EDX traverse of Test 24.....	191
Figure 6.2.7: A microhardness traverse of Test 24. ....	192
Figure 6.2.8: EDX spot analysis of fractured intermetallic films in Test 24. ....	192
Figure 6.2.9: A microhardness traverse of Test 21. ....	195
Figure 6.3.1: A comparison between an EDX traverses for minority and majority elements and an EDX traverse for Test 7b. ....	199
Figure 6.3.2: The interfacial microstructure of Test 9. ....	202
Figure 6.3.3: The ternary phase diagram for the Ni-Fe-Cr system at 900°C [153].....	202

Figure 6.3.4: A comparison between an EDX traverses for minority and majority elements and an EDX traverse for Test 4. ....	203
Figure 6.3.5: A comparison between EDX traverses for minority and majority elements and an EDX traverse for Test 9.....	204
Figure 6.3.7: A comparison between EDX traverses for both the BurTi powder – SCMV substrate and Ti-6-4 substrate – BurTi powder interfaces and the full microhardness traverse for Test 16. ....	207
Figure 6.4.1: EDX traverses for Test 19b detailing compositions both at the IN718 powder – IN718 substrate and IN718 powder – SCMV substrate interfaces. ....	212
Figure 6.4.2: Isothermal section of the Ni–Ta–Ti system at 927 °C, derived from experimental data [156]. ....	213
Figure 6.4.3: EDX traverses across the IN718 powder SCMV substrate interface for Test 18.....	214
Figure 6.4.4: A comparison between EDX traverses for minority and majority elements and an EDX traverse for Test 28.....	217
Figure 6.4.5: A comparison between EDX traverses for minority and majority elements and an EDX traverse for Test 30.....	219
Figure 6.5.1: A TTT diagram for hot rolled IN718 bar [158].....	222
Figure 6.5.2: Phase relationships and the effect of heat treatments in IN718 [158]. ...	223
Figure 6.5.3: A hardness traverse the HAZ of Test 29 (rapid, semi – solid condition). ....	224



## LIST OF TABLES

Table 2.2.1: A comparison of mechanical properties between commercially pure titanium, nickel and iron (data sourced from [6]).	4
Table 2.2.2: Some examples of commercial titanium alloys [8].	6
Table 2.3.1: List of elements and their effect on nickel alloys [14].	12
Table 2.3.2: List of elements and their effect on nickel alloys [15].	13
Table 2.6.1: A summary of joint and weld designs.	50
Table 3.1.1: A summary of mechanical properties for the Ti-6-4 material [7].	85
Table 3.1.2: The nominal chemical composition of alloying elements in the Ti-6-4 material.	86
Table 3.1.3: Nominal composition for the IN718 substrate material.	87
Table 3.1.4: A summary of mechanical properties for the IN718 material	87
Table 3.1.5: Nominal composition for the SCMV substrate material.	87
Table 3.1.6: Tabulated values for the gelation binder constituents.	90
Table 3.1.7: The nominal composition for the Nicrobraz LM brazing alloy.	91
Table 3.4.1: A full matrix of the Resistance bonding trials conducted.	98
Table 3.5.1: Test Matrix detailing bonds produced via the conventional HIP technique.	100
Table 4.1.1: A summary of process variables for the debinding trials performed.	108
Table 4.4.1 : Thermo physical property data for Ti-6-4, IN718 and SCMV.	121
Table 4.13.1: A Summary of the bonding conditions for bonds produced incorporating Nicrobraz.	145
Table 4.13.2: A summary of mechanical properties for all Nicrobraz brazed trial bonds produced.	151
Table 4.14.1: Mechanical properties for both the as bonded and the heat treated conditions.	168
Table 6.2.1: Selected experiments to describe IN718 to Ti-6-4 joints.	185
Table 6.2.2: A summary of reaction zone size for Ta coated and uncoated Ti-6-4 to IN718 bonds.	187
Table 6.3.1: Selected experiments to describe SCMV to Ti-6-4 joints.	196
Table 6.4.1: Selected experiments to describe SCMV to IN718 joints.	209
Table 8.1.1: The full statistically based testing matrix for optimisation of all bonding pairs.	231

## **ACKNOWLEDGEMENTS**

Firstly, the author wishes to express gratitude to Rolls-Royce Plc and EPSRC for providing the necessary funding for this research.

The supervision and guidance provided by Dr Wayne Voice and particularly Professor Martin Bache was invaluable and gratefully received.

Many thanks also for the useful discussions, comments and suggestions of Professor Steve Brown, Dr Jonathan James, Dr Stephen Tuppen, Dr Paul Jones, Dr Miles Willis and Mr John Forsdike.

Particular thanks is extended to the technical staff of Swansea University for their continued support throughout the project term, and specifically the support of both Mr John Morgan and Mr Peter Davies.

## 1 INTRODUCTION

Economic and technical constraints have led to a slow down in alloy development over the last decade, compared to the boom in advanced alloy production associated with the 40 years prior to that. Whilst the most successful alloy groups such as the  $\alpha$ - $\beta$  titanium alloys, nickel base superalloys and hardenable steels provide exceptional performance each is limited to certain regimes, defined by temperature, load or component weight and size. For this reason attention is now being focused on combining these alloy groups in service.

Joints between dissimilar materials provide the opportunity to produce hybrid components with a wide range of specific heterogeneous properties. Examples of this technology include wear resistant coatings in gas turbine casings, radiation resistant alloys for panels of the ITER reactor and joints between dissimilar boiler tube materials in the power generation industry. The benefits of these dissimilar joints have been recognised since the workable welding procedures were developed. For this reason dissimilar joining has received considerable attention, with varying degrees of success.

Typically, conventional welding procedures fall short of the joint integrity required for critical applications, particularly in relation to advanced alloys [1]. Their poor quality is normally due to both the rapid heating and cooling rates and wide heat affected zones associated with traditional fusion welding processes. Conversely, solid state diffusion bonding has been recognised for producing sound joints in dissimilar materials at temperatures significantly below their melting point.

Resistance butt welding, a variant of diffusion bonding, has previously been shown to produce near parent metal properties in dissimilar joints between dissimilar titanium alloys and similar nickel and steel pairings [2, 3]. In a further development to this technique that draws on the technology of field assisted sintering (FAST) and metal injection moulding (MIM), it has been suggested that introducing a powder interlayer

into the resistance butt welding technique may substantially improve bond quality between dissimilar pairings, as well as reducing pre-joint preparation times. These benefits have been recognised by the industrial sponsor of this investigation, Rolls-Royce Plc. The aim being to apply the technology to the production of hybrid aero-engine components of high structural integrity. Consequently an experimental technique for evaluating this novel joining process will be developed in an aim to both produce a more industrially relevant process and assess the feasibility of joining industrially significant dissimilar steel, titanium and nickel alloys by this method.

## **2 LITERATURE REVIEW**

### **2.1 Introduction to literature review**

The primary deliverable of this investigation is to complete joining feasibility / compatibility studies on three separate alloy groups each exemplified by one alloy, Ti-6Al-4V, SCMV and IN718. These alloys have been chosen because of their importance in the gas turbine engine, specifically in rotor applications [4, 5]. This requires detailed knowledge of the alloy systems in terms of base metal properties, effect of alloying additions, behaviour during thermo-mechanical processing and the most pertinent alloy microstructures. This information is presented in sections 2.2 to 2.4.

The second deliverable of the project was to facilitate the development of a novel powder interlayer joining technique. As a result, the scope of this investigation covers a very wide range of manufacturing topics including, process development and design, experimental design, welding, diffusion bonding, resistance heating and powder metallurgy. These topics are covered in sections 2.5 to 2.8.

Finally, a review of the most relevant available literature on both the existing techniques for powder interlayer bonding and dissimilar joining between titanium, nickel and steel are presented in sections 2.9 and 2.10 respectively. Conclusions of the literature review are presented in section 2.11.

## 2.2 Titanium and titanium alloys

### 2.2.1 Pure titanium

Titanium exists in two allotropic forms,  $\alpha$  and  $\beta$ . These two phases are distinguished by crystal structure with  $\alpha$  being hexagonal close packed (HCP) and  $\beta$  being body centred cubic (BCC). These two structures exhibit different mechanical behaviour, and their control results in a wide range of alloys with a wide range of properties and applications. The  $\beta$  transus temperature for pure titanium is 882°C. It has a high melting point and is extremely reactive and as a result it is a hard material to extract from its ores. This is reflected in the generally high price for titanium alloys compared to more conventional materials such as steels. However, it has very competitive specific strength and stiffness values (detailed in Table 2.2.1) and excellent corrosion resistance. These properties have driven the development of its alloys primarily for the aerospace industries but also in its pure form for specific corrosive environments.

Table 2.2.1: A comparison of mechanical properties between commercially pure titanium, nickel and iron (data sourced from [6]).

Property	Titanium	Nickel	Iron
Melting point (°C)	1665	1400 – 2002	1535
Density (Kg/m <sup>3</sup> x 10 <sup>3</sup> )	4.505	8.89	7.86
Young's modulus (GPa)	120	75	210
0.2% Proof stress (MPa)	340	103	185
Tensile strength (MPa)	440	380	340
Elongation (%)	29	40	39

## 2.2.2 Alloy classification

The titanium alloys can be split up into five distinct groups that are defined by their microstructure. These are  $\alpha$ , near  $\alpha$ ,  $\alpha/\beta$ , near  $\beta$  and metastable  $\beta$ . Alloy type is determined by stabilising elements that promote the creation of either the  $\alpha$  or the  $\beta$  phase. The effects of  $\alpha$  and  $\beta$  stabilisers are detailed in

Figure 2.2.1 (a) and (b) respectively. Effectively,  $\alpha$  stabilisers act to push up the  $\beta$  transus resulting in a higher proportion of  $\alpha$  in the final microstructure, whereas  $\beta$  stabilisers reduces the transus temperature yielding more  $\beta$ .

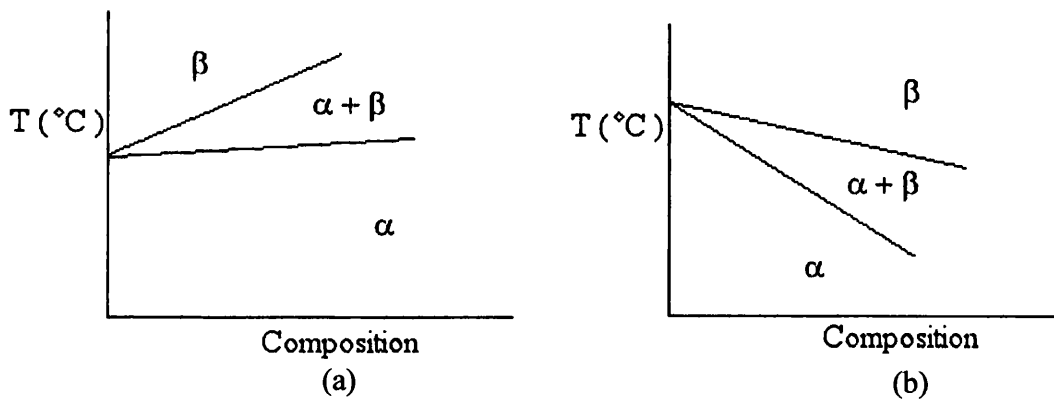


Figure 2.2.1: Effect of (a)  $\alpha$  stabilisers and (b)  $\beta$  stabilisers.

The two most common stabilisers are aluminium (Al) ( $\alpha$  stabiliser) and molybdenum (Mo) and as a result the effect of other stabilisers are expressed in terms of Al and Mo equivalents (equations 2.2.1 and 2.2.1).

$$\text{Al-equivalent} = \text{Al} + (1/3)\text{Sn} + (1/6)\text{Zr} + 10(\text{O} + 2\text{N} + \text{C}) \quad (2.2.1)$$

$$\begin{aligned} \text{Mo-equivalent} = & \text{Mo} + (0.67)\text{V} + (0.28)\text{Nb} + (0.2)\text{Ta} + (0.4)\text{W} + (2.5)\text{Fe} + (1.25)\text{Cr} + \\ & (1.7)\text{Mn} + (1.25)\text{Ni} + (1.7)\text{Co} \end{aligned} \quad (2.2.2)$$

### 2.2.3 Commercial alloys [7]

By careful control of the alloying elements above, many useful alloys have been produced. These are detailed in Table 2.2.2.

Table 2.2.2: Some examples of commercial titanium alloys [8].

Microstructure	Grade
Near $\alpha$	Ti-8Al-1Mo-1V (Ti - 811) Ti-6Al-5Zr-0.5Mo-0.25Si (IMI 685) Ti-5.8Al-4Sn-3.5Zr-0.7Nb-0.5Mo-0.35Si (IMI 834)
$\alpha/\beta$	Ti-6Al-4V (Ti - 6/4) Ti - 6Al - 2Sn - 4Zr - 6Mo (Ti - 6246) Ti - 4Al - 4Mo - 2Sn - 0.5Si (Ti - 550)
Near $\beta$	Ti -10V-2Fe-3Al (Ti - 10-2-3)
Metastable $\beta$	Ti - 15V - 3Cr - 3Sn - 3Al (Ti - 15-3-3)

Typically the  $\alpha$  alloys display excellent high temperature performance (especially the Ti - 834 and Ti - 685 grades) coupled with a low density (because of the high Al content). The  $\alpha/\beta$  alloys display high strength with good forgeability and excellent low cycle fatigue resistance. Near  $\beta$  and metastable  $\beta$  alloys also have good forging characteristics particularly at lower temperatures due to the stabilisation of the  $\beta$  phase at low temperatures.

### 2.2.4 Heat treatment processes

As well as making up the majority of engineering components in use today the  $\alpha/\beta$  processed alloys also provide the most scope for thermomechanical processing. Most processing steps in this group of alloys are designed to exploit the allotropic phase



transformation to produce microstructures ranging from near fully primary  $\alpha$  to fully Widmanstätten  $\alpha+\beta$  structures. This results in a wide range of mechanical properties in the subsequent alloys. Whilst the mechanisms involved in the microstructural evolution of these alloys is complex and has received considerable attention in the literature [9-11], only a basic appreciation of these factors is dealt with here. An excellent review of processing in titanium alloys is presented by Lutjering [12] and the four main heat treatments that are applied to the  $\alpha/\beta$  range of alloys are detailed below. These are:

1. Mill Anneal (MA). This is the most common of all heat treatments applied to titanium alloys and serves primarily as a retained strain reliever. In this respect it results in an alloy with good fatigue properties, moderate fracture toughness and reasonable fatigue crack growth rates (FCGR). However, has less of an effect on microstructure which is primarily dependant on prior thermo-mechanical work.

2. Re-crystallise Anneal (RA). This involves an isothermal treatment in the upper  $\alpha$ - $\beta$  phase field followed by slow cooling resulting in coarse grained bi-modal structures. The treatment results in increased ductility, leading to increased damage tolerance properties. This is offset by slightly reduced strength and fatigue performance. However, fracture toughness and FCGR are improved. A typical bi-modal structure is presented below in Figure 2.2.2.



Figure 2.2.2: Typical bi-modal structure observed in Ti-6242 [12].

3.  $\beta$  Anneal (BA).  $\beta$  annealing (sometimes termed  $\beta$  processing) involves solutioning the material in the  $\beta$  phase field and cooling to room temperature. Though the subsequent properties of the alloys, are dependant on cooling rate, in general the BA heat treatment yields the most damage tolerant materials. Strength is sacrificed and the fatigue strength is significantly degraded but fracture toughness and FCGR performance are both maximised. Three  $\beta$  annealed structures of different cooling rate are presented below in Figure 2.2.3.

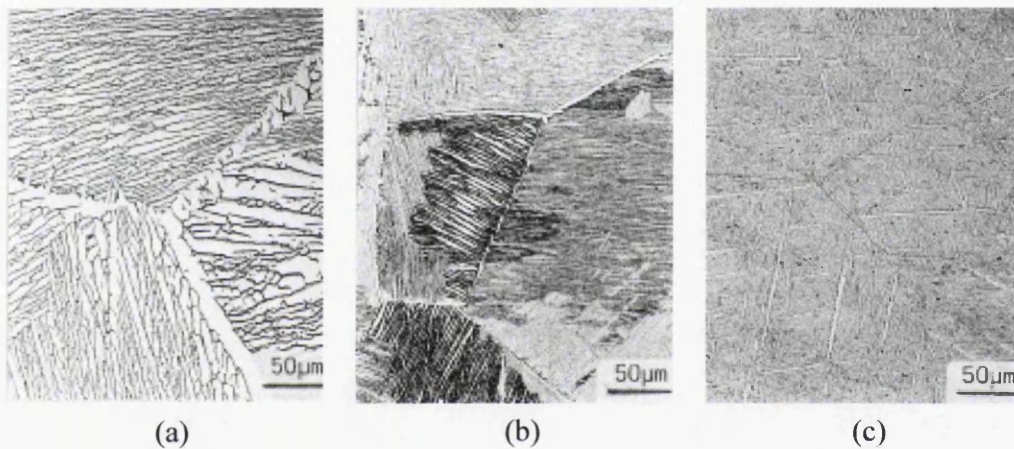


Figure 2.2.3: Three  $\beta$  annealed microstructures showing the effect of cooling rate from the  $\beta$  phase field, (a)  $1^\circ\text{C}/\text{min}$  (b)  $100^\circ\text{C}/\text{min}$  (c)  $8000^\circ\text{C}/\text{min}$  [12].

#### 4. Solution treated and aged (STA).

Essentially a two stage combination of BA and RA this heat treatment provides complete control over the microstructure and so can yield the broadest range of resultant mechanical properties. For this reason RA and STA microstructures can often appear very similar. However, recently it has been suggested the effect of prior mechanical processing on post HT mechanical properties in RA structures (specifically orientation effects), could account for differences in behaviour noted between similar RA and STA structures.

## **2.2.5 Application of titanium alloys in the aerospace industry**

Advantages of titanium alloys over conventional alloys such as weight and space savings, operating temperature, general corrosion and more specifically galvanic corrosion resistance lead them to be the materials of choice in demanding applications. Of course these superior properties come at an increased cost compared to alloys of iron and aluminium. These higher prices are dictated by both the difficulty of extraction of the pure titanium and to a greater extent the machining costs of titanium alloys components (which can be up to ten times the price for steels and aluminium). The use of titanium is virtually essential in many areas, such as components in a gas turbine engine. However, it is also applied in less demanding applications (purely because of its increased durability) where downtime can incur considerable cost e.g. in the power generation industry.

By far the biggest consumer of titanium alloys is the aerospace industry. Here all the advantages of titanium are exploited in different areas, from weight and space savings in the under carriage and fuselage of aircraft, to the high temperature performance in the gas turbine engines and corrosion resistance in the floor panels of toilets on commercial aircraft. Some of the most common alloy grades used in service will now be discussed in more detail.

### **2.2.5.1 The near $\alpha$ alloys**

These alloys sit at the high temperature performance end of the spectrum of properties for titanium alloys. Annealed near  $\alpha$  alloys such as Ti -3-2.5 have exceptional corrosion resistance and good formability which lends them to use in non-structural applications such as hydraulic tubing. Nevertheless, the two most widely used  $\alpha$  alloys are Ti -6242s and IMI 834. Ti-6242s is a popular material for discs, blades and rotors alike. This is mainly due to its good creep performance up to temperatures of around 540°C, combined with adequate fatigue properties and good corrosion resistance. This suits it for application in the early to mid stages of the high-pressure compressor. IMI 834 has similar properties but its structure

has been optimised to provide good mechanical performance at temperatures approaching 600°C.

It is worth noting here that beyond 540°C titanium alloys fail to meet the demanding requirements of the gas turbine engine (with the exception of IMI 834) and they are replaced by the nickel based super alloys in the super critical areas such as the combustor and turbine. This is because of a combination of factors, namely; the superior high temperature mechanical properties (i.e. fatigue and creep) of Ni based alloys, concerns that the titanium will ignite and burn, and oxidation problems leading to the formation of  $\alpha'$  and  $\alpha$  enrichment at the component surface severely degrading properties.

#### 2.2.5.2 The $\alpha/\beta$ alloys

Due to their microstructural versatility the  $\alpha/\beta$  alloys can be cast or forged. Castings tend to be used for more complex static components and forgings are used for the simpler rotating components. Ti-6-4 is the typical material of choice from the  $\alpha/\beta$  range of alloys as it is the commonly employed alloy of the industry. It is easily super plastically formed, to form complex shapes with good corrosion resistance; in the exhaust system for example. Furthermore, its resistance to galvanic corrosion allows it to be incorporated into structures using carbon fibre reinforced composites (CFRC) as well as being utilised as a matrix material for metal matrix composites. One in-service example being the vertical fin of the Boeing-777 [13].

Other alloys in the  $\alpha/\beta$  group include Ti-662, Ti-6-2-3, Ti-6-22-22, Ti-6246 and Ti-17. These are all alloys well suited to the demanding conditions of the aerospace industry and in fact some were specifically designed for it. Ti-6-22-22 for instance, was created in parallel with the construction of the American F-22 military aircraft. Unlike Ti-6/4 and its slightly stronger but less ductile partner Ti-662, Ti-6-22-22 offers strength coupled with excellent damage tolerance; evidently an important attribute in military aircraft. It has attracted considerable interest not only because of these properties but also because it

maintains the super plastic ability shown by Ti-6/4 at low temperatures following specific ('triplex') heat treatments.

At the other end of the  $\alpha/\beta$  alloy spectrum are the Ti-6246 and Ti-17 alloys. Ti-6246 offers high strength but only low damage tolerance. For this reason it has up until recently only been considered for military applications because the refits and checks required for civilian aircraft would become too costly. Ti-17 is a newer but more expensive alloy that has a slightly higher strength at an elevated temperature. Despite this advantage, the high temperature performance is the limiting factor for these alloys; this is mainly due to the creep performance at elevated temperature. Hence, although they can replace Ti-6/4 for strength, they cannot match the high temperature performance of Ti-6242s.

### **2.2.5.3 The $\beta$ alloys**

The applications of the  $\beta$  alloys range from landing gear and airframe components to their use as a spring material. The  $\beta$ -C alloy tends to be used for coil springs although it can also be shaped to rectangular springs for increased loads (at an increased cost). Ti-15-3 tends to be used in the manufacture of flat clock type springs, as sheet is its most popular form. It has excellent forming characteristics but tends to fail under triaxial stress conditions. Finally, Ti-10-2-3 is the most widely used of the  $\beta$  alloys. It is very versatile and can be produced at three different strength levels depending on the heat treatments employed. Typically companies favour the high strength variant as this results in weight and volume savings.

## **2.3 Nickel base Superalloys and Inconel 718**

IN718 is part of the Nickel – Iron based family of superalloys. All of these alloys share an (FCC) austenitic matrix composed of a solid solution of Nickel and Iron (Ni-Fe). This alloy group employs all three of the fundamental strengthening mechanisms of metallurgy, namely:

1. Solid solution strengthening.
2. Precipitation hardening.
3. Grain boundary strengthening (grain refinement).

All three of these mechanisms can be controlled by careful control of various alloying elements. The details of these elements and they're exact role in alloy strengthening will be dealt with in more detail later. However, a summary of common alloying additions and their role in microstructural and mechanical property development can be seen below in Table 2.3.1 and Table 2.3.2

Table 2.3.1: List of elements and their effect on nickel alloys [14].

	Matrix Class	Gamma prime class	Grain Boundary class	Carbide sub-class	Oxide scale sub-class
Ni	X				
Co	X				
Fe	X				
Cr	X			X	X
Mo, W, V	X			X	
Nb, Ta, Ti		X		X	
Al		X			X
C, B, Zr, Mg			X		

Table 2.3.2: List of elements and their effect on nickel alloys [15].

	Matrix Strengthening	Increase in $\gamma'$ volume fraction	Grain Boundaries	Other effects
Cr	Moderate	Moderate	$M_{23}C_6$ and $M_7C_3$	Improves corrosion resistance; promotes TCP phases
Mo	High	Moderate	$M_6C$ et MC	Increases density
W	High	Moderate		Promotes TCP phases $\sigma$ et $\mu$ (Mo,W)
Ta	High	Large		Promotes laves phase
Nb	High	Large	NbC	Promotes $\gamma'$ and $\delta$ phases
Ti	Moderate	Very large	TiC	Al improves oxidation resistance
Al	Moderate	Very large		
Fe		$\gamma' \rightarrow \beta, \eta, \gamma''$ or $\delta$		Decreases oxidation resistance; promotes TCP phases $\sigma$ , Laves
Co	Slight	Moderate in some alloys		Raises solidus; may raise or lower solvus
Re	Moderate			Retards coarsening; increases misfit
C	Moderate		Carbides	
B, Zr	Moderate			Inhibit carbide coarsening; improve grain boundary strength; improve creep strength and ductility

The nickel – iron family of alloys can be divided into four classes, these being;

**1. Alloys strengthened by way of (FCC)  $\gamma'$  precipitation.**

This class of alloys can be further subdivided into those that are iron (Fe) rich with nickel (Ni) contents between 25 and 30wt% and those which are Ni rich with Ni contents of around 40wt%. The Fe rich alloys (e.g. V-57) rely on titanium additions (to around 2wt %) for precipitation. Typically these alloys retain good mechanical properties up to 650°C. The Ni rich alloys (e.g. In-x750) utilise more solid solution strengthening with higher volume fractions of strengthening precipitates, resulting in improved strength and temperature capability over the Fe rich alloys.

**2. Nickel rich alloys strengthened by (BCT)  $\gamma''$  precipitation.**

This class includes IN718. Typically these alloys retain excellent mechanical properties from cryo-temperatures to 650°C.

**3. Iron rich Fe-Ni-Co based alloys.**

This group of alloys is also predominantly strengthened by  $\gamma'$ . However, it combines high temperature capability with low coefficient of thermal expansion through elimination of ferrite stabilisers such as Cr and Mo. Unfortunately this comes at the expense of oxidation resistance on account of the low Cr levels. Alloys in this group include Incoloy 903 and 909.

**4. Alloys strengthened by carbides and nitrides.**

These alloys are strengthened solely by the formation of carbides throughout the microstructure and do not utilise any precipitation hardening. Hence their high temperature



performance is far superior to that of the other alloys in the Ni-Fe group with ceiling temperatures of around 1000°C. Hastalloy X is a typical example.

### 2.3.1 Metallurgy

The metallurgy of iron – nickel superalloys and in particular IN718 is complex, the following section deals with the most common constituents in detail, but also touches on the numerous minority phases which present in IN718 specifically. The relationship between phases described in this section and the microstructure can be better visualised with reference to Figure 2.3.1 and Figure 2.3.2 below.

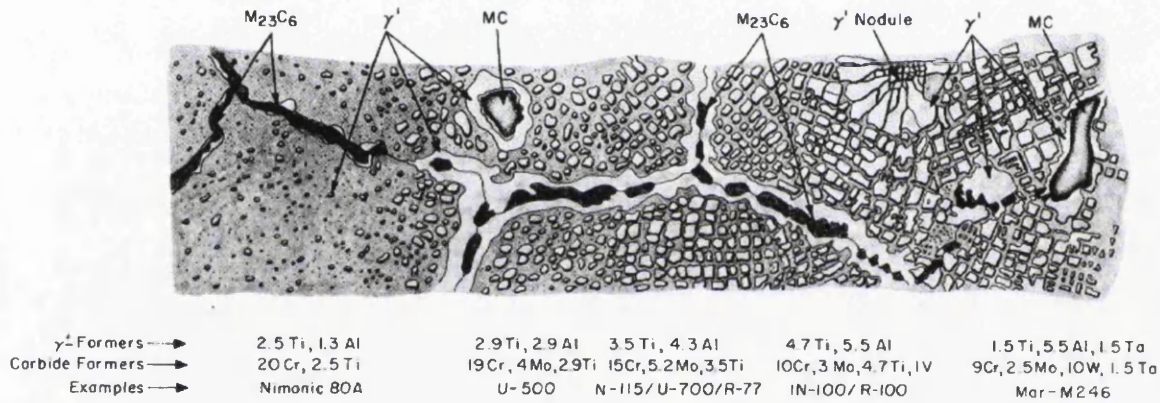


Figure 2.3.1: Nickel alloy microstructure, 5000x [16].

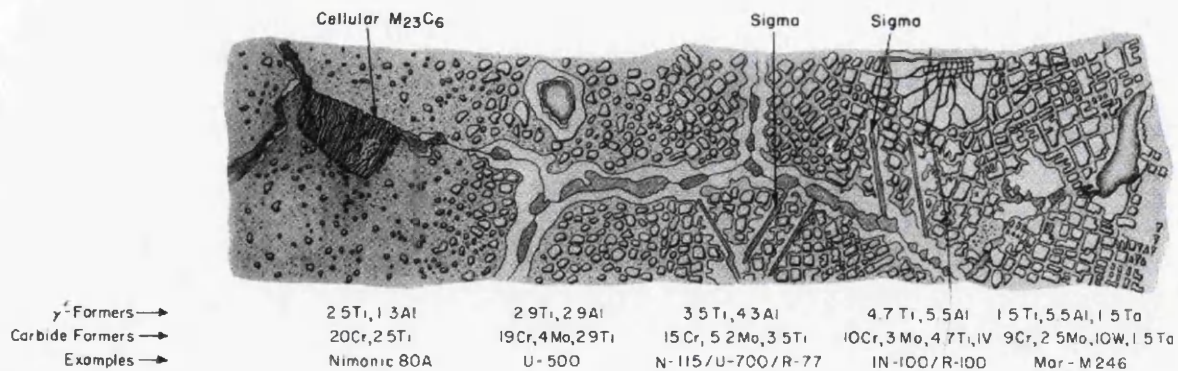


Figure 2.3.2: Common unwanted phases or structures, 5000x [16].

### **2.3.1.1 Austenitic matrix**

As mentioned previously, the austenite matrix of Ni-Fe alloys can range from Ni lean (~35wt%) to Ni rich (>40wt%). This basic consideration is important as it has a large effect on both the alloy's cost and its effective temperature range. Low carbon levels and high amounts of Mo and Cr (ferrite stabilisers) can force the minimum Ni content to 25wt% in order to preserve the austenitic matrix. Additions of Co (and other) austenite stabilisers can reduce the Ni content required to considerably less than this. Iron rich matrices lack the stability of their Ni rich counterparts which limits the amount of solid solution and precipitation hardening elements that can be added. Typically as the Fe:Ni ratio increases, cost is reduced at the expense of corrosion resistance, but forgeability is increased.

### **2.3.1.2 Solid solution strengtheners**

Cr (10-25wt%), Mo (0-9wt%) and to a lesser extent Tungsten (W) form the three main elements used for solid solution strengthening of the austenitic matrix. Chromium (Cr) acts to expand the lattice while Mo contracts it. Hence, the solubility of the precipitation hardening elements such as Ti, Aluminium (Al) and Niobium (Nb – Columbium) in the matrix is substantially reduced. This effect enables the use of solid solution strengthening elements in minimising the required level of these precipitation hardening elements. The alloying also helps to reduce stacking fault energies impeding cross slip at elevated temperatures. Generally it can be said that as well as strengthening effects, solid solution alloying elements have a considerable effect on precipitation hardening.

Aside from strengthening, Cr also has a large effect on oxidation resistance by the formation of a sacrificial oxide film. The threshold value for the formation of this film is around 9wt%, and generally Cr additions are well in excess of this value. However, it must also be acknowledged that increased chromium leads to an increased coefficient of thermal

expansion. If this is to be minimised then low Cr alloys must generally incorporate a protective coating at temperatures in excess of 480°C.

### **2.3.1.3 Precipitation Strengthening**

As previously mentioned the two principle phases used in precipitation hardening of Ni-Fe alloys are (FCC)  $\gamma'$  and (BCT)  $\gamma''$ . Both precipitates are  $A_3B$  type compounds.

$\gamma'$  forms in the presence of Ti and Al, which are the principle age hardening constituents in alloys such as A-286 and A-901. As the Ti:Al ratio increases the  $\gamma'$  lattice parameter increases. To minimise the misfit between the  $\gamma$  and  $\gamma'$  phases a high ratio is required. At a ratio of around 2:1 a metastable  $\gamma'$  forms which can then transform to a hexagonal  $Ni_3Ti$  at high temperature with a consequent detrimental affect on mechanical properties.

$\gamma''$  forms in the presence of Nb as the principle constituent for  $\gamma''$  precipitation in alloys like IN718 and the IN706. In the case of In-718 certain amounts of Ti and Al are also included so that  $\gamma'$  and  $\gamma''$  are able to coexist within the microstructure; for In-718 the  $\gamma':\gamma''$  rations is between 2.5 and 4.0. It has been shown that below 0.2wt% Al  $\gamma''$  predominates, while over 0.5wt%  $\gamma'$  is dominant. The large effect of small Al additions is due to the high solubility of Nb in  $Ni_3Al$  compared to the low solubility of Al in  $Ni_3Nb$ .

### **2.3.1.4 Other alloying elements**

Boron (B), zirconium (Zr) and carbon (C) are the most significant of the minority alloying elements in Ni-Fe alloys. Both Zr and B aid spherodization of secondary phases and precipitates leading to an increased ductility over platelet structures. Both are also key contributor to an increase in stress rupture strengths. It is worth noting that B content is generally restricted to low levels because it resists  $\gamma'$  formation. Carbon, and sometimes manganese (Mn), are typically used as a deoxidants. In the case of carbon this leads to the formation of MC type carbides that are useful in pinning grain boundaries and hence

refining grain size. Finally, small additions of magnesium (Mg) help to improve rupture strength and ductility by modification of grain boundary and secondary phase morphology.

### **2.3.1.5 Other phases**

There are various different carbide types found in this family alloys the most popular of which is the MC type. These form with idiomorphic, irregular, large globular and film (highly detrimental) morphologies on solidification. The particles tend to form preferentially at grain boundaries Heat treatments and hot working appear to have little effect on these phases post freezing. Depending on alloying either NbC or TiC are the predominant forms of carbide though other carbides can form with Ta, V and Mo. Other less common carbides include  $M_6C$  (which forms in the presence of Mo (3wt %)) that grows within IN718 grains and more importantly  $M_{23}C$ .  $M_{23}C$  carbides (mostly  $Cr_{23}C$ ) grow at the expense of MC type films that can form during service, through specifically designed heat treatments. This results in vastly improved ductility and overall mechanical integrity.

Finally, compressibility factors in most Ni-Fe alloys can cause the formation of TCP ( $A_2B$  type) phases e.g.  $\sigma, \mu, \chi$  or laves. IN718 is particularly susceptible to laves phases which are considered to have a deleterious effect on mechanical properties. These and other minority phases of importance will be dealt with later.

## **2.3.2 Strengthening mechanisms**

### **2.3.2.1 $\gamma'$ precipitation**

As with all precipitation hardened alloys, for a constant volume fraction ( $V_f$ ) of  $\gamma'$  strength increases as the  $\gamma'$  precipitate size increases up to an optimum size. Beyond this the strength decline rapidly and the alloy is termed over aged. This occurs as a result of optimum conditions for the precipitate to resist particle cutting and looping by dislocations

passing through the matrix during deformation; similar to the formation of GP zones in precipitation hardened aluminium. FCC  $\gamma'$  is coherent with the matrix, but coherency strains are low and not a major source of alloy strengthening compared to that explained above.

### **2.3.2.2 $\gamma''$ precipitation**

Ordered BCT  $\gamma''$  results primarily as a result of Nb addition and is the principle strengtheners in IN718. It is considered as a superior strengthening precipitate to that of  $\gamma'$ , mainly due to its increased resistance to cutting by dislocations. This is due to the difference in long range order between the BCT and FCC lattices i.e. whereas FCC  $\gamma'$  requires only two  $a/2 \langle 110 \rangle$  dislocations to be reordered in any direction, BCT  $\gamma''$  requires two out of three directions for the super dislocation to progress. Furthermore, unlike  $\gamma'$ ,  $\gamma''$  also provides strengthening through coherency strains between itself and the  $\gamma$  matrix. Unfortunately, these strains are also a source of instability in temperatures above 650°C.

The presence of  $\gamma''$  precipitates also accounts for the excellent weldability of IN718 compared to other superalloys. This direct influence comes through the slow age hardening characteristics of the phase, preventing hardening post welding. Commercial heat treatment processes aim to produce  $\gamma''$  precipitates with a disc morphology in IN718 with an optimum diameter of around 600Å and thickness of 50-90Å.

### **2.3.2.3 Over aging**

As well as the more fundamental particle coarsening effects leading to reduced strength (Orowan [17]) that are observed in Ni based superalloys, other more complex phase transformations occur in Ni-Fe alloys as a result of over aging. Metastable forms of  $\gamma'$  and  $\gamma''$  can transform to  $\eta$  and  $\delta$  respectively. The importance of these phases will now be discussed in more detail.

#### 2.3.2.4 The $\eta$ phase

The HCP  $\eta$  phase can form as intergranular platelets (sometimes widmanstatten) or in cellular grain boundary forms. As with its parent phase,  $\eta$  formation is dependant on the level of Ti in a given alloy, with the  $\eta$  proportion increasing with increasing concentrations of Ti. However, the other main  $\gamma'$  former, Al results in  $\eta$  retardation as the HCP lattice has no solubility for Al. Hence  $\eta$  forms only as a result of diffusion of Al leading to local depletions. Furthermore the presence of Al also reduces the  $\gamma$ - $\gamma'$  mismatch and therefore the driving force for  $\eta$  formation.

On the whole  $\eta$  formation is considered to have a detrimental effect on mechanical properties. Growth of both ( $\gamma$ + $\eta$ ) lamellar and widmanstatten structures which have both been shown to degrade mechanical properties. Typically lamellar structures form between 600 and 850°C, whereas widmanstatten structures tend to form at temperatures above 800°C; an important consideration when dealing with Ti rich Ni-Fe superalloys. Even so  $\eta$  is sometimes used as a grain refiner by heat treating and quenching from around 720°C. The resulting intergranular platelet structure yields increased strength at the expense of rupture ductility.

#### 2.3.2.5 The $\delta$ phase [18]

Forming in a similar manner to that of  $\eta$  from  $\gamma'$ , orthorhombic  $\delta$  ( $\text{Ni}_3\text{Nb}$ ) is an important phase with regard to the IN718 alloy. Typically, high silicon (Si), Nb and low Al contents promote  $\delta$  formation. In IN718  $\delta$  occurs between 650 and 980°C with platelet morphology, and to a lesser extent in randomly orientated globular forms at the grain boundaries. Below 700°C  $\delta$  formation is slow, but above 700°C rapid acceleration in both  $\delta$  formation and  $\gamma''$  precipitate growth occurs. At around 885°C  $\gamma''$  solutioning occurs and between 850 and 950°C  $\delta$  formation is at its most rapid (resulting in a highly detrimental and widespread widmanstatten structure in a matter of hours). Cellular forms of  $\delta$  are not observed in commercial alloys. Nevertheless, studies on experimental alloys have shown that cellular morphologies are dominant at temperatures below 700°C whereas platelet morphologies

predominate at temperatures in excess of this value (this is consistent with the morphology relationship observed for the  $\gamma'$  to  $\eta$  transition).

Increased forging below the  $\delta$  solvus (1000°C) results in rapid nucleation kinetics and the regular intragranular precipitation. This is effective in producing extremely fine microstructures. Forging and heat treatments also result in globular  $\delta$  which is found to both aid grain size control and prevent long range grain boundary sliding in IN718. Nonetheless, it is important to balance these benefits with the fact that the formation of  $\delta$  gradually degrades properties over time as a result of the decreasing  $\gamma''$  proportion (as a result of the  $\gamma''$  to  $\delta$  transformation) and  $\gamma''$  coarsening. It is also important to note that these effects accelerate considerably over temperatures of 650°C; hence the quoted ceiling temperature for IN718.

#### **2.3.2.6 Minority phase formation**

Ni-Fe alloys are more prone to G, $\sigma$ , $\mu$  and laves phase formation than the Ni based superalloys. All of these phases are considered to be detrimental to mechanical properties, causing severe embrittlement. The laves phase is promoted by increasing amounts of Nb, Ti and Si, and as such is especially relevant to IN718. Additions B and Zr go some way to counteract both laves and  $\mu$  phase formation. The complex cubic G phase (e.g. NiTi and NiSi) acts to reduce stress rupture life, but has little negative effects on other mechanical properties.  $\sigma$  forms with a platelet morphology. Brittle fracture at the interface between these platelets and the parent material can lead to large scale embrittlement, but growth of the  $\sigma$  phase can be retarded by careful control of Cr and Mo. While each of these phases have a real effect on overall mechanical properties, their formation during service is relatively rare. This is largely due to the fact that most Ni-Fe alloys operate at temperatures below 760°C. Furthermore, the lean nature of the alloys makes large volume fractions of these minority phases unlikely.

### **2.3.3 Processing Ni-Fe alloys**

#### **2.3.3.1 Ingot production / purification**

Vacuum induction melting (VIM), vacuum arc re-melting (VAR) and electroslag remelting (ESR) form the basis of clean homogenised ingot production [19]. VIM minimises light elements such as nitrogen (N) and oxygen (O) which may go on to form compounds at the expense of useful reactive elements such as Ti and Al. Crucially VIM also removes any pre-existing carbides to form CO which is extracted by the vacuum. VAR and ESR work in similar ways to increase homogeneity by systematically remelting an ingot to segregate unwanted impurity elements and carbides from the parent alloy. Subsequently, ingot breakdown incorporates thermal homogenisation (at 1100 to 1200°C) to remove  $G$ ,  $\sigma$  and laves phases etc. This also helps to reduce a pre-existing local concentration gradients i.e. partitioning of Nb and Ti.

#### **2.3.3.2 Structure / property control**

As with all alloys grain size is the most important controllable metallurgical factor i.e. development of coarse grained microstructures for creep resistance and fine grained microstructures for fatigue resistance and increased strength. In this respect the main advantage Ni-Fe alloys over their Ni based counterparts is the use of the  $\eta$  and  $\delta$  phases in grain size control. During recrystallisation the temperature must bridge the  $\gamma'$  and  $\gamma''$  solvus'. After this the temperature is kept below the  $\eta$  and  $\delta$  phase solvus' so that these phases may then be used for grain size control. For instance, heat treating below the  $\gamma''$  solvus in In-718 produces little or no grain growth because they are pinned by intragranular globular  $\delta$ ; such heat treatments tend to over age the  $\gamma''$ , resulting in reduced strength. Considering these factors, typical treatments normally involve forging followed by hot deformation and quenching to preserve the forged microstructure. This is termed 'direct ageing' and results in very high strength alloys.



## 2.4 Cr-Mo-V Steels

Whilst the superclean Cr-Mo-V (Super CMV) system under investigation is a specialist alloy, much of its properties and material behaviour are controlled by fundamental metallurgy. The following sections summarise the pertinent issues relating to the SCMV alloy from this basic metallurgy through alloy development and onto more complex structure / property control considerations.

### 2.4.1 Basic metallurgy

Like titanium, iron is allotropic and can exist in three different forms dependant on temperature BCC  $\alpha$  (ferrite), FCC  $\gamma$  (austenite) and BCC  $\delta$  ferrite. Through the use of  $\alpha$  and  $\gamma$  stabilisers both ferrite and austenite can be retained at room temperature but  $\delta$  ferrite exists so close to the iron melting point at such a narrow temperature window that it can be ignored in terms of physical metallurgy. Carbon remains soluble in these phases up to a point where orthorhombic cementite  $\text{Fe}_3\text{C}$  then becomes the most stable phase. As a result, carbon additions alone can then be used to produce a range of steels of vastly different properties. This can be better visualised with reference to the iron-carbon phase diagram below in Figure 2.4.1. Most conventional steels have carbon concentrations between 0.1 and 0.8% as these are hypo eutectoid microstructures that retain primary ferrite and pearlite (a ferrite / cementite contiguously grown lamellar eutectoid microstructure). Increasing carbon content between these values will;

- Increase tensile strength
- Increase hardness
- Decrease ductility
- Decrease fracture toughness

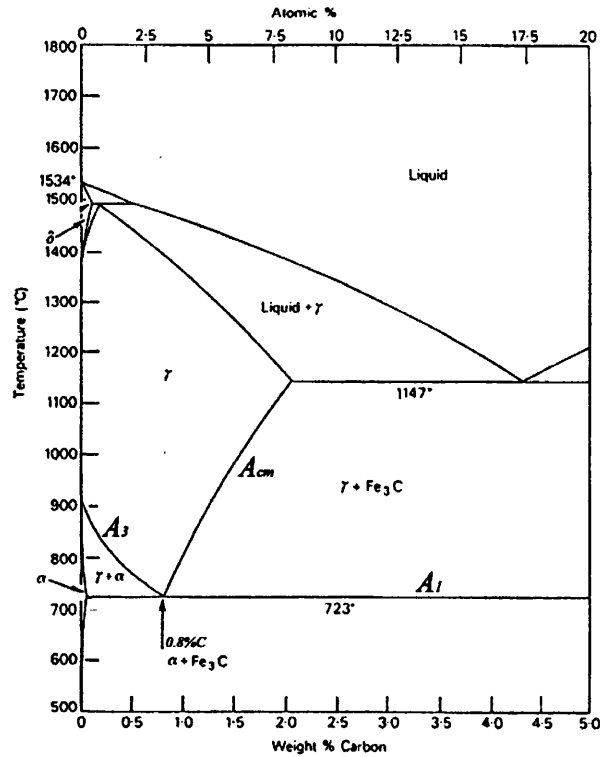


Figure 2.4.1: The iron-carbon equilibrium phase diagram.

In addition to this, carbon steels can also exist in two further microstructural forms via displacement transformations; these are martensite and bainite. BCT martensite forms as a result of a displacive / military transformation that occurs when quenching from the high temperature austenite region to room temperature. The temperature at which martensite first forms is known as the  $M_s$  temperature and is a key materials property in steels. Whilst this can be controlled by advanced alloy additions, it is most strongly dependent on carbon content (equation 1.3.1). Several constitutive equations have been put forward that attempt to quantify the effect of alloying additions on the  $M_s$  temperature, one of which is shown below in equation 1.3.1. However, for the most part it is acknowledged that with the exception of cobalt all alloying additions act to depress the martensite start temperature.

$$M_s (\text{°C}) = 561 - 474C - 33\text{Mn} - 17\text{Cr} - 21\text{Mo} \quad (1.3.1) [20]$$

Bainite forms by a combination of shear and diffusion to result in a plate or lath structure of ferrite and cementite. It exists in two states, feathery upper bainite which forms at higher temperatures over a short time and acicular lower bainite which is formed at lower temperatures over much longer times. Lower bainite tends to be much harder and less ductile than upper bainite. The influence of carbon on the martensitic and bainitic transformation can be seen in Figure 2.4.2.

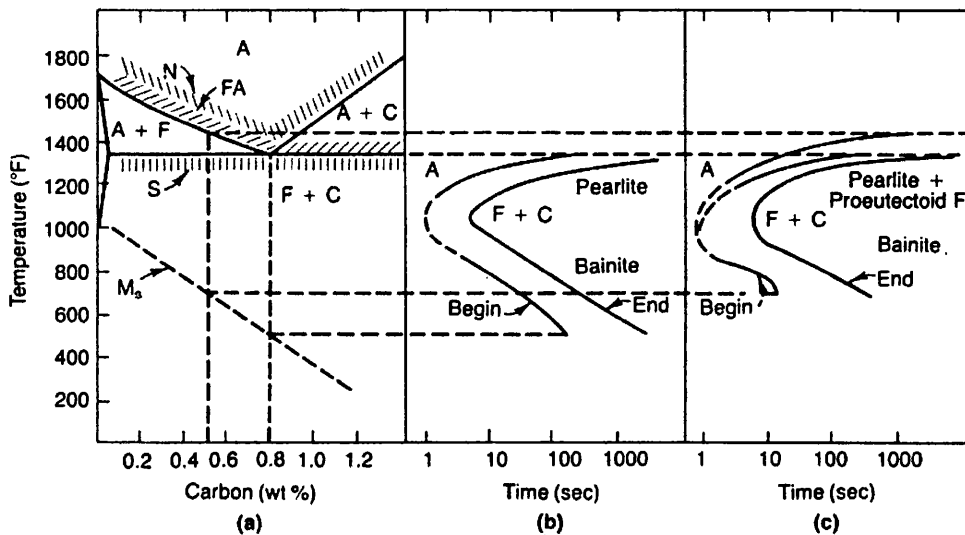


Figure 2.4.2: Relationship to Fe-C phase diagram (a) of IT diagrams of eutectoid steel (b) and steel containing 0.5% carbon (c) [21].

### 2.4.1.1 Martensite

Unlike the transformation between austenite and ferrite or cementite, room temperature martensite and high temperature austenite have the same carbon concentration as no diffusion occurs during the transformation. The concentration of carbon in austenitic iron is not stable at room temperature, so expansion in the FCC austenite lattice to produce a BCT crystal structure occurs to accommodate it. This creates an associated strain in the lattice known as the Bain strain. This strain is directly comparable to the amount of carbon present in the lattice (as more carbon atoms require more interstitial sites and so cause a greater lattice distortion). The Bain strain in the crystal results in shear, producing the displaced material as BCT martensite, hence the term displacive transformation. The nature of this shear and subsequent microstructural features depend on the habit plains (crystal plains in

the austenite on which displacive phenomena occur) on which the shear occurred, dislocation density, temperature and most importantly the carbon content. These are in turn, defined by certain orientation relationships (Kurdjmov-Sachs and Nishiyama) which will not be dealt with in detail here. However, as a result, martensite presents in two microstructural forms, plate and lath.

Plate martensite tends to form in alloys with a carbon concentration in excess of 0.6% and consequently at lower temperatures. A typical plate microstructure can be seen in Figure 2.4.3 (b). Typically the plates formed are relatively coarse i.e. easily viewed under standard optical microscopy and also tend to form in quite irrational orientations and directions relative to the parent austenite structure. This is mainly due to the fact that the high carbon content (1.5-2%C) associated  $\{259\}_A$  habit plane on which they form has twenty four variants; a variant being a different orientation of an  $\{hkl\}$  plane as defined by a different arrangement of the hkl indices e.g. (295), (529) and (592) etc. At slightly lower carbon contents (0.9-1.4%C) the  $\{225\}_A$  habit plane predominates, (12 possible variants) leading to less randomly orientated microstructure. Hence, within plate martensitic structures deductions can be made on carbon concentration depending on plate orientations.

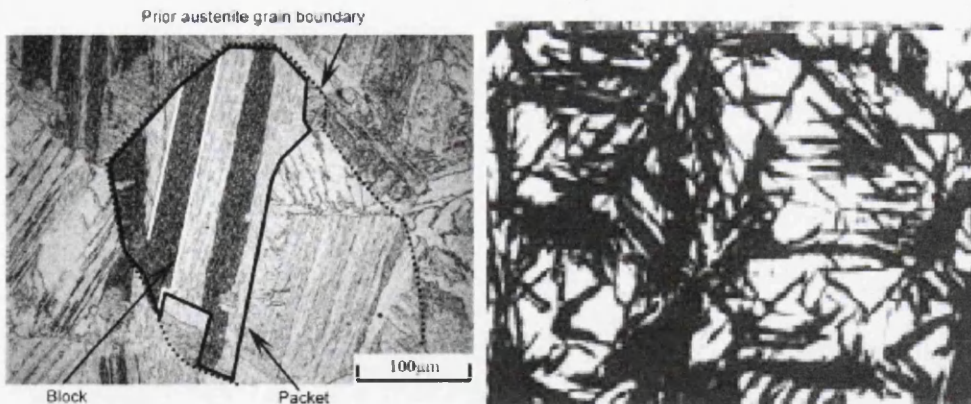


Figure 2.4.3: Microstructures of (a) lath and (b) plate martensite [22].

Lath martensite forms in alloys with a carbon content less than 0.6% and consequently at higher temperatures. Lath microstructures are more ordered and considerably finer in appearance and tend to align themselves parallel to one another. A typical lath structure can

be seen in Figure 2.4.3 (a). With reference to this figure it is clear to see that whole parent austenite grains can be occupied by as little as two or three variants. The areas occupied by each variant are known as packets. In actuality each packet may be made up of up to three variants itself. These are variants of the  $\{557\}_A$  irrational plane (close to  $\{111\}_A$ ). These three variants are clustered around the four  $\{111\}_A$  variants but have been found to have a misorientation of no more than  $16^\circ$ . This results in parent austenite grains being occupied by up to four packets defined by  $\{111\}_A$  variants which in turn contain up to three low angle  $\{557\}_A$  variants. Typically increases in carbon content lead to an increasingly varied orientation of laths i.e. a greater number of packets, as the microstructure converges on that of plate martensite.

#### 2.4.1.2 Bainite

The bainite formation may be thought of as part displacive, part diffusional. As in the case of pearlite, bainite is made up of ferrite and cementite but unlike pearlite it grows in non-lamellar arrays that are dependant on temperature and local alloy element concentration. As such, the growth of bainite is controlled both by diffusional rejection of carbon from ferrite to form cementite and the temperature at which the growth takes place. The transformation may also be considered displacive in so much as ferritic plates form with ordered dislocation paths and so to an extent rely on shear to form.

Upper bainite is characterised by the growth inter-lath cementite through the rejection of carbon into these areas. This results in a similar lath structure to that observed in high  $M_s$  martensite formation, but without the regularity of the purely martensitic transformation. The upper bainite structure itself grows in austenite in a more feathered and less ordered in nature than that of martensite. Interestingly some steels will see some of the carbon enriched austenite between bainite laths remain stable at room temperatures. However, more often than not, any retained austenite in the structure during cooling transforms to martensite.

Lower bainite forms at lower temperatures and is characterised by an acicular structure of large plates. It tends to be identified by the precipitation of carbides within the ferrite plates rather than between them. Furthermore, these carbides are much finer than the inter-lath carbides of upper bainite. This structure leads to a substantial difference in strength and ductility between the two bainitic forms.

### 2.4.2 Structure / property control

Heat treatment of steels can produce a variety of microstructures, from simple hypoeutectoid ferrite / pearlite microstructures through eutectoid steels to austenitic and duplex grades. Only those pertinent to this investigation will be dealt with in detail here, namely quenching or hardening treatments and tempering treatments for martensitic steels. Nevertheless, a basic appreciation of fundamental heat steel heat treatments is outlined below.

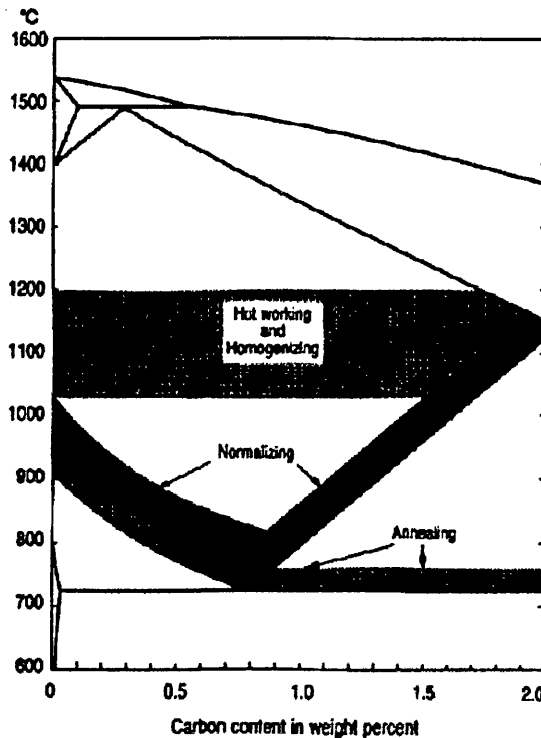


Figure 2.4.4: A section of the Fe-C phase diagram with temperature ranges for full annealing, normalizing and homogenisation indicated.

Figure 2.4.4 summarises well the basic heat treatments applied to ferritic and pearlitic steels, though it is worth pointing out that normalizing also has beneficial effects on hardenable steels. Annealing is performed just inside the single phase austenite region (above  $AC_3$ ) and results in spherodization of the cementite phase. This improves both ductility by making the ferrite matrix more continuous and fracture toughness by removing intergranular cementite that promotes catastrophic intergranular failure. Homogenisation occurs during hot work well within the austenite phase field. This reduces solute segregation and concentration gradients and dissolves harmful carbides via a diffusion controlled process. Finally normalizing occurs just above the  $AC_3$  and  $AC_{cm}$  temperatures and is designed to produce uniform but fine microstructures consisting of ferrite and pearlite. Normalizing post hot work generally results in a fine prior austenitic grain size and so can be a useful tool in steel hardening. Unfortunately, normalising tends to result in the precipitation of harmful grain boundary carbides, these can be spherodized or solutioned during subsequent homogenisation.

#### **2.4.2.1 Quenching / hardenability**

Hardenability may be defined as the susceptibility to hardening by rapid cooling and is the single most important attribute in high strength steels. As mentioned in section 2.4.1.1, carbon is the most important element in controlling hardenability in steels. The relationship between carbon content and resultant hardness can be seen in Figure 2.4.5. Having established this relationship, it can then be balanced against process parameters such as quench rate (quench medium). As is shown in this section the effect of carbon content and cooling rate can then be further manipulated by the addition of other alloying elements. This enables comprehensive control of alloy properties within the hardenable steels sector.

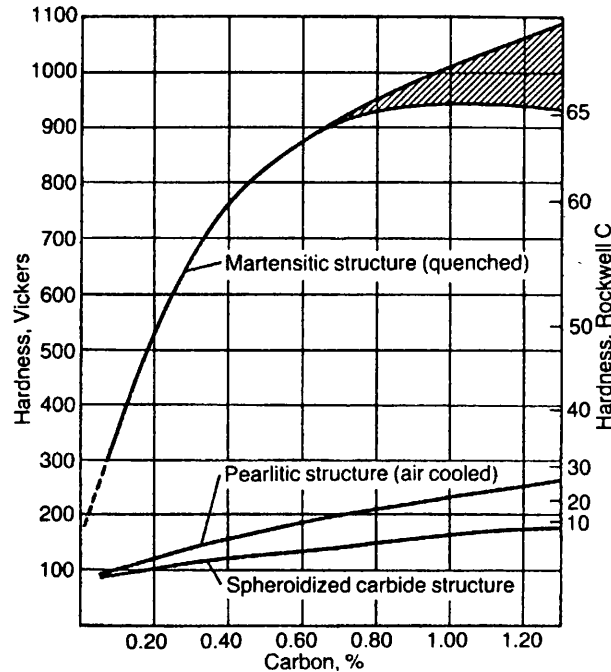


Figure 2.4.5: The effect of temperature and carbon content on plain carbon steels (hatched area denotes retained austenite as a result of high carbon content).

Given this relationship, cooling rate or more specifically ‘quench severity’ must be considered. Quench severity (H) is dependant not only on the medium but also crucially on material thermal diffusivity. As a result, cooling rates during a quench vary over a specimen cross section, being high at the extremities and gradually reducing towards the centre. In addition, local cooling rates are non linear and tend to follow the three stage process. This is characterised by slow initial cooling as a result of vapour insulating the specimen surface, rapid cooling as this ‘blanket’ breaks down allowing new media – surface contact and slow conduction / convection controlled cooling to ambient temperature below the medium boiling point. As a result of these effects, a considered choice of bar / specimen size, quench medium and any agitation to the quench (to disrupt the insulation effect) must be applied to alloys of varying carbon content.

The fundamental goal of introducing alloying elements to hardenable plain carbon steels is to limit the ability of the material to transform from austenite to ferrite or mixtures of ferrite and cementite. This can allow martensite formation at far reduced cooling rates to



those required for plain carbon steels. The effect of some typical steel alloying elements on hardenability can be seen in Figure 2.4.6.

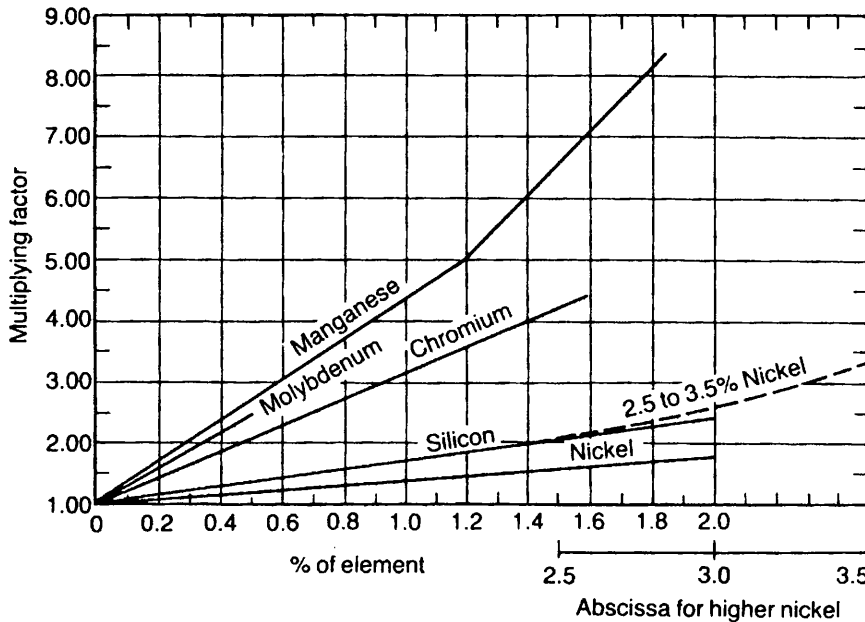


Figure 2.4.6: The effect of alloying elements on the quantitative hardenability of plain carbon steels [23].

To better visualize this effect in real terms it is useful to observe the changes that alloy additions can have on the CCT diagrams. This is demonstrated with reference to difference between the positions of the phase fields in the experimentally derived CCT diagrams shown in Figure 2.4.7 and Figure 2.4.8. The extension of the martensite field to encompass oil quenches and even rapid air cools are immediately apparent as is the depression of the  $M_s$  temperature. Bainite evolution has also been depressed significantly and pushed to slower cooling rates. Perhaps most influential of all is the considerable retardation of ferrite and pearlite formation, strongly limiting the possibilities of its occurrence in the microstructure. The use of bar diameter to define transformation also helps to emphasise the real effect that shifts in the fields bring. Namely that bars of increasing diameters may be fully hardened (full hardening is accepted as a microstructure containing more than 50% martensite) at given cooling rate and therefore quantitative hardenability may be said to have increased.

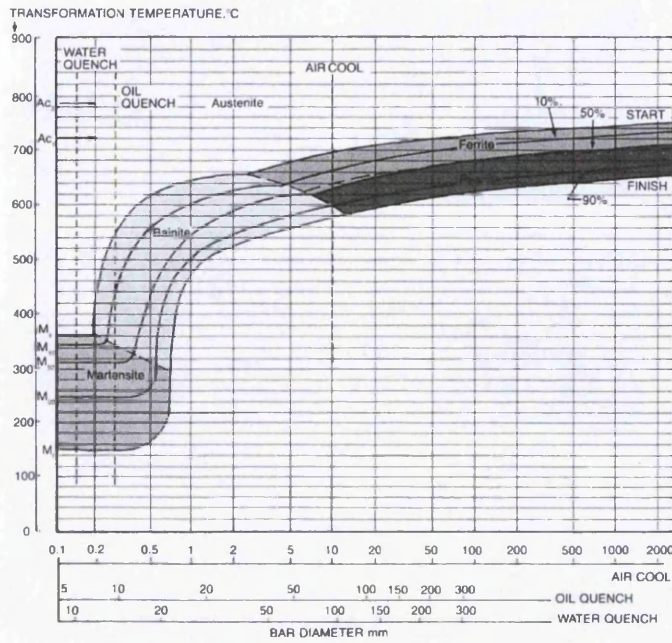


Figure 2.4.7: CCT diagram for a plain carbon steel containing 0.38%C and 0.7%Mn, transformations are plotted as a function of bar diameter [24].

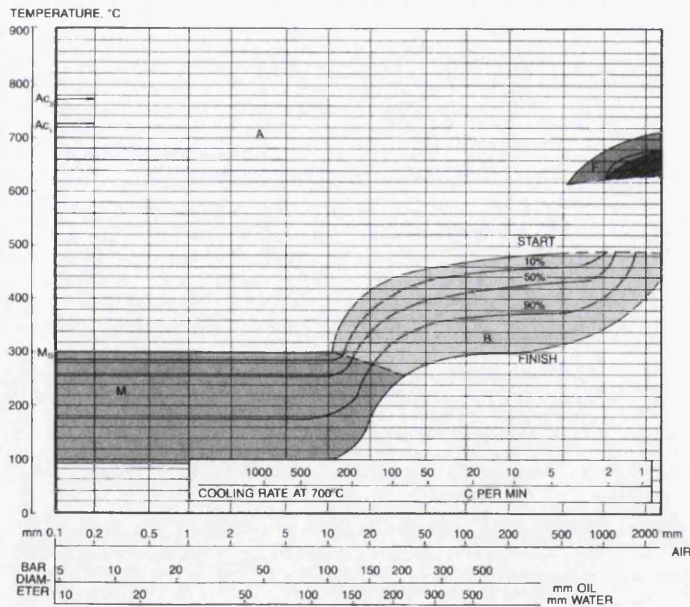


Figure 2.4.8: CCT diagram for an alloy steel containing 0.4%C, 1.5%Ni, 1.2%Cr and 0.3%Mo [24].

Quantitative hardenability is generally defined in terms of 'ideal size'  $D_1$  and proves useful in comparative and practical terms. It is essentially the size of bar which will fully harden

under a variety of quench severities. The effect of alloy additions are normally expressed as multipliers of this value, as they are in Figure 2.4.6.

#### 2.4.2.2 Tempering

Tempering can be defined as the heat treatment of brittle steels to improve ductility and fracture toughness. It is driven by the poor thermodynamic stability of martensitic phases at room temperature, with its high energy state allowing significant microstructural modification by diffusion even at relative low temperatures. Tempering is typically performed within two temperature windows around 150-200°C and 425-500°C. The lower window produces mild tempering associated with tool steel heat treatments, conversely the upper window is associated with a significant degree of softening and tends to be reserved for elevated temperature applications. It is important to note that the range between these two windows of around 350°C is associated with a hardening effect referred to as tempered martensite embrittlement or TME.

The tempering process may be considered temperature – time interchangeable, i.e. 5 hours in the lower window may produce similar effects to 30 minutes in the upper window. This relationship is quantitative and can be described by equation 2.3.2.2 below. Phase evolution during tempering can be broken down into three stages:

1.  $\epsilon$  carbide precipitation within martensite laths (150°C)
2. Transformation of retained austenite to ferrite and pearlite (200°C)
3. Replacement of martensite by ferrite and cementite (350°C)

Alloying additions can have the effect of retarding the softening effect during tempering. These are primarily carbide formers e.g. Cr, V and Mo. The effect of these elements is to produce carbides which limit martensite decomposition by forming inter and intra lath carbides. The effect of various elements for the two main tempering windows is summarised in Figure 2.4.9 and Figure 2.4.10.

$$T(20+\log t) \times 10^{-3}$$

(2.3.2.2)

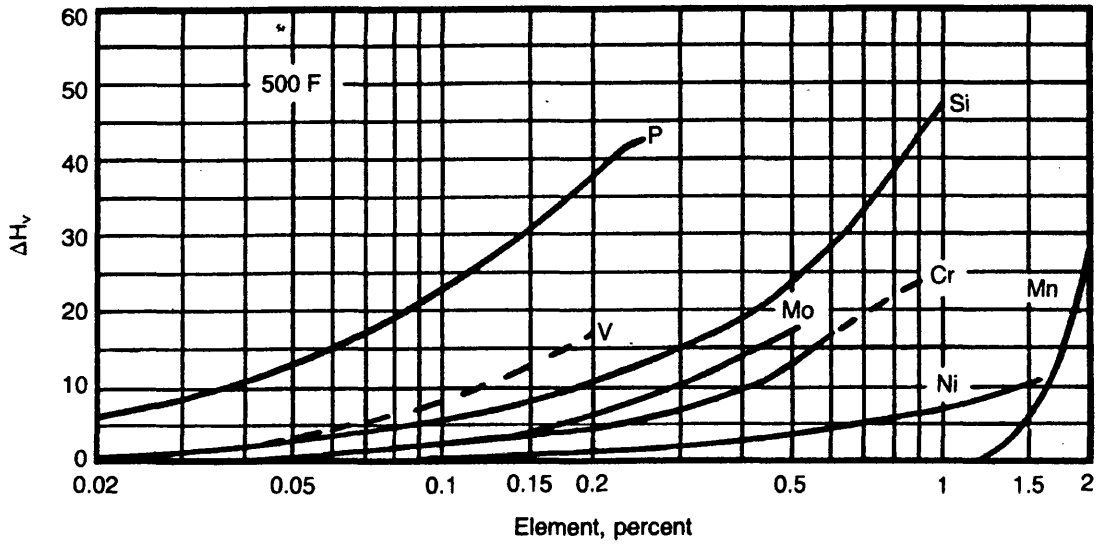


Figure 2.4.9: The effect of alloying elements on the retardation of softening during tempering at 260°C [25].

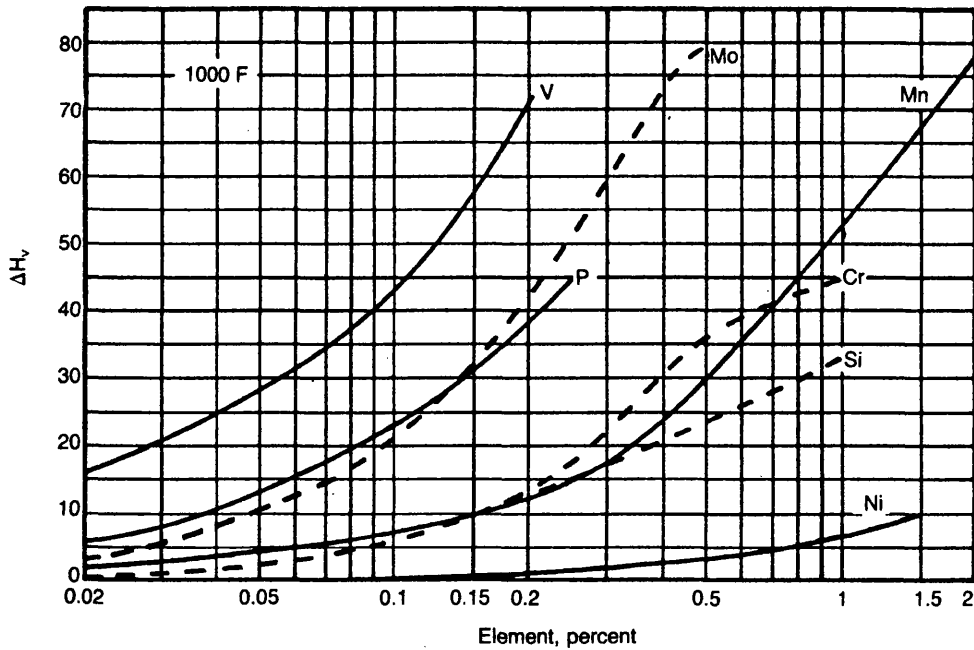


Figure 2.4.10: The effect of alloying elements in the retardation of softening during tempering at 540°C [25].

With reference to Figure 2.4.9 in particular, the impression is given that phosphorous is a useful element in retardation of tempering. However, its effect is so great that it can result in embrittlement effects summarised as temper embrittlement. Temper embrittlement (TE) is a major point of concern in processing steel, particularly those steels which require high temperature stability and hence undergo significant tempering (e.g. rotor steels in turbine engines). TE occurs within the high temperature window in tempering (375 – 575°C) and is associated with increased ductile / brittle transition temperatures. Embrittlement is a reversible process, for example, it could develop within an hour at 550°C but be eradicated in 15 minutes at temperatures in excess of 575°C. As previously mentioned TE relies on elements such as P, S, An, and Sn in small amounts and Si and Mn in large amounts to become prevalent, as these elements form carbides segregate to grain boundaries to induce brittle intergranular failure. In response to these additions of Mo help to form (Mo,Fe<sub>3</sub>)-P and Mo-P clusters that prevent segregation. To reinforce this effect, steps have also been taken to reduce Mn and Si to very low levels as they have also been found to directly segregate to grain boundaries to exasperate TE. These refinements tend to be achieved through VIM, VAR, ESR and ladle refining.

### **2.4.3 Alloy development and application**

Whilst significant microstructure / property control is possible through the manipulation of carbon content in the early plain carbon steels, attention soon focussed on the benefits of tertiary and quaternary systems to further influence mechanical properties; in particular hardenability. As such alloying additions were controlled by the effects outlined in sections 2.4.2.1 and 2.4.2.2. This led to a progression in alloy development, from the early hardenable steels to the Super CMV alloy, which is outlined below.

Early forms of the hardenable steels exclusively employed chromium and molybdenum such as the standard 2.25Cr – 1Mo grades. Despite enhancement, these grades were shown to be susceptible to temper embrittlement and poor creep ductility. This led to additions of vanadium and trace amounts of titanium and boron leading to the 2.25Cr-1Mo-0.25V and 3Cr-1Mo-0.25V-Ti-B grades. These alloys displayed improved creep properties and so

higher temperature capability [26]. Nevertheless, as demands on the materials increased a need for further improvements in strength and temperature capability was apparent.

It has been long recognised that inclusions and more specifically non-metallic inclusions have a deleterious effect on mechanical properties. The relationship between reduced non-metallic elements and improved creep, fracture toughness and fatigue properties are widely reported [27, 28]. As oxygen, phosphorous and sulphur are the most abundant residual elements and present the greatest problems in this regard, they draw the most attention. Many of the low alloy tempered steels (such as some tool steels) destined for sub critical application required little refinement beyond that which basic refining processes such as BOS and ladle refining could produce. However, for the more demanding aerospace and reactor vessel applications, the need for further alloy development through refinement was identified. This led to the concept of clean steels.

As pointed out by Kiessling [29], this is a debatable concept and no steel may truly be considered clean. Conversely, given that the tensile strength of pure iron is inferior to that of most steels, some may argue that steels can be 'too clean'. Here it is noted that cleanliness cannot be considered purely in terms of concentration but in a more holistic manner that assesses inclusion size and distribution. Taking critical inclusion size as an example, steels of given oxygen content can exhibit lower critical size where refinement has led to a wider distribution of inclusions. In an attempt to simplify these considerations it's generally accepted that cleanliness may be considered to be a probabilistic concept dependant on application. i.e. steel may be considered clean when the probability of finding non-metallic inclusions is small enough to satisfy the needs of the application. This synopsis proves useful in putting clean steel development into perspective as in reality it is almost always the applications that drive the alloy development.

It is much along these lines that the Rolls Royce developed Super CMV alloy was produced. The reasoning behind the advance is summarised well by Ford [30]. As engines evolved from the Olympus, through the RB211 and on to the Trent series, demands on efficiency led to higher bypass ratios and reduced core size. This in turn led to an increased demand on the shaft which also had to match the size constraints imposed by the

bore of the HP turbine disc. As a result the shaft material would have to withstand twice the torque (in the LP shaft) and deliver on a 25% weight reduction. In addition to this, the material also had to withstand the bend and uniaxial stresses associated with takeoff and a built in contingency for the high cycle fatigue regimes associated with a blade off scenario. The Rolls Royce engineered S/CMV alloy was the material of choice through the Olympus – RB211 era but it soon became apparent that this would not stand up to the demands placed on it by the Trent designs. As a result, the new Super CMV alloy was developed that was improved on the original alloy in three main areas:

1. Reduced tempering temperatures were employed to increase UTS which also produced an improvement in LCF life (Figure 2.4.11).
2. Alloy chemistry was adjusted to improve hardenability.
3. Triple vacuum remelting techniques were employed to improve cleanliness and hence enhance fracture toughness and HCF resistance.

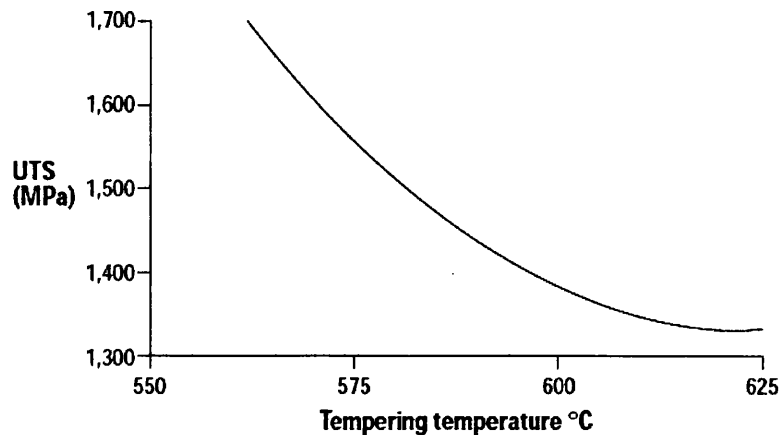


Figure 2.4.11: The relationship between tempering temperature and UTS for the S/CMV alloy [30].

The result was an alloy that delivered on both strength and weight criteria and also crucially was able to be processed under the same route as its predecessor. These developments coupled with design alterations pertaining to splined couplings between shafts lead to excellent shaft components that are still in use today.

## 2.5 Powder metallurgy

The primary role of powder metallurgy (PM) is as an alternative to conventional casting, facilitating solid state net shape component manufacture in materials for which conventional processes pose great difficulty. This includes materials susceptible to solidification cracking and hot tearing, refractory materials of high melting point (ceramics) and materials requiring high permeability such as filters and metal sponges. The solid state nature of the process lends itself to application for materials prone to segregation (high alloy materials) during rapid solidification, resulting in smaller volume fractions of deleterious intermetallic precipitates and inter-dendritic segregates [31] (PM is limited to as cast / sintered components and can produce forgeable materials which can achieve exceptional mechanical properties such as alloy RR1000 [32]).

As with any process, powder metallurgy has its disadvantages. The nature of many of the alloys produced by powder metallurgy (especially ceramics) result in low defect tolerances. Whilst deleterious solidification microstructures can be avoided, porosity, the primary defect source in PM components, cannot. Although smaller mean particle sizes help to reduce this effect, often subsequent thermo-mechanical processing is required to remove these defects. It is generally accepted that the multiple steps involved in conventional PM processes from powder production, compaction, sintering (consolidation) and on to subsequent component heat treatment define an inherent complexity and cost for the process. However, despite these drawbacks, PM manufacturing is increasingly popular in the aerospace industry.

The following section details the most pertinent aspects of powder metallurgy technology as it is applied to this investigation. The two 'second generation' powder metallurgy processes of metal injection moulding (MIM) and field activated sintering (FAST) receive particular attention.



### 2.5.1 Production of powders

The fundamental goal in powder production is to make as uniform a powder as possible in respect of particle size, morphology (e.g. irregular, clustered, spherical) and size distribution. Generally, finer powders (of highest apparent density) are considered to result in the highest quality components [33] but wide particle size distributions have also been shown to be beneficial [34]. In reality, decisions on powder quality are made by compromise between application and price. For instance, the small net shape components produced in metal injection moulding processes tend to use smaller, more expensive powders (1-40 $\mu\text{m}$ ), whereas for larger wrought components particle sizes in excess of 100 $\mu\text{m}$  may be acceptable [35].

Whilst several commercial powder preparation routes have been developed (mechanical, chemical and electrolytic), inert / soluble gas atomisation processes are acknowledged as the most effective. Although there are many variations on the theme the basic principles of gas atomisation are depicted in Figure 2.5.1. Essentially, a molten metal held in a tundish is fed through an annular nozzle into the atomisation tower. On falling from the nozzle the molten metal is separated into discrete particles as it comes into contact with a fluidised bed of gas. The rapidly solidified particles are then drawn by gas flow to a collector for storage and subsequent refinement. The resultant particles are typically of near spherical geometry with relatively low levels of porosity [36].

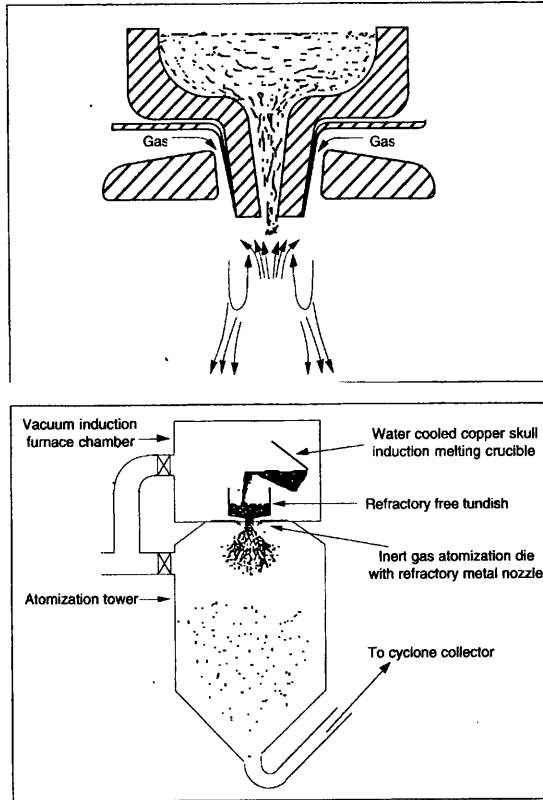


Figure 2.5.1: A schematic representation of the gas atomization process [36].

## 2.5.2 Compact consolidation – sintering

Following powder production and subsequent selection, cold compaction of the powders (with and without the presence of binders and lubricants) result in ‘green’ compacts, these can be (and often are) formed to near to net shape specifications (allowing for shrinkage during compact consolidation). Compaction is achieved by a variety of techniques including powder rolling, powder forging and unidirectional / isostatic pressing. These compacts maintain a ‘green strength’ which can allow them to be checked for tolerances and stored prior to consolidation. However, little increase in apparent density is noted at the compaction stage. Green compacts that have incorporated lubricants or binders undergo a further debinding stage prior to consolidation whereby they are heated (often in the presence of a vacuum) to allow vaporisation and degassing. The resultant debound compacts are said to be in the ‘brown’ state and maintain a ‘brown strength’.

Sintering is the heating of green or brown compacted metal powders to facilitate bonding between the particles within the compact. Traditional methods for sintering almost exclusively employ ambient / furnace heating and include, hot pressing, hot isostatic pressing and cold isostatic pressing etc [37]. However, over the last 20 years the implementation of electric current to facilitate consolidation through resistance heating has received increasing attention [38-41]. Known as field assisted sintering (FAST), the process has demonstrated significantly improved sintering capabilities at lower temperatures than that of its conventional counterparts [42]. Obviously, the mechanisms of FAST are of great relevance to this investigation. Consequently, inherent factors in PM such as inter-particle contact (and so particle size and shape), particle composition and particle structure will be discussed in the following section with particular reference to their role in the FAST process.

#### **2.5.2.1 Powder considerations**

Basic sintering process kinetics can be shown to be related to diffusion distance squared. Particle size determines the diffusion distance and hence has marked effect on the effectiveness and rapidity of compact consolidation. Particle size becomes especially important when considering the homogenisation of blends where the particle size of a minor constituent isolated in matrix particles (left indiscernible by the compaction process) becomes crucial. Blending is of high importance to the quality of the finished product. Poorly blended powders tend to homogenise more slowly as the inter-diffusion distances are large. The proportion of minor constituent within a blend has also been shown to effect process kinetics, reducing them as its proportion decreases.

Particle structure also affects both contact area and the diffusion distance, as in the case of a hard particle that is not easily deformed during the compaction stage. Particle shape is less important as the diffusion field itself is a more dominant factor in determining process kinetics. Only extreme variations in particle shape cause the diffusion field to deviate from a spherical nature. Finally, individual particle composition also plays an important role as it

defines the initial heterogeneity of the powder compact and so the concentration gradients that provide the initial driving force for diffusion.

In addition to these fundamental factors, further consideration is appropriate in FAST processes where heat is generated as a function of compact resistivity and thermal conductivity. These properties are known to change throughout compact consolidation and so particle microstructure (and subsequent hardness) and local thermoelectric properties are of importance [43]. Initial consolidation also depends strongly on complex local contact resistance effects at particle interfaces which will amplify the particle shape and size effects noted in conventional sintering. Finally, the use of blends may also affect local electric fields depending on their electrical properties, though these effects have not received attention in the literature.

#### 2.5.2.2 Process parameters

The primary influence of temperature in sintering is on atomic mobility, defined by the diffusion coefficient for the system, which can be given by the following Arrhenius relationship:

$$D_i = D_0 \exp\left(\frac{-Q_i}{RT}\right)$$

Where  $D_i$  is the inter-diffusion coefficient,  $Q_i$  is the activation energy for lattice diffusion,  $D_0$  is a material dependant constant,  $R$  is the universal gas constant and  $T$  is the temperature (K). Evidently, as temperature increases the rate of diffusion increases. Whilst these mechanisms apply to FAST it is important to note that the temperature profile is transient, being localised at inter-particle interfaces initially, and becoming more uniform throughout the process; therefore rates of diffusion and consolidation kinetics behave proportionally [44]. This initial concentration of energy can be considerable resulting in micro level arcing between particles. Far from being deleterious, this behaviour is thought to be beneficial as it helps to break down surface oxides (discussed in section 2.8.1) at the

interfaces and is cited as one of the primary reasons for the improvement in consolidation kinetics associated with the process [45]. Aside from temperature, current flow *itself* has also been shown to increase atomic mobility and subsequent phase transformation kinetics, phase evolution, crystallisation and defect mobility [46, 47]. These effects are thought to improve latter stage consolidation through the promotion of lattice / grain boundary diffusion.

Mechanical working prior to, during and after sintering can all have a marked effect on final alloy quality. Increased pressure during compaction results in a higher compact density resulting in better inter-particle contact and hence increased inter-diffusion. Work during sintering both induces lattice defects (increasing inter-diffusion coefficient) and alters particle / overall compact dimension. The lattice defects tend to anneal out rapidly at the high temperatures employed in conventional heat treating processes and so have little effect on subsequent component properties. Particle geometry on the other hand affects the inter-diffusion process throughout the process as it changes from spherical to tubular to planar. The increased area results in increased inter-diffusion, but the radical change in shape also transforms the diffusion field from 3D-2D-1D, reducing process kinetics. Nevertheless, large deformations that lead to these changes in particle geometry, usually result in increased homogenisation kinetics overall. More recently it has been shown that the plasticity of materials can substantially increase in applied electric fields, due to the effect of an “electron wind” which improves dislocation movement at a given temperature [48].

Whilst time is a key factor in manufacturing, as a process parameter it exists in a constitutive relationship as a function of pressure and temperature. Hence, for cold pressing processes longer times and higher pressures tend to be employed and *visa versa*. Given its importance on an industrial scale, often pressure and temperature are optimised to provide the shortest time possible whilst still maintaining component quality. Information available in the literature to date suggests that FAST processing can result in reduced consolidation times for a given temperature, pressure and quality compared to conventional processes.

### **2.5.3 Microstructural features of consolidated PM materials**

The microstructure of alloys produced by powder metallurgy generally consist of:

- The matrix
- Pores
- Un-dissolved particles
- Films of bonding material
- Precipitates
- Impurities

Each of these features, properly studied, can elucidate useful information on original powder quality, the degree of mixing, green strength, sources of defects and the post sintering process history of the alloy.

#### **2.5.3.1 Matrix**

The appearance of the matrix material can vary from a multicrystalline granular structure to one that is almost indistinguishable from that of the powder compact that preceded it. In this respect it provides the most obvious indication of the quality of the alloy produced. However, there are other more discreet features of its make up that can reveal a great deal about the specific history of the alloy. For instance, twinning is possible as a result of extensive pressing of the alloy followed by sintering. Further, grain boundary migration can be indicated by a polycrystalline mass surrounded by filamentary porosity (explained later). On the whole, improperly developed structures serve as a sign of under pressing or under sintering, whereas well developed structures are a sign of proper sintering, often at a temperature approaching fusion.

### 2.5.3.2 Pores [49]

The nature of powder metallurgy makes porosity the most important consideration in terms of the quality of the product. For this reason porosity defines the quality of an alloy produced by powder metallurgy. This leads to these alloys being grouped according to their total porosity levels:

- Materials with less than 10% porosity are termed high density material and tend to be applied to electrical contacts, magnets and hard carbides.
- Materials with 10-20% porosity form the majority of all parts produced as mass production engineering materials.
- Materials with 20-30% porosity generally have such high levels for a reason, porosity dedicated as oil reservoirs for self lubricating bearings for instance.
- Materials with around 70% porosity are reserved for specialised filter materials. [36]

Here it is worth noting that a material that contains 5% total porosity concentrated in a small area may have poorer mechanical properties than a material with 20% porosity distributed over a wide area. The total porosity must not only be quoted but *defined*. The fundamental factors to consider are outlined below.

#### 2.5.3.2.1 Porosity type

There are four different types of porosity. *Primary* porosity comes as a result of pores that were present prior to sintering and were not removed by the sintering process. *Secondary* porosity forms during the sintering process, generally from the formation of gas evolved on heating or precipitated from a liquid on melting. *Interconnected* porosity occurs at the interface between the original particles, these pores are eventually eliminated by solid state diffusion and grain boundary migration. Finally, *closed* porosity occurs from a combination of the closure of filamentary pores and surface tension effects acting at the pore interface; these are often, but not always, spherical. The appearance of closed pores indicates that a steady state is being approached in the process.

### 2.5.3.2.2 Porosity shape and distribution

Porosity shape is often defined by its mode of formation and can so elucidate information on process conditions:

- Filamentary porosity forms along the dividing lines between particle aggregates. They can be found in sintered or unsintered material.
- Irregular porosity is unsurprisingly related to neighbouring irregular particles. As sintering continues mass transfer, evaporation and surface effects lead to spherodization. Hence monitoring these irregular pores can help to monitor the progress of the sintering process.
- Lamellar porosity generally comes as a result of overlaying particles and more popularly from air trapped between flake material.
- Cuspid porosity occurs at the mid-stage of the spherodization of irregular particles.
- Spherical porosity can occur initially as a result of gas evolution but also forms as a result of the spherodization of other pores and so generally gives an indication of an approach to steady state transformation kinetics.

The distribution of pores throughout the structure is equally as important as the amount, shape, size and type of the porosity present in the material. Generally a uniform distribution indicates good mixing, pressing and sintering techniques and is obviously a sign of a narrow particle size distribution. Variable pore distribution is mainly due to a wide particle size distribution, although uneven temperature distribution is also a factor. Similarly, random porosity is unintentional and undesirable but tends to be as a result of the spherodization of isolated particles described above. Further to these general considerations four more specific pore locations are normally apparent:

- Myriad porosity accounts for minute pores created by gas evolution during sintering these are almost always of a closed type.
- Inter-particle porosity is an example of primary porosity, this is generally, but not always, a sign of poor sintering.



- Intergranular pores act as grain refiners and tend to be as a result of shrinkage in the liquid phase or air expelled by an advancing liquid phase (especially if the pores are large).
- Intragranular pores are closed pores within a grain due to insufficient ability to escape via filamentary porosity prior to grain boundary migration.

Careful consideration of a combination of the factors affecting porosity during microstructural evaluation would help to refine the properties of a material to best suit its application without the need for large scale mechanical testing.

### **2.5.3.3 Other defects**

There are two further defects traditionally associated with powder processed microstructures. These are un-homogenised particles and inter-particle carbide and oxide precipitation at prior particle boundaries (PPBS). In most cases impurities can be traced back to powder production in the form of surface oxides. Less likely, but still possible, is the introduction of impurities during the sintering stage. Impurities accrued at this stage tend to be due to inadequate atmospheric control.

### **2.5.4 Metal Injection moulding (MIM)**

Metal injection moulding is a 'second generation' powder processing technique that is of particular relevance to this investigation. Derived from the conventional injection moulding technology of the polymer industry, the process has the ability to produce complex parts at high productivity levels. The fundamental working principles of PIM are outlined in Figure 2.5.2. The process involves the mixing of a powder with a binder which is injected into a die through conventional techniques. The compacted green parts are then subjected to a debinding stage and the brown parts are then sintered to full density to produce the finished component. Crucially, the process is not associated with post consolidation thermo-mechanical processing which allows many hundreds of parts simultaneously and continuously in a production line setting.

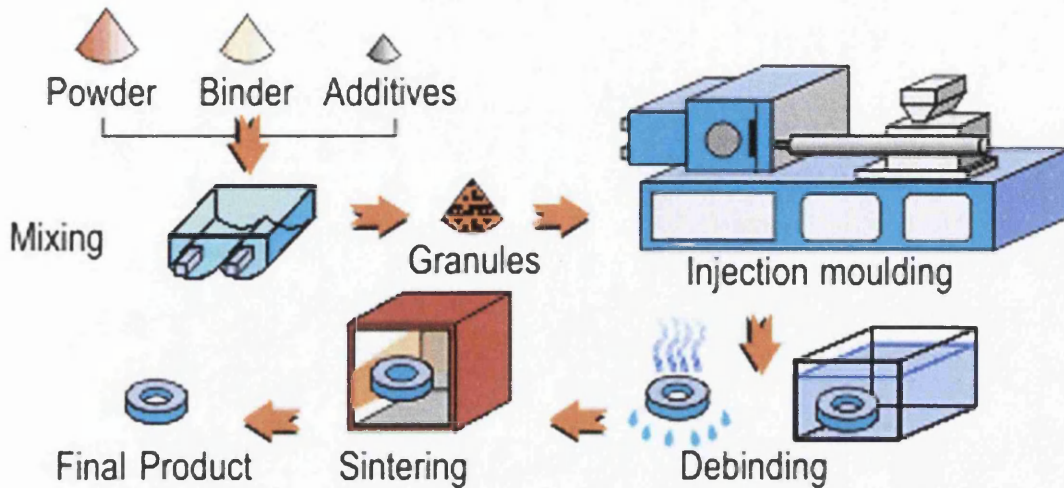


Figure 2.5.2: A schematic representation of the MIM process [50].

As a result of the aforementioned manufacturing benefits, the MIM industry is growing rapidly. Recently, refinements in the process have led to the production of high quality, high tolerance components which can compete with that of investment castings. With relative densities of 92 – 98%, these components are now being considered for more critical applications [51]. Some examples of MIM components can be seen below in Figure 2.5.3.



Figure 2.5.3: Examples of the complex geometry components that can be produced by the MIM process [52].

## **2.6 Fundamentals of welding**

Prior to the development of modern welding techniques the joining method of choice for metals came in the form of fasteners, normally bolts or rivets. For certain applications these are still the method of choice, in bridges and aircraft fuselage for instance. This is generally because the interconnecting but discrete panels or girders prevent large scale crack growth throughout entire structures which has been known to cause catastrophic failure in the past [53]. In this respect fasteners provide peace of mind but local joint strength is not comparable to that of a weld and crucially the level of productivity associated with welding is considerably greater. Careful choice of welding process, base metals, filler metals and joint design can yield excellent joined components rapidly and efficiently. Although conventional fusion welding does not fall under the scope of this investigation it is important to have an appreciation of these techniques when considering its findings. Some of the key aspects of welding / metallurgical joining are outlined in the following section.

### **2.6.1 Common considerations**

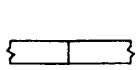
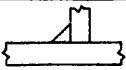


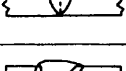
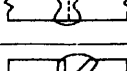
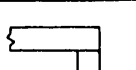


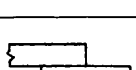
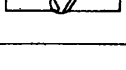
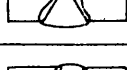
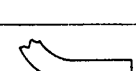




The main considerations for welded joints can be broken down into the following areas:

- Joint design
- Joining process
- Metallurgical factors / joint chemistry
- Cleanliness
- Post weld heat treatments
  
- A summary of all the joint designs can be viewed in

Table 2.6.1; these are T, Butt, Corner, Lap and Edge joints. Each can be broken down into several subdivisions which will not be dealt with in detail here. Choice of design is often intuitive. Nevertheless, briefly:

- Butt joints can be performed on a range of section sizes and tend to employ grooves to improve through section adhesion (
- Table 2.6.1).
- T and corner joints are similar in nature and often require little preparation, but corner joints in particular are hard to set in position and so suffer from low productivity.
- Lap joints are perhaps the most common joint designs for thin sections such as sheet. Easy lay up of these joints allows for exceptional productivity and lend them selves to high speed processes such as resistance spot / can welding.

Table 2.6.1: A summary of joint and weld designs.

Types of joints		Types of welds		
			Single	Double
Butt		Fillet		
T		Square		
Corner		Bevel groove		
Lap		V-groove		
Edge		J-groove		
		U-groove		

The results of previous investigations have shown that cleanliness is a fundamental factor in joint quality [2] and as described in section 2.4.2 the elements associated with dirty inclusions (Si, C and S) can have a severe effect on base metal properties. The level of cleanliness for welds depends on application and operating conditions and can range from clean room type conditions for aero and nuclear applications to minimal efforts for non structural components.

Metallurgical factors and standard heat treatments are discussed in the following sections with the plethora of the established welding techniques developed to date summarised in section 2.7

## 2.6.2 Weld microstructure and basic metallurgical factors

This section focuses on the typical metallurgical factors associated with fusion welds. Whilst some these may not have a direct bearing on the process under investigation many of them are pertinent, especially factors affecting the heat affected zone (HAZ). The two most useful theoretical tools for assessing metallurgical factors in welding are TTT and CCT diagrams. Of these the CCT diagram provides the most useful information, as isothermal transformations in welds are so short as to be non-existent. These diagrams are not referenced specifically in this section however it is important to remember that many of the factors touched upon herein can be deduced with reference to them.

### 2.6.2.1 Weld Structure

The typical weld structure was researched by Szekeres *et al* [54] who presented a methodology by which welds may be considered. This is summarised in Figure 2.6.1.

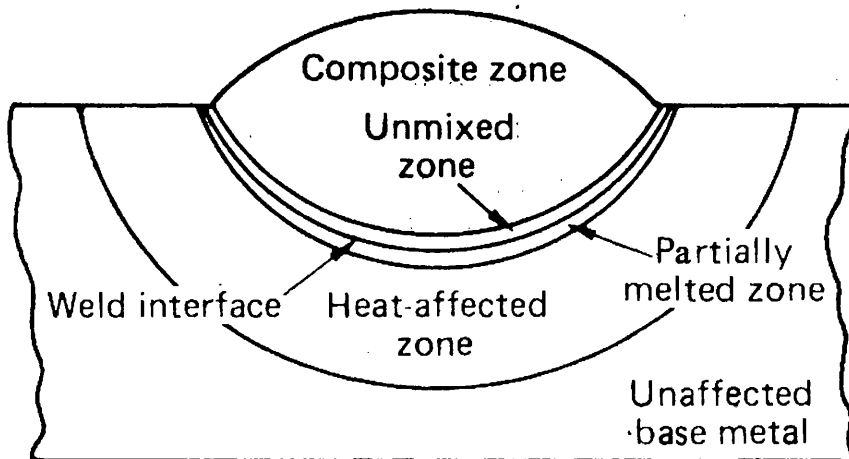


Figure 2.6.1: A summary of weld structures as presented by Szekeres *et al* [54].

The composite zone consists of a mixture of base metal and filler metal, where the mixing occurs as a result of convection. As the name suggests the unmixed zone consists of solidified base metal that solidified before mixing. The weld interface marks the transition between the melted region or fusion zone and the HAZ and is generally bordered by areas of partially melted material. Finally, the HAZ is defined as an area where microstructural changes have occurred as a result of solid state diffusion driven processes.

In the fusion zone the weld microstructure evolves through epitaxial growth of columnar grains from pre-existing lattice sites in the HAZ. The morphology of these grains can range from regular and perpendicular to weld direction with a well defined centerline (associated with a tear drop weld pool formed during rapid weld speeds), to more randomly orientated columnar structure (associated with a more spherical pool formed for low weld speeds). Generally high heat input and rapid weld speeds result in significant solute segregation to the centerline of the associated microstructure and poor weld quality. The solidification structure of columnar grains ranges from dendritic to cellular depending on the amount of constitutional supercooling (CS). Interfacial stability with reference to CS is presented in Figure 2.6.2, but in general the rapid cooling rates associated with fusion welding tend to result in dendritic substructures. This can result in a number of detrimental effects including the retention of high temperature phases in weld microstructures that are preserved within solute rich dendrite cores such as  $\delta$  ferrite in steels.

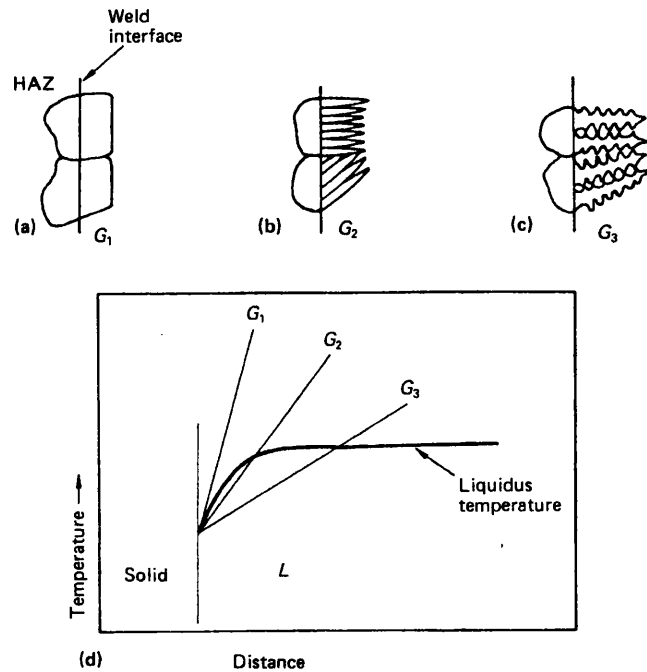


Figure 2.6.2: Effect of thermal gradient on the mode of solidification in welds for a constant growth rate (a) planar growth (b) intermediate or cellular growth (c) dendritic growth (d) solidification of the weld.

The HAZ microstructure shows the largest grain size immediate to the weld interface, from where grain diameter decreases with increasing distance. Aside from this effect the HAZ in single phase systems (such as Ni) is often indistinguishable from the base metal. However, the HAZ in allotropic systems (such as Fe and Ti) can show a wide variety of microstructures (sections 2.2.4 and 2.4.1) depending on local temperatures and cooling rates.

### 2.6.2.2 Typical Weld Defects

Unfortunately porosity is common in fusion welds and it tends to occur as a result of absorption of ambient gases at high temperature which then precipitates at low temperatures and becomes trapped. For this reason porosity is associated with rapid cooling rates. Susceptible metals like titanium are those which exhibit high solubility for gases such as sulphur, hydrogen and nitrogen. However, gases may also evolve heterogeneously, from vaporization of any oils and / or volatile metals (Ga, Se, Pb) present. Less common but also

of note is the homogenous evolution of gases through the reduction of metal oxides in the presence of hydrogen. Furthermore, it is not uncommon for porosity to occur in solid state joining processes for some binary systems [55].

Cold cracking is a phenomenon relative to hydrogen absorption and is a considerable problem in welding. Cold cracking results when hydrogen stored in weld material diffuses to vacancies created at stress concentrations where it agglomerates, resulting in crack formation. This cracking can be inter or trans-granular and can occur from 300°C down to sub zero temperatures. This effect is particularly prevalent in martensitic microstructures as they exhibit poor fracture toughness and high internal strains; hence it is of particular interest to this investigation. In welding specifically, the effect is known to occur as a result of tensile shrinkage stresses. This effect can be avoided by preheating welds to allow gases time to diffuse to the metal surface. The trapping effect of MC type carbides has also been known to mitigate this effect [56].

The other common weld defects are reheat cracking and hot cracking. Reheat cracking occurs as a result of precipitation hardening in the HAZ which weakens grain boundaries leading to intergranular cracking. Cracking in these cases can be initiated by internal residual stresses as well as applied stresses and is associated with residual elemental contamination [28]. Hot cracking is specific to fusion welding and affects alloy compositions with large solidification ranges where dendritic solidification structures are prominent [57]. Cracking is caused when inter-dendritic solute rich liquid is separated by solidification shrinkage effects prior to overall weld solidification. Hence alloys with large solidification ranges are harder to join well via fusion welding.

### **2.6.3 Standard heat treatment process**

A wide variety of heat treatments are applied to welds, the specifics of which depend on service conditions and metallurgical factors. However, one common goal in HT processes is stress relaxation. As pointed out above, residual stresses can lead to or exasperate a number of weld defects and the redistribution of strain through the destruction of



dislocation pile ups and lattice defects goes a long way to relieving these problems. Many of the common treatments have previously been touched upon, such as normalizing and tempering. Nevertheless, it is worth noting that other treatments such as solution treating and ageing to unify strength in precipitation hardenable alloys and specific treatments to counteract hydrogen embrittlement by outgassing are also employed.

## **2.7 Established welding techniques**

A wide variety of conventional fusion welding techniques are applied to joining in the industrial sector from oxy – acetylene welding, explosive and thermite welding to electro-arc based techniques and power beam (laser / electron heated) methods. Whilst the merits of some of the more basic processes are acknowledged those outlined below offer the most success in joining for high demand applications and specifically the ability to join dissimilar metal pairs.

### **2.7.1 Metal inert gas (MIG) welding**

MIG welding is the most widely employed of the arc welding processes due to its high rates of productivity, low cost equipment and versatility. Heat is generated by the formation of an arc between a consumable metal electrode (which can also act as a filler metal) and the metal surface. The arc itself is shielded by a controlled flow of inert gas (normally argon, helium or argon / hydrogen mixes) that flows around it. For optimum weld quality joining is normally carried out using direct current with both electrode negative and positive polarities (DCEN and DCEP respectively), with DCEN providing a greater degree of penetration for joints in thicker sections. Unfortunately the nature of the process makes it susceptible to contamination from the necessary electrode flux, short circuits between the electrode and the workpiece and excessive weld spatter from the electrode. An extension of this technology known as submerged arc welding (SAW) involves the metal electrode being submerged in a flux which prevents spatter and scavenges oxygen, nitrogen and phosphorus making it especially attractive for welding hardenable steels and nickel alloys.

Although primarily applied to steels, MIG welding can be used for welding nickel alloys but care must be taken to ensure the electrode has seen a bake out procedure to prevent hydrogen evolution. MIG welding is often ignored for joining titanium due to its poor success in the past. Nevertheless its poor performance can be mainly attributed to the poor surface finish of the titanium products that resulted in rapid tip wear. Modern titanium products no longer suffer from this problem and the advantages of MIG can now be better exploited.

### **2.7.2 Tungsten inert gas (TIG) welding**

A schematic representation of the TIG welding process is outline in Figure 2.7.1. The configuration is similar to that of MIG welding except a non consumable tungsten electrode is employed. TIG welding of nickel base alloys is typically shielded in an argon helium mix utilising direct current electrode negative (DECN) conditions to allow close control of arc stability. Normally, shielding is sufficient for welds to be conducted in air, producing superior weld quality to that associated in MIG welding [58]. Further advantages over MIG welding include the ability to join reactive metals, less weld spatter (as a result of the inert electrode), the use of current pulsing to control heat in the workpiece and the ability to join without filler metals. Weld quality is achieved through sacrifices in speed and the low deposition rate can have adverse effects in thick sections.

TIG can be readily employed for all the materials under investigation here is ideally suited to welding titanium. In fact, if stringent cleaning and shielding techniques are employed, titanium is one of the easiest metals to weld by this process. The low density of the material together with the high surface tension in the weld pool allow an excellent control of weld speed and quality to be attained. TIG has the added advantage that it can be operated manually or automatically as well as having very little weld spatter.

# TIG Welding

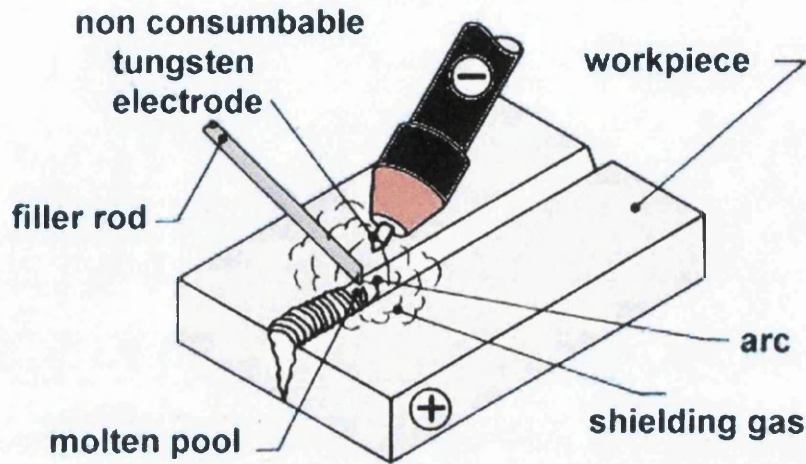


Figure 2.7.1: A schematic diagram of the TIG welding process.

## 2.7.3 Plasma arc welding (PAW)

Heat is generated in PAW through the creation of an arc between an ionised (helium argon mixtures) gas and the electrode and as a result much higher heat intensities are possible for a given power input. Decreased power input also facilitates much greater arc control at high temperatures allowing PAW to maintain the high weld quality seen in TIG at the high speeds productivities associated with MIG. Furthermore, the process does not suffer the tungsten contamination effects associated with TIG welding. These benefits have to be balanced against increased cost, reduced positional versatility, a greater required operator knowledge and skill and large torch diameter and associated HAZ.

The use of plasma also enables precise 'key hole' welds to be performed at critical areas in a component. Here the torch vaporises material to produce a hole in the workpiece. As the torch is moved along the joint the melt from advancing surface passes the torch and coalesces at its trailing edge through surface tension effects. This allows thick sections to be bonded without the requirement for multiple passes and produces a uniform weld bead

with no cracking. Unfortunately, to shield the weld, a backing inert gas is required for the underside of the workpiece.

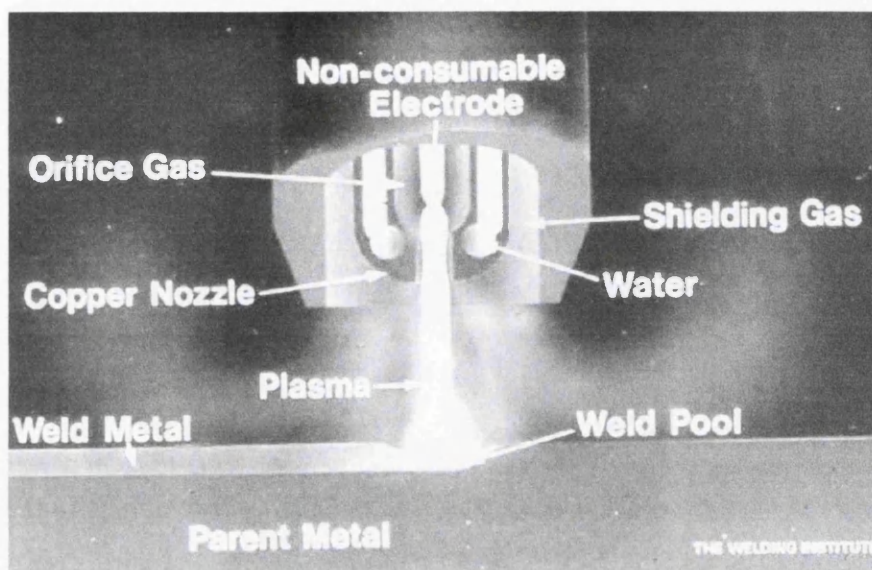


Figure 2.7.2: A schematic diagram of the plasma arc welding process.

#### 2.7.4 Friction welding

As the name suggests, friction welding involves the fusion of two species via their heating and softening due to abrasive forces. The process encompasses over ten different techniques of which only the most pertinent are described here. It is often applied to titanium alloys because neither a shielding atmosphere nor filler metal are required, unlike all other welding processes involving fusion. In this respect it has also been used to join numerous dissimilar systems as detailed in [59].

The simplest of the friction welding techniques is rotary friction welding. It involves the rapid rotation of a cylindrical piece that is subsequently abutted to a stationary one with a slight induced pressure until material at the interface has heated and softened. The force is then increased creating the necessary contact for fusion of the bond whilst expelling flash

material from the interface. The technique offers exceptional weld quality but components are limited to cylindrical sections.

Another similar incarnation is linear friction welding. Again, as the name suggests the technique involves one moving piece oscillating over a linear amplitude of around 2mm, abutted to a second stationary piece. Once the desired interface temperature is reached, the moving piece stops and a sufficient force is imparted on the joint to produce adequate fusion. This process has the added advantage of its ability to join more complex components, and is, in fact, currently being used by Rolls Royce to produce integrally bladed compressor discs [24].

A more modern development is friction stir welding. The process involves the use of a tertiary element in the form a rotating disk. The disk passes over the joint between the bonding species heating and softening material in front of it whilst depositing the softened material behind it to form a continuous solid-state fusion zone. This process is illustrated in Figure 2.7.3. The versatility gained by this particular technique allows it to be employed when joining plates and large sheets as well as more complex components. Friction stir welding is perhaps the most significant step forward for the process as a whole. It offers much of the versatility of other welding processes such as TIG and electron beam welding, whilst still retaining the added benefits associated with these techniques.

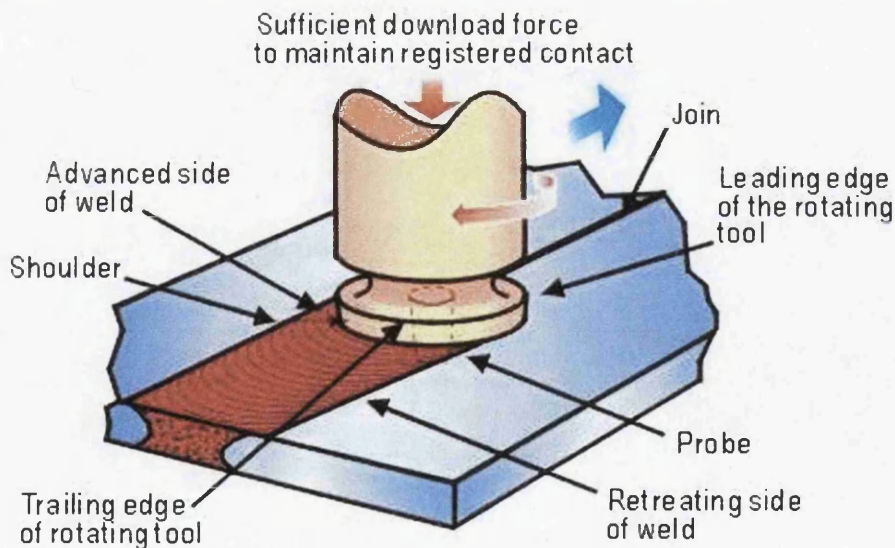


Figure 2.7.3: An illustration of the friction stir welding technique.

### 2.7.5 Power beam Processes

The two front-runners in this area are laser beam welding and electron beam welding. Both offer the added advantage of a focussed heat source and therefore minimal distortion and detrimental microstructural damage. Improved weld quality comes at a cost and both processes have high associated running costs. Typically, high-powered CO<sub>2</sub> lasers are used for higher penetration joining, whereas Nd-YAG lasers tend to be used in low power intricate operations as they have the advantage of flexible fibre-optic delivery. Both offer exceptional weld integrity, yet suffer from weld spatter.

Electron beam processes have exceptional weld quality and sometimes parent metal integrity, with little oxide / nitride formation on account of the vacuum employed for the electron gun. Spot size for the beam can be refined to sub-micron resolutions resulting in exceptionally small fusion and heat affected zones with the associated high heat intensity allowing uniform single pass welds in thick sections. As a result of this highly concentrated beam EBW may also be used in a keyhole technique similar to that of PAW. However, it's important to note that with such a small spot size tolerances in joint fit / preparation are considerably reduced. Unfortunately, the use of a vacuum limits the size of the component to be welded and adds considerable cost to the operation through a low productivity. An additional consideration is that only non-magnetic / degaussed materials (e.g. clamps and jigs etc) can be employed within the chamber to prevent beam distortion through magnetic fields; this effect must also be considered when joining magnetic materials.

## Electron beam welding

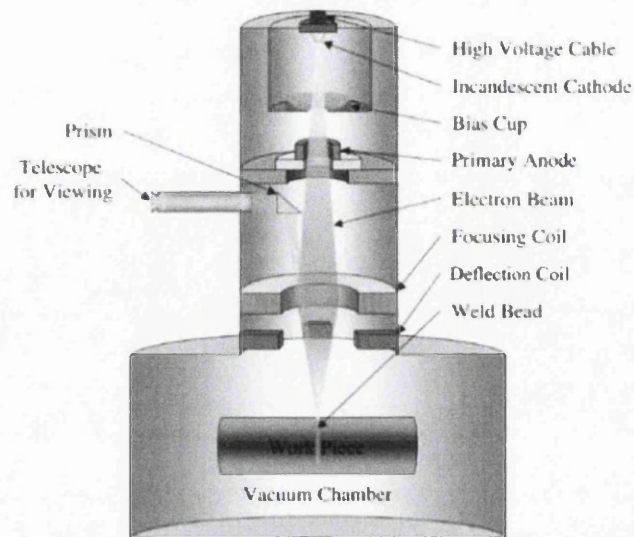


Figure 2.7.4: A schematic diagram of the electron beam welding process.

Power beam processes and in particular EBW welds in nickel base superalloys have shown considerable success [60]. However, EBW of hardenable steels is not found to be susceptible to significant HAZ cracking mainly due to the rapid single pass through thickness nature of the welds produced, some of these effects can be overcome by preheating. Due mostly to atmospheric conditions, EBW appears well suited to joining titanium compared to other fusion welding processes [61] and in fact for thin sections can have lower associated costs than TIG welds of similar quality.

### 2.7.6 Resistance welding

Though several resistance welding techniques are in use today the most popular are spot welding flash welding (where the work pieces themselves transmit current) and seam welding (with electrodes in the form of wheels that allow rapid continuous welds, usually in thin sheet). These processes exploit the main advantages of resistance heating, which are its capability for rapid weld speeds and automation. For this reason, resistance heating is the joining method of choice for large automated assembly lines in the automotive (spot welding) and canning (seam welding) industries.

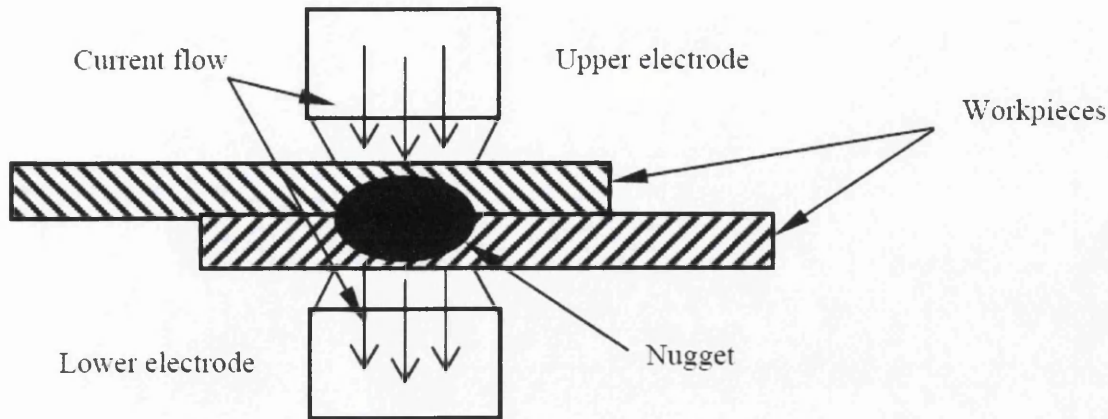


Figure 2.7.5: A Schematic representation of the resistance spot welding technique.

A schematic representation of the spot welding technique can be seen in Figure 2.7.5. Specific thermo-physical interactions in resistance heating are discussed in detail later in sections 3.2.1, however, in simple terms heat is generated in the workpiece as a function of local resistance. The amount of heat generated is governed by the joule heating equation (2.7.1); where  $H$  is the heat generated,  $I$  is the current flow,  $R$  is the local resistance and  $t$  is the time for which the current is applied. The electrodes provide the compressive force necessary for bonding, transmit current to, and conduct heat away from the work piece. The result is a four stage process:

Force  $\longrightarrow$  Weld  $\longrightarrow$  Cool  $\longrightarrow$  Off.

$$H = I^2 R t \quad (2.7.1)$$

Ignoring the resistance of interfaces briefly, the capacity of a material to heat under current flow is controlled by its resistivity ( $\rho$ ), as resistivity increases so does the heat generated. The amount of heat retained in the material during heating is controlled by its thermal conductivity ( $k$ ), as thermal conductivity increases more heat is removed from the material and the net temperature decreases for a given resistivity. Hence, careful selection of electrode material with respect to  $k$  and  $\rho$  is required to localise heating within the work piece (copper alloys are generally the preferred choice). Electrical factors must then be balanced against the strength required to exert force on the joint without significant



deformation of the electrode. Providing these conditions are met, heat within the work piece can be concentrated at the interface as a result of the high local resistance associated with the imperfect contact between the bonding species [62]. These factors must also be considered in joint design.

Resistance welding is employed in a wide range of application but tends to be concentrated on joining steels (as these are the most common automotive materials) [63]. Interestingly, steels are not ideally suited to resistance welding because of their high  $k$  and low  $\rho$ , meaning large amounts of power are required to join them. However, the productivity and automation associated with the technique out way these problems. Research has also been conducted into spot welding titanium in inert atmospheres [64] which revealed moderate integrity bonds in a material well suited to resistance heating in respect of  $k$  and  $\rho$ . Little research was noted on nickel base alloys.

## **2.8 Solid state joining processes (diffusion bonding)**

Diffusion bonding may be defined as a process of joining without the creation of a liquid phase. As such it avoids many of the difficulties associated with fusion welding that have been detailed in the previous section. The overall reduction in joining temperature also results in less deleterious effects in the HAZ such as sensitization and cold cracking. In addition to this the heat affected zone can be considerably smaller than that observed in fusion welding, including the power beam processes. A well designed and completed diffusion bond can show so little microstructural disruption that it becomes difficult to identify the bond line. This allows truly 'homogeneous' components to be manufactured through diffusion bonding that exhibit parent metal properties [65]. An overview of the diffusion bonding process is outlined below, together with a discussion of the relevant articles pertaining to advances and developments in the field.

### **2.8.1 Mechanisms of bonding**

Investigation into the mechanisms involved in diffusion bonding have been the focus of much scientific attention in the last 20 years. For this reason a plethora of different models have been published dealing with a range of different aspects of the process [66-69]. Universal agreement has been reached on the fundamental mechanisms controlling bonding which can be split up into three distinct stages:

1. Instantaneous deformation – The flattening of asperities created during surface preparation to form mechanically stable (load bearing) surfaces between the two parent metal surfaces.
2. Time dependant deformation (Creep) – The steady deformation of the asperities to establish intimate interfacial contact.
3. Diffusion – Elimination of the interface by diffusional mass transfer between the metal contacts to form a homogenous metal bond.

The mechanical behaviour in stage one can be shown to directly relate to the individual material hardness values. These values give information on the yield strength and the work hardening factor and so define the load bearing capabilities of the original asperities, i.e. materials of high hardness (hardenable steels for instance) will undergo little stage one deformation compared to those of low hardness at a constant temperature for a given pressure.

Not all diffusion bonding occurs under forces that exceed the yield point of the material. In these cases creep can be the predominant mechanism in the deformation stages of diffusion bonding. Obviously creep controlled deformation stages lead to much longer overall bonding times but in reality the bonding time is most notably effected by time, temperature and surface preparation irrespective of mechanical properties [68]. At high temperature and pressure there is an instantaneous local plastic deformation reducing the necessity for

creep. In comparatively cold conditions, creep and diffusion are insignificant and stage one gains more importance.

There are several mechanisms suggested for stages 3 of the bonding process all involving diffusion by interstitial, vacancy and bulk (grain boundary) diffusion. Early models based on this three stage mechanism such as those presented in [66] described the deformation of asperities in terms of flattening a series of spheres followed by a bulk diffusion from areas of least curvature to areas of greatest curvature. These models, although adequate, were found to differ from experimental data during the deformation stages. New models such as that put forward by Hill and Wallach [67] moved to consider the space between asperities as ovals; this led to a much better agreement with the corresponding experimental data. More recent developments have moved to consider power law creep in respect of both mechanics and diffusion and have also found good agreement with experimental data [70-72]. Not only do these models help in the understanding of the mechanisms but they also help visualise the micro processes at work during bonding, a summary of which can be seen below in Figure 2.8.1.

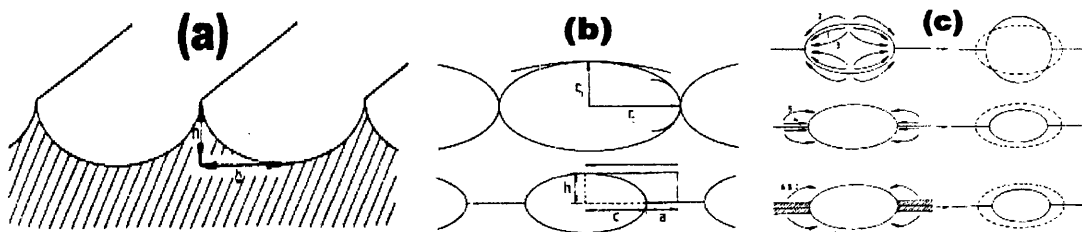


Figure 2.8.1: (a) Asperities created by machining (b) Initial oval voids formed by the two mating surfaces (above) and voids after deformation stages (below) (c) Three separate examples of bulk diffusion for final closure of the voids at the interface [67].

Whilst the mechanisms described above are inherent to all diffusion bonding processes, they must be balanced against metallurgical factors. The two factors considered to have the greatest effect on bonding are the dissolution of surface oxides and recrystallisation. The argument for recrystallisation states that grain nucleation results in a new grain structure that forms over the existing interface, eliminating it. It is a likely model but cannot be the only mechanism at work, as excellent bonds have been produced in materials only

marginally above their recrystallisation temperature [73]. Furthermore, these bonds have been produced without evidence of any significant new grain growth.

The main explanation for these observations has been the dissolution of surface metal oxides. This dissolution allows near perfect contact between the metal surfaces and the production of homogeneous bonds. Dissolution may be considered as a two stage process of oxide dissociation ( $MO \rightarrow M + O_2$ ) and diffusion of oxygen into the bulk material. Whilst it has been shown that the dissociation stage is significant at low temperatures it is the diffusion of oxygen in the bulk material that is the dominant factor [74]. In fact, it is widely claimed that a materials affinity for oxygen is one of the most important factors in the ability to join it via diffusion bonding [72, 75, 76]. Materials such as titanium, copper, tantalum and most steels either show high oxygen affinity / weak oxide layers and as such are more suited to diffusion bonding. However, materials with tenacious oxides like aluminium establish interfacial contact purely through mechanical break up of the oxide, making bonding inherently harder. In nickel base superalloys a combination of effects is evident and whilst the nickel base matrix shows less oxygen solubility, oxides readily form on its surface on account of the various reactive alloying elements it contains (Cr, Ti, Al). In these cases special oxide removal techniques need to be applied to produced high integrity bonds [77].

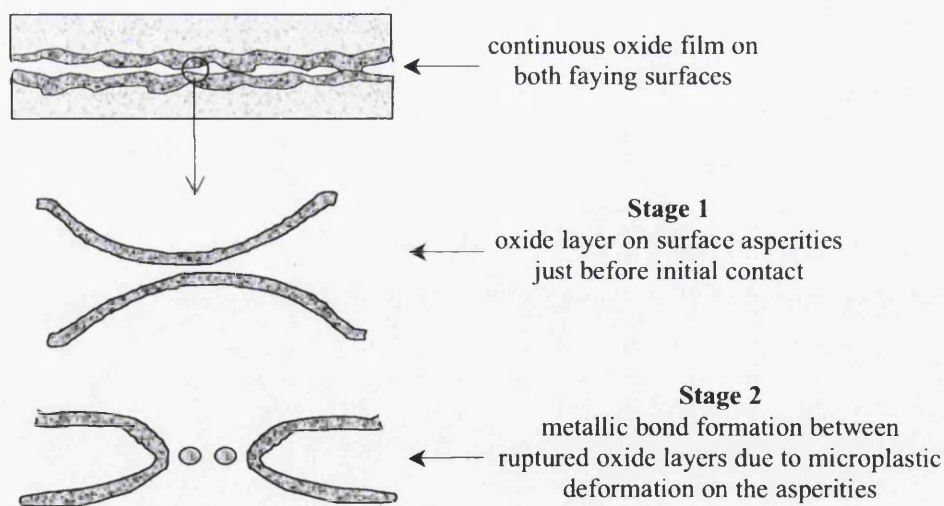


Figure 2.8.2: A Schematic illustration of the process of interfacial oxide break up [78].

## **2.8.2 Effect of bonding conditions**

There are three fundamental bonding conditions that control the speed and quality of the bonding: pressure, time and temperature. Careful control of these variables enables a wide range of different materials to be bonded at a rate specific to the material and component requirements. Through the study of the investigations cited in section 2.8.1, and reference to more practically based reviews [79], a summary of the role of each of these variables in controlling the mechanisms described above is presented in the following section.

### **2.8.2.1 Temperature**

Changing temperature can have a profound effect on the physical, mechanical and transformational characteristics of a material. In addition, it is also an easy variable to control (especially in HIPing procedures). With reference to the mechanisms outlined in section 2.8.1, it is easy to see how great an effect temperature can have. Increased temperature results in decreased yield strength and therefore more efficient development of intimate contact between the metals, as well as increasing the diffusion rate at the interface. This in turn results in an increased bond integrity and increased bonding speed. Another effect particular to titanium alloys is the allotropic phase transformations that can be induced at increased temperatures. In the case of titanium and iron, this leads to the creation of the more ductile  $\beta$  /  $\gamma$  phase (BCC / FCC) which have enhanced diffusivity compared to the low temperature HCP and BCC  $\alpha$  phases. Subsequent cooling through the respective transus temperatures may then result in grain growth across the interface leading to improved bond integrity. However, it is important to note that whilst in theory this is beneficial to bond strength, in practice it is much more important to preserve parent microstructures; for this reason super-transus bonding conditions are generally avoided.

### 2.8.2.2 Time

Assuming that stage 1 is instantaneous; time can have a major effect on the quality of bonds produced. As discussed above, the creep dependence is reliant not only on time but also crucially on the mechanical properties. However, the stage three diffusion is heavily dependant on time. This dependence is illustrated by Fick's first law of diffusion (equation 2.8.3.1). The recovery and recrystallisation process described in section 2.8.1 plays a significant part in these stages. The driving force for recrystallisation at constant temperature diminishes due to a reduced internal energy in the system as the microstructure develops. During this process atomic mobility does not decrease significantly, but the thermodynamic driving force for bulk diffusion is reduced. In reality the bonding time depends much more on surface finish and the bonding apparatus used.

$$dm = -DA \left( \frac{dc}{dx} \right) dt$$

(2.8.3.1)

Where D is the diffusion coefficient of the material C is the concentration, t is the time and dm represents the mass diffused.

### 2.8.2.3 Pressure

The single biggest effect of pressure in diffusion bonding is in the physical deformation stages. An increase in pressure at constant temperature and time produces better joint quality because it promotes the breakdown of asperities. It has also been shown that as deformation increases the recrystallisation temperature decreases [80], leading to an increasing diffusion rate with increasing pressure at constant temperature. This is achieved by lattice distortion. The distortion of the lattice creates more vacancies in the structure, increasing the rate of vacancy diffusion. However, these advantages do come at both a financial and technical cost because controlling higher pressures is both complex and costly.

### 2.8.3 Common diffusion bonding processes [81]

Diffusion bonding processes can be separated into three groups that are defined by temperature:

- Cold welding (or deformation welding), which encompasses lap welding, slide welding (low deformation) and upset butt welding, applies to joining processes that are conducted at or close to room temperature. It is generally applied to soft inert materials (typically of FCC crystal structure) such as gold, lead and platinum. Normally deformations of 50% - 90% are required to produce sound joints under these conditions.
- Thermo-compression welding is conducted at temperatures up to around  $0.5T_m$  and tends to be reserved for micro-joining processes in the electronics industry e.g. for PCBs.
- Forge welding refers to processes conducted at temperatures much closer to the melting point typically  $0.7 - 0.9 T_m$ . On the whole these processes require much lower deformations of around 25%. Examples of these kinds of processes would be butt welding, roll welding and extrusion welding.

Bonds produced in these three regimes can be produced via a number of practical techniques. The most commonly employed methods to date are roll welding, resistance bonding and hot isostatic pressing (HIP). Roll diffusion bonding is a common process which can be employed in both the cold welding and thermo-compression welding regimes. Roll welding is almost exclusively employed in cladding and has successfully been employed for various dissimilar metal pairs [82].

Resistance diffusion bonding by its nature relies on heating and so is generally carried out in the thermo-compression and forge welding regimes. Applications of solid state resistance welding range from flash butt welding [83](e.g. engine ring manufacture) to

recent applications in the automotive industry which exploit the high productivity of conventional resistance welding on assembly lines [84]. Considerable research has also been conducted into solid state upset welding (and variations thereof) [85-89], the process employed in this investigation. Considerable success has been noted in joining previously “unweldable” alloys such as precipitation hardened aluminium alloys and Haynes 25 (high temperature cobalt superalloy) [85]. Critical applications range from sealing nuclear waste containers [90] to pressurised resistance welding for reactor fuel pin fabrication [89].

HIP is the most readily employed method of diffusion bonding for high integrity components, despite limitations on component size and its considerable expense compared to other processes. This is mainly due to the fact that isostatic pressure holds considerable advantages over other loading regimes. Namely, very little upset / whole scale deformation, unprecedented interfacial contact, an ability to collapse interfacial voids and the capacity to bond at lower temperatures, minimising deleterious microstructural effects [91]. The use of evacuated cans and backfilled inert atmospheric furnaces also enables bonding of reactive materials. As such it is the solid state joining process to which all others are compared. HIP diffusion bonding has been exploited in this respect to provide information on the feasibility for joining various material pairs. These included, similar conventional materials [92] and ceramics [93], dissimilar alloys [94, 95] and ceramics [96] and ceramics to metals [97] most of which have found success by this method. Applications of HIP diffusion bonding are almost exclusively reserved for critical components including layer structured panels for the ITER experimental fusion reactor, applying high wearing surfaces to valve assemblies, complex lay up copper heat exchangers and most notably its association with super plastic forming [98, 99].

## **2.9 Existing techniques for solid-state joining with powders**

Joining with powders involves using metal powders as intermediate constituents of a bond between two solid pieces. The use of powders has been shown to produce bonds of near parent metal properties whilst minimising damage to the microstructure of the two bonding pieces. Controlling temperature can also lead to a wholly solid state bonding process



resulting in high quality bonds produced at low temperatures. These solid state processes have received attention [100-107], the techniques employed in these investigations vary from conventional HIP bonding [106], co-extrusion [100], reactive sintering [107], pulsed electric current sintering [105] and auto vacuum welding [104].

Of particular interest here was auto vacuum welding, for which the joint design can be seen in Figure 2.9.1. The use of a sealed shell about the powder interlayer acted to both hold the powder in place and protect the interface from atmospheric contaminants. Within this shell, scavenging tablets (barium / aluminium compacts) were employed to help remove moisture and intrinsically evolved gases from the interface.

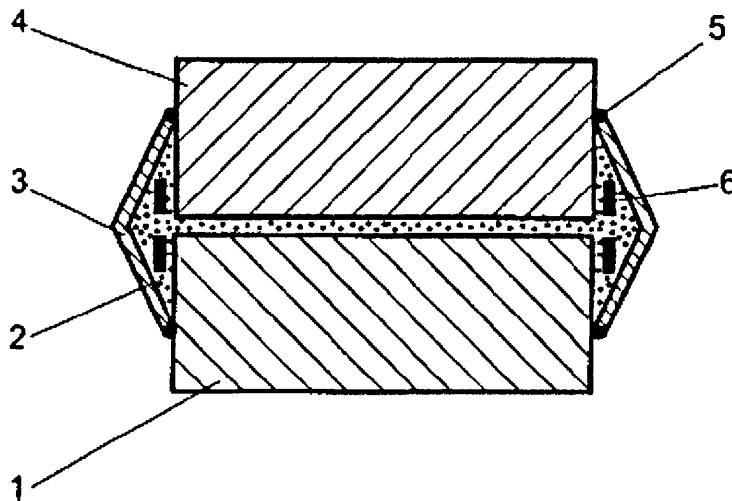


Figure 2.9.1: The powder interlayer arrangement used in bonds produced in [104]. (1/4) the solid substrates being joined, (2) the powder interlayer, (3) the protective shell, (5) a sealing joint, (6) gas absorbing tablets.

Crucially the investigation also explored powder interlayer resistance butt welds (similar to the process adopted in this investigation). The experimental setup for this process can be seen below in Figure 2.9.2. Of all the processes covered within this review this experimental design is the most pertinent. The investigation cites ‘good’ resultant mechanical properties of subsequent joints between steel and copper alloys; though neither specific mechanical properties nor alloy grades are presented. Interestingly, powders of high ohmic resistance and oxygen affinity (but undefined composition) were deliberately employed to improve thermal concentration oxide layer dissolution at the interface.

Unfortunately this resulted in widespread melting of the interlayer in some trials, resulting in reduced mechanical integrity.

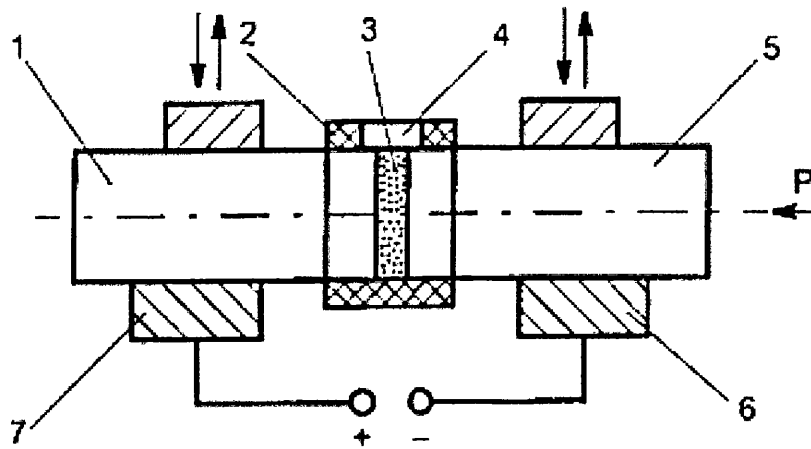


Figure 2.9.2: The powder interlayer resistance butt weld technique adopted in [104]. (1/5) the solid substrate materials (2) non conducting sleeve (3) powder (4) slit (6/7) current conducting jaws.

Considerable success has also been found when integrating a controlled proportion of liquid phase to the process [108]. Liquid phase sintering is an established part of powder metallurgy and cannot be considered as a joining technique in its own right. However, the majority of powder joining techniques studied in this investigation have employed some form of liquid phase sintering. The main advantage of a liquid phase during sintering as opposed to a wholly solid state process is the increased densification and diffusion rates. This leads to production of more dense products, faster. Nevertheless, most materials formed by powder metallurgy are done so for a reason and a large proportion of liquid phase within the compact can lead to significant segregation of solute throughout the microstructure (and poor resulting mechanical properties). The aim in LPS is to control temperature and powder composition such as to produce some liquid, but not enough to completely fill the porosity of the compact simply by viscous flow and capillary action. Adequate densification then relies on a change in shape of the solid particles (Figure 2.9.3) to a point where the gas volume in the compact is low enough for it to be fully consumed by the liquid phase. The process is driven by the reduction in energy associated with the removal of the liquid-gas interfacial area. The application of this technique in joining (with

and without powder interlayers) is referred to as transient liquid phase bonding (TLPB) [109].

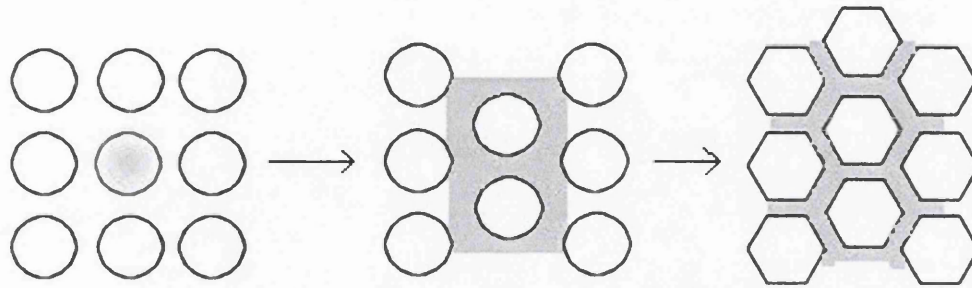


Figure 2.9.3: A schematic representation of the liquid phase sintering process.

When applied to practical bonding procedures more chemically uniform powders tend to be used and external liquid feeding of a lower melting point melt is employed. This ensures a minimum liquid constituent and isothermal freezing via diffusion of melting point depressants (MPD) from the liquid phase throughout the microstructure as a whole. However, another technique gaining popularity is super-solidus liquid-phase sintering [110], whereby pre-alloyed powders are blended with MPD powders to effect compact consolidation. Finally, investigations into the use of MPD coated powders to effect TLPB have also shown success [111].

Although the general principles of joining with powders remain the same (whether it be wholly solid state or not) a variety of different processes have been investigated. The most prominent of these is liquid infiltrated powder interlayer bonding (LIPIB) [112-114]. It was developed primarily by Zhuang and Eagar at MIT on the back of numerous previous investigations into powder infiltration. The process is essentially a variant of TLPB with the exception that joint wetting is achieved by the placement of wafers of MPD rich material at the interfaces between the powder and the bonding species. The joint design is illustrated in Figure 2.9.4 (a) and (b). Heating the assembly to a suitable temperature leads to melting of the wafer and infiltration of the liquid through the powder compacts. During infiltration, diffusion of MPD from the liquid results in steady isothermal solidification and eventual completion of the bond.

Similar silver and copper bonds were produced using a Cu/Ag of eutectic composition as the infiltrate. Consequently concerns were raised regarding localised dissolution causing erosion or slumping of the compact. Conversely, dissolution is thought to aid access to closed pores by dissolving solid-solid particle interfaces that would have left them isolated. One factor important to both considerations is that with rapid dissolution of solid material comes rapid saturation of the infiltrant and therefore a sharp reduction in mutual solubility. This in turn leads to a reduced infiltration of the liquid into the compact. It was found that by selecting MPD level that was both sufficiently high to enable dissolution of closed end capillaries without drastically affecting the mechanical properties of the joint, sound joints could be produced.

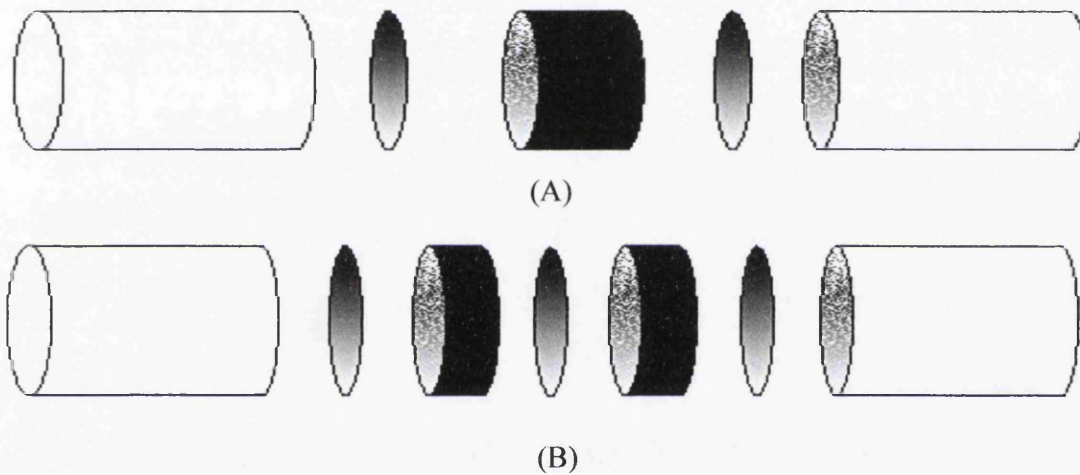


Figure 2.9.4: Two joint designs employed for the LIPIB bonding technique.

By employing joint design B, joint widths of up to 22mm were produced. It was shown that subsequent heat treatments further decreased the MPD concentration in the joint, theoretically improving mechanical properties.

## 2.10 Joining dissimilar alloys

In principle, the advantages of using homogenous dissimilar metal components in demanding applications are huge. In effect, one may be able to produce a series of components that use the advantages of a range of different alloys in their most favourable positions on those components. For instance, consider a turbine disc operating at high temperature. During service the disc will experience two principal mechanical loading types. The CF loading exerts a radial stress and hoop stress in the disc. At the centre of the disc the radial stress is at a minimum and the predominant hoop stress will yield a low frequency fatigue cycle (LCF) during power up and power down of the engine. The exterior of the disc, where the radial stress is maximised, will experience extensive creep deformation. It is known that a larger grain size yields better creep resistance as it reduces the number of grain boundaries that act as the principal mechanism of creep deformation. In contrast, fatigue strength is maximised by employing a small grain size.

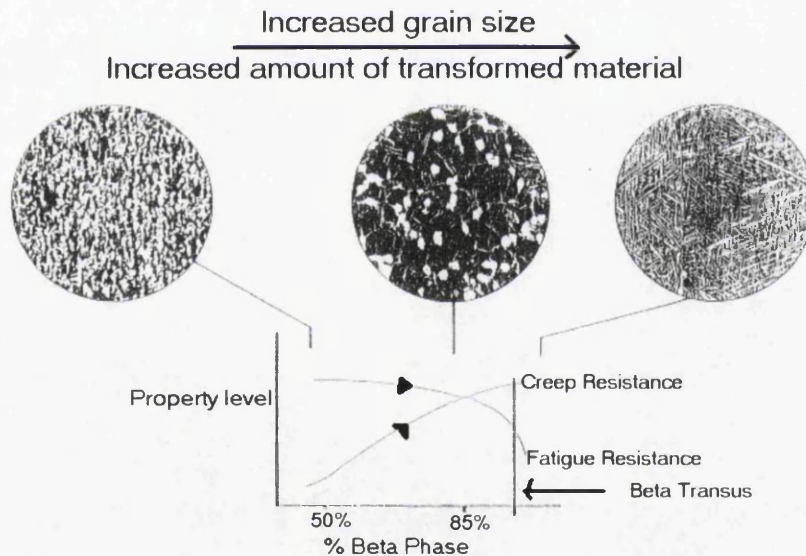


Figure 2.10.1: A summary of microstructural effects on the creep and fatigue resistance of titanium alloys [115].

Taking titanium as an example, alloys that display a lamellar structure exhibit the best fatigue resistance, whereas alloys made up of larger grain widmanstatten structures provide

better creep resistance (Figure 2.10.1). Previously this problem would be overcome by using duplex structures containing elements of each microstructure. However, employing this technique leads to inherent trade-offs between the two sets of properties. If a homogenous bond between two separate alloys, each displaying their own individual set of properties on the rim and core of the disc were to be created, then these trade offs would become redundant.

Unfortunately, the practicalities of creating these bonds are far from simple. The enormous metallurgical considerations presented in previous sections must be deliberated in selecting a joining method. This without even considering the subsequent process conditions that should be applied. Problems are also encountered when considering the optimisation of materials. Post-weld heat treatments that may be beneficial to one of the constituent materials in a component may be severely detrimental to the other e.g. bulk grain refinement effects on the rim of the above turbine disc. Hence, it is important that manufacturers optimise the structure of the constituent materials before they are joined and that subsequent joining temperatures are not detrimental to the optimised structure of either constituent. This demonstrates the technological complexity faced when joining dissimilar materials before the issue of compatibility has even been approached.

## **2.10.1 Case studies on dissimilar alloy welds**

### **2.10.1.1 Titanium to steels**

Bonding titanium to stainless steels has received considerable attention. Most studies focus on bonding commercially pure (CP) titanium to conventional austenitic stainless steels. The aim being to enable increased strength and weight savings whilst maximising corrosion resistance, typically for demanding applications such as nuclear power generation. On the whole bonding trials have been successful. Nevertheless, some inherent difficulties in bonding the alloys have also been highlighted. The following paragraphs summarise a spectrum of the literature available to date.

It has long been recognised that titanium may not be joined directly to steels by way of fusion welding [116]. This is primarily due to the evolution of brittle intermetallic phases and Fe-Ti eutectics, but crevice corrosion of iron rich areas in welds has also been highlighted [117]. For this reason developments in this area are focussed on solid state processes (with the exception of explosive welding [118]). Work has tended to focus on the bonding commercially pure (CP) titanium to both microduplex and 304 grade stainless steels. Though several parties have undertaken research in this area, an especially comprehensive body of research has been conducted by Ghosh and Chatterjee [119-123].

Initial work on CP titanium to 304 stainless steel reported optimum bonding conditions of 850°C at 3MPa uniaxial pressure for 2 hours produced the best tensile strengths of 222 MPa. It was noted that at temperatures above this, significant embrittlement occurred as a result of the evolution of Fe<sub>2</sub>Ti and FeTi type intermetallics. Significant diffusion of Ni and Fe into the titanium was reported with a lesser mobility of Ti in the opposite direction. Interestingly all bonds produced in these early investigations employed 1µm polished faying surface finishes. Later research moved onto the implementation of 300µm Ni interlayers which yielded a modest improvement in strength to around 302 MPa [124]. The main reason for this was that the introduction of the interlayer retarded intermetallic formation below temperatures of 950°C allowing a wider process window. Previous research that explored copper interlayers had noted a broad array of intermetallics in the joints but similar strengths [125]. However, the results were attributed to the improvement in interfacial contact associated with the softer copper interlayer.

Early work on bonding Ti-6-4 to Micro-Duplex stainless steels by Ohran *et al* [126] identified the evolution of Fe-Cr-Ti based intermetallic bands at the interface (Figure 2.10.2) as the primary consideration in the process. Whilst bonds were said to be of “*good quality*” bond strength was not quantified.

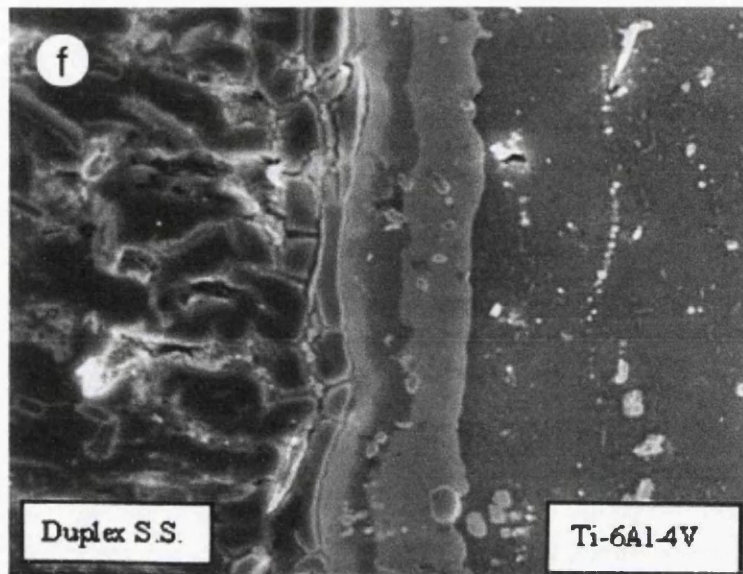


Figure 2.10.2: The typical banding of intermetallics observed by Ohran *et al* in diffusion bonds between micro-duplex stainless steels and Ti-6-4 [126].

Independent further work on the alloys [127] reported similar microstructural effects and bond strengths similar to those observed with 304 in [124]. Very recently research by Chatterjee *et al* [123] has shown that bonds between the microduplex alloys and CP titanium display comparable mechanical properties to those alloys tested in their previous investigations.

To the authors knowledge no evidence of studies on solid state diffusion bonds between Ti-6-4 and Super CMV steel appears in the literature.

### 2.10.1.2 Nickel to titanium

Limited literature is available on welds between nickel and titanium, demonstrating the difficulty in producing sound joints between the two groups of alloys. Even appreciations of joints between Ti-6-4 and IN718 (widely considered to be the most weldable grades of each alloy group) are rare. However, several studies have noted excellent properties in bonds produced in similar [128-131] and dissimilar IN718 welds [132-135]. Agreements in the findings pertaining to process conditions are outlined below:



- Significant interfacial precipitation of  $\delta$  was observed at temperatures above 940°C (particularly around 970°C, the  $\gamma''$  solvus).
- Excessive grain growth occurred (and subsequent HAZ formation) in bonds performed above 1030°C.
- Evacuated atmospheres were identified as beneficial on account of the adverse effects of interfacial oxide layers that were insoluble in the parent at temperature.
- Fusion welding processes all noted considerable laves phase formation in the HAZ.

Despite there being so much attention focussed on joints between dissimilar nickel based superalloys, little of this experience has been applied to joints between nickel and titanium. Studies on joints between bulk substrate materials are rare, however some investigations into three microscale bonding processes between Ti-6-4 and IN718 powders provide useful insight into interfacial features [136]. Here three techniques were investigated, laser powder deposition, wire welding and ultrasonic solid state welding of thin foils. All techniques induced interfacial cracks. The degree of cracking was related to reaction zone width at the interface, these zone were much more prominent in the fusion welds which displayed poor adhesion.

Of the few reports available to date on large scale joining the most useful are those presented by Zhang, Chatterjee and Locci [120, 137, 138]. The fusion welds presented by Chatterjee reported asymmetric weld shapes on account of differences in thermal diffusivity, poor mixing and macro segregation in the weld metal. Weld microstructures were dominated by eutectic phases and associated intermetallic formation. The solid state studies completed by Zhang and Locci also revealed significant intermetallic phase evolution but it was found to be concentrated at the interface. Locci found that reaction zone size may be limited by the use of a vanadium interlayer. No qualification of joint strength was presented by these investigations.

To date only one example of a study on solid state diffusion bonds between Ti-6-4 and IN718 (concurrent to this investigation) has come to light [139]. As yet this work remains unpublished.

### **2.10.1.3 Nickel to steels**

Compared to nickel – titanium joints, investigations into bonds between nickel and steel are plentiful. Fusion welding processes such as those carried out in [140] and [141] reported modest weld quality. This was partially attributed to the formation of both the  $\sigma$  and laves phases, but mostly to solidification cracking susceptibility of the nickel based alloy. This susceptibility was caused by solute partitioning (Nb, Al) in the dendrite cores, which was found to relate to increasing iron content. Notably, titanium concentrations within the fusion zone in excess of 1wt% were found to have a severely detrimental effect on bond strength.

Investigations into solid state welds such as that presented by Chandel *et al* [142] have also shown limited success. Here joints between IN718 and stainless steel were produced at 1000°C for an hour at pressures up to 60 MPa. Whilst tensile strength reached 70% of the stainless steel all bonds failed in a brittle manner at continuous intermetallic films present on the interface. Chemical analysis at the bond line elucidated high concentrations of Nb and Ti. Brazing processes have shown more promising results [143, 144]. It was found that braze constituents such as boron and silicon aided inter-diffusion and restricted the formation of continuous oxide films. This resulted in an overall improvement in bond strength but promoted the formation of borides in the base metal and silicides at the interface.

To date no evidence of studies on solid state diffusion bonds between IN718 and super CMV steel appears in the literature.

## 2.11 Conclusions of literature review

The following points, with direct relevance to the proposed theme of study, have been drawn from the extensive literature review:

- The  $\alpha$ - $\beta$  titanium alloy Ti-6Al-4V has been shown to possess substantial versatility in respect of microstructure and mechanical property control.
- A review of Inconel 718 has suggested that although it is considered to be a weldable alloy, its microstructure and resultant mechanical properties are highly dependant on local concentrations of titanium, aluminium, molybdenum and iron, all present in SCMV and Ti-6-4.
- Inconel 718 has also demonstrated the ability to form deleterious  $\sigma$ , laves and  $\epsilon$  phases under certain thermo-mechanical process conditions.
- Trends in the development of CrMoV steels have suggested that they are highly susceptible to microstructural anomalies during welding, with particular reference to temper embrittlement and the effect of alloying additions on microstructural stability.
- A review of field activated sintering processes has shown that it enables reduced sintering times for given pressures and temperatures compared to conventional sintering techniques, but that variations in electrical field can adversely effect heat generation and atomic mobility.
- It has been shown that apparent compact density and sintering kinetics are strongly dependant on powder particle size and size distribution.
- Conventional welding techniques have proved to be successful in joining various aerospace grade materials. Unfortunately, fusion welding processes have been shown to be

characterised by various defects, including hot tearing, cold cracking and intermetallic phase formation.

- A review of the diffusion bonding process has highlighted the significant effect of pressure, temperature, time and crucially basic materials properties such as reactivity, ductility and creep behaviour on the mechanisms controlling bonding.
- Of the solid state processes available to date, resistance upset welding and HIP diffusion bonding draw the most attention due to their ability to produce high integrity bonds between previously un-joined alloy pairings.
- Previous investigations into solid state resistance butt welding of similar and dissimilar aerospace grade titanium alloys have noted considerable success and also made recommendations for process improvements which shall be considered for this investigation.
- Existing powder interlayer bonding techniques have been evaluated which have demonstrated excellent bond strengths in similar and dissimilar bonds between nickel alloys.
- Investigations employing powder interlayer resistance butt welding processes similar to that envisaged here have shown that sound bonds can be produced between dissimilar copper and steel alloys.
- The available literature on titanium – steel pairings suggests that moderate bond strengths can be achieved. However, significant intermetallic phase evolution was noted. The introduction of a nickel interlayer was found to substantially retard this effect.
- A review of titanium – nickel joining investigations revealed that a limited amount of literature was available on the subject. However, studies noted considerable growth of intermetallics and deleterious phases associated with IN718.

- The nickel – steel literature also highlighted intermetallic film formation as a primary cause of bond failure during mechanical testing, and found that titanium concentrations greater than 1% at the bond line severely degraded mechanical properties.

## **AIMS OF THE PRESENT RESEARCH**

In light of the technical background covering the joining of dissimilar metal alloys the feasibility of producing bonds between various titanium / nickel / steel variants will be explored in greater detail through the current thesis. A systematic investigation into the use of a resistance bonding facility was suggested incorporating various metal powder / brazing foil interlayers. The sponsors of the research, Rolls – Royce Plc, have initiated an interest in this area for the potential manufacture of hybrid components that would require the highest possible levels of structural integrity. Although through the use of a Gleeble 1500 thermo-mechanical simulator the research builds upon previous studies performed at Swansea University [2, 3, 145] there are a number of unique aspects of the project. These include the use of a versatile MIM type powder paste interlayer in joining dissimilar materials, the use of resistance butt welding in joining dissimilar metal systems (in particular titanium to nickel and steel systems), and the development of novel experimental methods and unique bonding techniques.

### 3 EXPERIMENTAL PROCEDURE

#### 3.1 Material

The three main materials under investigation were Ti –6Al-4V, Inconel 718 and super CMV steel.

##### 3.1.1 Ti -6Al – 4V (Ti-6-4)

The Ti-6-4 material was received in the form of cylindrical Gleeble samples, machined parallel to the extruded / rolling direction from conventional bar stock, produced by TIMET UK. The as received microstructure is presented below in Figure 3.1.1, exhibiting a bimodal structure elongated in the principle direction. Nominal compositions for the titanium material are detailed in Table 3.1.2 along with parent microhardness measurements and quoted mechanical properties in Table 3.1.1.

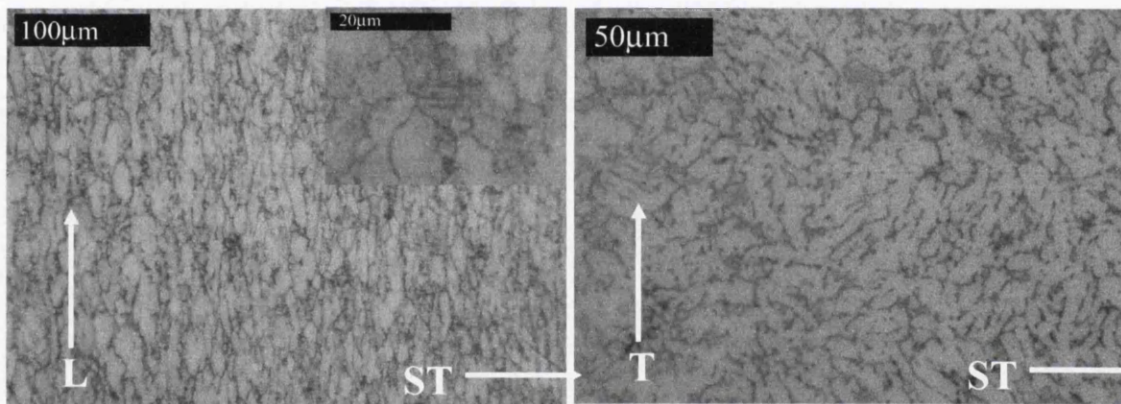


Figure 3.1.1: The parent microstructure of the Ti-6Al-4V material (nominal gleeble specimen orientations indicated).

Table 3.1.1: A summary of mechanical properties for the Ti-6-4 material [7].

UTS (MPa)	Yield stress (MPa)	Failure strain (%)	Young's Modulus (GPa)	Average Vickers Hardness (H <sub>v</sub> )
1103	983	10	95-130	350

Table 3.1.2: The nominal chemical composition of alloying elements in the Ti-6-4 material.

	Al	V	Fe	O	C	N	H
Max (wt %)	6.75	4.5	0.4	0.2	0.08	0.05	0.015
Min (wt %)	5.5	3.5	-	-	-	-	-

### 3.1.2 Inconel 718 (IN718)

IN718 Gleeble samples were received in the solution treated condition. Parent microstructures for the material are presented in Figure 3.1.2. The microstructure exhibits intragranular  $\gamma'$ , intergranular  $\gamma''$  and some coherent carbonitride precipitation. A small degree of twinning was also noted in the microstructure. Nominal compositions, average microhardness values and quoted mechanical properties for IN718 are presented in Table 3.1.3 and Table 3.1.4.

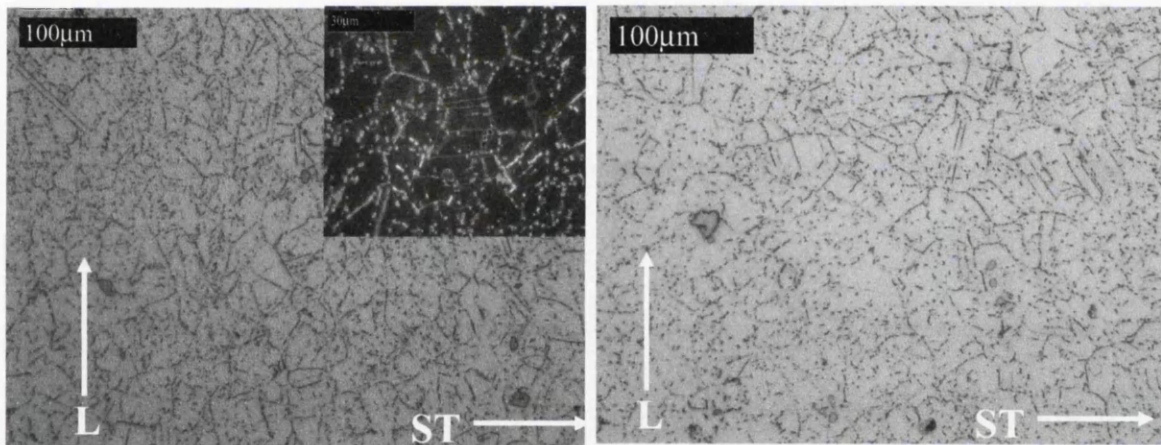


Figure 3.1.2: The parent microstructure of the IN718 material (nominal gleeble specimen orientations indicated).



Table 3.1.3: Nominal composition for the IN718 substrate material.

Component	Wt. %	Component	Wt. %	Component	Wt. %
Al	0.2 - 0.8	Cu	Max 0.3	Ni	50 - 55
B	Max 0.006	Fe	17	P	Max 0.015
C	Max 0.08	Mn	Max 0.35	S	Max 0.015
Co	Max 1	Mo	2.8 - 3.3	Si	Max 0.35
Cr	17 - 21	Nb	4.75 - 5.5	Ti	0.65 - 1.15

Table 3.1.4: A summary of mechanical properties for the IN718 material

UTS (MPa)	Yield stress (MPa)	Failure strain (%)	Young's Modulus (GPa)	Average Vickers Hardness (H <sub>v</sub> )
1375	1100	18	200	250

### 3.1.3 Super CMV steel (SCMV)

SCMV gleeble samples were received in the tempered martensitic condition, parent microstructures for the material are presented in Figure 3.1.3. A very fine lath martensite microstructure is apparent, with an average prior austenite grain diameter of 60 microns. Nominal composition, average microhardness and quoted mechanical properties are presented in Table 3.1.5.

Table 3.1.5: Nominal composition for the SCMV substrate material.

	C	Si	Mn	P	S	Cr	Mo	Ni	V	Fe
Composition (wt %)	0.35-0.43	0.1-0.35	0.4-0.7	<0.007	<0.002	3.0-3.5	0.8-1.10	<0.3	0.15-0.25	Bal

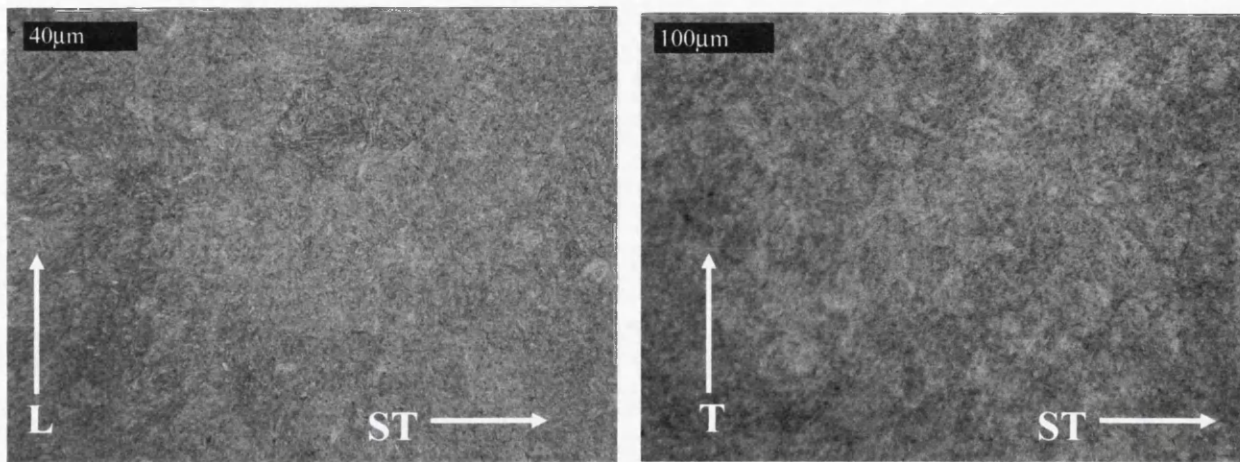
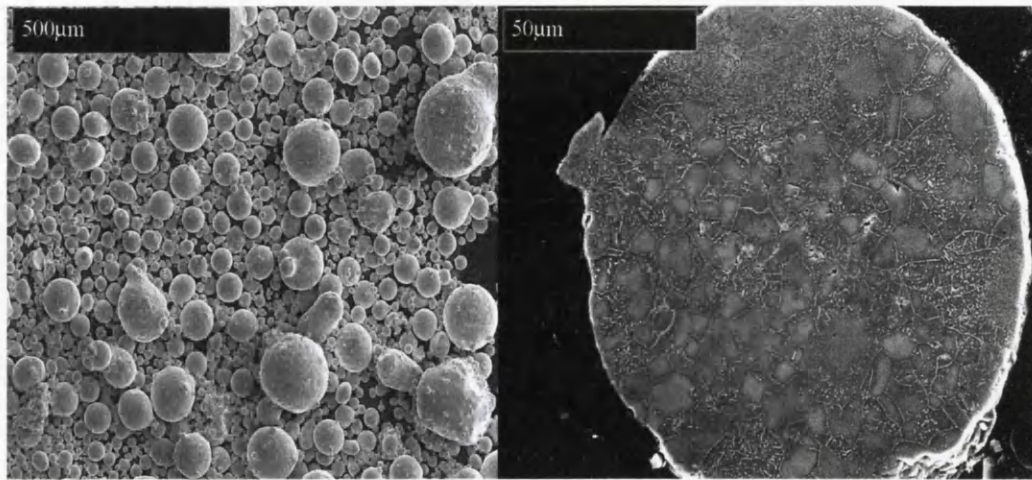


Figure 3.1.3: The parent microstructure of the SCMV material (nominal gleeble specimen orientations indicated).

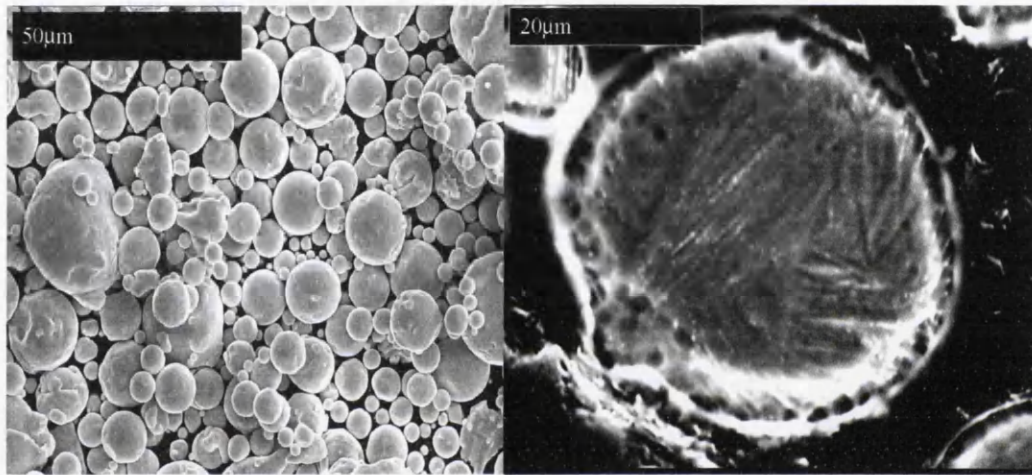
#### 3.1.4 Powder material

Three separate powders were assessed during the investigation, Ti-6-4, BurTi, and IN718. All powder material received was produced by gas atomisation at crucible powders, USA.

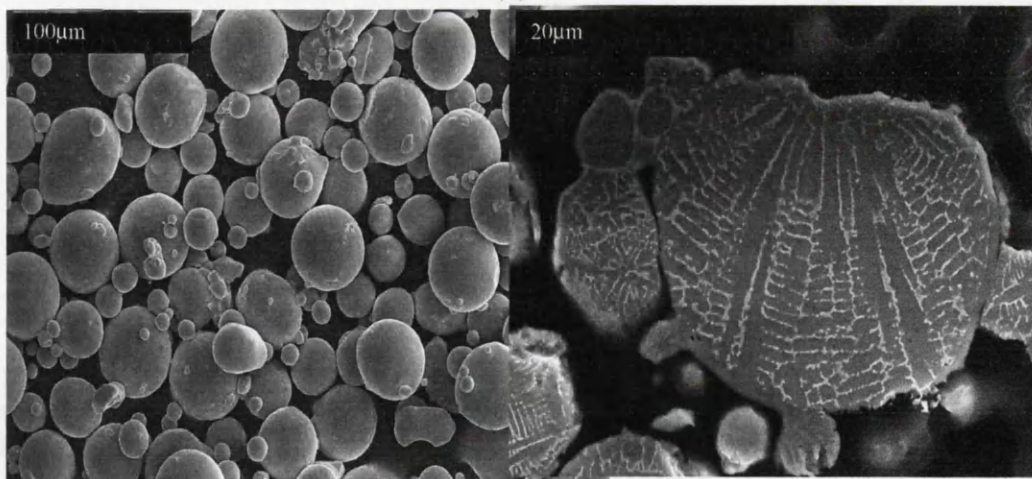
SEM images of the supplied Ti-6-4, IN718 and BurTi powders, complete with their respective microstructures are presented in Figure 3.1.4. SEM image analysis confirmed mean particle diameters for the three variants as 42µm, 25µm and 100µm respectively. Though particle size distribution was not quantitatively measured, the BurTi powder appeared to have a much greater variation in particle size than either the IN718 or Ti-6-4. The BurTi powder microstructure comprises of  $\beta$  grains inter-dispersed with intergranular precipitates. Grain size is approximately 10µm. The Ti-6-4 powder microstructure shows a very fine Widmanstatten structure with clearly defined packet size of approximately 10µm. Finally, the IN718 powder has a dendritic structure, elucidated by  $\gamma''$  precipitation in the interdendritic spacings.



(a)



(b)



(c)

Figure 3.1.4: Powder morphology and microstructure for as received (a) BurTi powder (b) Ti-6-4 powder and (c) IN718 powder.

### 3.1.5 Powder paste

The powder interlayer was incorporated into the bond by the use of a powder paste wherein the powder was suspended in a gelation binder to facilitate easy application of the powder interlayer to one of the faying surfaces prior to bonding. This technique was derived from similar practices used in metal injection moulding (MIM).

The following binder composition was used for every bonding trial:

Table 3.1.6: Tabulated values for the gelation binder constituents

Binder content by weight relative to one unit of powder	
Powder	1
Cellulose	3/400
Water	9/100
Glycerol	1/400

All powder pastes were mixed in ultrasonically cleaned glass containers placed on enclosed weighing scales accurate to 0.1 mg. All other mixing equipment was rigorously cleaned in acetone prior to use.

### 3.1.6 Coated material

A variety of electro deposited coatings were applied to some of the super CMV and IN718 substrate material, these included nickel, tantalum and a nickel-chromium-vanadium triple coating. In the case of nickel and tantalum, the aim was to provide a diffusion barrier during bonding, leading to a thinner reaction zone that will help to avoid the development of harmful brittle intermetallic phases close to the bond line. The triple coating was investigated as a means of providing a common 'buffer' between two dissimilar materials (Ti-6-4 and SCMV) to facilitate transition joint production. The nominal coating thickness for each metal was 2 $\mu$ m in all cases.

### 3.1.7 Brazed material

Some brazing trials were also conducted using both copper and Nicrobraz LM brazing alloys. These layers were electrodeposited with a nominal coating thickness of 2µm in both cases. The composition of Nicrobraz LM is presented in Table 3.1.7.

Table 3.1.7: The nominal composition for the Nicrobraz LM brazing alloy.

Element	C	Si	Cr	Fe	B	Ni
Nominal Composition	0.06	4.5	7.0	3.0	3.1	Bal

### 3.2 Bonding Apparatus: The Gleeble 1500 thermo-mechanical simulator

The use of the Gleeble 1500 thermo-mechanical simulator (Figure 3.2.1) during this research follows previous research conducted by Tuppen [145]. One of the major outcomes of his investigation was that the Gleeble system offers a convenient method of bond fabrication for laboratory scale research into diffusion / resistance bonding. The nature of the apparatus offers easy control of all the fundamental bonding parameters of time, temperature and force. This facilitates a detailed 'in house' analysis of the factors effecting optimum bonding conditions. Subsequent to the extended research in this area [2, 3], efforts are ongoing to replicate the Gleeble bonding conditions in the industrial manufacturing / repair environment.

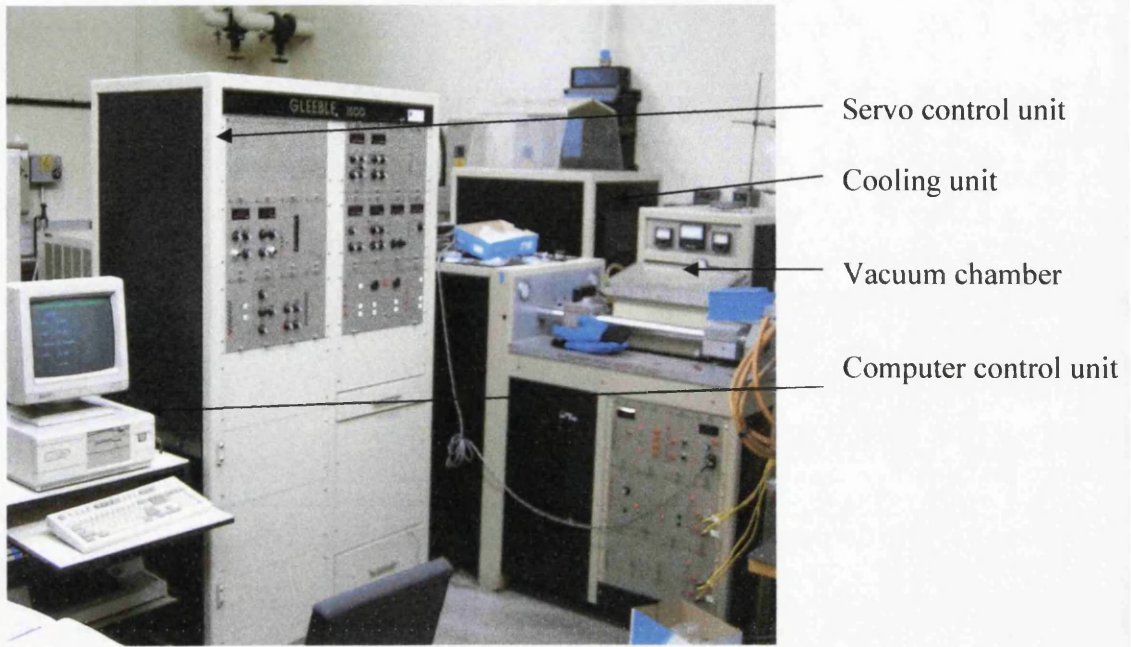


Figure 3.2.1: The Gleeble 1500 thermo-mechanical simulator.

### 3.2.1 Resistance heating

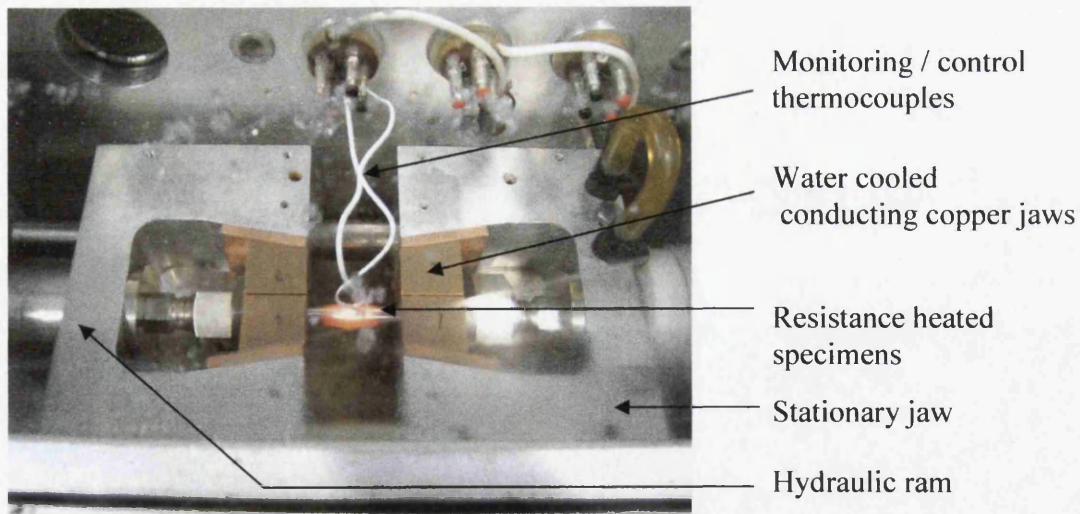


Figure 3.2.2: The interior of the vacuum chamber during bonding.

Figure 3.2.2 shows how the Gleeble setup affects the resistance heating technique. A current (I) is passed through the copper conducting jaws. This is in turn passed to the specimens and then travels to the interface. There is an associated resistance (R) at the interface between the two specimens. The heat generated at the interface can then be given by;

$$E = I^2Rt \quad (3.2.1.1)$$

Where E is the heat energy in Joules, and t is the time for which the current is applied. A more accurate comparison has been made by Brown *et al* [146]. Here, a computational model was used to map the heat transfer across the specimen using steady state heat transfer equations. The heating effect was found to be parabolic with a suitably isothermal region of around 4mm astride the interface. Good agreement was found between the model and experimental data. A summary of the results can be seen below in Figure 3.2.3.

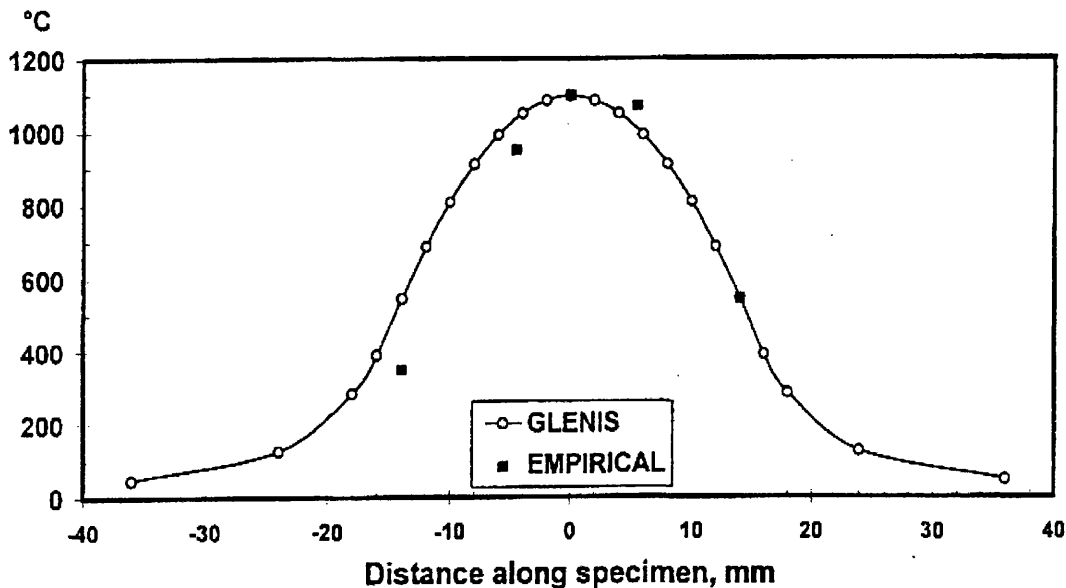


Figure 3.2.3: The resistance heating profile as predicted by steady state heat transfer equations (adapted from [146]).

Here the nature of resistance heating can be clearly seen. This parabolic heating effect is typical of the technique, as resistance to electrical current will gradually increase with the distance from the copper electrode with a peak at the highest point of resistance, the

interface. The parabolic nature of the heat comes from a combination of the increase in resistance and the conduction of heat away from the peak temperature condition at the interface. This non-uniform temperature condition should always be considered when working with resistance heating techniques and can be the cause of some considerable difficulty with some processes.

In reality the exact resistance at the interface would be virtually impossible to calculate accurately, so the use of control thermocouples allows the use of a feed back system to monitor temperature. Resistance heating is essentially controlled by the electrical / physical contact at the interface and the area over which the current is acting; obviously a smaller interfacial area will result in a greater current density and increased temperature [146]. Good electrical/physical contact is required to prevent arcing at the interface, which would irrevocably damage the specimens and the solid state electrical control system.

### 3.2.2 Specimen geometry

All Gleeble specimens were produced using conventional CNC turning operations. Specimen geometry is set out in Figure 3.2.4 below. The faying surfaces were ground to a uniform 5 $\mu$ m finish perpendicular to the specimen length.

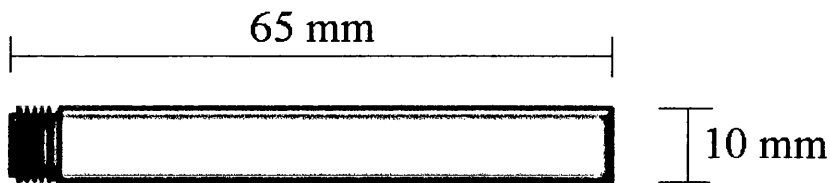


Figure 3.2.4: The dimensions of the Gleeble specimens used in the bonding processes.

Monitoring thermocouples were spot welded to the specimens prior to specimen loading as close to the interface as practically possible. To further ensure reproducible results these welds were always placed in the same place and on the same side of the bond for each of the tests. Locations of these welds are illustrated in Figure 3.2.5.



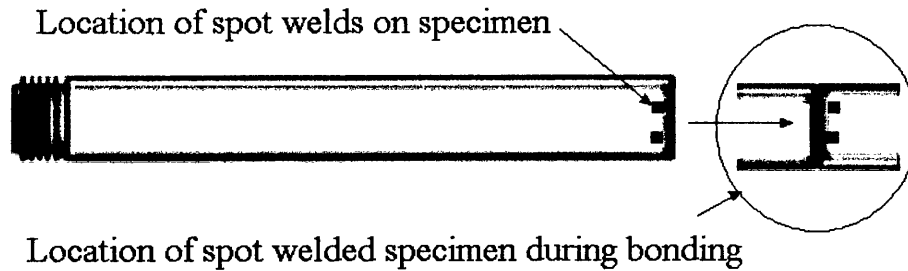


Figure 3.2.5: An illustration of the location of spot welds on Gleeble specimens.

### 3.3 Bonding Procedure

#### 3.3.1 Gleeble specimen preparation

Cleanliness has been recognised as a major contributing factor to bond quality in previous research [2]. Prior to bonding and the application of the powder, all Gleeble specimens were thoroughly cleaned in an acetone ultrasonic bath. All cleaned specimens were then placed up right in an airtight desiccator. Specimens were transported throughout further specimen preparation in this manner until they were loaded into the Gleeble.

#### 3.3.2 Preparation of powder interlayer

Prior to bonding, the powder interlayer was applied to the faying surface of one half specimen, preferably the most similar side metallurgically. A method of application was developed whereby interlayer thickness could be controlled to the nearest 50 microns. This involved the use of a tube (into which the specimen fits) and a calibrated nut, that while being rotated on the thread of the Gleeble specimen reduces the height of the specimen below that of the tube; in doing so leaving a 'cup' of the desired depth. This cup can then be filled by the powder paste and subsequently compressed to both remove excess paste and give a durable powder layer onto the specimen of adequate packing density. This can be visualised with reference to Figure 3.3.1.

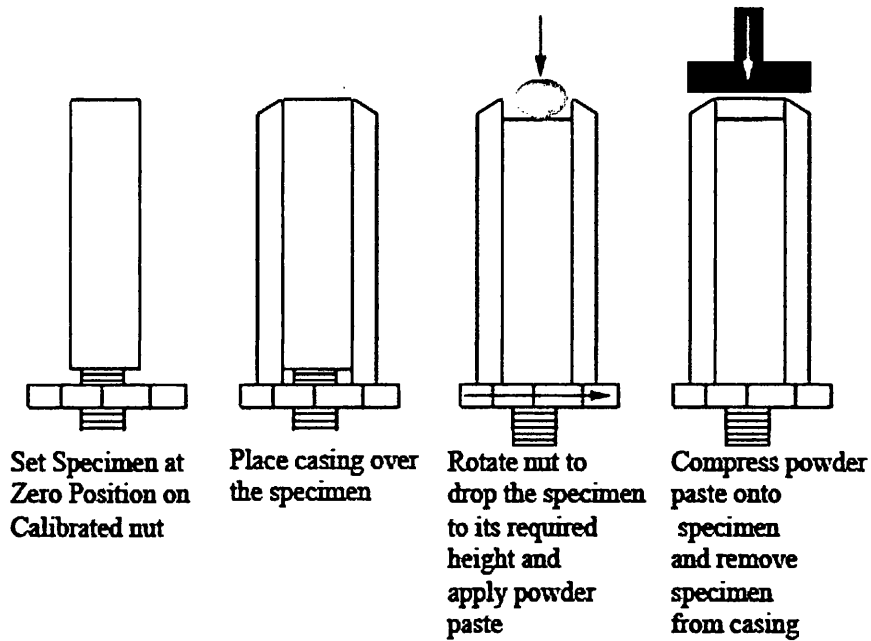


Figure 3.3.1: A schematic representation of the powder application equipment.

Following powder application three different pre-bond routines were trialled. The first involved a debinding stage whereby powder coated samples were placed into a vacuum furnace in an attempt to both remove contamination and partially sinter the powder interlayer prior to bonding. The second involved natural drying whereby the powder topped specimen was stored in a desiccator for approximately 12 hours prior to bonding. In the third cases specimens were bonded immediately following powder application and an 'in situ' debinding cycle was employed. Further discussion on comparisons between these routes will be dealt with in both the Results and Discussion sections.

### 3.3.3 Loading / unloading of specimens

A strict loading and unloading procedure was employed. This ensured repeatable alignment and hence good surface contact between specimens. It also ensured that the preloading of the specimens was the same in all cases. The procedure is outlined below:

1. Weld the monitoring / control thermocouples to one specimen half.
  2. Screw hexagonal backing nuts onto specimens ensuring that the specimen with the monitoring thermocouples is on the right hand side.
  3. Place two sets of copper jaws around each specimen.
  4. Attach alignment jig (Figure 3.3.2) around each specimen taking care not to allow the two bonding surfaces to come into contact at any time.
  5. Remove the glass lid of the vacuum chamber.
  6. Locate the specimen assembly into the hydraulic ram within the vacuum chamber.
  7. Secure copper jaw on RHS into place using the first locking nut.
  8. Switch to stroke control on Gleeble 1500 servo control unit.
  9. Move hydraulic ram backwards to locate copper jaws within it.
  10. Secure LHS copper jaw with second locking nut.
  11. Switch to force control on Gleeble 1500 servo control unit.
  12. Apply 1kN compressive holding force to specimen to ensure adequate alignment and interfacial contact.
  13. Remove alignment jig.
  14. Connect thermocouples to the servo control unit.
  15. Replace vacuum chamber lid.
  16. Set necessary compressive load for test.
  17. Start test.
- 
18. On completion of the bonding routine, carefully remove the joined specimen halves by reversing the procedure above.

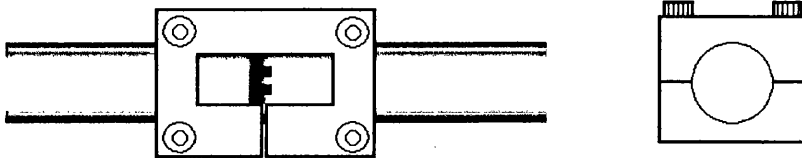


Figure 3.3.2: A schematic illustration of the alignment jig assembly.

### 3.4 Bonding trials

A matrix of resistance bonding trials was conducted in order to ascertain the critical process parameters for successful bonding and where possible optimise the process parameters. Full details of these tests is provided in Table 3.4.1.

Table 3.4.1: A full matrix of the Resistance bonding trials conducted.

Test Matrix				
Test Number	Description	Force (KN)	Hold Time (minutes)	Max Temperature (oC)
1	Ti-6-4 to Ta coated IN718 with Ti-6-4 powder interlayer	1.25	37	925
2	Ti-6-4 to uncoated IN718 without interlayer	0.5	37	925
3	Ti-6-4 to Ta coated IN718 without interlayer	0.5	37	925
4	Ti-6-4 to Ni coated SCMV with Ti-6-4 interlayer (1KN for 2 min, backed off to 0.5KN 37 min hold)	0.5	37	925
5	Ti-6-4 to Ni coated SCMV with Ti-6-4 interlayer same conditions, oxidation	0.5	37	925
6	solid dummy specimen cool jaws	-	-	-
7	solid dummy specimen hot jaws	-	-	-
8	Ti-6-4 to Ni coated SCMV with Ti-6-4 powder interlayer (HOT JAWS LHS)	0.5	37	925
9	Ti-6-4 to Ni coated SCMV with Ti-6-4 powder interlayer (Hot jaws : FAILED on grinding)	1	57	925
10	Ti-6-4 to Ni coated SCMV with BurTi powder interlayer (Hot jaws : failed on unloading)	1	57	925
11	Ti-6-4 to Ni coated SCMV with BurTi powder interlayer (Hot jaws : successful)	1	57	925
12	Ti-6-4 to Ni coated SCMV with BurTi powder interlayer (5min debind at 200 - 57 at 925 10min cool : Failed thrcple off)	1	57	925
13	Ti-6-4 to Ni coated SCMV with BurTi powder interlayer (As above : suceesful)	1	57	925
14	Ti-6-4 to Ni-Cr-V coated smcv with BurTi interlayer (5min debind at 200 - 57 at 925 10min cool : Failed no adhesion)	1	57	925
15	Ti-6-4 to Ni-Cr-V coated smcv with BurTi interlayer (5min debind at 200 5min at 500- 57 at 970, 10 Min cool : Failed theple off)	1	57	970
16	Ti-6-4 to Ni-Cr-V coated smcv with BurTi interlayer 5min debind at 200 5min at 500- 57 at 970	1	57	970
17	IN718 to Ta coated SCMV with a In718 Interlayer Full in situ debinding procedure, Ten minute slow cool.	2	57	925
18	IN718 to Ta coated SCMV with a In718 Interlayer No binder, Radial constraint employed	3	57	925
19	Ti-6-4 to Ta coated IN718 with a BurTi interlayer Full in situ debinding procedure, Ten mintue slow cool	2	57	970
20	IN718 to Ta coated SCMV with a In718 Interlayer No binder, Wider radial constraint employed	4	57	970

Test Matrix (continued)				
Test Number	Description	Force (KN)	Hold Time (minutes)	Max Temperature (oC)
21	Copper coated Ti-6-4 to IN718 no interlayer	1	57	925
22	Copper coated Ti-6-4 to IN718 no interlayer	1	57	970
23	Ti-6-4 to Ta coated IN718 with copper impregnated powder Full in situ debinding procedure, Ten minute slow cool.	1	57	925
24	Ti-6-4 to Ta coated IN718 with copper impregnated powder Full in situ debinding procedure, Ten minute slow cool.	2	57	925
25	Microbraz LM coated IN718 to uncoated SCMV No Interlayer	3	60	970
26	Microbraz LM coated IN718 to uncoated SCMV No Interlayer - for mechanical testing	3	60	970
27	Microbraz LM coated IN718 to uncoated SCMV No Interlayer	3	990	60
28	Microbraz LM coated IN718 to uncoated SCMV No Interlayer	5	990	60
29	Microbraz LM coated IN718 to uncoated SCMV No Interlayer (control system failure - joined in semi-solid state)	5	1050	60
30	Microbraz LM coated IN718 to uncoated SCMV IN718 powder interlayer (full in situ debinding procedure)	3	990	10

### 3.5 Production of HIPed bonds

In addition to the bonds produced at Swansea University, further bonds produced via a conventional Hipping route were produced at Birmingham University. The aim was to validate not only the compatibility of the bonding pairs but also the process as a whole. It is worth noting that such comparisons have been made previously [145], but not in relation to powder interlayer bonding nor bonding between wholly dissimilar metal systems.

#### 3.5.1 Production route

Alloy pairs (coated with suitable barrier / braze layer if applicable) being assembled together within a mild steel can which was then evacuated for approximately 12 hours. This container was then sealed and HIPed for 2 hours at 920°C under a 100MPa isostatic. All samples were bonded under the same conditions. 22 different pairs were bonded and these are summarised in table 1.5.1 below.

Table 3.5.1: Test Matrix detailing bonds produced via the conventional HIP technique.

Test Matrix (HIPed Bonds)	
Test Number	Description
1	Ti-6-4 to Ta coated SCMV With 250µm Ti-6-4 interlayer without binder
2	Ti-6-4 to Ta coated SCMV With 500µm Ti-6-4 interlayer without binder
3	Ti-6-4 to Ta coated SCMV With 500µm Ti-6-4 interlayer With binder
4	Ti-6-4 to Ta coated In718 With 250µm Ti-6-4 interlayer without binder
5	Ti-6-4 to Ta coated In 718 With 500µm Ti-6-4 interlayer without binder
6	Ti-6-4 to Ta coated In718 With 500µm Ti-6-4 interlayer With binder
7	Ti-6-4 to Ta coated SCMV without interlayer
8	Ti-6-4 to Ta coated In 718 without interlayer
9	T-6-4 to Ta coated SCMV substrate With 250µm BurTi interlayer without binder
10	T-6-4 to Ta coated SCMV substrate With 500µm BurTi interlayer without binder
11	Ti-6-4 to Ta coated SCMV With 500µm BurTi interlayer With binder
12	T-6-4 to Ta coated In718 substrate With 250µm BurTi interlayer without binder
13	T-6-4 to Ta coated In718 substrate With 500µm BurTi interlayer without binder
14	Ti-6-4 to Ta coated In718 With 500µm BurTi interlayer With binder
15	Ti6-4 substrate to SCMV substrate
16	Ti-6-4 Substrate to In718 Substrate
17	SCMV substrate to In718 Substrate
18	SCMV substrate to Ta coated In718 Substrate
19	SCMV to Ta coated In718 with 500µm In 718 powder interlayer Without binder

### **3.5.2 Specimen preparation**

Post HIPing samples were wire cut from the mild steel can and sectioned perpendicular to the bond line. They were then ,metallographically prepared for inspection. Selected specimens were also sectioned and mechanically tested for means of comparison.

## **3.6 Bond Characterisation**

Bond characterisation was carried out primarily on appropriately sectioned specimens that were then prepared using various metallographic techniques. These sections were initially assessed via both optical and electron microscopy and in some cases both chemical and crystallographic information on the specimens was obtained via EDX and EBSD analysis respectively. Mechanical integrity using monotonic tensile, fatigue and Vickers microhardness testing. Fractured specimens were inspected via SEM fractography and selected specimens were sectioned and metallographically prepared.

### **3.6.1 Sample preparation**

Metallographic characterisation of bonded pairs encountered significant difficulty as a result of the vast differences in specific metallographic preparation routes associated with each material. As such new preparation procedures were devised that found a compromise between preparation time / complexity and surface finish between the material pairings.

### **3.6.2 Sectioning**

All specimens were sectioned perpendicular to the bond line using a Struers Secotom - 10 sectioning machine and the sectioned samples were subsequently mounted in conductive Bakelite. This high performance sectioning machine was employed because of its accuracy and because of the hardening effects observed in some bonds (up to 700Hv). For this reason, sectioning the bonds proved to be challenging. Cuts would often tend to drift due to the large differences hardness between the materials and it was found that starting the cut



in the harder material was beneficial. Choice of cutting medium was also complex. No one wheel material was found to adequately cut all three materials and as a consequence slow cutting speeds were adopted to allow wheels to be changed mid-way through the cuts for longer sections. Although time consuming, this proved to be the most efficient method and helped to prevent costly wheel replacements and machine damage. Generally silicon carbide wheel material was found to be most suited to the titanium material, whereas the steel and nickel material was better sectioned with an aluminium oxide based wheel.

### **3.6.2.1 Grinding procedures**

The first major problem to contend with whilst preparing metallographic sections through dissimilar pairs was the difference in hardness between the two materials as it results in differences in height across a specimen as one material is worn away more easily than the other. In more extreme cases a noticeable step appeared at the interface between the two materials. Whilst small differences could be tolerated for optical inspection alone these can pose severe difficulties when conducting more detailed mapping techniques such as EDX chemical analysis especially EBSD. On a more basic level one has to consider that when studying an interface with a large difference in height the two sides the observed microstructures are not related and the image is not wholly representative. It was found that the effect predominated at the fine grinding stages. Although wheels, tables and counter rotating auto grinders were trialled, it appeared that the method of grinding had little bearing on the outcome and that in fact the best way to avoid the effect was to do as little grinding as possible. Hence the refined sectioning techniques outlined above. For the most part samples were prepared by hand on grinding tables to allow close control of the grinding procedures.

### **3.6.2.2 Polishing Procedures**

Most common alloys such as the ones under investigation here have specific polishing routines that are universally employed. It was found that both the steel and nickel alloys under investigation shared similar techniques but that the titanium was more distinct. Both the nickel and the steel could be polished to a mirror finish using standard 6 $\mu$ m and 2 $\mu$ m



diamond pastes on fine cloth polishing wheels with a paraffin lubricant. However, when titanium was prepared in this way it resulted in significant pitting. This could then be removed by using a standard colloidal silica slurry, which when acting on the nickel produced a negligible effect but when acting on the steel produced a significant degree of pitting itself. For the small number of successful titanium to steel bonds produced it was found that pits left in the titanium after the initial preparation were eradicated to an acceptable degree during etching.

Where a finer surface finish was required (for EBSD analysis for instance) a two stage sub-micron polishing regime was adopted whereby the pairs were polished with two types of colloidal silica suspension. Firstly, Struers OP-S solution mixed 10:1 with hydrogen peroxide and then subsequently with Bueler Mastermet. It should be acknowledged that repeated re-polishing of the bonds resulted in the interfacial step outlined in the previous section and as a result it was important to use the appropriate procedure first time to avoid re-preparing the sample from scratch.

Finally, also of note was the 'balling' of hard carbo-nitride precipitates from the IN718 i.e. carbides pulling out of the matrix which resulted in considerable scratching both to the IN718 matrix and its bonding pair. Although there are some specific recommended polishing techniques to prevent this from happening they are impractical and add further complexity to the preparation technique. In an attempt to minimise this effect, careful control of polishing force was employed.

### 3.6.2.3 Etching procedures

All three alloys investigated required different etches to reveal their microstructure. These are outline below in 3.6.1.

Table 3.6.1: Details of etching procedures for all materials.

Material	SCMV	Ti-6Al-4V	IN718	BurTi
Etch Name	Nital	Kroll's Reagent	10% Orthophosphoric eletro-etch	Kroll's Reagent
Etch Composition	2% HNO <sub>3</sub> in distilled water	2% HNO <sub>3</sub> and 1% HF in distilled water	10% H <sub>3</sub> PO <sub>4</sub> In distilled water	2% HNO <sub>3</sub> and 1% HF in distilled water
Etching time	Approx 30 seconds	Approx 30 seconds	Approx 60 seconds at 5V EMF	Approx 60 seconds

Unfortunately, for the titanium to steel and nickel to steel combinations, a simple two stage etching process proved to be insufficient on account of the susceptibility of the steel substrate to over etching by the Orthophosphoric and Kroll's reagents. This was overcome by masking the steel with Teflon tape for the initial etch and performing a secondary Nital etch which minimal effect on either the titanium or nickel substrates. Whilst the technique was successful, the precise nature of the masking required to preserve the interfacial microstructures (between 20 and 500µm wide) meant that often two or three iterations were required for each bond. This can account occasional uneven etching observed in the microstructures presented in the results.

### 3.6.3 Optical microscopy

Initial optical inspection each bond was carried out using a Reichert-Jung Mef3 optical microscope at magnifications ranging from x10 to x1000 with images recorded with a Nikon digital camera.

#### **3.6.4 Scanning electron microscopy (SEM)**

Closer inspection of the bond was achieved through scanning electron microscopy using the JSM 6100 scanning electron microscope. Images were captured on a PC control unit linked to the microscope using an Oxford Instruments 'ISIS Link' unit that allowed close control of image size as well as scanning speed and resolution. Magnifications between x200 and x20,000 were employed. High magnification inspection of the bond allowed detailed assessment of grain interactions and assimilation as well as helping to identify any micro porosity present at, or around the bond line. All samples were thoroughly cleaned with pressurized air prior to inspection.

#### **3.6.5 Chemical analysis (EDX)**

EDX spectro-chemical analysis was employed to study both elemental diffusion across the bond line and fracture initiation sites in fractured samples during the optimisation process. The analysis was carried out using a JSM 35C scanning electron microscope incorporating ISIS link hardware. Readings were taken at 2  $\mu\text{m}$  intervals either side of the bond line. Sampling was continued until levels of alloying elements reach typical levels for the parent alloys. Each sample was rigorously cleaned prior to the analysis to avoid surface contamination.

#### **3.6.6 Microhardness testing**

Hardness traverses of the bond were performed at 0.2mm intervals using a Leco M400 GI Vickers microhardness tester. Microhardness traverses were performed only on bonds produced under an optimised set of conditions. Hardness tests were also be performed on the parent materials to provide a means of comparison for the bond traverse results.

### **3.7 Mechanical testing**

Due to material constraints, only selected optimised bonds were mechanically tested using non standard, strip specimens. The strips were sectioned across the bond line using milling

and grinding techniques to produce samples of approximate size 60 x 5 x 2 mm. It is acknowledged that these tests give only a comparative indication of bond strength and cannot provide standardised mechanical properties. All tests were performed on a calibrated ESH servo hydraulic test rig employing an MTS extensometer with a 12mm nominal gauge length. Rates of extension of 1mm/min were employed for all tests.

## 4 RESULTS: Resistance bonded joints

*During this section each bonding trial shall be referred to by the test numbers assigned in Table 3.4.1.*

### 4.1 Debinding procedures

*For definitions / descriptions of brown / green strength refer to section 2.5.2 of the literature review.*

As mentioned in the previous section, the powder interlayers was subjected to three separate debinding routes prior to bonding. The first of these was the use of a vacuum furnace, with an aim to both debind and partially sinter the green powder interlayer. The equipment used can be seen in Figure 4.1.1 below.

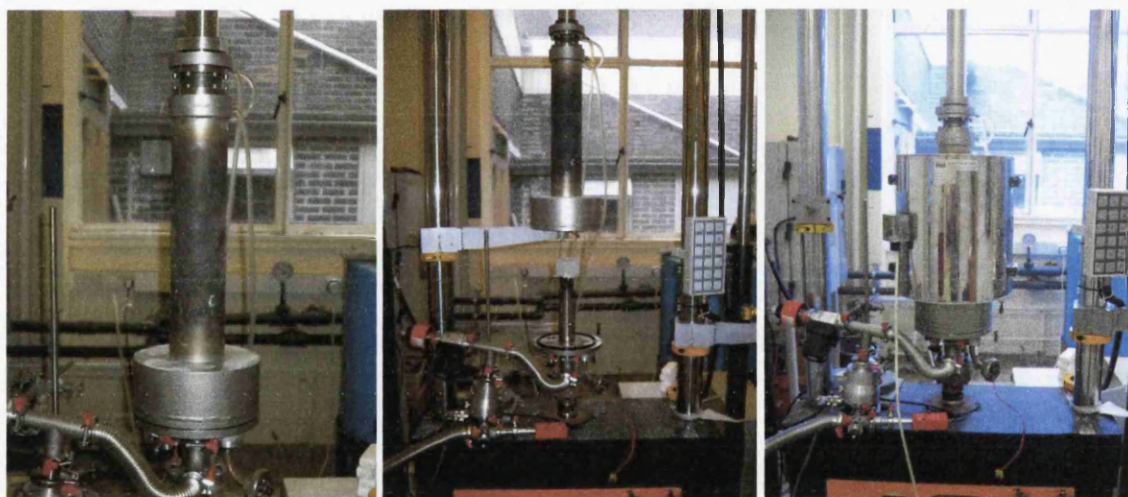


Figure 4.1.1: The vacuum used during initial debinding trials.

Initial trials on this debinding route illustrated problems with the green strength of the powder compact, as it was found that the interlayer would pull away from the surface of the specimen whilst establishing the vacuum. This effect is illustrated in Figure 4.1.2. In an attempt to improve green strength prior to debinding a drying time of approximately 12 hours was imposed. This improved green strength sufficiently to facilitate a full debinding procedure. Debinding times and temperatures can be viewed in Table 4.1.1.

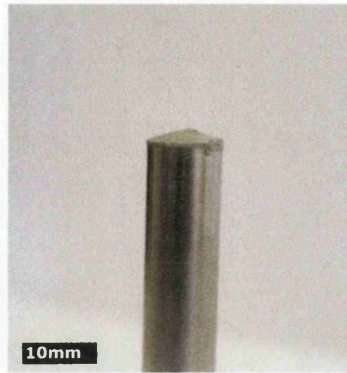


Figure 4.1.2: Disintegration of the powder interlayer during vacuum debinding.

Table 4.1.1: A summary of process variables for the debinding trials performed.

Condition	Temperature (°C)	Hold time at maximum temperature (hrs)
Initial (1)	500	4
Long time (2)	500	14
High temperature and long time (3)	700	14

Following the initial trials it became evident that the process variables were sufficient to facilitate complete debinding, but the brown strength of the resulting interlayer was not sufficiently strong to prevent its disintegration prior to bonding. As a result debinding times were increased to 14 hours. Unfortunately, although brown strength had improved it was still not satisfactory. Considering this temperature was then increased to 700°C (the ceiling temperature of the equipment in use). Following these trials a fully debound interlayer was produced that maintained the necessary strength to be applied during bonding trials. SEM and EDX analysis of the compacts (the results of which can be seen in Figure 4.1.3 and Figure 4.1.4) showed both good packing density and low relative levels of the carbon based binder.

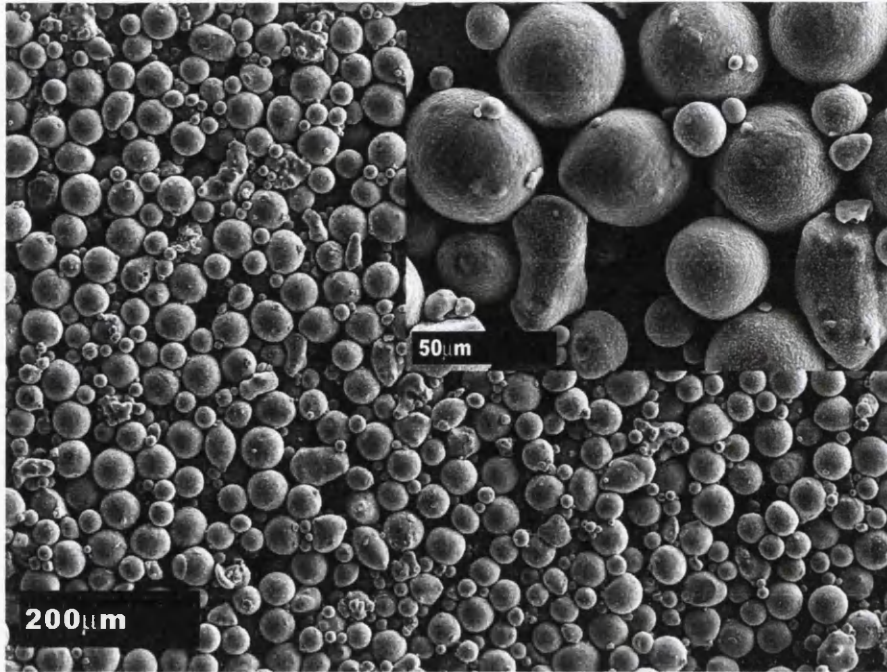


Figure 4.1.3: SEM images of the debound brown powder compacts produced at high temperature over 14 hours.

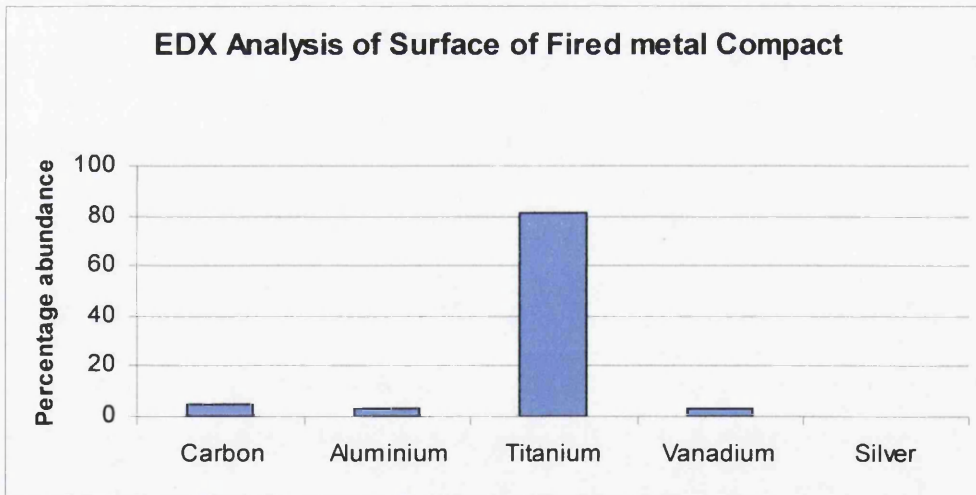


Figure 4.1.4: Results of EDX chemical analysis of the brown compacts debound at condition 3.

## 4.2 Tantalum coated Inconel 718 to Ti-6-4 with Ti-6-4 powder interlayer

### 4.2.1 Surface analysis

Figure 4.2.1 shows a macroscopic image of Test 1. The sample failed on removal from the Gleeble immediately after the bonding procedure. Considerable upset had accrued in the Ti-6-4 specimen, to the extent that the IN718 sample had become embedded in its surface. Significant oxidation was also noted.

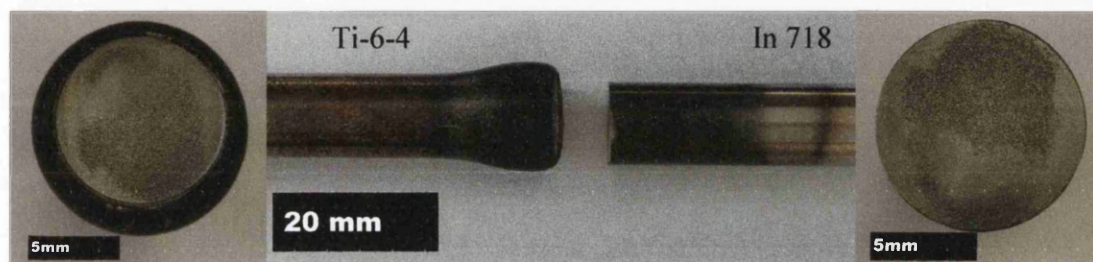


Figure 4.2.1: Plan and transverse macros of Test 1.

SEM and EDX analysis of the bond surfaces can be seen in Figure 4.2.2 and Figure 4.2.3 respectively. With reference to Figure 4.2.2 (a) and (c), partial sintering and adhesion between the powder and the substrate material was observed on both halves of the bond. As would be expected the degree of adhesion was greater between the Ti-6-4 powder and its substrate counterpart, with only a thin layer of sintered powder on the surface of the IN718 material. Also a varied degree of powder consolidation was observed over the area of the bond as a whole. This can be clearly seen in the differences between Figure 4.2.2 (a) and (b), as well as in Figure 4.2.2 (c). This effect is also noticeable from the ‘patchy’ appearance of the bond surfaces on the macroscopic scale, Figure 4.2.1.



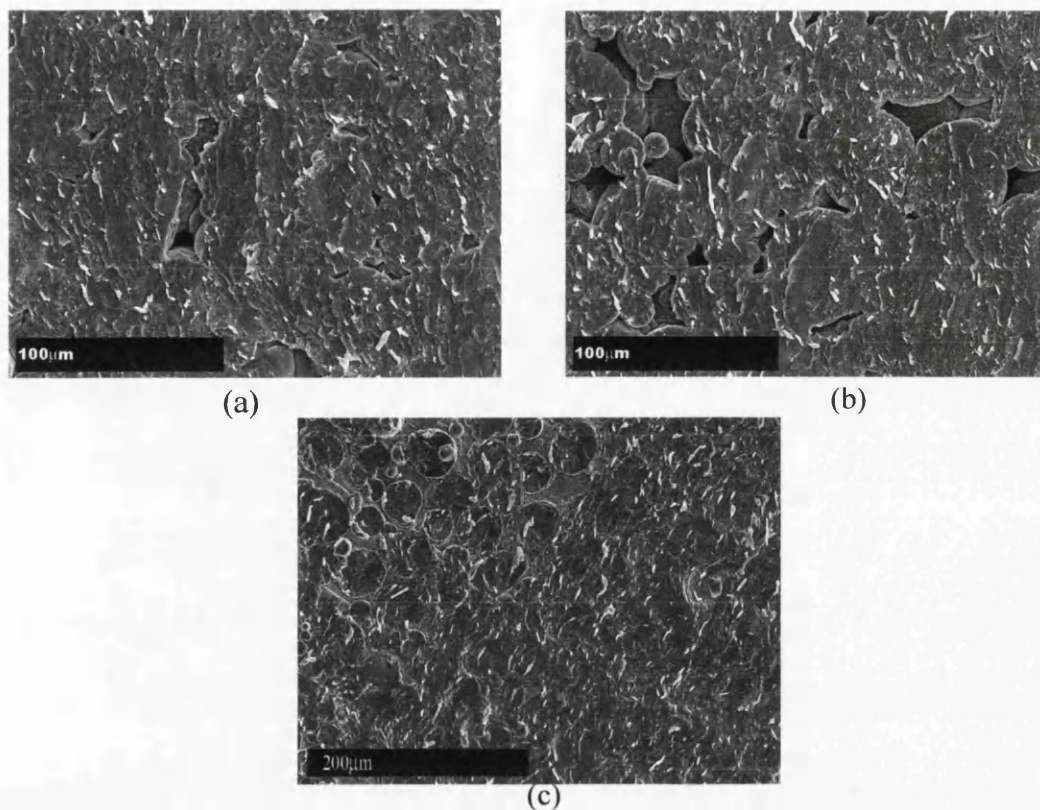


Figure 4.2.2: (a) Ti-6-4 sintered to Ti-6-4 substrate (b) less consolidated Ti-6-4 powder on Ti-6-4 substrate (c) Ti-6-4 powder bonded to IN718 substrate.

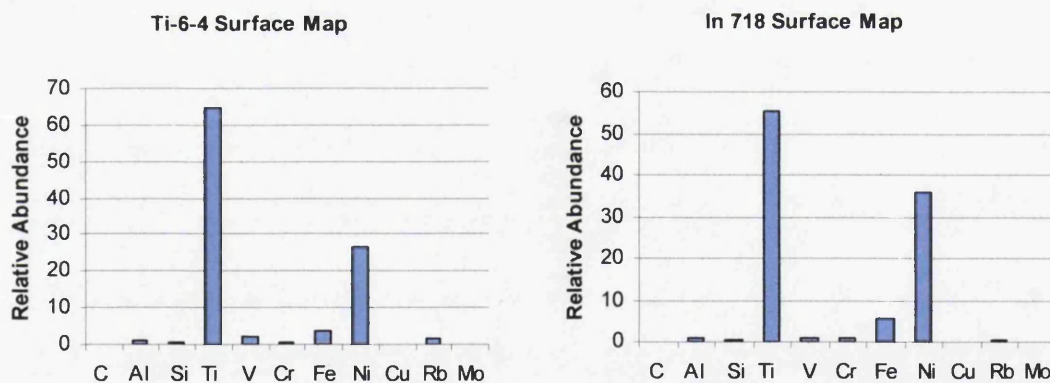


Figure 4.2.3: EDX Surface maps for both fracture surfaces in Test 1.

Elemental measurements were taken off either face of the board i.e. EDX focussed upon the Ti-6-4 and IN718 halves respectively. The EDX analysis indicated a significant degree of diffusion between the two halves, especially in the case of nickel and iron which appeared to diffuse freely at the surface of the Ti-6-4 interlayer. The exceptionally low

relative levels of carbon were also noted and were further evidence of the success of the debinding process employed at this stage.

#### 4.2.2 Metallography

The failure of Test 1 led to a more fundamental approach and the powder interlayer was excluded. Hence, joint quality was assessed by direct diffusion bonding between the substrate materials. Test 2 is a diffusion bond between IN718 and Ti-6-4 without a tantalum braze. Test 3 is the same bond incorporating a tantalum braze. The bonding force was also decreased as a result of the excessive upset accrued in the Ti-6-4 material during Test 1. Both bonds showed good initial adhesion and were successfully removed from the apparatus. Sections from the bonds were polished and etched and can be seen in Figure 4.2.4 and Figure 4.2.5.

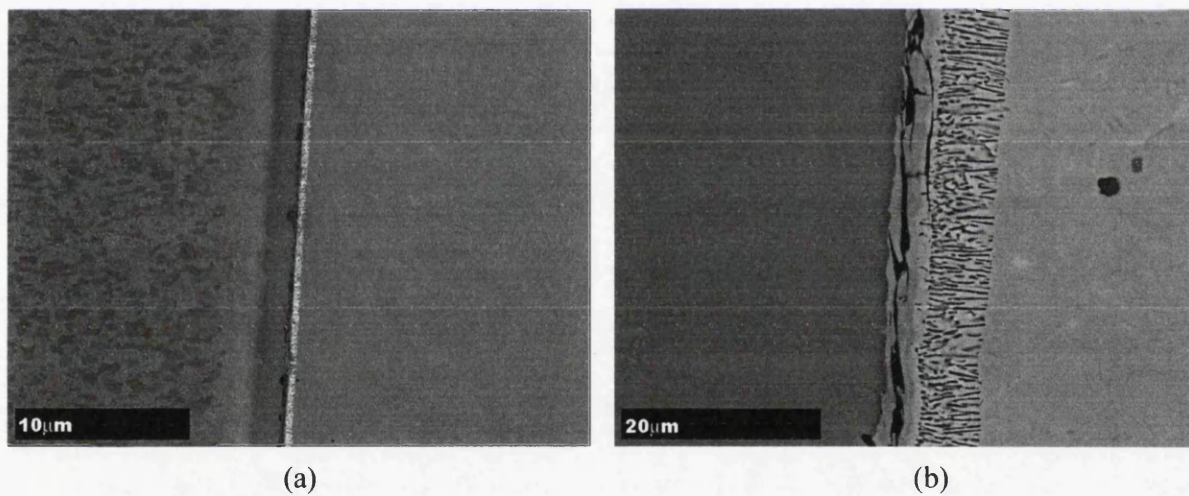


Figure 4.2.4: Sections through the bond line in Test 2 at (a) low and (b) high magnification.

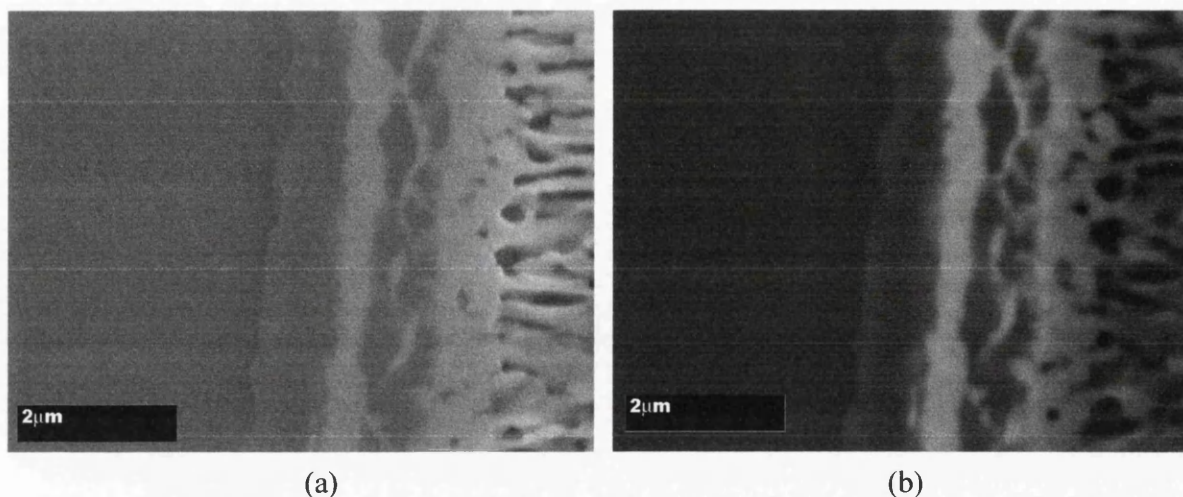


Figure 4.2.5: Sections through the bond line in Test 3 in (a) normal secondary electron and (b) backscattered electron modes.

Figure 4.2.4 (a) and (b) clearly show fracture of the bond at the interface. This fracture probably occurred in the mounting press during preparation of the section. An overview of the bond shows a distinctly unetched / under attacked region in the Ti-6-4 immediately adjacent to the bond line. The other major feature is the microstructural disruption observed in the In718 at the interface. On closer inspection this disruption was revealed as a porous / depleted zone. This can be clearly seen in Figure 4.2.4 (b).

Test 3 displayed increased adhesion without any evidence of fracture at the interface. At low magnification the bond appeared similar to that of Test 2. However, on closer inspection (seen in Figure 4.2.5 (a) and (b)) the existence of a more multi layered interface microstructure became apparent. This is reinforced with reference to Figure 4.2.5 (b) where the backscattered electron mode reveals more noticeably the changes in chemistry close to the bond. Figure 4.2.6 shows how this image relates directly to variations in chemical concentration over the bond line. Significant diffusion of nickel and iron over the interface has occurred, with relatively low levels around the depleted zone, suggesting the susceptibility to Kirkendall porosity [55].

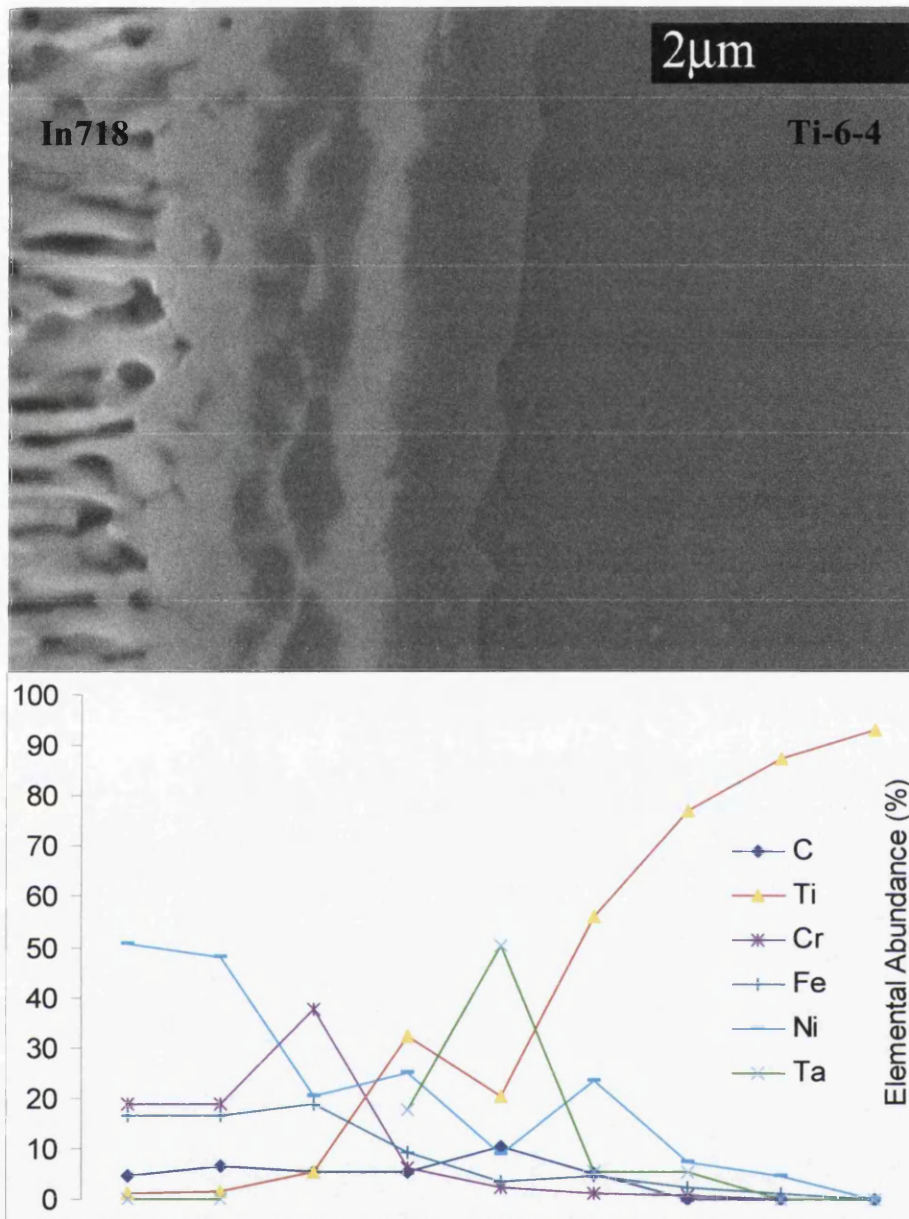


Figure 4.2.6: An EDX traverse matching a high magnification backscattered image of Test 3.

### 4.3 Nickel coated SCMV to Ti-6-4 with Ti-6-4 interlayer

Following the results gained above and those from supplementary research, a move was made away from Inconel to titanium bonds, and towards Ni coated SCMV material to titanium, again using a Ti-6-4 powder interlayer. After practical issues relating to the brown strength of the powder interlayer produced via vacuum debinding route trialed for

Test 1, these bonds were produced with interlayers that had been solely subjected to a 12 hour drying time. Again, a reduced force was applied to attempt to minimise upset in the T-6-4. Both bonds trialed under these conditions failed prior to removal from the apparatus and a very low level of adhesion was noted. In all cases the powder interlayer adhered well to the Ti-6-4 specimen. A macro of the typical appearance of the bonds can be seen in Figure 4.3.1. Follow up SEM images can be viewed in Figure 4.3.2.

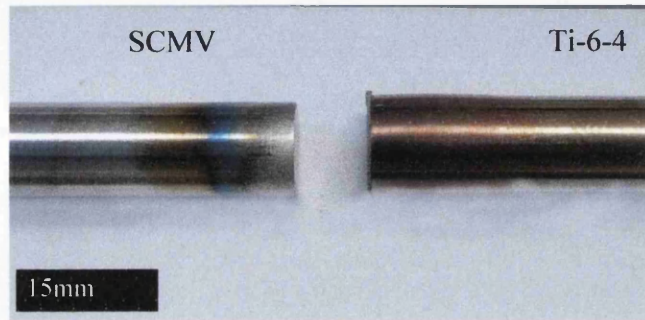


Figure 4.3.1: A Macro of Test 4.

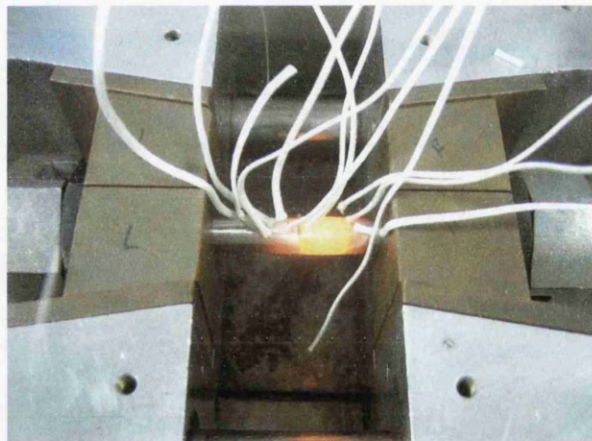


Figure 4.3.2: An illustration of the differential heating effect observed in Tests 4 and 5

### 4.3.1 Surface Analysis

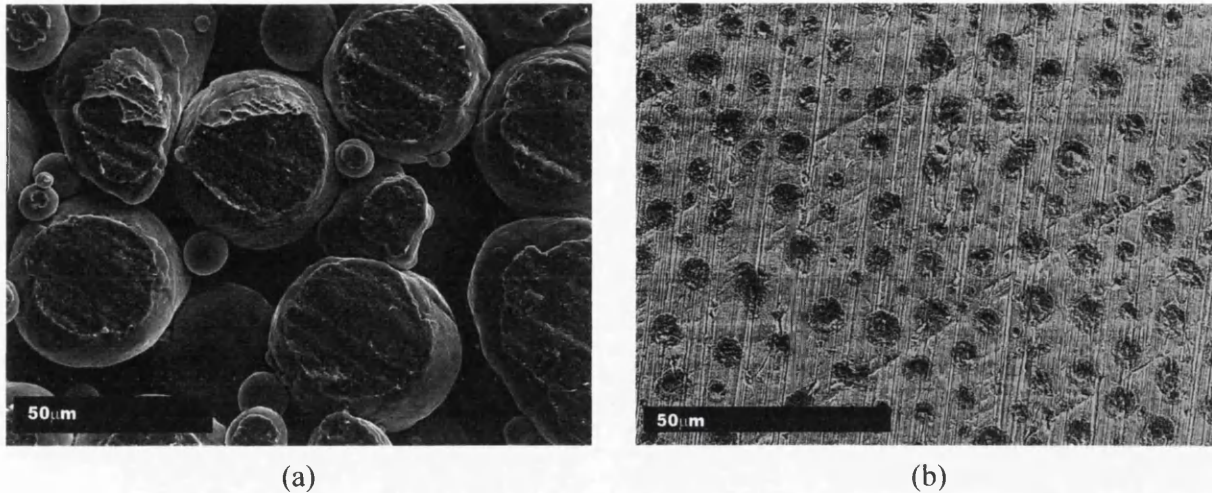


Figure 4.3.3: SEM images of (a) Ti-6-4 powder on Ti-6-4 substrate and (b) a backscattered image of adhesion sites on SCMV substrate.

With reference to Figure 4.3.1 a small heat affected zone can be clearly seen in the SCMV specimen. This was due to a non-uniform heating effect observed in both tests conducted under these conditions. The resistance heating effect was concentrated in T-6-4 material, with comparatively less heating occurring in the SCMV. This effect was most noticeable at the beginning of the tests, gradually normalising during the bonding process. Nevertheless, after the full hold time was completed this effect was still significant. Figure 2.3.2 shows the appearance of the bond approximately mid-way through the hold time.

Minimal upset has accrued in either specimen especially the SCMV. Considerable oxidation was noticeable on the Ti-6-4 specimen. This may be due to out-gassing from the binder during bonding. An SEM image of the surface of the powder interlayer can be seen in Figure 4.3.3 (a). Poor consolidation is noted compared to Test 1. Only limited sintering appears to have taken place. Furthermore, only a small proportion of the compact appears to have made contact with the SCMV material. This is characterised by the small fracture surfaces apparent on individual particles. To corroborate this, the SCMV faying surface revealed areas of adhesion and subsequent fracture on its surface. Backscattered electron images such as that seen in Figure 4.3.3 (b) helped identify compositional differences between these areas of adhesion and the non-connected parent material.

EDX chemical analysis confirmed these indications, finding that the adhesion sites on the SCMV show much higher levels of titanium and reduced levels of iron and nickel as compared to the surrounding material. The results of this analysis can be seen in Figure 4.3.4. Relative levels of carbon in these tests were also much greater than those recorded for Test 1.

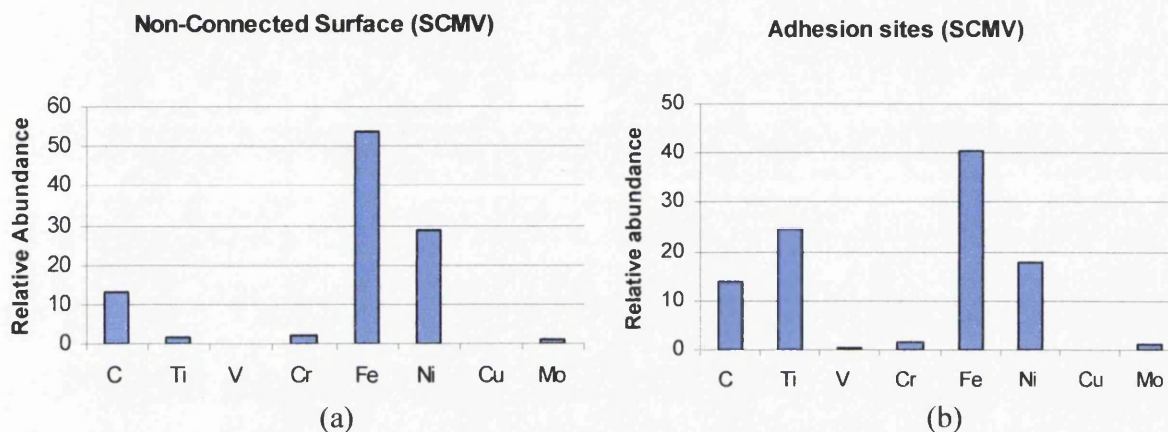


Figure 4.3.4: A comparison between EDX chemical analyses of adhesion sites on the SCMV surface and the substrate SCMV.

### 4.3.2 Metallography

A section of the Ti-6-4 powder compact from Test 4 is presented in Figure 4.3.5. The very poor consolidation of the powder interlayer is immediately apparent. Some inter-particle joining has occurred (see high magnification image inset), providing enough strength to both maintain the integrity of the interlayer and hold it onto the substrate of the specimen. However, the resultant faying surface area has been significantly reduced. The poor degree of consolidation remains consistent throughout the interlayer suggesting that the whole compact has seen insufficient temperature / force to facilitate consolidation. Despite this, some microstructural effects were noted in the Ti-6-4 substrate, indicating that conditions in the substrate would have been sufficient to induce elemental diffusion.

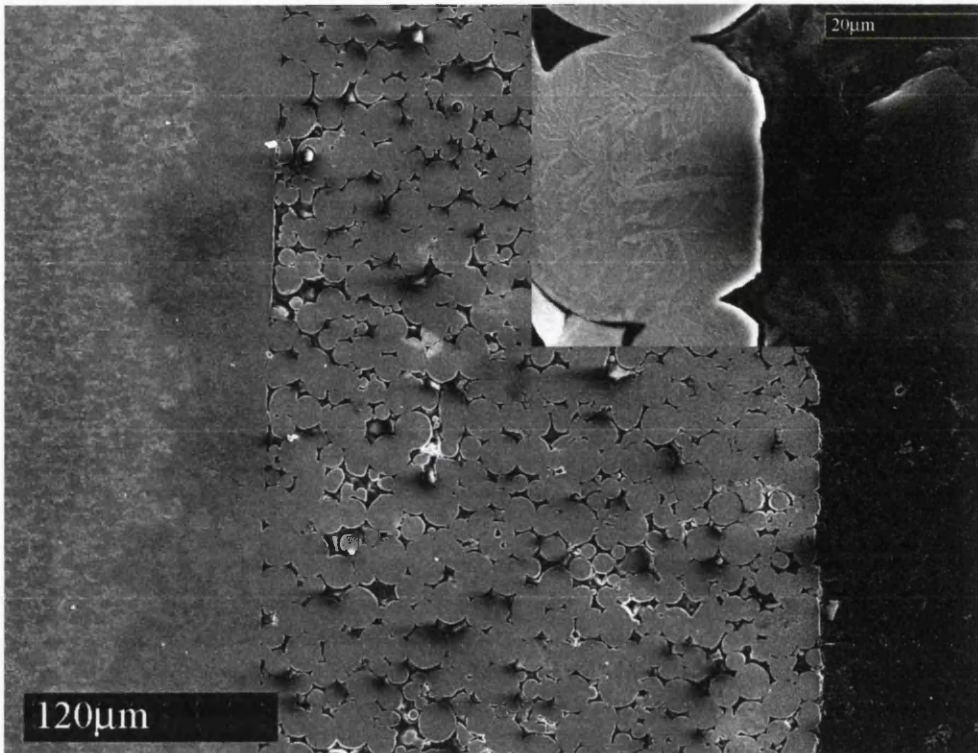


Figure 4.3.5: A metallographic section of Ti-6-4 powder on Ti-6-4 substrate in Test 4 with high magnification image inset.



#### 4.4 Differential Heating

The relatively poor quality of Tests 4 and 5 compared to Test 1 raised questions, particularly in relation to the non uniform heating that was observed. It seemed likely that the main reason for the poor adhesion in these tests was that not enough heat was being equally distributed across the interface. To better understand the reason for these effects and the process as a whole a more fundamental appreciation of the process was required. This is outlined below.

As outlined in section 3.2.1, the resistance bonding process is in turn governed by the Joule heating effect (equation 3.2.1.1). When broken down to its fundamental components, this effect is in turn reliant on both the applied voltage and the thermo physical properties of the material to be bonded. The following series of equations show how each of these factors relate to each other and the relative effects of their interactions.

As a nominal voltage  $V$  is applied to a continuous specimen at any one instance in time, a steady state electrical field is established where by its separate components can be defined by Laplace thus:

$$\frac{\partial^2 V}{\partial x^2} + \frac{\partial^2 V}{\partial y^2} + \frac{\partial^2 V}{\partial z^2} = 0 \quad 4.4.1.1$$

From this established electrical field, current density vectors ( $i_x$ ,  $i_y$ ,  $i_z$ ) can then be calculated for each component by references to a materials resistivity  $\beta$ .

$$i_y = \frac{1}{\beta} \frac{\partial V}{\partial y} \quad i_x = \frac{1}{\beta} \frac{\partial V}{\partial x} \quad i_z = \frac{1}{\beta} \frac{\partial V}{\partial z} \quad 4.4.1.2$$

A nominal current density vector can then be given by Pythagoras:

$$i^2 = i_x^2 + i_y^2 + i_z^2 \quad 4.4.1.3$$

This value may then be incorporated into a joule heating term with the Fourier heat transfer equation to give the temperature at any instance in time.

$$\frac{\partial T}{\partial t} = \frac{k}{c\rho} \left( \frac{\partial^2 T}{\partial x^2} + \frac{\partial^2 T}{\partial y^2} + \frac{\partial^2 T}{\partial z^2} \right) + \frac{i^2 \beta}{c\rho} \quad 4.4.1.4$$

For a given span B (figure 4.4.1) the temperature gradient across the specimen can be given by:

$$\frac{\partial T}{\partial x} = \frac{k}{c\rho} \left( \frac{\partial T}{\partial t} \right) \left( x - \frac{B}{2} \right) \quad 4.4.1.5$$

*At B/2 (the midpoint of the specimen)  $\frac{\partial T}{\partial x} = 0$  i.e. there is no heat flow and no temperature gradient*

The result would then be the parabolic temperature profile illustrated in Figure 3.2.3.

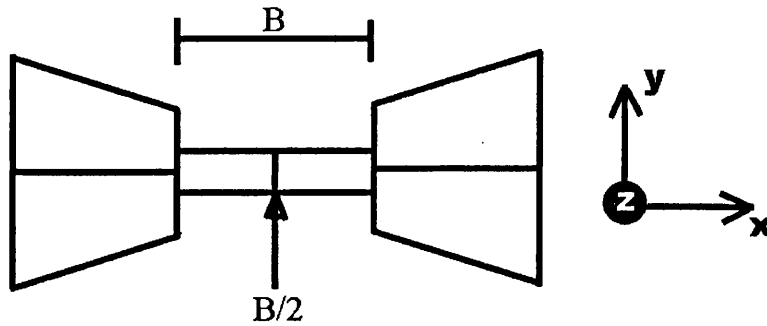


Figure 4.4.1: A schematic representation of the jaw / specimen configuration of the Gleeble 1500.

Although these equations relate to a continuous sample where no interface is present, they give a crucial insight into the factors affecting resistance heating; these being, resistivity ( $\beta$ ), thermal conductivity ( $k$ ) and specific heat capacity ( $c$ ). Considering these factors and their importance then elucidates the considerable difficulty to be found in maintaining a uniform heating effect between two samples with different thermo physical properties. This led to the assessment of material compatibility with respect to these properties set out below in section 4.4.1.

#### 4.4.1 Material compatibility

Using the principles set out above attention was then focussed on their relevance to the materials under investigation. Table 4.4.1 both gives values for the three fundamental properties to be considered in terms of resistance bonding for each material. It also draws comparison between these values in terms of the differences between the values for each bonding pair.

Table 4.4.1 : Thermo physical property data for Ti-6-4, IN718 and SCMV.

Raw data	Material	CTE ( $\mu\text{m m}^{-1}\text{°C}^{-1}$ )	Electrical Resistivity ( $\mu\Omega \text{ cm}^{-1}$ )	Specific Heat capacity ( $\text{J g}^{-1}\text{K}^{-1}$ )	Thermal conductivity ( $\text{Wm}^{-1}\text{K}^{-1}$ )	Compatibility (Difference in values)	Material	CTE ( $\mu\text{m m}^{-1}\text{°C}^{-1}$ )	Electrical Resistivity ( $\mu\Omega \text{ cm}^{-1}$ )	Specific Heat capacity ( $\text{J g}^{-1}\text{K}^{-1}$ )	Thermal conductivity ( $\text{Wm}^{-1}\text{K}^{-1}$ )
	SCMV Steel <sup>1</sup>	10 - 13	2.30E-05	0.46	26.1		Inconel to Ti-6-4	4.4	5.30E-05	0.091	4.7
Inconel 718 <sup>2</sup>	13	1.25E-04	0.435	11.4	SCMV to Ti-6-4	3.4	1.55E-04	0.066	19.4		
Ti-6Al-4V <sub>3</sub>	8.6	1.78E-04	0.526	6.7	CMV to Inconel	1-2	1.02E-04	0.025	14.7		

Of all three pairs it appears that SCMV to Ti-6-4 would be the most incompatible especially in terms of thermal conductivity and electrical resistivity, the two most important properties to consider in heat generation through resistance bonding. Inconel and Ti-6-4 were the most compatible in terms of heating related properties, but less so in terms of more general joining factors such as specific heat capacity and coefficient of thermal expansion. Conversely, SCMV and Inconel showed the exact opposite relationship. It was acknowledged that these comparisons do not take into account effects of chemistry and physical factors such as specimen morphology. Nevertheless, it was important that they were considered for future bonding trials.

<sup>1</sup> Data sourced from Thyrotech <sup>2</sup> Data sourced from Timet UK <sup>3</sup> Data sourced from special metals

#### 4.4.2 Experimental design modifications

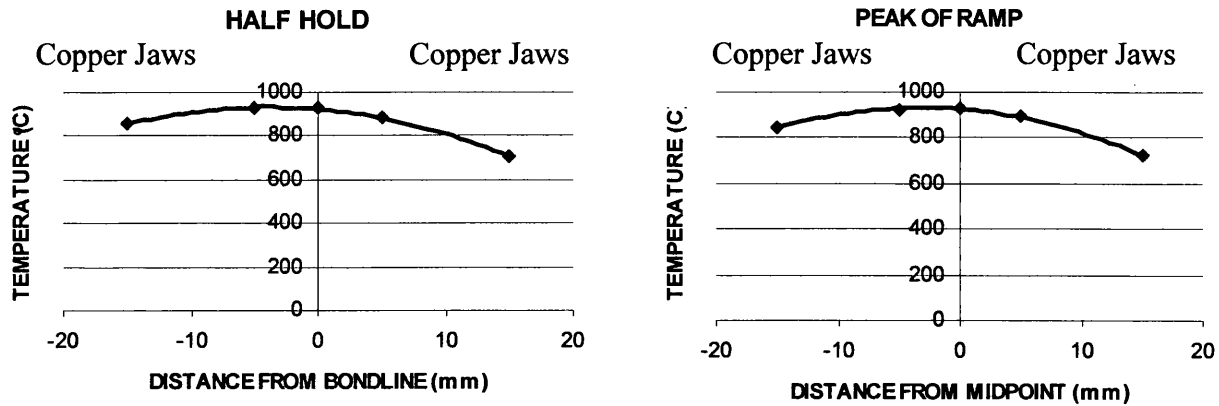


Figure 4.4.2: Temperature profiles for the standard copper jaw configuration.

To try and properly examine the integrity the of these SCMV to Ti-6-4 bonds despite the associated difficulties outlined above, a new jaw system was introduced to the Gleeble apparatus; the aim being to produce a more comparable heat between the SCMV and Ti-6-4 material. The jaw system achieved this by providing a smaller heat sink to the SCMV side of the bond. These were termed 'Hot jaws'. To examine their effect, trials (Tests 6 and 7) were conducted on solid specimens using both the original and hot jaw assemblies. Temperature profiles were recorded using the gleeble logging system. The results of these trials are illustrated in and Figure 4.4.2 and Figure 4.4.3.

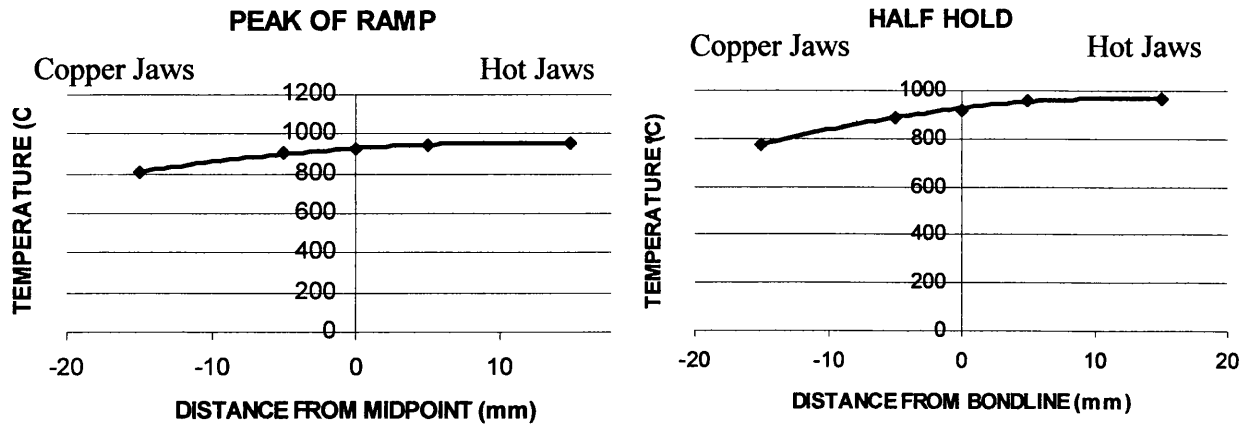


Figure 4.4.3: Temperature profiles for the uniform hot jaw configuration.

The result of the hot jaw configuration is a heating effect biased towards the hot jaws. This can be clearly seen in the comparison between the two sets of temperature profiles. This was then employed in bonding trials for Tests 8 and 9 to offset the differential heating effect.

#### 4.5 Ti-6-4 to Nickel coated SCMV with Ti-6-4 / BurTi interlayer

Tests 8 and 9 were performed using hot jaws on the SCMV side of the bond. Macros from these tests can be seen in Figure 4.5.1 and Figure 4.5.2. Figure 4.5.1 shows the heating distribution across the bond whilst using the new hot jaw assemblies (LHS). It is clear here that the SCMV material is subjected to a vastly increased heating compared to the original jaw configuration.

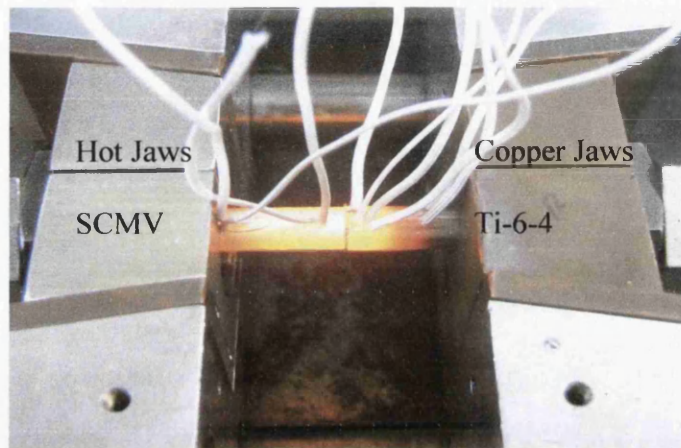


Figure 4.5.1: The effect of the hot jaw configuration on the visible temperature profile.

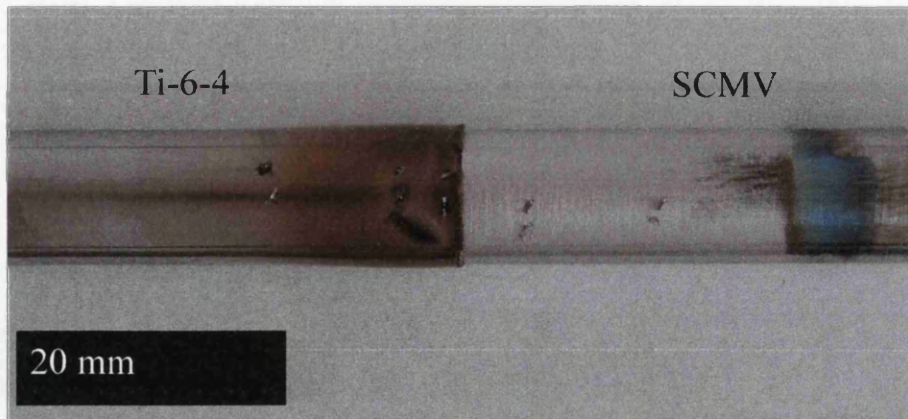


Figure 4.5.2: A macro of Test 9.

Figure 4.5.2 shows the resultant bond macro. The heat affected region of the specimen has increased substantially compared to that view in previous tests (Figure 4.3.1). Furthermore,

both tests were successfully removed from the apparatus without failure. Unfortunately, the bond strength was not sufficient enough to prevent fracture of the bonds during sectioning. Improved consolidation of the Ti-6-4 powder compact was evident, Figure 4.5.3. However, powder adhesion to the SCMV was again limited as in Tests 4 and 5.

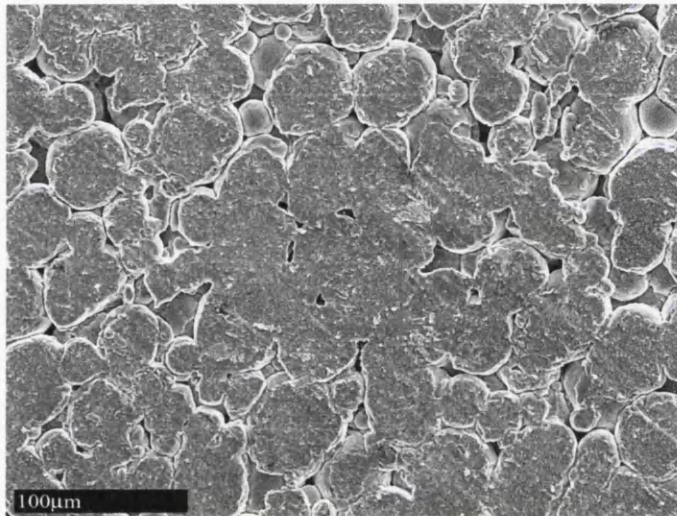


Figure 4.5.3: SEM fractography of Ti-6-4 powder on Ti-6-4 substrate.

Following these unsuccessful results a burn resistant titanium alloy (BurTi) interlayer was trialled and bonding conditions were modified, applying an increased force to try and aid powder consolidation. Macroscopic images of these early BurTi interlayer bonds can be seen in Figure 4.5.4. As in Test 1 significant deformation has occurred in the titanium material which has enveloped the SCMV specimen, Figure 4.5.4. Of more concern was the severe oxidation on the Ti-6-4 material. Following the failure on sectioning of previous bonds an attempt was made to grind through the bond to prevent excessive stress being imparted on it. Nevertheless, although specimens were successfully removed from the apparatus, failure occurred during this grinding procedure. Finally, a large heat affected zone was once again noted in the SCMV. Subsequent Vickers hardness measurements confirmed a considerable hardening of this material up to 700H<sub>v</sub>.

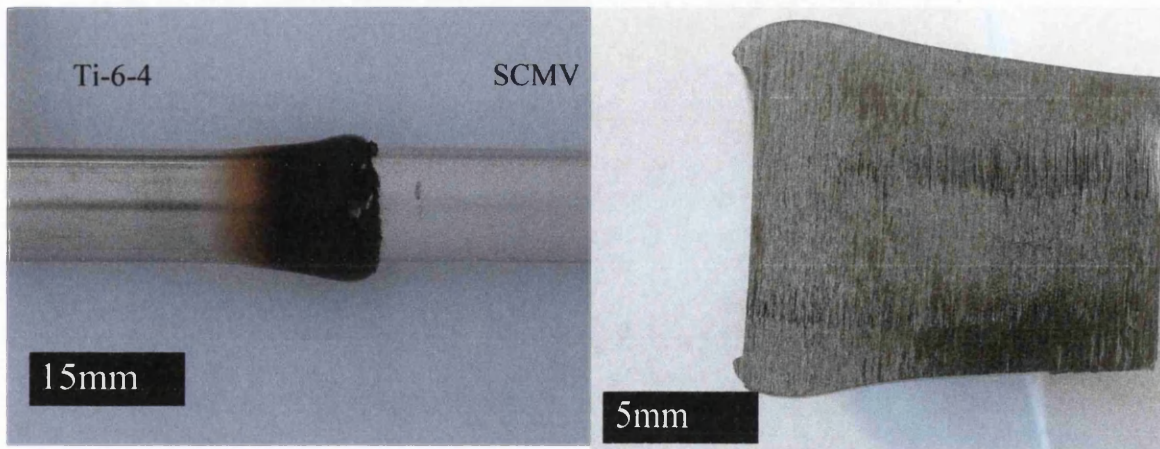


Figure 4.5.4: Macros of initial BurTi interlayer trial, with a section illustrating the deformation in the Ti-6-4 material.

In an attempt to reduce oxidation and improve bond quality, an in situ debinding stage was applied to the following two tests. Figure 4.5.5 shows the macros of (a) Test 12 and (b) Test 13. A 5 minute debinding stage at 200°C was employed for Test 12, whereas two 5 minute debinding stages at 200°C and 500°C were employed for Test 13. At the end of the bonding sequence a 10 minute cooling ramp to room temperature was also incorporated to try and prevent the hardening observed in the previous two tests. A clear reduction in the degree of oxidation was noted. Despite this, the degree of powder consolidation did not increase between the tests. No decrease in the degree of hardening was noted either. Powder interlayers remained bonded to the more common Ti-6-4 side in all tests with a typical appearance of that seen in Figure 4.5.6.

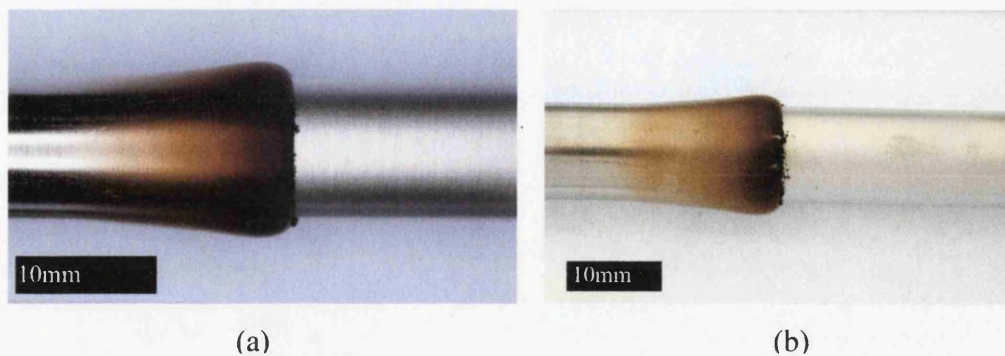


Figure 4.5.5: Macros of Tests (a) 12 and (b) 13



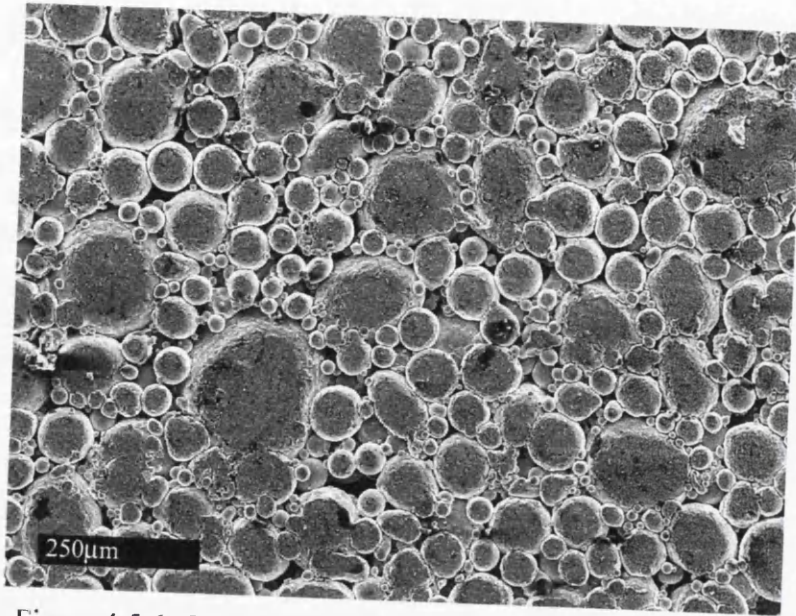


Figure 4.5.6: Consolidation at the BurTi to SCMV interface.

## **4.6 Chemical compatibility**

During this stage of the investigation, results of supplementary work had shown that satisfactory bonds could be produced by adopting the same process variables to those previously employed to manufacture homogenous Ti-6246 bonds [149]. Conversely, despite altering a range of different process variables little effect seemed to have been made on improving bond quality in this investigation. This suggested that the problems experienced here may be due to chemical differences / incompatibilities at the interface. The primary cause of poor bond quality appeared to be due to brittle phase evolution at the bond line. These phases were often found to have fractured before the bonds had left the apparatus, suggesting that other factors may have contributed to the cracking in these phases. The most plausible explanation is that differences in coefficient of thermal expansion between both titanium and steel (Table 4.4.1), have led to residual stress in the phases. This stress may then result in failure of the bond following the removal of the compressive bonding pressure. A review of the relevant literature showed that 'transition joining' techniques incorporating multilayer brazes lead to improved bond qualities in alloy pairings that are difficult to join [147]. Consequently a decision was made to investigate the use of a triple brazed Ni-Cr-V layer that was to act as a buffer between the two materials.

### **4.6.1 Comparisons to conventional HIP technique**

During the course of the investigation, the bonds produced using conventional HIPing techniques had yielded superior results in respect of powder consolidation. The fundamental difference between this HIPing technique and resistance bonding was the increased force applied. However, the HIPing equipment used allowed the implementation of a long (twelve hours) 'cold' vacuum debinding stage prior to bonding. All other bonding parameters were similar to the conditions employed in the Gleeble. Preliminary results showed some structural integrity.

Compared to this HIP technique the fundamental factor limiting the force to be applied in the Gleeble was the severe upset that occurred under large loads. This coupled with the differential heating effect made Ti-SCMV pairings less practical. On these grounds more attention was then focussed on SCMV-IN718 and Ti-6-4-IN718 pairs. Furthermore, early plans for the development of an isostatic force condition (detailed in section 4.6.2) were under development. In addition, the continued success of similar Ti-6246 resistance heated powder interlayer trials suggested that chemical incompatibility may be a major factor in controlling bond quality.

#### 4.6.2 Further modifications

The HIPed bonds had suggested that increases in applied force provided considerable improvements in bond quality. Therefore a method was devised by which these conditions may be replicated in this investigation. The isostatic force was achieved by applying a radial constraint in the (form of a sleeve) to the bond which, during upset, resisted radial flow, creating a quasi isostatic force condition. A schematic of the sleeve design can be seen in Figure 4.6.1.

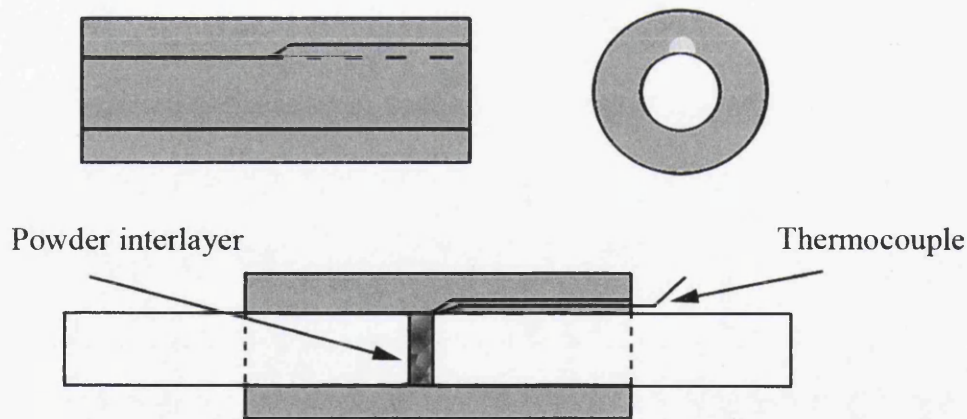


Figure 4.6.1: A schematic diagram of the sleeve design.

At this stage of development the sleeve was machined from mild steel and coated with a refractive powder lubricant to prevent bonding between itself and the specimens. However, it is the intention to manufacture a sleeve with a ceramic inner section. This will help to both reduce sleeve – specimen adhesion and will also electrically insulate the sleeve from

the specimens more effectively. Finally, the sleeve also holds the powder interlayer in place, negating the need for a binder and reducing overall bond contamination.

#### 4.7 Ti to Ni-Cr-V (triple) coated SCMV with BurTi interlayer

The macro of Test 14 can be seen in Figure 4.7.1. With reference Table 3.4.1 this test was carried out under the same conditions as the previous bonds. The bond had failed prior to its removal from the apparatus. Considerable oxidation was noted on the SCMV side although again the degree of oxidation in the Ti-6-4 appears to have been limited somewhat by the debinding procedures. The severe oxidation was noted only in the region of the triple braze.

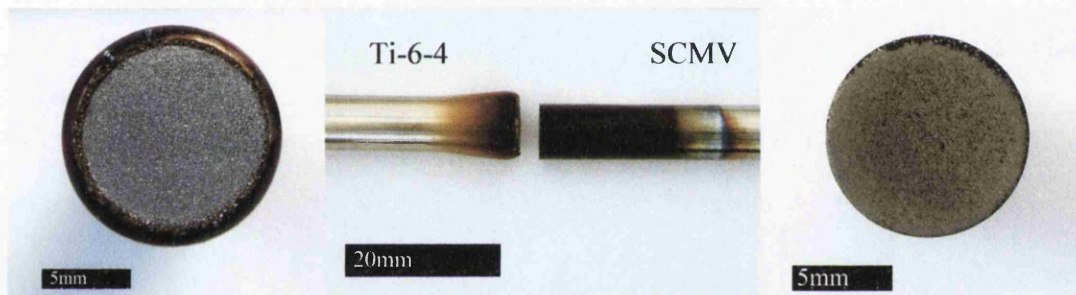


Figure 4.7.1: A macro of Test 14.

Considering the poor results from Test 14, temperature and pressure were increased for bond 16 in an attempt to improve bond quality. Some difficulty was encountered in bonding titanium at these temperatures as the welds between the control thermocouples and the titanium specimen tended to fail close to these temperatures. A successful bond was produced (Test 16) and the macro of this can be seen in Figure 4.7.2. Nevertheless, bond quality did not improve.

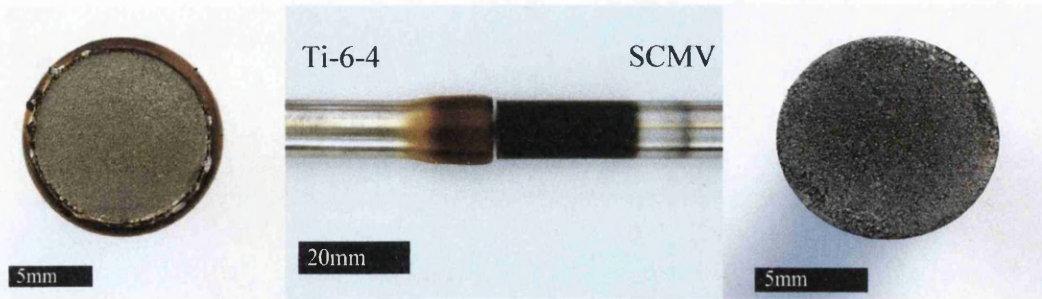
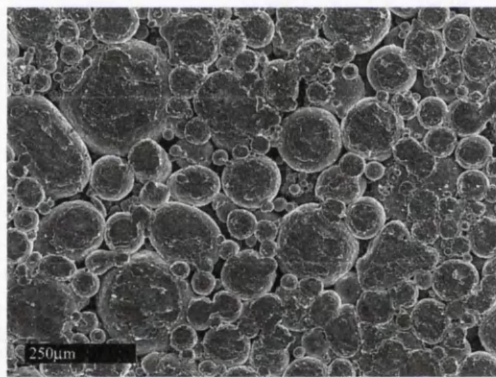
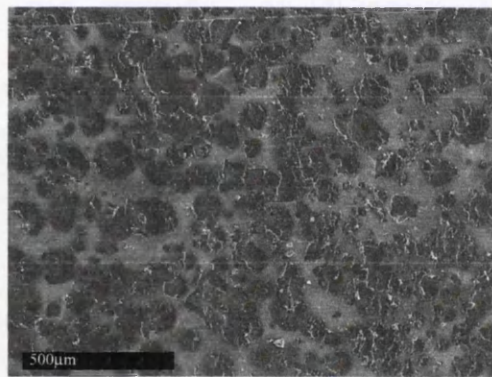


Figure 4.7.2: A macro of Test 16 bonded at 970°C.

The results of SEM fractography along with corresponding surface EDX analysis can be seen in Figure 4.7.3. Again, consolidation of the powder interlayer is poor. Only low levels of consolidation are seen with small contact surface areas between particles. The surface of the SCMV shows corresponding adhesion sites. Backscatter analysis again revealed these to be different in composition to the substrate material, indicating partial diffusion and bonding of the powder interlayer to the triple coated SCMV.



Triple coated Burti Interlayer 970C : Ti-6-4 Side



Triple coated Burti Interlayer 970C : SCMV Side

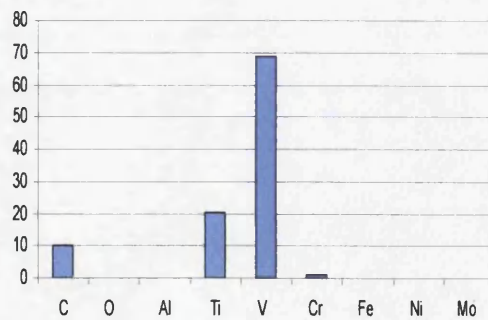
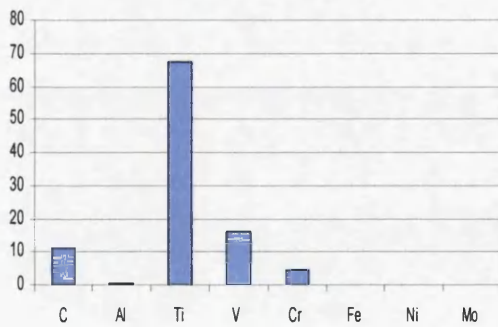


Figure 4.7.3: SEM fractography and corresponding EDX analysis of fractured specimen halves from Test 16.

The first feature noted in the EDX data was the relative carbon levels found both in the compact and the areas of adhesion on the SCMV. Though the levels are higher than that found after fully debinding the interlayer prior to bonding, they are also less than those found in bonds produced with no in situ debinding procedure. This indicates some level of success in that respect. The second noticeable feature is the mirror image noticed between the two with respect to levels of titanium and vanadium. Indicating the presence of a secondary interface at the point of fracture.

A section of the BurTi powder interlayer can be seen in Figure 4.7.4. Compared to the performance of Test 9, overall compact consolidation has substantially improved. However, the degree of consolidation decreases approaching the bond line, resulting in the distinct particles viewed in the plan view of the BurTi interlayer in Figure 4.7.3.

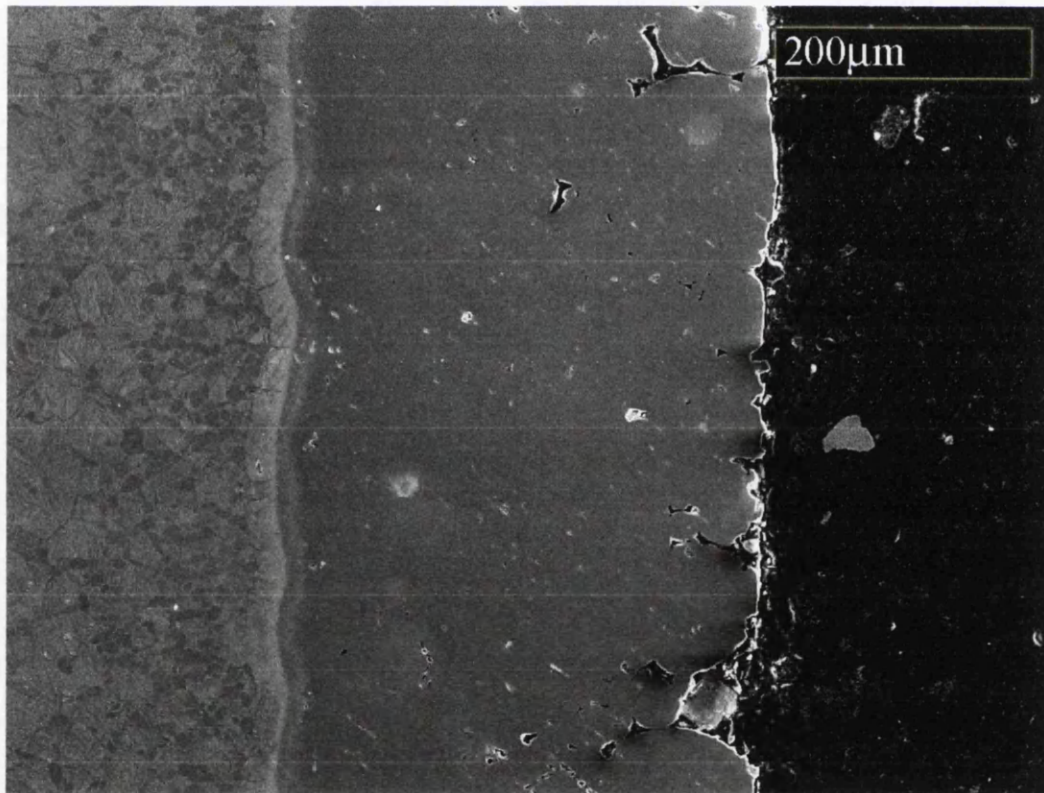


Figure 4.7.4: A metallographic section of BurTi powder on Ti-6-4 substrate in Test 16.

#### 4.8 Tantalum coated SCMV to Inconel 718 with Inconel 718 powder

Following the failure of previous bonds, and considering the compatibility issues raised in section 4.4.1, further trials looked at bonding attempts on materials with a more similar compatibility with respect to the resistance heating effects. All of these tests were conducted without needing the ‘hot’ jaw configuration. Macros of Test 17 can be seen in figure 2.8.1, with corresponding fractography in Figure 2.8.2. The strength of both materials at high temperature allowed an increased force to be used without fear of significant upset. Despite this, bonding was still unsuccessful, and the bond had failed before the specimens were removed from the apparatus. The powder interlayer remained attached to the common Inconel. SEM images revealed poor consolidation of the compact and low effective bond area with reference to the adhesion sites seen in Figure 4.8.2 (b). Again the backscattered image (inset) showed a minor degree of material transfer onto the SCMV specimen.

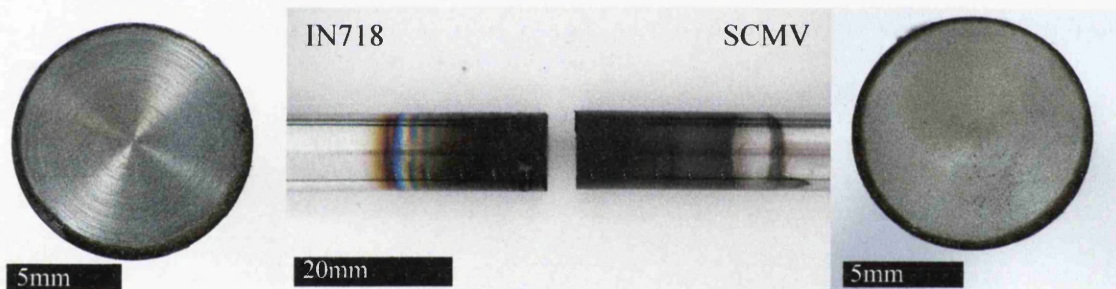


Figure 4.8.1: A macro of Test 17.

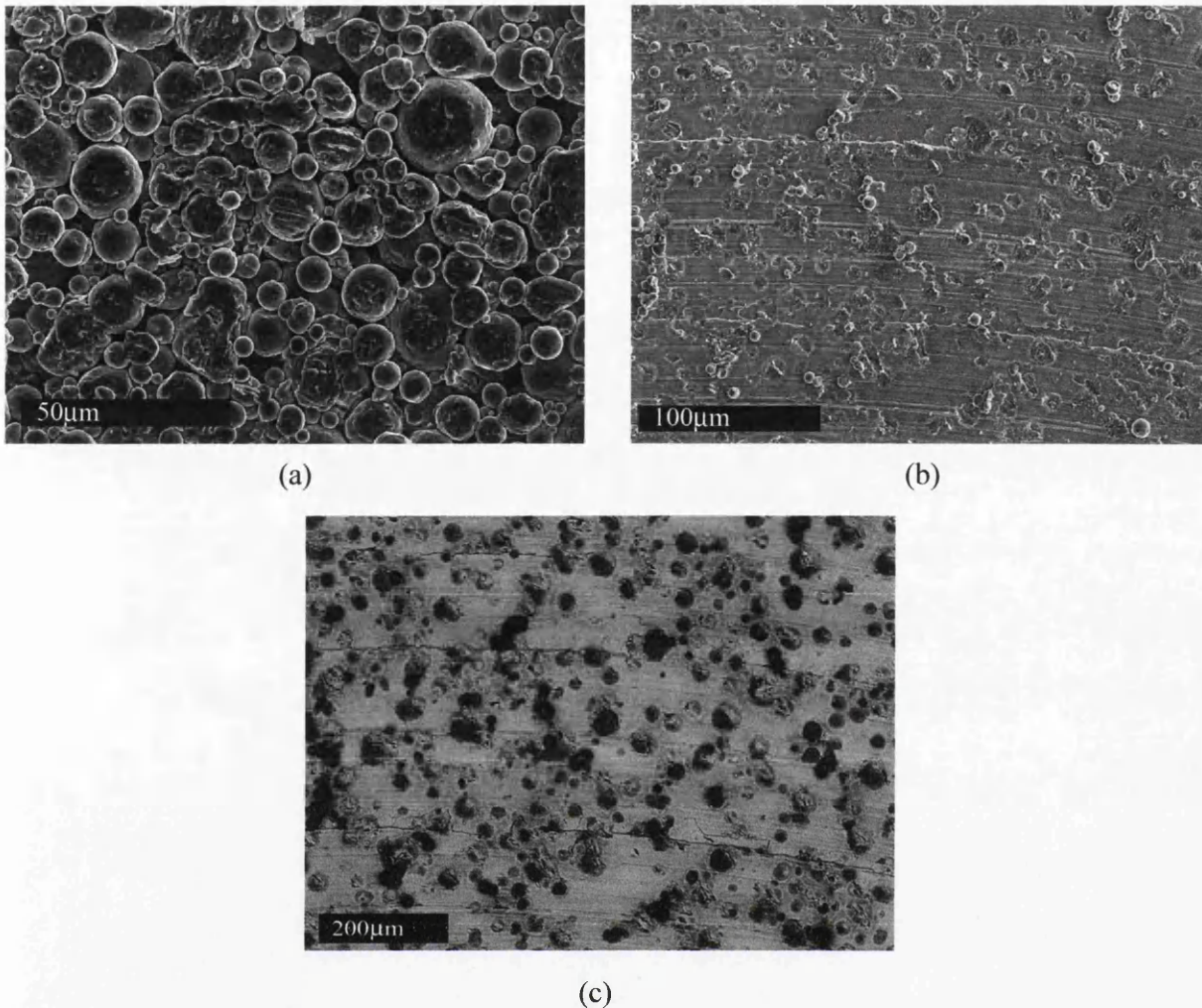


Figure 4.8.2: SCMV images of (a) IN718 powder on IN718 substrate and (b) adhesion sites on SCMV substrate with a corresponding backscattered image (c).

#### 4.9 Quasi isostatic forces during resistance bonding (QUIP)

Tests 18 and 20 were initial trials of the quasi HIPing procedure proposed in section 4.6.2. The tests were conducted successfully and the bond / sleeve assembly was removed from the apparatus intact. The bond was also successfully removed from the sleeve without damage, however, it fractured during subsequent evaluation. The macros of Test 18 can be seen in Figure 4.9.1. The discolouration of the area surrounding the interface was partly due to oxidation but also to the considerable build up of the powder based lubricant used within the sleeve. Plan views of the bonds also indicate both a higher degree of powder consolidation and adhesion to the uncommon material. This was reinforced with SEM



analysis of the fracture surfaces as seen in Figure 4.9.2. Figure 4.9.2 (a) clearly shows an increased degree of adhesion between the Inconel powder and the tantalum coated SCMV specimen. Figure 4.9.2 (b) shows both low and high (inset) magnification of the surface of the Inconel specimen. A superior degree of consolidation is evident.

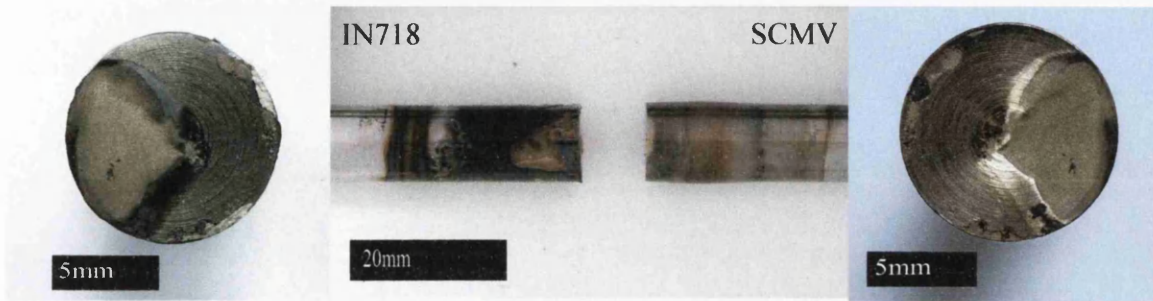


Figure 4.9.1: A macro of test 18.

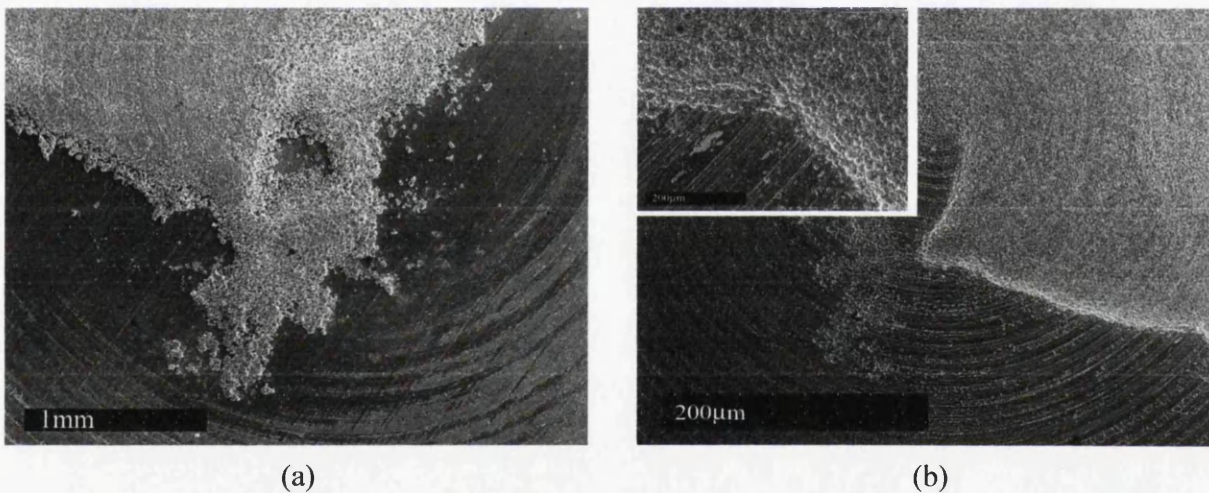


Figure 4.9.2: SEM images of (a) IN718 powder on uncommon SCMV substrate and (b) well assimilated IN718 powder on IN718 substrate with a higher magnification image inset.

Despite these promising results, some difficulties were encountered during the bonding process. The most significant of these was the length of the sleeve. It appeared during bonding that the sleeve was not sufficiently wide to cover the whole expanse of the ‘hot’ zone within the Gleeble. This meant a reduced force was required to prevent upset around the sleeve. In order to overcome this problem Test 20 was conducted using similar

conditions but a wider sleeve, in the hope that this would allow the use of higher forces during bonding. The results of this test can be seen below.

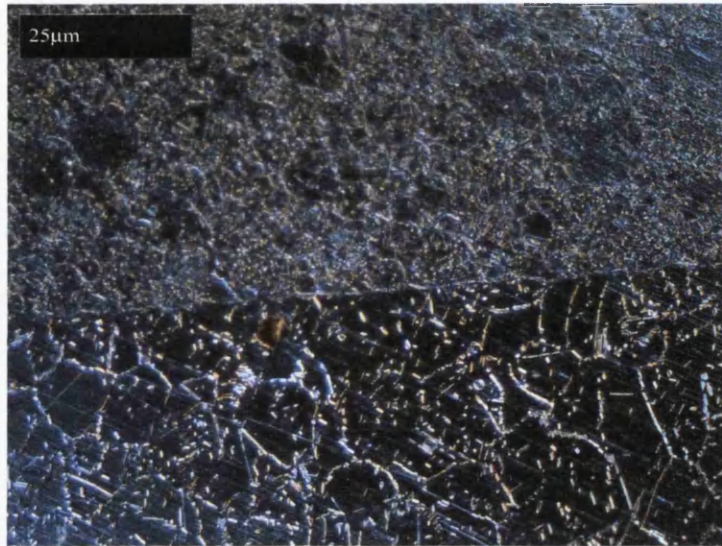


Figure 4.9.3: An optical micrograph of the IN718 powder - IN718 substrate interface viewed under polarized light.



Figure 4.9.4: A macro of Test 20.

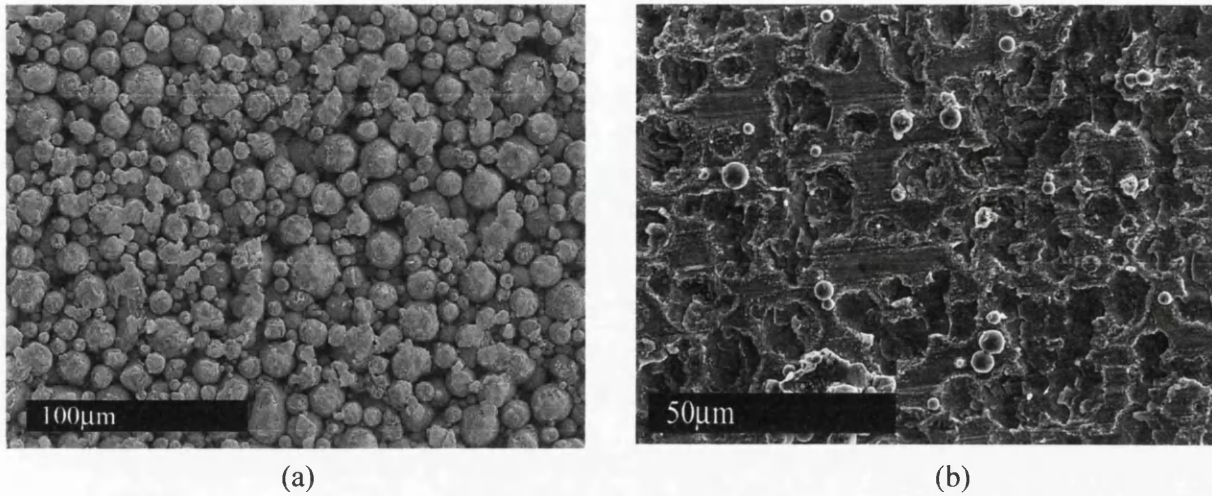


Figure 4.9.5: SEM analysis of (a) IN718 powder on IN718 substrate and (b) adhesion sites of SCMV substrate for Test 20.

Surprisingly, much less consolidation was noted in this test compared to its lower force counterpart, Test 18. Friction or bonding between the sample and the sleeve is the most likely reason for this. Under these high temperature / high force conditions it is likely that some bonding between the sleeve and the specimens occurred before restabilising interfacial contact reducing effective bond force. Despite this, a significant degree of adhesion was recognised on the SCMV material.

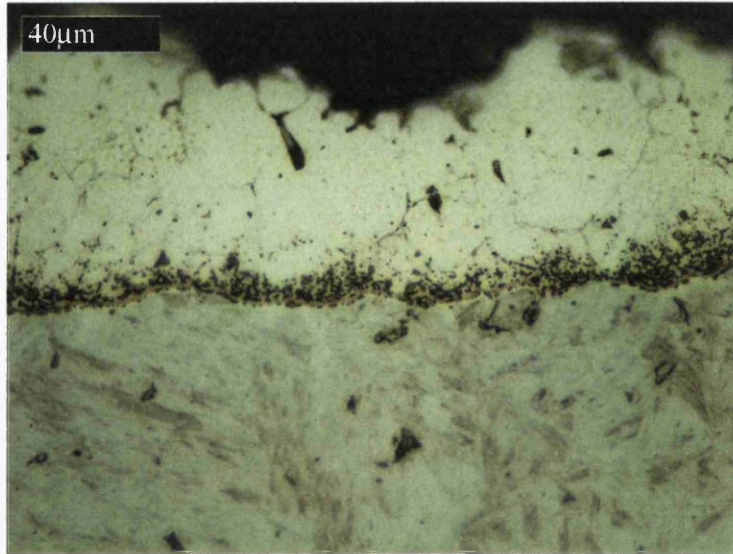


Figure 4.9.6: A high magnification optical micrograph of the SCMV - IN718 powder interface.

#### 4.10 Tantalum coated Inconel 718 to Ti-6-4 with BurTi powder

Another pair attempted was the tantalum coated Inconel to Ti-6-4 with a BurTi interlayer. Considering the poor performance of the bonds previously attempted using the original technique, this test was conducted at high force over a long period of time to ascertain initial material compatibility. The heating effect between the materials was more uniform than that observed between Ti-6-4 and SCMV confirming the link between the values in Table 4.4.1 and real heating effects. Despite this and the high force, little or no adhesion was observed, with the bond failing prior to being removed from the apparatus. Macros of the bond can be seen in Figure 4.10.1. An apparent difference in upset between the two specimens is noted. SEM images showed low degrees of powder consolidation and similar areas of adhesion on the uncommon Inconel specimen to those seen in previous tests. These can be seen in Figure 4.10.2. High magnification images of the adhesion sites (Figure 4.10.2 (b) and inset) showed a fibrous appearance that was common to most sights in all fracture surfaces of a similar appearance.

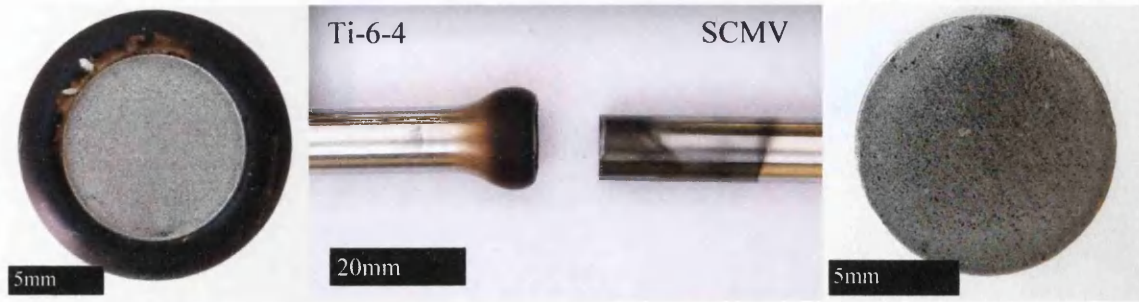


Figure 4.10.1: A macro of Test 19.

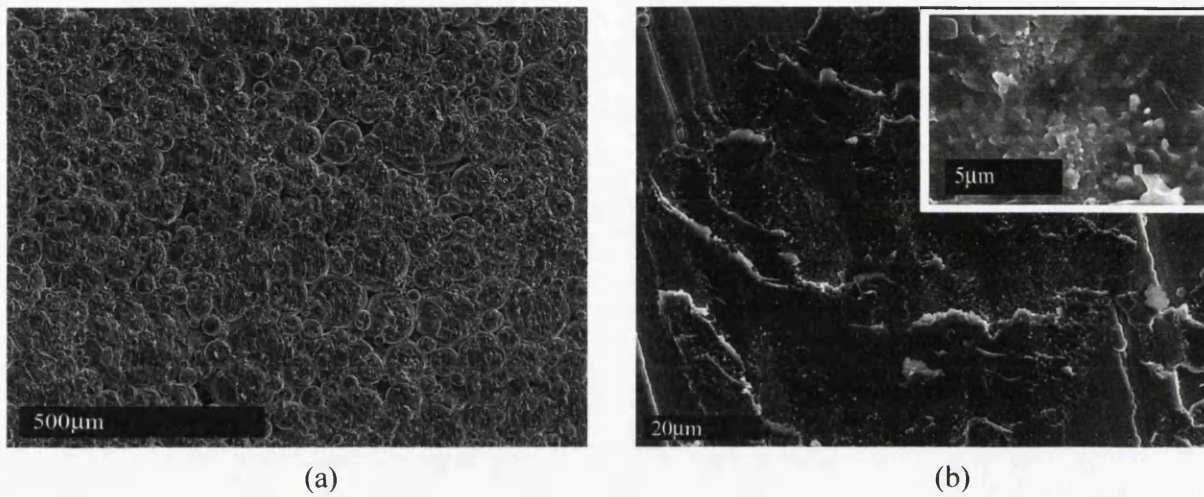


Figure 4.10.2: SEM images (a) BurTi powder on Ti-6-4 substrate and (b) an image of an adhesion site on the SCMV substrate with a high magnification image inset.

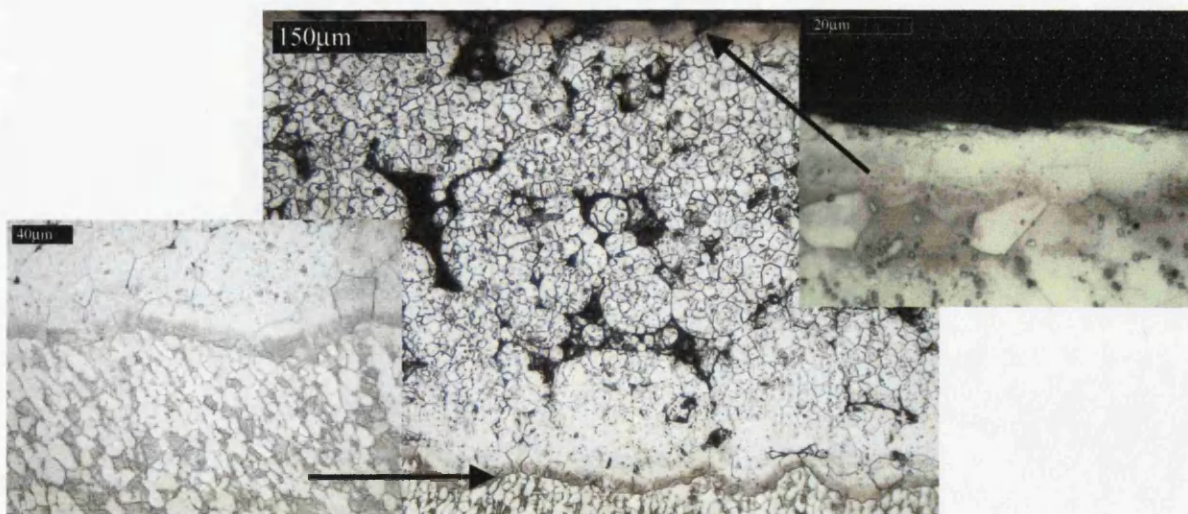


Figure 4.10.3: An optical micrograph of the BurTi powder interlayer on Ti-6-4 substrate with high magnification detail inset.

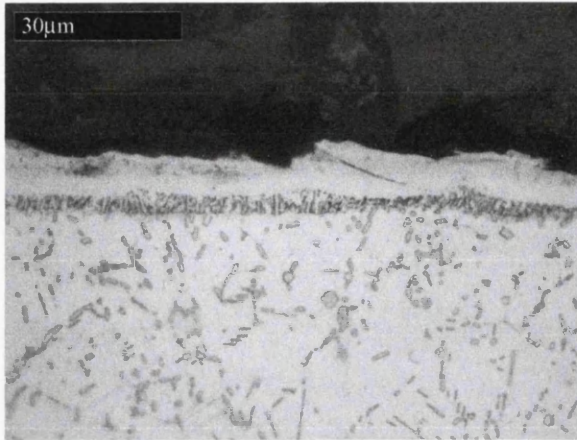


Figure 4.10.4: A high magnification optical micrograph of the tantalum coated IN718 bond half.

#### 4.11 Copper impregnated powder interlayers

In Test 21 Ti-6-4 was bonded to Ta coated IN718 using an impregnated powder interlayer in an attempt to see how this would effect both powder consolidation and bond integrity. The technique is essentially one of transient liquid phase bond as described in section 2.9 whereby melting point depressants are mixed into the powder to aid diffusional mass transport and facilitate joint wetting. The copper powder was mixed with that of the Ti-6-4 at 6% by weight. The impregnated powder was then mixed with the binder and the bond was performed under the conditions outlined in table Table 3.4.1.

The resulting micrographs can be seen below in Figure 4.11.1 and Figure 4.11.2. Figure 4.11.1 (a) shows an overview of the powder compact. Immediately recognisable is the substantial improvement in powder consolidation, in fact no porosity was viewed throughout the interlayer. However, Figure 4.11.1 (a) shows how despite this radical improvement the fracture of the bond appears again to have occurred at a brittle intermetallic at the interface with portions of this clearly visible at the IN718 interface.

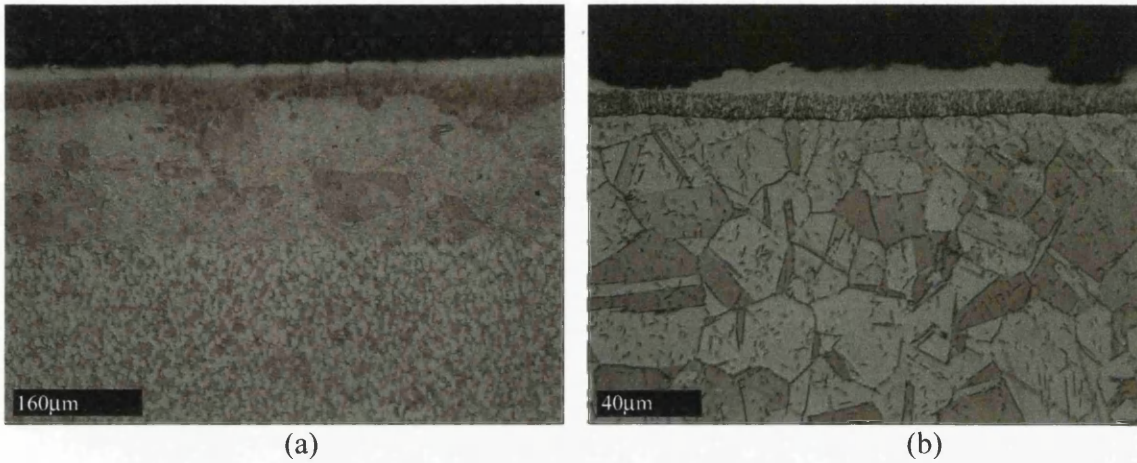
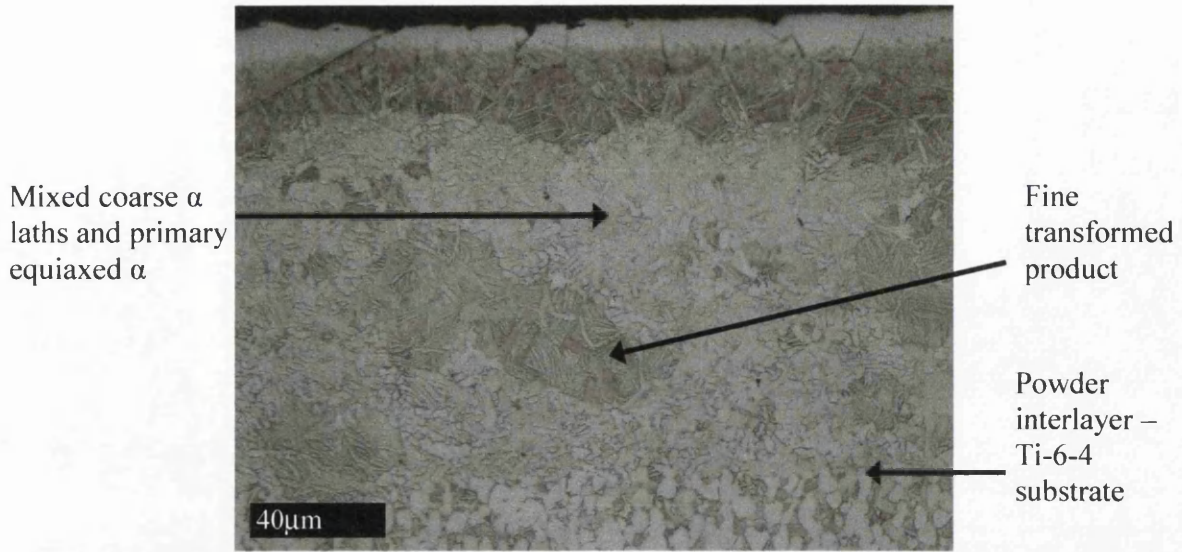
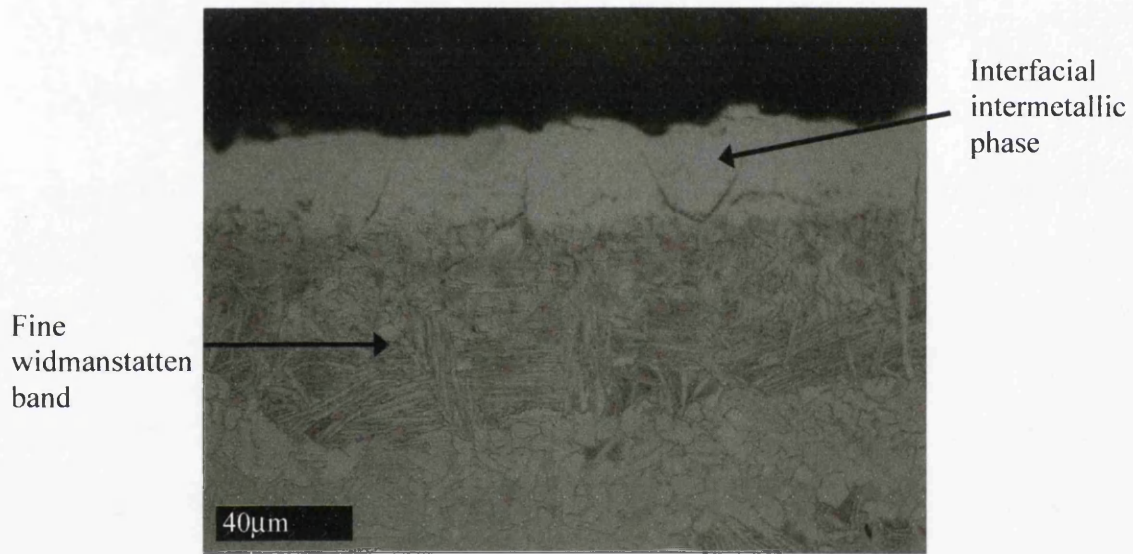


Figure 4.11.1: An overview of bond 21 from (a) the Ti-6-4 side and (b) the IN718 Side.

Figure 4.11.2 shows detailed photomicrographs of (a) the powder compact and (b) the compact to IN718 interface. Considering (a), for the most part a mixture of fine equiaxed primary  $\alpha$  and coarse  $\alpha$  lath dominates the microstructure with localised areas of significant growth of a coarse widmanstatten transformed  $\beta$ . This is particularly evident in Figure 4.11.2 (b) at the powder / IN718 interface where a coarse 50µm band of widmanstatten structure gives way to the intermetallic interfacial structure. There appears to be evidence that the structures are related as growth of  $\alpha$  needles into the intermetallic can be seen.



(a)



(b)

Figure 4.11.2: Detailed views of the microstructures of (a) the impregnated powder compact and (b) the powder to IN718 interface.



#### 4.12 Titanium substrate to IN718 substrate using a Copper braze interlayer

This bond chemistry exhibited minimal adhesion as can be seen in figure 2.12.1. A relatively high degree of oxidation of each specimen was again noted with a characteristic darkening of the IN718 specimen in particular. Crucially, macroscopically these bonds produced without powder show little differences in appearance to those previously produced with powder.

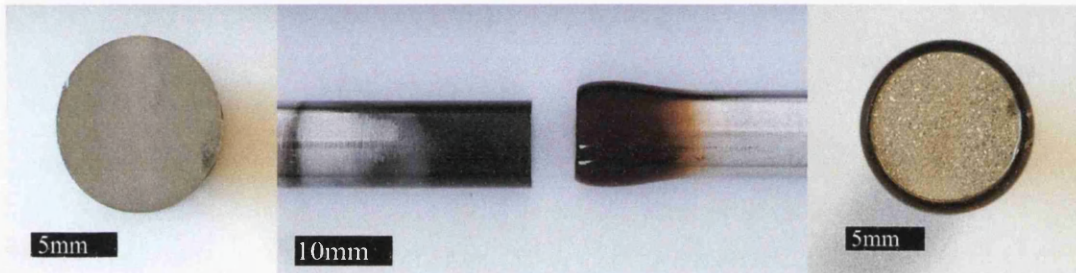


Figure 4.12.1: A macro of bond 26.

Detailed fractography of the interface of each alloy was conducted and this is presented in figures 2.12.2 (a) and (b). The smooth surfaces suggested that the braze had successfully wetted the joint. With reference to (b) the backscattered images showed similar amounts of the braze had adhered to each faying surface.

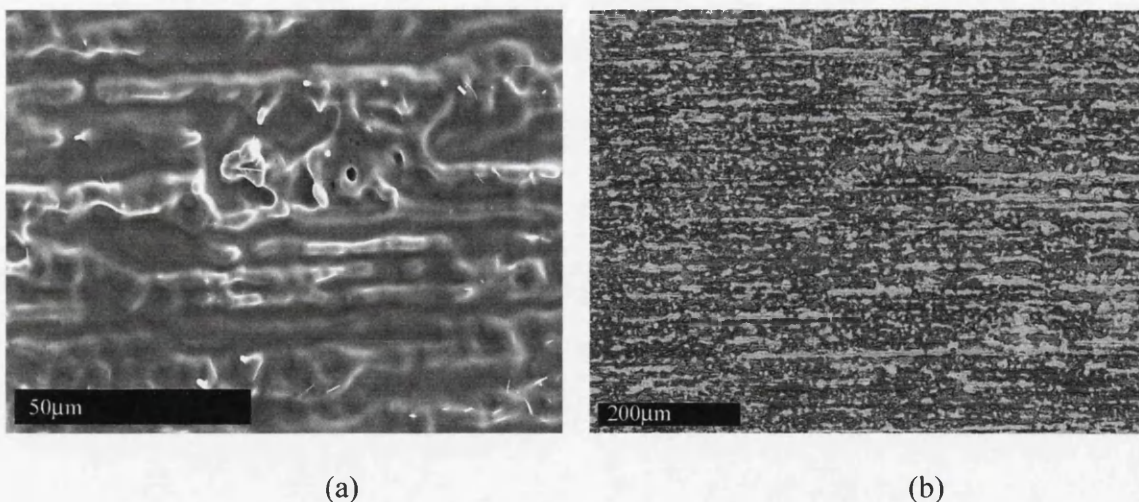


Figure 4.12.2: (a) A high magnification SEM image typical of the faying surface condition post bonding (b) a corresponding backscattered image.

A lesser degree of microstructural disruption was noted in these bonds in comparison to those employing an impregnated copper interlayer. Diffusion of copper into the titanium appears to be limited to a 70 – 100  $\mu\text{m}$  band immediate to the interface, whilst a clear band can be seen along the faying surface of the IN718 in figure 2.12.3 (b). Again the immediate interface between the two pairs shows a similarity to that of the copper impregnated powder interlayer bonds described above.

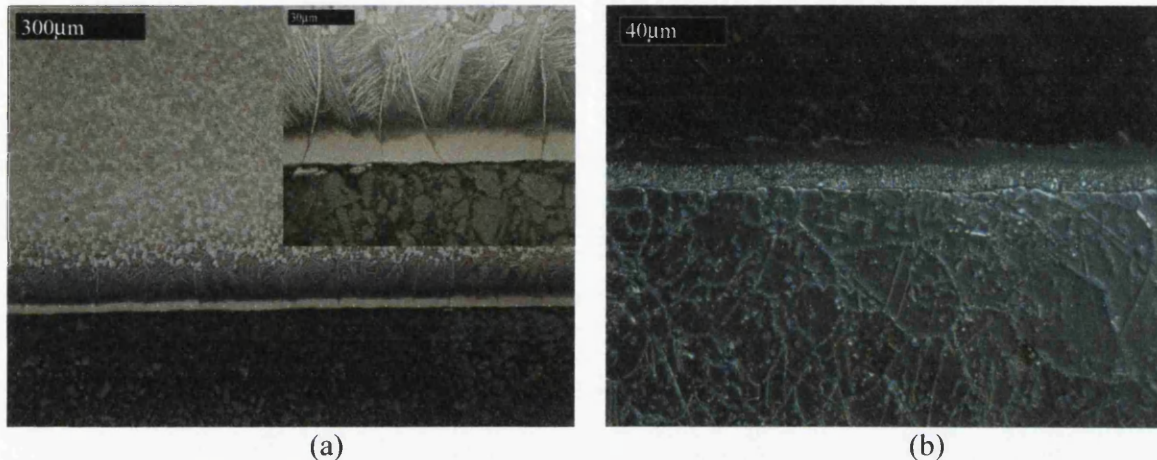


Figure 4.12.3: (a) A medium and high (inset) magnification micrograph typical of the appearance of the Ti-6-4 side and (b) the interfacial microstructure of the IN718 side of bond 21.

#### 4.13 IN718 Vs SCMV using a Microbraz LM braze

The use of the Microbraz braze in IN718 to SCMV bonds was adopted after reported improvements in bond quality through the use of silicon and boron based brazing alloys [133]. Detailed information on Microbraz LM is presented in section 3.1.7.

All these bonds showed some level of adhesion and were the first to produce specimens suitable for mechanical assessment. Unfortunately the number of tests allowed by the scale and number of the resistance bonded specimens was limited. For this reason non – standard mechanical tests pieces were machined to allow each bond to be assessed metallographically and mechanically. The technique proved useful and it is suggested that

this could be employed in future investigations also at the developmental stage. A matrix of the trials performed is laid out below in table 2.13.1.

Table 4.13.1: A Summary of the bonding conditions for bonds produced incorporating Microbraz.

<b>Test Number</b>	<b>Time (Minutes)</b>	<b>Temperature (°C)</b>	<b>Force (KN)</b>
25,26 (Two Bonds Produced)	60	970	3
27	60	990	3
28	60	990	5
29 (Test Failed at TC)	60	1050	5
30	10	990	3

Initially bonds were produced that aimed to match the bonding parameters set out for the titanium to steel bonds (Tests 9 through to 16). After brief metallographic examination it became clear that the scope for increasing temperature and pressure without severe microstructural damage and significant upset was large. Test 29 was denoted as a high temperature test but failed when a thermocouple became detached during the bond. This led to a malfunction in the temperature control system resulting in the melting of the specimen. Despite this apparent ‘failure’ the bond was included in the investigation as a means of comparison to more conventional welding techniques (flash butt welding). Macro images of some of the bonds produced are displayed in Figure: 4.13.1 below.

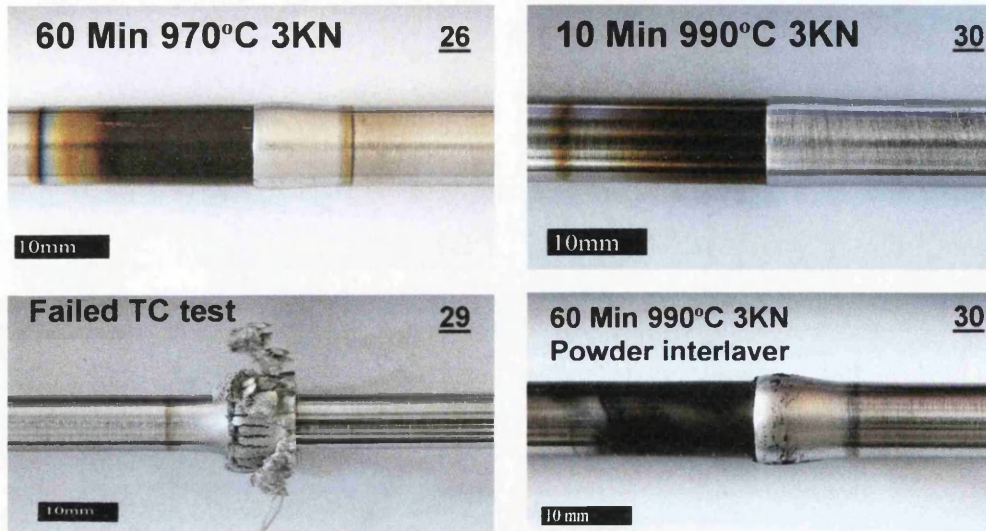


Figure: 4.13.1: Macro images for post bond appearance of various Microbraz brazed SCMV to IN718 joints.

The four bonds presented show varying degrees of oxidation with Test 4 showing the least oxidation due to its short time at temperature. Interestingly Test 6 produced the greatest amount of oxidation with apparent carburization of the binder products and a soot residue over the specimen surface. Whilst these bonds were produced at significantly higher pressures than those involving titanium comparatively little upset was displayed in any of the 6 bonds.

#### 4.13.1 Bond microscopy

Bond microscopy revealed interesting and once again complex microstructural features. The figures below characterise some of the common features observed in the bonds concentrating primarily on interfacial microstructures. However, other macro scale microstructural anomalies were also observed which are dealt with in detail in section 4.14.

Considering first the IN718 side and with particular reference to Figure 4.13.2 a considerable increase in precipitation of secondary and tertiary phases is evident. This precipitation is highlighted particularly well by polarized light as it tends to differentiate between  $\gamma''$  and tertiary  $\delta$  phase well. Here a mass proliferation of both these precipitates can be seen in a band approximately 50  $\mu\text{m}$  wide spanning the whole interface (Figure

4.13.3). Also shown are signs of interfacial porosity (indicated). Interestingly, when considering the SCMV side of the bond little or no microstructural disruption is apparent. Finally, the absence of any remainder of the Nicrobraz braze at the interface was of interest. This is in stark contrast to the interface morphology in the powder interlayer bonds displayed in Figure 4.13.4.

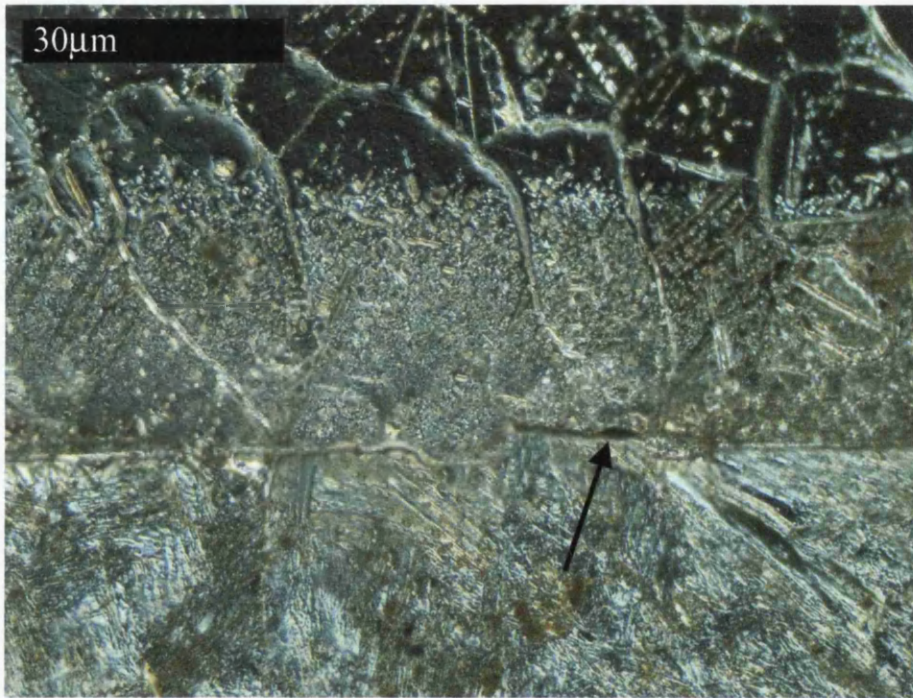


Figure 4.13.2: A polarized light micrograph of the interface between SCMV and IN718 pairs using a NicroBraz braze.

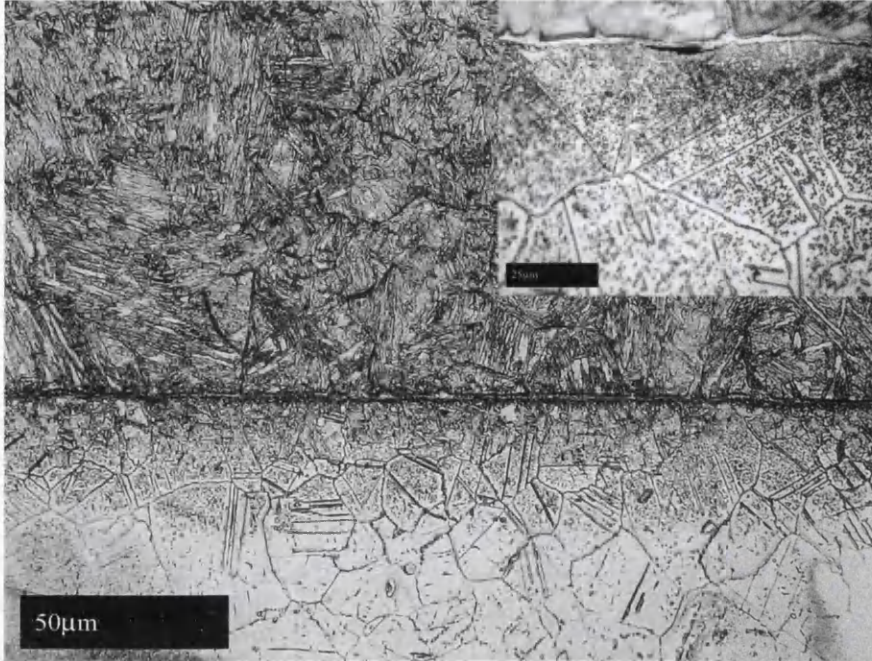


Figure 4.13.3: An overview of the interfacial microstructure of a Microbraz brazed SCMV to IN718 bond with high magnification detailed image inset.

In Figure 4.13.4 three marked differences in microstructure were observed compared to that seen in the bonds not employing a powder interlayer. Firstly, the Microbraz Braze layer appears to be intact at the IN718 powder / parent interface. Secondly, the level of precipitation in the IN718 observed in other tests was not noted at the IN718 / powder parent interface. Thirdly, a good level of adhesion was noted between the In718 powder and the SCMV parent material. However, there also appeared to be evidence of a thin band of an indistinguishable phase created at the interface.

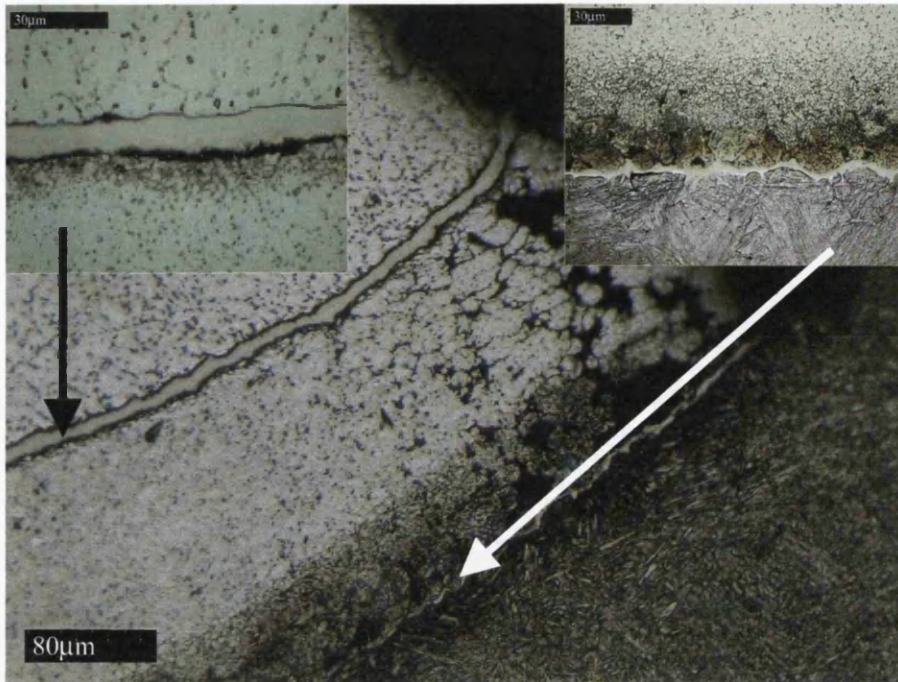


Figure 4.13.4: An overview of the interfacial microstructure for a Microbrazed bond between SCMV and IN718 employing a powder interlayer with high magnification detail inset.

Finally, considering Figure 4.13.4 variable levels of powder consolidation were observed across the bond line. Although the majority of the powder interlayer appeared to sinter well, the packing density diminished towards the flanks of the bonds.

Figure 4.13.5 represents the typical pore size found within the powder interlayer. Whilst the size is representative the distribution is not and in actuality the location of such pores was widely scattered.

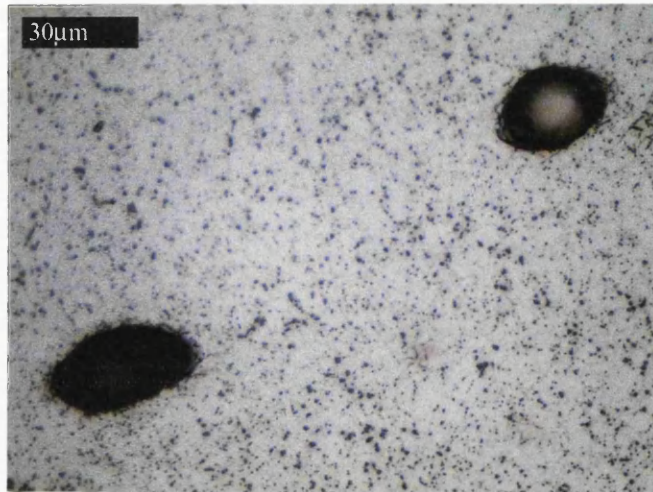


Figure 4.13.5: An image of the representative pore size found within the powder interlayers.

#### 4.13.2 Mechanical testing

Figure 4.13.6 shows engineering stress strain curves for each of the bond trials conducted employing a Microbraz Braze. The fundamental mechanical properties are also summarised below in Table 4.13.2. Referring to both, a clear correlation can be seen between increasing time, temperature and pressure and improved mechanical response. This trend continues up to the vastly superior performance of the fusion weld which, whilst not performing well in comparison to parent metal properties, shows marked increases in ductility and UTS. The extremely low ductility of the solid state bonds is the primary indicator of poor bond strength.



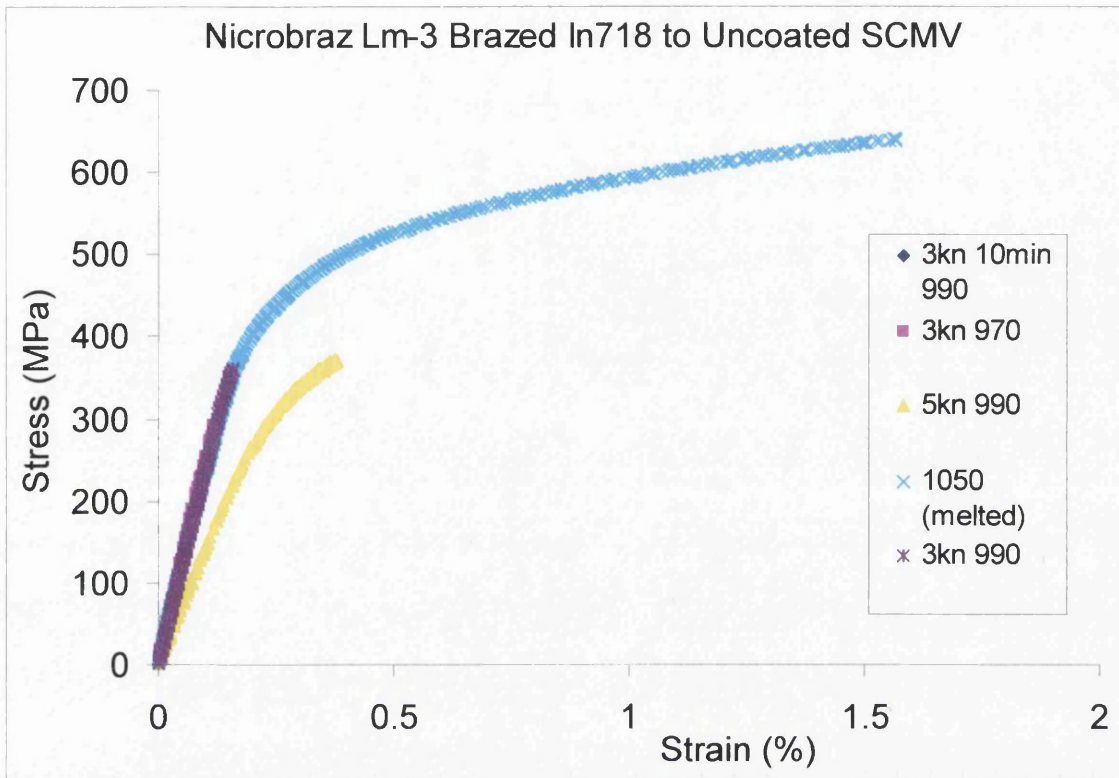


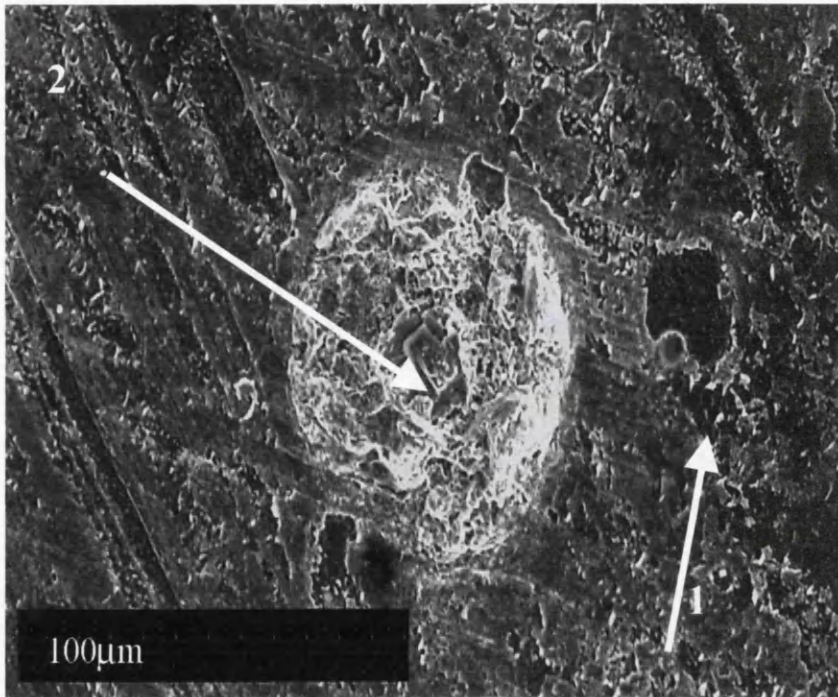
Figure 4.13.6: Engineering stress vs strain plots for all Microbraz brazed trial bonds produced.

Table 4.13.2: A summary of mechanical properties for all Microbraz brazed trial bonds produced.

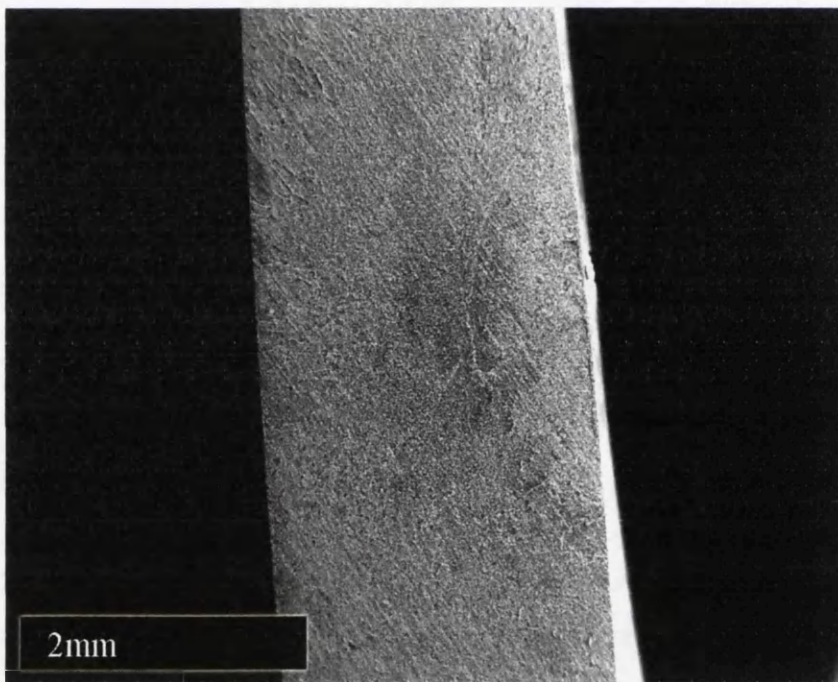
Condition	Yield Stress (MPa)	UTS (MPa)	Modulus (GPa)	Failure Strain (%)
10 Min 990° 3KN	N/A	130	240	0.05*
60 Min 970° 3KN	N/A	292	250	0.12*
60 Min 990° 3KN	N/A	360	210	0.15*
60 Min 990° 5KN	329	368	144	0.37
Failed Test (Melted)	375	639	227	1.57

\* Elastic strain

All bonds, including the fusion weld, failed at the bond line. Subsequent SEM inspection of the bond fracture surfaces revealed some areas of non-fusion. However, it appeared that in the majority of cases the bonds were simply overloaded over the whole interfacial area, displaying a uniform fibrous appearance throughout. An example of such a fracture surface can be seen in Figure 4.13.7. The other interesting feature of this fracture surface is the subtle ridges or asperities running across the fracture surface. These are evidence of both poor initial deformation required for good interfacial contact and low interdiffusional mass transport during the bonding process. These asperities appear in the high magnification SEM image inset to Figure 4.13.7, which also shows evidence of both non-fusion defects (indicated at 1) and hot spots (indicated at 2), likely created by foreign inclusions. These defects were typically between 5 and 25  $\mu\text{m}$  in diameter. Whilst their presence was noted, no evidence that they contributed directly to the bond failure was found during the post failure fractography.



(a)



(b)

Figure 4.13.7: An SEM image typical of the fracture surface found in failed SCMV to IN718 Microbraz brazed joints (b), with evidence of non-fusion defects (a).

For consistency Figure 4.13.8 shows a high magnification image of the fractured powder interlayer test. The two most important features of this fracture surface were both the decrease in consolidation towards the specimen edge (as noted in the microscopy in Figure 4.13.4) and the appearance of asperity marking across the sample as was seen in the substrate to substrate bonds. It is also worth noting that a clear transition in fracture surface morphology was noted approximately 150  $\mu\text{m}$  from the edge of the specimen.

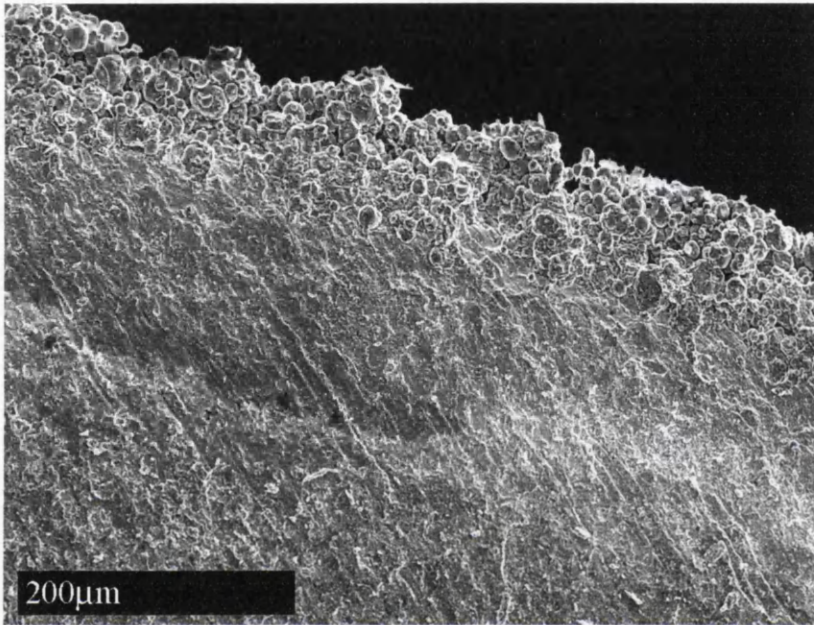


Figure 4.13.8: A high magnification image of an SEM image of the brazed powder interlayer trial (plan view of fracture surface).

In terms of providing useful insight into the secondary effect of bonding, the fusion weld test provided the most interesting results from the fractography conducted, particularly with reference to the HAZ banding observed and its likely effect on macro mechanical properties. The far superior strength of the joint elucidated interesting inhomogenities in the mechanical response of the test piece. Figure 4.13.9 shows the fracture surface of the joint from the IN718 side. The differences between this and the surfaces seen in the solid state bonds are clear. The level of ductility at the bond line is clearly increased, there is no evidence of bonding asperities on the fracture surface and fracture of the bond appears to have occurred within both substrates. Whilst this fracture surface morphology appears more fibrous and ductile in nature Figure 4.13.10 shows this is not where the majority of

the bond ductility comes from. Indicated at location 1 is a concentrated area of plastic deformation through the thickness of the specimen immediately adjacent to the bond line. It is likely that the majority of bond ductility is as a result of this deformation.

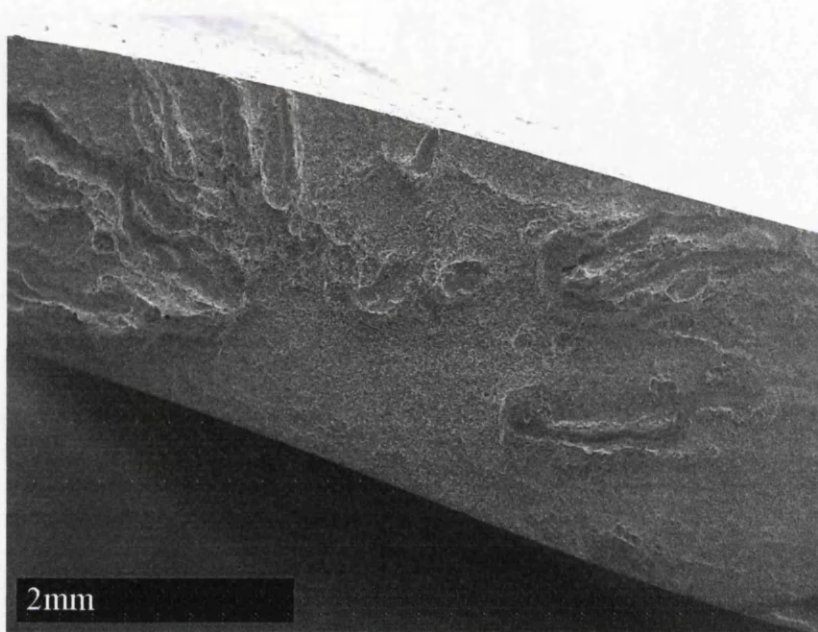


Figure 4.13.9: The fracture surface of the Microbraz brazed fusion weld (plan view).

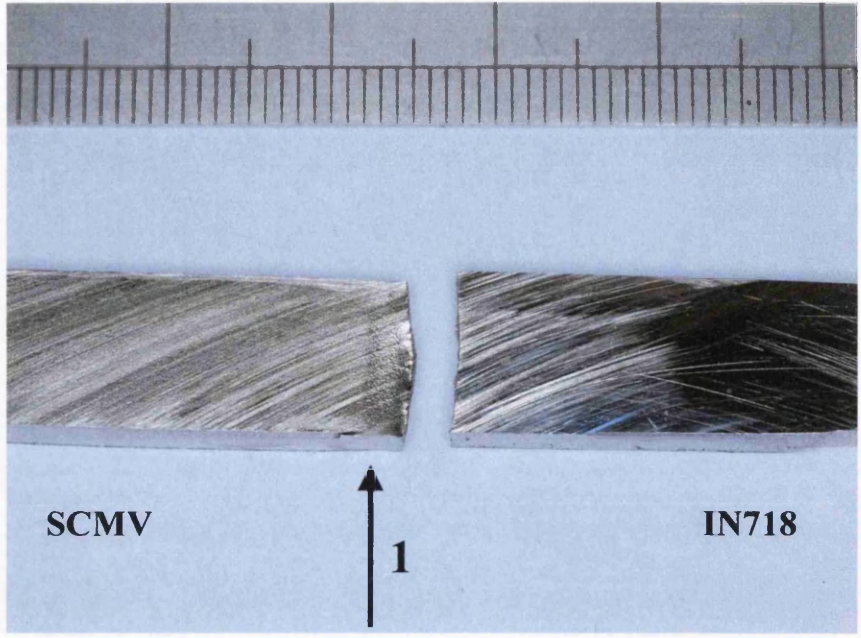


Figure 4.13.10: A section through the failed Microbraz brazed fusion weld mechanical test piece.

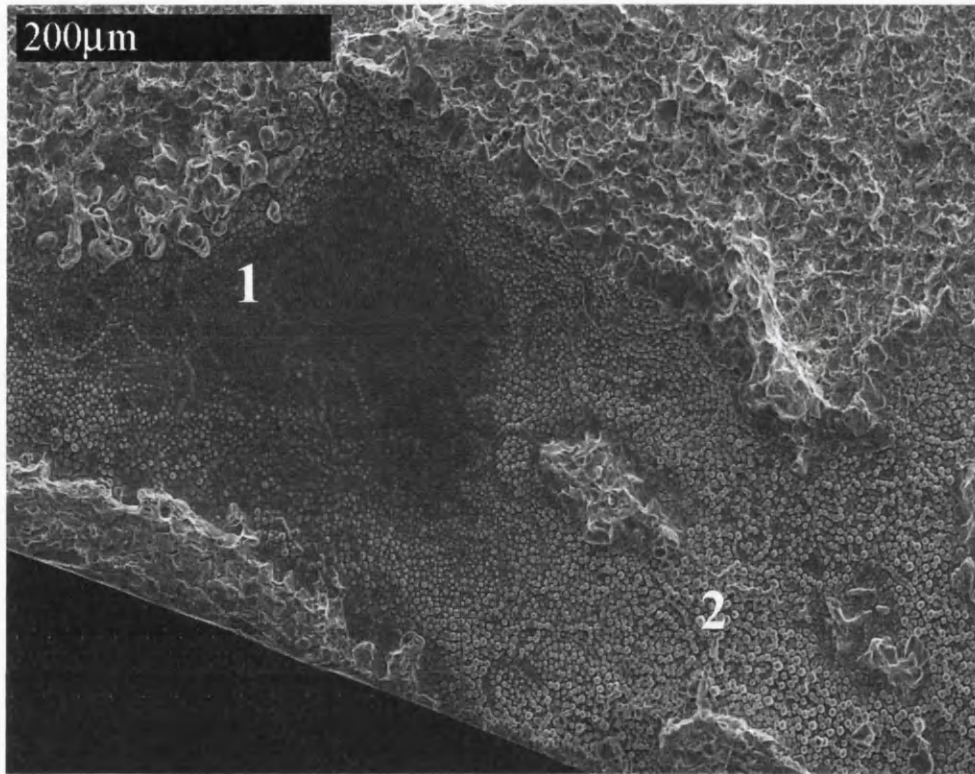


Figure 4.13.11: An area of non-fusion observed in the IN718 side of the melted trial bond.

Finally, the fusion bond also displayed an interesting area of what appears to be non-fusion, Figure 4.13.11. The typical fibrous fracture surface surrounds the non-fused (1) area which exhibits a granular shaped texture effect. However, in zone 2 an intermediate region is noted with fine equiaxed particles visible.

#### 4.14 Heat affected zones (HAZ)

Throughout the project attention was drawn to the formation of HAZ's across the width of bonded specimens (both successfully bonded and not). Typically these bands were only elucidated subsequent to metallographic preparation and etching as they tended to be attacked much more readily by chemical reagents. Whilst initially the effect was noted and some metallographic characterisation was undertaken, at the time attention was more focussed on bond adhesion and banding was designated a secondary consideration. However, once successful bonds had been produced that also displayed this effect, attention was refocused on their detailed characterisation. The production of the thin mechanical specimens aided this investigation as it was possible to metallographically prepare whole bonded specimens for a full and thorough microstructural and mechanical assessment. The following section details the results of this inspection.

Figure 4.14.1 shows an intact bonded specimen that has been sectioned perpendicular to the bond line, metallographically prepared and etched using both Nital and Orthophosphoric acid. The banding that can be seen on both materials was found to closely correlate to the width of the hot zone across the specimen during Gleeble bonding. As such, this effect is herein referred to as heat affect zone banding or HAZ banding.

Starting from the top of the IN718 side of the bond parent microstructures were observed in areas outside the HAZ as one might expect. In fact this microstructure remained consistent until less than 100 $\mu$ m prior to the visible band within the IN718 (1). The band itself is very distinct, appearing over a narrow area. Microstructurally the 'band' appears to have been formed as a result of concentrated and dense intragranular precipitation. This phase appears to be precipitating at the expense of the gamma matrix alone as both grain boundary and pre-existing intragranular precipitates seem to be generally unaffected. Interestingly, towards interface of the bond the microstructure begins to normalize again despite experiencing higher temperatures. Nevertheless, this region does show a lesser degree of twinning and intragranular precipitation. This microstructure remains consistent until the bond interface (described in section 4.13.1) is reached.



On the SCMV side of the bond a alternative banding was observed but it was much more diffuse in nature (2). Furthermore, the banding also appeared closer to the bond line than in the IN718 which is likely to be due to the differential heating effect. Micrographs revealed a coarsening of the martensitic structure in the area immediate to the bond line, with  $\alpha$  ferrite laths at least doubling in size. As the banding gradually intensifies it is noted that the microstructure becomes refined and evidence of primary precipitation, possibly of cementite carbides becomes more prevalent. There a band consisting of a complex microstructure of coarse  $\alpha$  laths, primary carbide precipitates and retained martensite was observed. Finally this gave way to parent microstructure over a similarly short distance to that observed in the IN718 material.

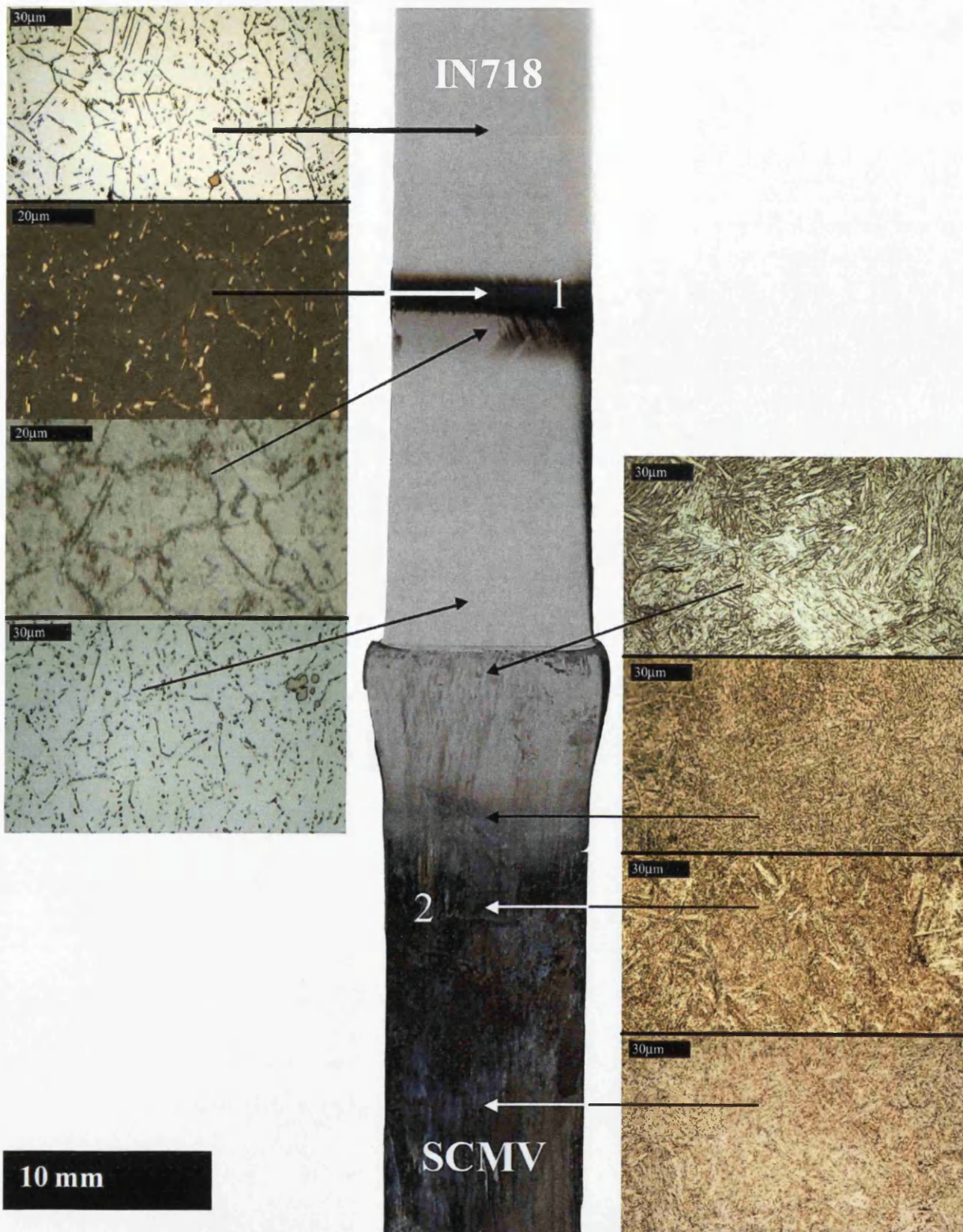


Figure 4.14.1: A full microstructural assessment of HAZ banding in a bond between SCMV and IN718 employing a powder interlayer.

Further to the microstructural assessment a microhardness traverse was also employed to try and quantify the microstructural changes that were observed. This yielded very interesting results which are displayed in Figure 4.14.2. Whilst the IN718 side showed a softening (compared to parent properties) in the less precipitated material close to the bond line a considerable increase in hardness was displayed in the ‘band’. This increase developed slowly in the IN718 HAZ before falling sharply to parent properties on the cold side of the band, correlating well with the microstructural features that were observed.

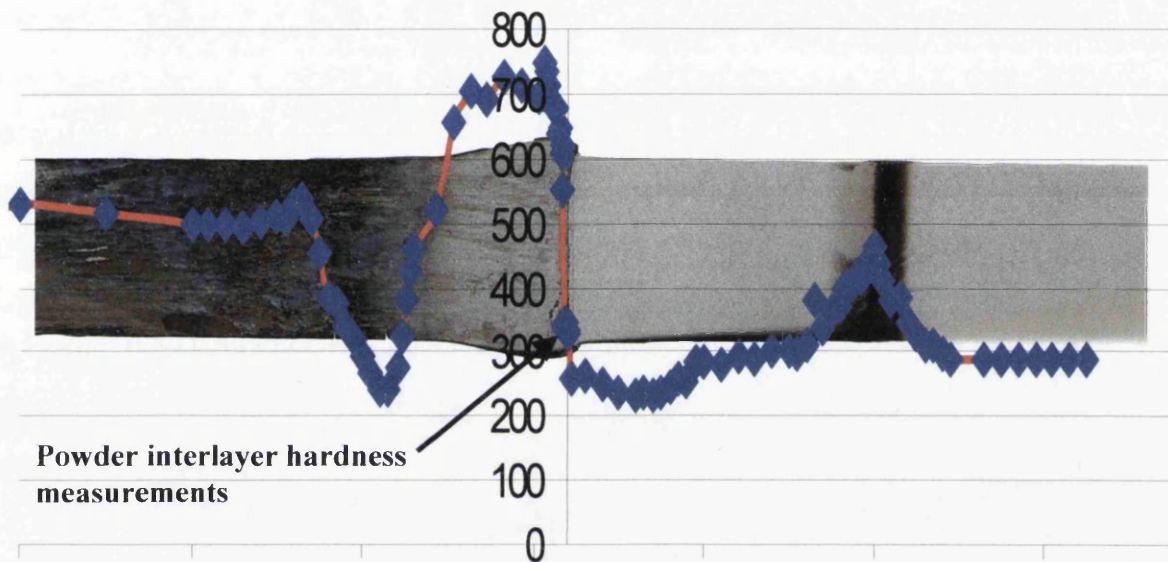


Figure 4.14.2: A Vickers microhardness traverse across a bonded specimen displaying HAZ banding.

The effects in the SCMV material were considerably more severe. Following a hardness measurement of approximately 350Hv for the powder interlayer the hardness then double in the space of 50µm to over 700Hv within the area corresponding to the coarse microstructure seen in Figure 4.14.1. The hardness then falls to approximately 2/3<sup>rd</sup>s its initial value, around 230Hv. Finally as the traverse leaves the HAZ the hardness then returns to approximate parent properties of around 500Hv.

Following the observations made for the IN718 to SCMV bonds, the microstructures of the Ti-6-4 to IN718 and Ti-6-4 to SCMV bonds were reviewed to see if any HAZ banding effects were noted in these tests. The SCMV and IN718 halves of these bonds presented banding in all tests. In contrast, only one condition revealed significant microstructural changes in the Ti-6-4 material, this being the hot jaws configuration employed for the Ti-6-4 to SCMV trials. With reference to Table 3.4.1, the crucial parameter was temperature, which was 970°C in this case. The observed microstructural features and corresponding hardness traverses are presented in Figure 4.14.3 and Figure 4.14.5 respectively. Starting at the powder – substrate interface, a substantial amount of primary  $\alpha$  was noted up to 200 microns from the interface (a). This is rapidly replaced by a typical  $\beta$  annealed structure dominated by transformed product with a clearly defined prior  $\beta$  grain structure (b). This remained consistent for approximately 2-3 mm before primary  $\alpha$  nucleation at the prior  $\beta$  triple points was observed (c). Over the next 10 mm primary  $\alpha$  grain size was seen to increase steadily at the expense of the transformed product to around 40 $\mu$ m in diameter (d – f). Coarsening of the laths of transformed product was also noted. Finally over the next 5mm the microstructure becomes dominated by primary  $\alpha$  which tends to the elongated grain morphology associated with the parent material (g).

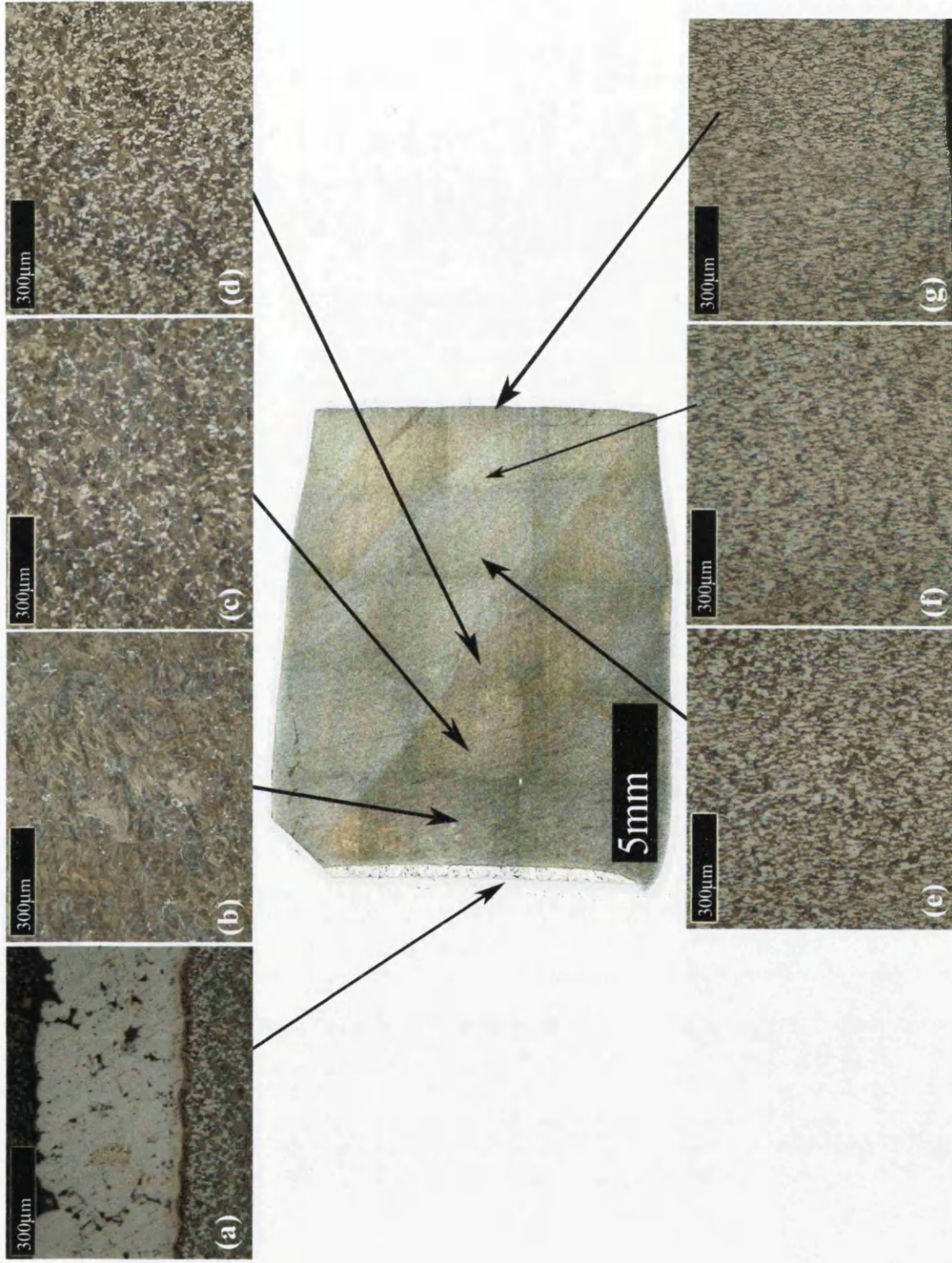


Figure 4.14.3: Microstructural variations noted in the Ti-6-4 substrate of trials performed employing the 'hot jaws' configuration.

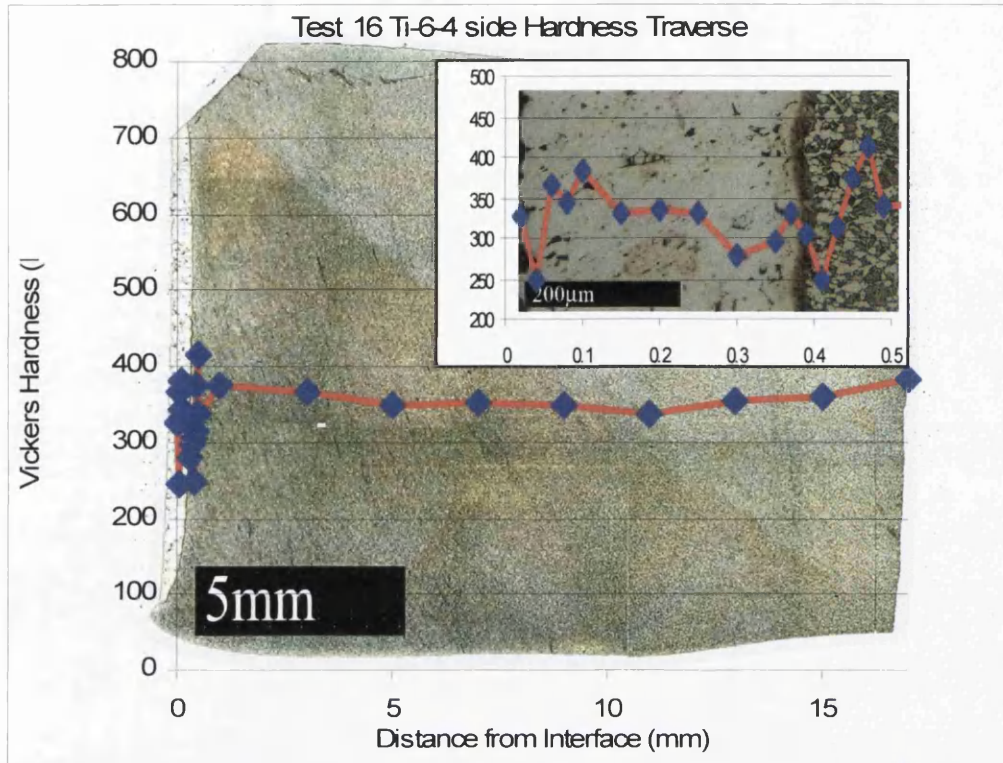


Figure 4.14.5: A microhardness traverse across the heat affected zone in Ti-6-4 substrate from Test 16.

Compared to the changes noted in the SCMV and the IN718 substrates, the microstructural changes in the Ti-6-4 substrate appear to have less effect on variations in microhardness over the heat affected zone. Significant reductions in hardness close to the powder - SCMV and powder - Ti-6-4 interfaces were noted. The subtle effects of the changes in the bimodal microstructure away from the bond line are reflected in only minor variations in the hardness throughout the remaining HAZ (Figure 4.14.5).

#### 4.14.1 IN718 / SCMV post weld heat treatment (PWHT)

As a result of the distinct HAZ observed in IN718 / SCMV bonds a limited assessment of post weld heat treatments was performed. The goal was to eradicate the sharp HAZ banding effect whilst trying to maintain parent properties in the substrate materials. All heat treatments were carried out in radiant furnaces capable of temperatures in excess of 1000°C. The simplest and most effective of these was a soak at 1000°C for 15

minutes followed by quenching in water. The results of this heat treatment are dealt with in the following section.

A micrograph of the typical SCMV structure can be seen below in Figure 4.14.6. The two main features of note are the more prominent prior  $\gamma$  austenite grains and the grain boundary segregation of cementite that helps to define them. Also of note was the differing morphology of the martensitic structure itself appearing more equiaxed close to the bond line but taking on a more tempered structure further from the bond line, such as that seen in Figure 4.14.7.

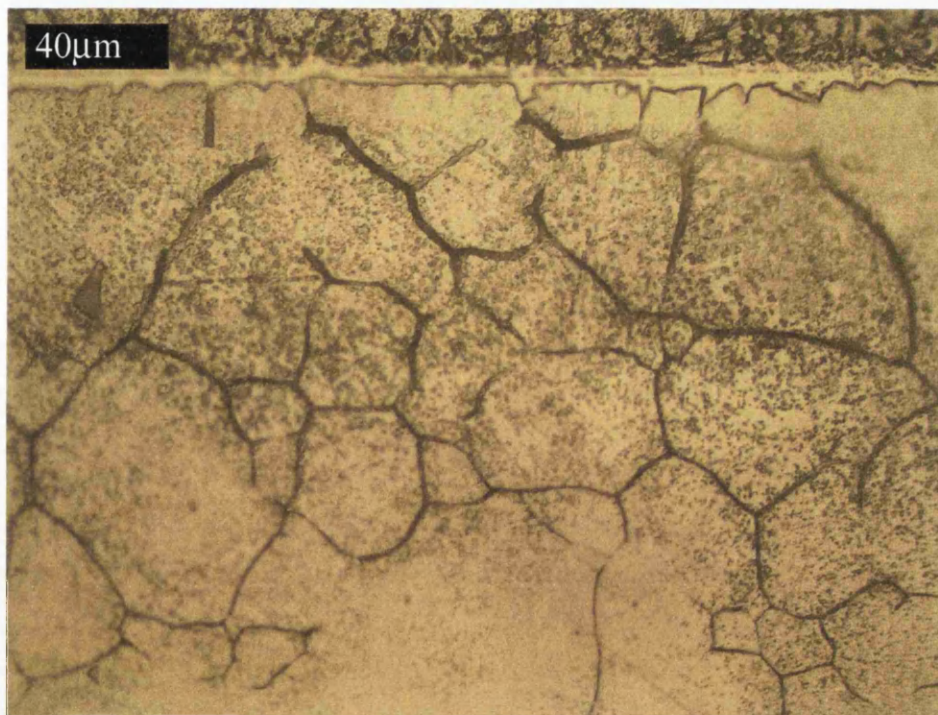


Figure 4.14.6: PWHT microstructure of SCMV closer to the bond line.

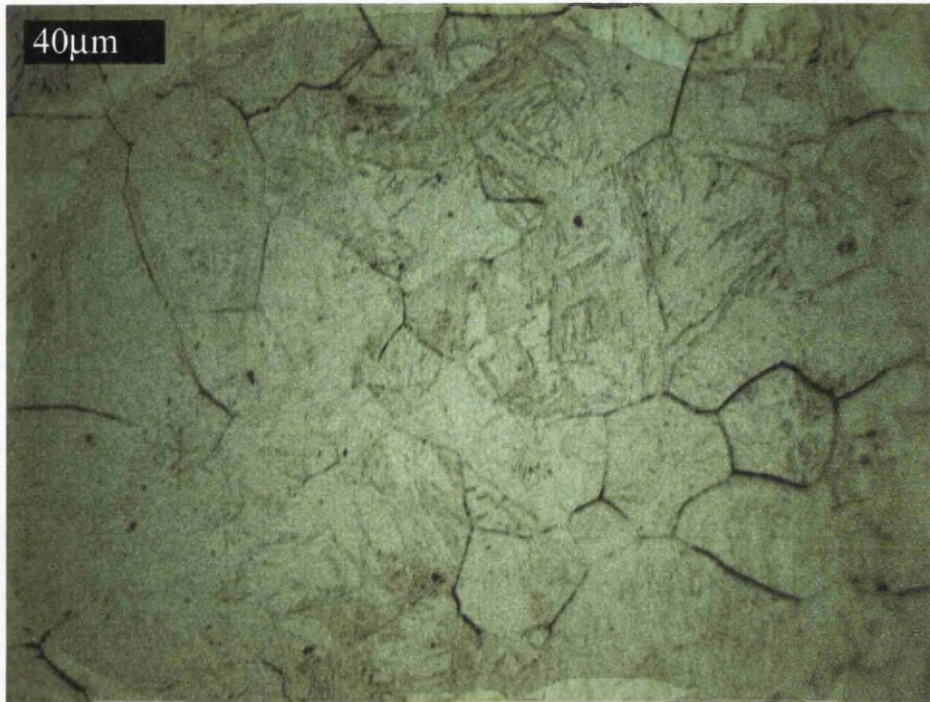


Figure 4.14.7: PWHT structure of SCMV remote of the bond line.

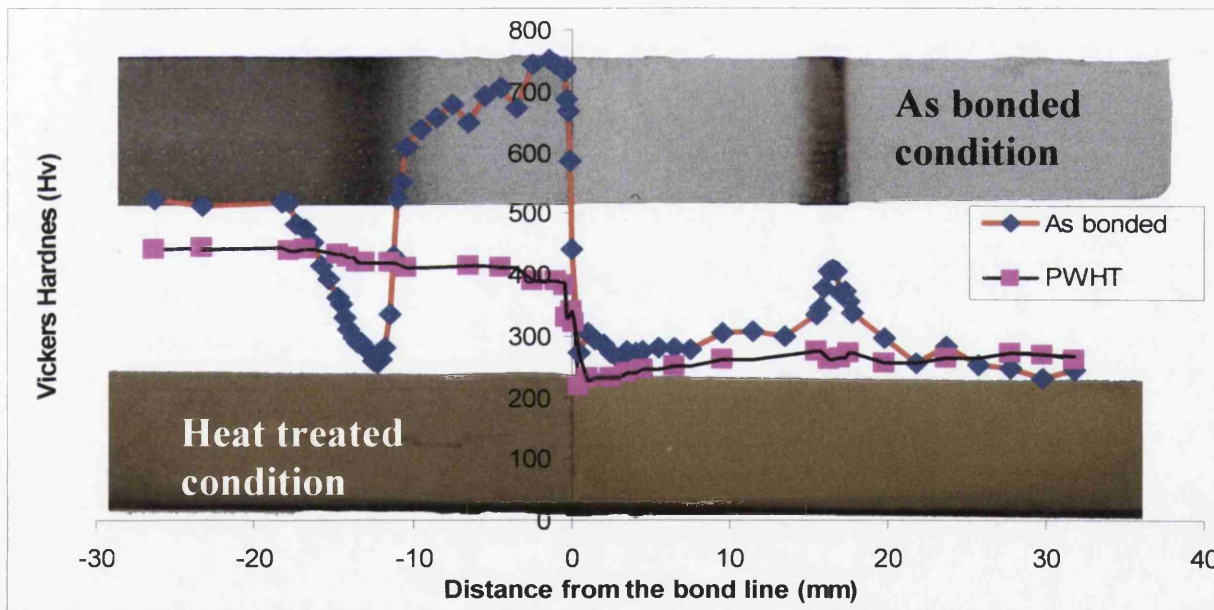


Figure 4.14.8: A comparison of microhardness traverse for the as bonded and heat treated condition.

A comparison between the microhardness traverses for the as bonded and post weld heat treated condition can be seen in Figure 4.14.8. The traverses have been overlaid on images of polished and etched specimens to display the marked differences in both



material properties and microstructural features. Clearly, on a microstructural level banding has been completely eradicated as confirmed by the microscopy presented above. Furthermore, the stark peaks and troughs in hardness have also been normalised. Nevertheless, weakening of the material at the interface is evident in both bonding species. The SCMV has suffered more in this regard and displayed an overall drop in parent hardness of around 75 Hv. Finally, a comparison of the tensile stress – strain response of the two conditions can be seen in Figure 4.14.9 below with mechanical properties summarised in Table 4.14.1. A clear improvement in mechanical properties was observed as a result of the heat treatment. However, the mechanical properties of the heat treated condition may still be considered to be poor in respect of parent metal properties or those observed in the fusion weld produced in the original trials.

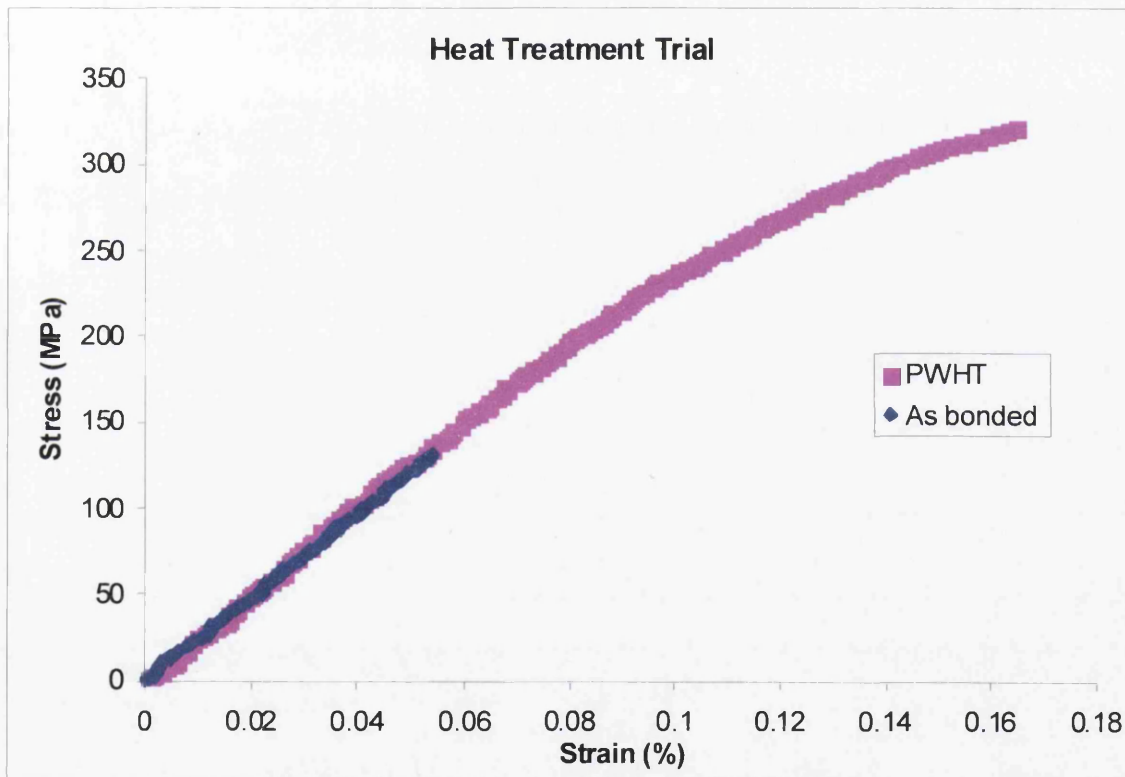


Figure 4.14.9: A comparison of Engineering stress- strain behaviour between the as bonded and PWHT conditions.

Table 4.14.1: Mechanical properties for both the as bonded and the heat treated conditions.

<b>Condition</b>	<b>Yield Stress (MPa)</b>	<b>UTS (MPa)</b>	<b>Modulus (GPa)</b>	<b>Failure Strain (%)</b>
<b>10 Min 990 3KN (As Bonded)</b>	N/A	130	240	0.05
<b>10 Min 990 3KN (Heat treated)</b>	273	312	254	0.16

## 5 RESULTS: HIPed joints

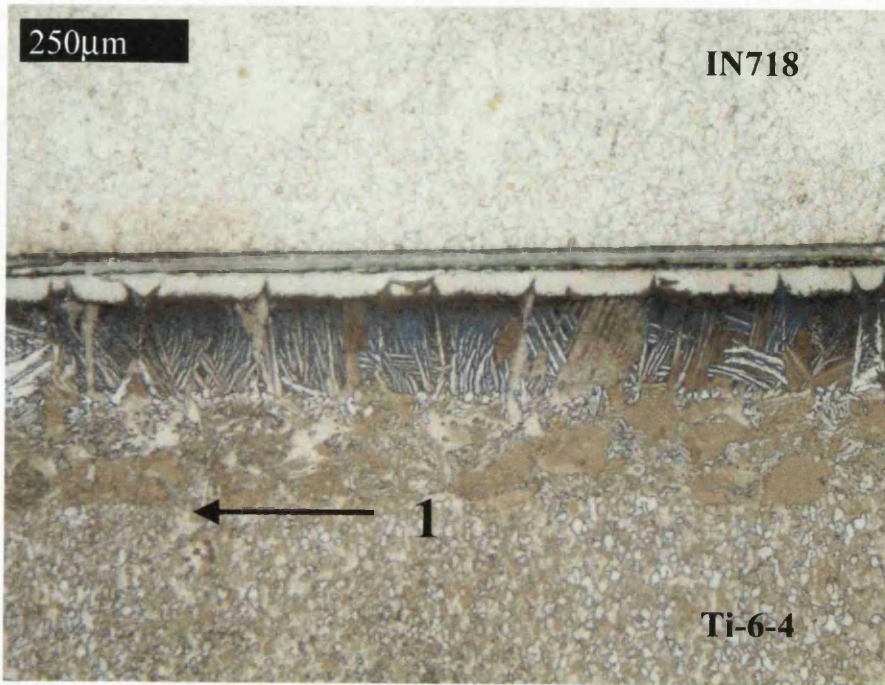
In this section, joints manufactured via a HIP process utilising similar alloy pairings to those employed for the previously described resistance bonding experiments will be described. Overall bond quality and microstructures appeared similar with the exception of powder consolidation where marked differences in the degree of consolidation, interfacial contact and interparticle diffusion were noted.

### 5.1 Tantalum coated Inconel 718 to Ti-6-4 with Ti-6-4 powder interlayer

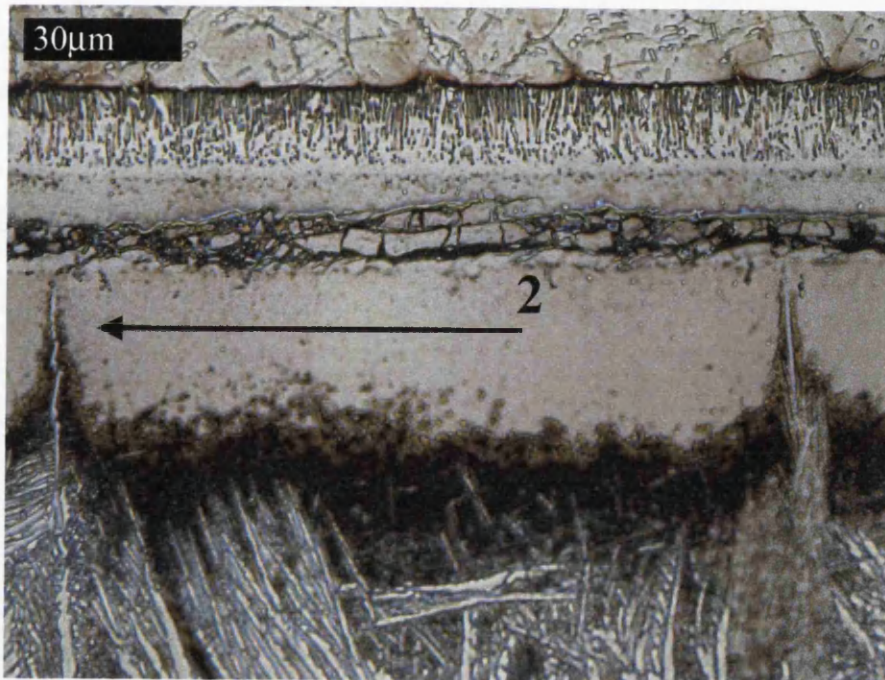
Figure 5.1.1 shows an overview of the microstructural features of the Tantalum coated IN718 to Ti-6-4 bonds with a more detailed high magnification image inset. The first noticeable feature is the prominent band of secondary acicular  $\alpha$  within the Ti-6-4 immediate to the interface. The  $\alpha$  band is approximately 150 $\mu\text{m}$  in width and spreads nearly half way into the former powder interlayer. The powder interlayer itself is approximately 350 – 400  $\mu\text{m}$  in width and shows very little sign of porosity. The interface between the powder interlayer and the Ti-6-4 substrate (indicated at 1) is contiguous and of high quality. The IN718 substrate shows minimal microstructural damage in the majority of the as bonded material. However, the interfacial microstructure shows similar growth of precipitates perpendicular to the bond line as those seen in the resistance bonded specimens. With reference to the inset high magnification image at 2, growth of acicular  $\alpha$  laths through the tantalum rich intermetallic band was observed; this effect was also observed for various other bond chemistries (Figure 5.5.3). These laths grew in a similar manner across the bond line and were associated with a highly brittle intermetallic zone. This zone was fractured throughout the majority of the bond although it cannot be ascertained as to when this fracture might have occurred.

Figure 5.1.2 shows two bonds produced without a powder interlayer, one of which incorporates a tantalum interlayer (Test 8b). Both tests provide an interesting comparison to the results seen in both Test 5b of the HIPed bonds and Test 1 of the

resistance bonds. Clearly, the tantalum coated bond suffered from cracking on a brittle intermetallic as did the powder interlayer test. The width of the acicular  $\alpha$  band in both bonds was approximately equal, however, the laths appeared coarser in the tantalum coated case. Whilst banding at the interface was evident in both trials it was larger and more distinct in the tantalum coated test. Finally, when comparing the microstructures seen in Figure 5.1.2 to those seen in Figure 4.2.4 and Figure 4.2.5 (Tests 2 and 3), it is interesting to note that the resistance bonded samples cracked example without a tantalum coating but showed an improvement in those where tantalum was employed.



(a)



(b)

Figure 5.1.1: Overview (a) and detailed interfacial microstructure (b) of bond 5b, HIPed, IN718 to Ti-6-4 with Ta interlayer.

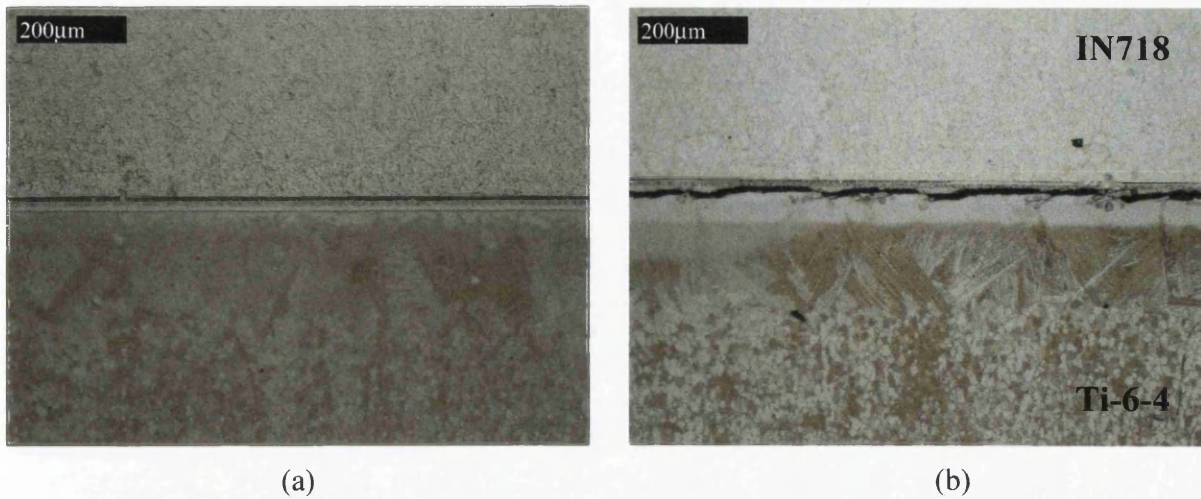


Figure 5.1.2: Optical micrographs of (a) Test 16b with no tantalum interlayer and (b) Test 8b with a tantalum interlayer.

## 5.2 Ti-6-4 to SCMV with Ti-6-4 / BurTi Powder interlayer

Figure 5.2.1 shows the typical microstructure observed in the SCMV - BurTi - Ti-6-4 HIP specimens. The powder interlayer consolidated to a thickness of approximately 350 – 400 µm despite the relatively coarse average powder particle size of around 100µm. Close inspection of the interlayer revealed excellent consolidation with very few pores evident. Indications of the size of the prior powder particles were visible at the SCMV to BuTi interface, in contrast to the BurTi powder / Ti-6-4 boundary.



Figure 5.2.1: An overview of Test 11b.

There is remarkably little microstructural disruption for this bond pairing. Detailed microscopy of the interface can be seen in Figure 5.2.2. The most striking feature is the significantly more diffuse transition between the BurTi powder and the Ti-6-4 substrate compared to that noted between BurTi and SCMV. Although some acicular growth was noted at the Ti-6-4 - BurTi interface, it was limited. Figure 5.2.2 (b) shows clearly the tantalum coating at the BurTi - SCMV interface. It appears wider than the 2µm initially deposited and is therefore likely to be an expanded intermetallic phase. Finally, minimal microstructural alteration seems to have occurred in the SCMV virtually no evidence of inter diffusion beyond the tantalum rich band.

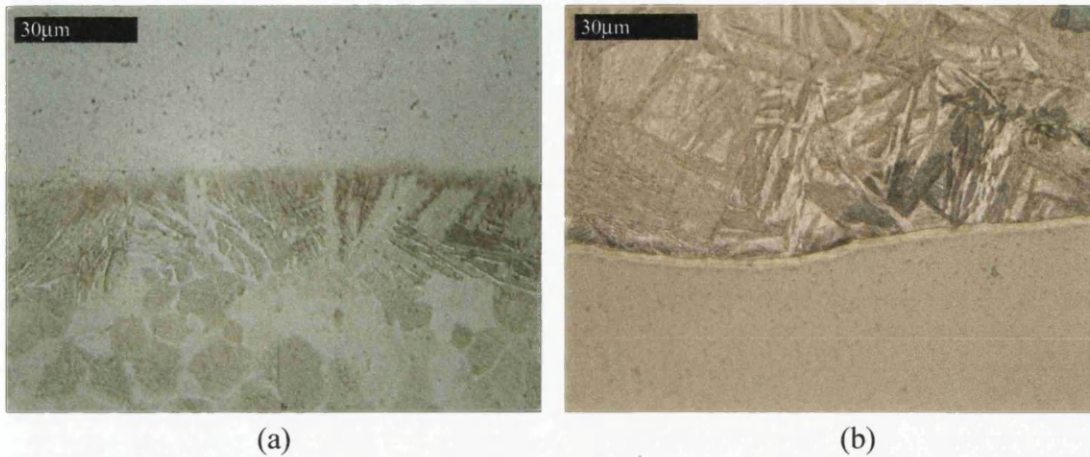


Figure 5.2.2: High magnification optical micrographs of (a) the Ti-6-4 substrate to BurTi powder interface and (b) the SCMV to BurTi powder interface.

### 5.3 Tantalum coated SCMV to IN718 with IN718 Powder interlayer

This bond configuration provides a useful comparison to the QUIP bonding trials conducted under resistance heating (section 4.9). Figure 5.3.1 (a) shows the interface between the IN718 powder and the uncoated IN718 substrate. Here a clear band has formed which acts as an easy path for crack propagation, suggesting the formation of a brittle intermetallic layer. This is interesting considering there should be little or no difference in chemistry between the powder and the substrate. (b) Shows the interface between the IN718 powder interlayer and the tantalum coated SCMV substrate. The majority of the IN718 powder interlayer compares to that seen at the IN718 substrate interface (Figure 5.3.1(a)). However, local modification is noted at approximately 60  $\mu\text{m}$  from the SCMV interface. At the interface itself PPBs become more noticeable and in some cases distinct particles appear. The interface is marked by a narrow band of a tantalum rich phase, confirmed by EDX, which appears to have ingressed into the SCMV substrate at certain points such as that indicated at 1 in (b). Finally the SCMV substrate microstructure whilst somewhat tempered from its parent condition, does not show any signs of significant microstructural disruption.



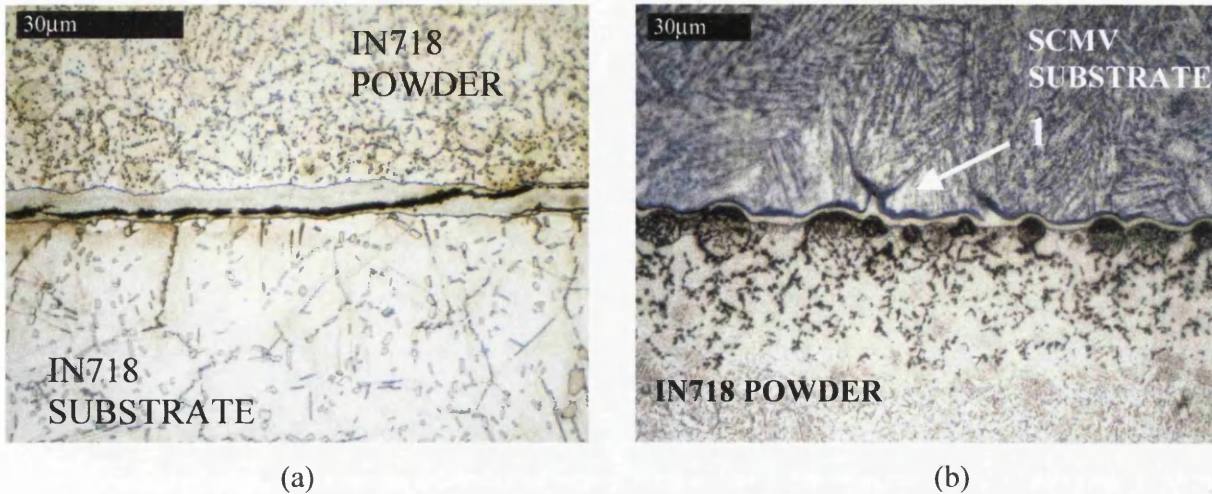


Figure 5.3.1: High magnification optical micrographs of Test 19b at (a) the IN718 substrate to IN718 powder interface and (b) the IN718 powder to tantalum coated SCMV substrate.

Figure 5.3.2 shows the typical pore size found within the compact. This compares well to the pore size and distribution found in the Microbraz brazed powder interlayer bond between SCMV and IN718 using resistance heating (Figure 4.13.5).

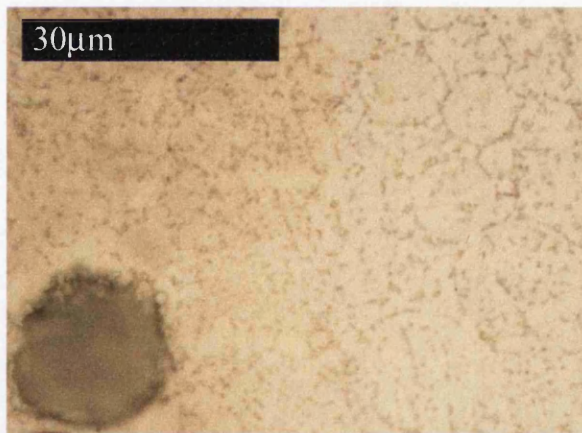


Figure 5.3.2: A high magnification optical micrograph of Test 19b illustrating the typical pore size found in the powder interlayer.

#### 5.4 Tantalum coated IN718 to Ti-6-4 with BurTi interlayer

Powder consolidation in these bonds was very successful. In this case PPBs can be clearly seen within the compact. This illustrates that in some locations as few as two particles span the interlayer. Despite this, evidence of deformation of the largest particles was noted (indicated on Figure 5.4.1).

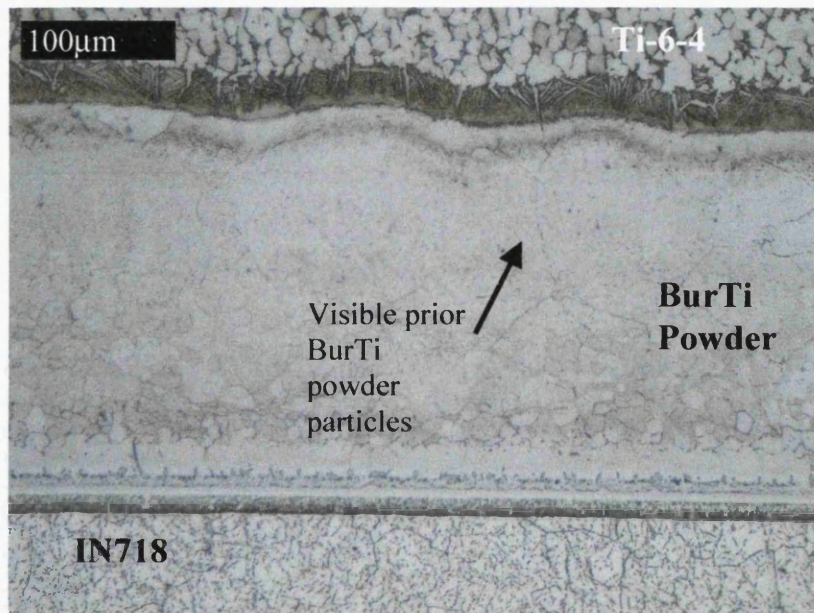


Figure 5.4.1: An overview of the interfacial microstructure of Test 14b.

Microstructural detail for this bond configuration is displayed in Figure 5.4.2 (a) and (b). Figure (a) shows the BurTi - IN718 interface. It shows that the disruption to the IN718 microstructure is near identical to that seen in bonds between IN718 and Ti-6-4. However, the BurTi does not display the interfacial acicular structure of the Ti-6-4, instead exhibiting precipitates which gives way to an intermetallic band that is at first marked by an extremely fine dispersion of two indistinguishable phases much like that seen in bond 2 (Figure 4.2.5). Figure 5.4.2 (b) shows the interface between the BurTi powder interlayer and Ti-6-4 substrate. Although the interface appears diffuse a thin band of acicular  $\alpha$  still remains at the interface and evidence of growth of  $\alpha$  laths across the interface was also noted.

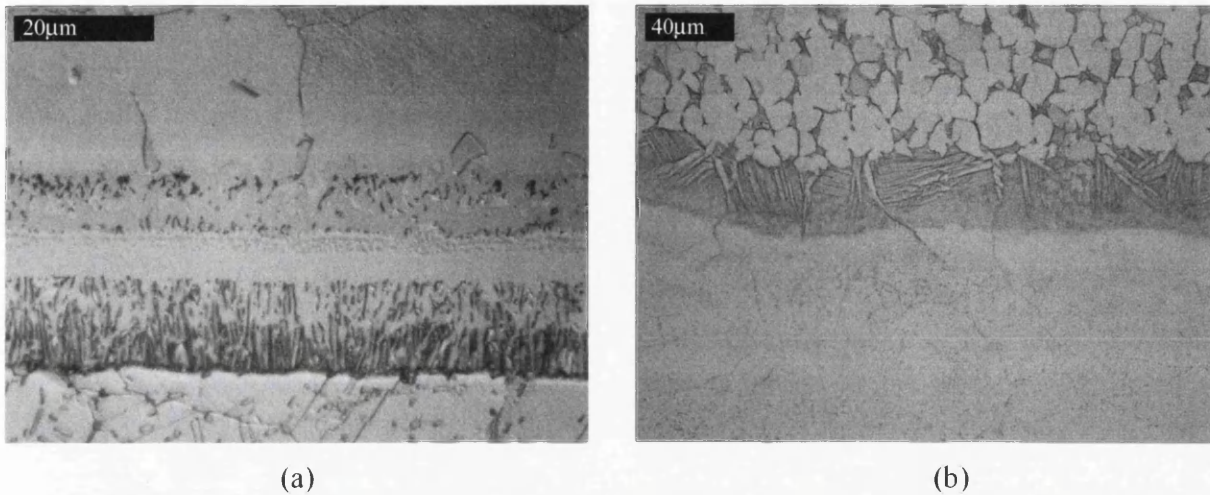


Figure 5.4.2: High magnification optical micrographs of the interface between (a) In718 substrate and BurTi powder and (b) BurTi powder and Ti-6-4 substrate.

### 5.5 Ti-6-4 to copper brazed IN718 without powder interlayer

The HIPed bonds for this configuration were produced at by a different sub contractor (Bodycote) on behalf of Rolls Royce rather than at Birmingham university. Unfortunately the parent Ti-6-4 alloy used contained a different microstructure to that used in the other bonding trials up to this point (Figure 5.5.1 shows the bond overview). However, it does allow comparison to the interfacial characteristics of the resistance heated Tests 21 and 29 As with previous HIPed bonds, good initial adhesion was observed in contrast to that seen for the same bond chemistry under resistance heated conditions. A section of this HIPed bond was subjected to tensile testing in an attempt to ascertain the microstructural fracture path. The results of which can be seen in Figure 5.5.2.



Figure 5.5.1: An overview of the interfacial microstructure of Test 33b (IN718 to Ti-6-4 including Cu braze).

Figure 5.5.2 shows sections of each half of the fractured specimen. The similarities between these microstructural features and those observed in Figure 4.13.3 are strong. Both exhibit similar fracture characteristics across the same band. Both have similar sized areas of acicular  $\alpha$ , intermetallic band widths and IN718 precipitate morphology. More specifically they both also show growth of  $\alpha$  laths from the Ti-6-4 through the intermetallic bands and into the IN718. This has been noted in several other bond coatings. This can be seen more clearly with reference to Figure 5.5.3. A reciprocal effect can be seen in Figure 5.5.2 (b) where voids from the growth of such laths (indicated) were also observed.



(a)



(b)

Figure 5.5.2: Optical micrographs of the interfacial microstructure of (a) the copper brazed Ti-6-4 substrate and (b) the IN718 substrate.



Figure 5.5.3: A high magnification optical micrograph showing evidence of primary  $\alpha$  growth remote of the Ti-6-4 substrate material.

## **6 DISCUSSION**

The following section will discuss pertinent aspects of the experimental techniques employed during the present study and the fundamental physical / chemical processes controlling diffusion across the bond interfaces of interest. From the outset it has to be recognised that despite the guidance given from the industrial sponsor, none of the requested dissimilar alloy pairings provided joints with any reasonable structural integrity. However, it is important to discuss the reasons for such incompatibility in order to influence future directions of research.

### **6.1 General considerations**

#### **6.1.1 Design of experiments**

The key goal in the design process was to formulate relatively simple, reproducible and robust experimental methods that could be applied to a wide range of materials on a laboratory scale. The use of resistance heating and in particular the Gleeble 1500 in previous investigations has highlighted that the technique offers an excellent method for producing small scale laboratory trials with relative ease. However, these tests had so far been restricted to similar bonds or bonds between dissimilar alloys of the same system [2, 3]. Though this study incorporated many of the procedures developed during these investigations it also took on board their recommendations, specifically in relation to cleanliness and repeatability. The incorporation of a powder interlayer required some novel modifications to the process. The aim being to bring together the two technologies of metal injection moulding and solid state resistance butt welding. As highlighted in the literature, previous techniques have been developed that employ powder interlayers and some aspects of these processes were explored in this investigation. Drawing on this, the novel the use of powder pastes provided both the most convenient and industrially suitable method in this respect.

### **6.1.2 Resistance heating in the experimental and industrial fields**

The literature has pointed to the various applications of resistance heating in industry from spot welding through to seam welding. Its advantages in high productivity and versatility have been highlighted as the main reasons it receives great attention in industry. The localised nature of the heating effect also lends the process to investigations at laboratory scale. The one most significant advantage of using a homogeneously generated heat source such as that produced by the Gleeble 1500 is that its effect remains consistent for a given test piece geometry. This meant that tests produced in the laboratory could be used as a direct reference for the industrial scenario; i.e. the process could be accurately scaled to give the required joining parameters (nominal current, heat sink geometry and interlayer thickness for instance) to commission a large scale industrial process.

These factors were kept in mind at all stages of the investigation; however, the primary goal was to assess the compatibility of the bond pairs proposed. In this respect resistance heating was found to have considerable advantages over other solid state processes such as HIPing, pressure welding and roll bonding, specifically in the relative simplicity of the process. This allowed many different process designs and bond chemistries to be assessed within the bounds of the project.

### **6.1.3 Considerations for the powder interlayer**

The powder interlayer posed several problems during the investigation. The most prominent of these was that the Gleeble 1500 has a horizontal load train. This meant that if the powder was to stay between the two test pieces then it would have to be supported in some manner. In many ways this provided a useful proof for the process on an industrial scale. Applying the technology of metal injection moulding (MIM) and powder metallurgy, a binder was employed. Whilst this technique has been proven for MIM by maintaining green strength (Figure 4.1.3), the use of a binder for adhering to metal substrates had not. Initially it was found that merely spreading the paste onto the

surface of the specimens was not sufficient enough to hold it in place nor provide adequate packing density in the compact (designated a key consideration in MIM [148]). More importantly it did not give any real control of interlayer thickness. This led to the development of the powder application process described in section 3.3.2 which provided enough force to hold the powder compact in place and yielded a compact with adequate packing density of uniform thickness that could be controlled to within 50 $\mu\text{m}$ .

Having established this application procedure, attention focussed on a debinding route that would grant a brown strength (the strength of the debinded powder) adequate to allow subsequent bonding. It was known that the HIPed bonds produced in parallel to this investigation were to undergo a 12 hour / overnight debinding stage prior to bonding. It was felt that it was important to replicate these conditions as closely as possible to improve the validity of any subsequent comparisons that were to be made between the two processes. Still, it is important to note that the debinding stages for the fully contained HIP bonds were not required to generate any brown strength prior to the bonding procedure itself.

EDX analysis of the compacts produced showed that the procedures could adequately drive off the binder and any associated contaminants, but struggled to maintain brown strength. Though the process window imposed by the equipment did restrict temperature during these trials, it is likely that the lack of pressure on the compact during debinding was a contributory factor here. The fired compacts showed little or no inter-particle joining (Figure 4.1.3) except at the small areas of direct contact which accounted for the small degree of brown strength associated with the most successful trial. On reflection, had this debinding trial been conducted employing negligible uniaxial pressure under resistance heating then heat would have been concentrated at these contact areas, which would have likely resulted in an improved brown strength. Whilst one bond was successfully produced with a prior debinded interlayer, the merits of the procedure were not thought to outweigh its extensive and complex nature. Nevertheless, a debinding stage was still a recognised component of the process as a



whole which is why it was revisited within the investigation at a later date (Section 4.6).

#### **6.1.4 Cleanliness and noise factors**

Great care is taken in the powder metallurgy industry to ensure that the powders produced contain very low levels of contamination and defects not just within the powder particles themselves but also foreign particles introduced to the powder post processing. Therefore, it was important that these levels of purity were maintained through the paste preparation and application stage, through to the sample loading and subsequent bonding procedures. The significant effect of foreign contaminants on solid state resistance butt welds has already been documented [2], so several steps were taken to avoid these factors during this and any subsequent investigations into the technique. These included:

- Wearing new nitrile based powder less gloves whilst handling experimental equipment at all times.
- Storing bonding equipment in sealed containers to prevent contamination.
- Regular cleaning of the Gleeble 1500 vacuum chamber and all associated tooling
- Sterile storage areas for all powders, specimen halves and binder constituents.
- Rigorous cleaning of all powder application and mixing apparatus prior to every use.
- Wearing lab coats at all stages up to and including bonding and avoiding loose clothing or items which may shed fibres and contaminate the bonds.

There was some concern that these steps may affect the industrial relevance of the process as such conditions are both hard to achieve in an industrial setting and adversely affect productivity. However, isolating and removing factors from the process was deemed to be a more important consideration and in fact no defects resulting from of foreign induced contamination were found during the entire investigation.

---

Testimony to the success of the process developed for this investigation is that it has been applied to three subsequent investigations. One of which has been published during the course of this investigation [149]. These additional studies have shown that when applied to more compatible materials the technique can result in near parent metal mechanical properties in both monotonic and cyclic loading regimes. As a result, the process is now being considered for industrial scale commissioning studies. This implies that the lack of success in performing bonds between the dissimilar alloy pairings of current interest was not a consequence of experimental procedure – but instead due to more fundamental incompatibilities of chemistry.

Having dealt with the wider aspects of the process as a whole this section will now concentrate on the physical and chemical processes relating to specific dissimilar bonding pairs.

## 6.2 Ti-6Al-4V to Inconel 718

Overall bond quality for Ti-6-4 to IN718 pairs was poor. None of the trials showed significant strength after bonding and many fractured during removal from the apparatus. Unfortunately, this gave no option for optimisation and so attention had to be focussed on the reasons for the failures themselves. To examine the possible reasons for the failures a selection of bonds that displayed differing degrees of success, produced under various conditions have been selected (Table 6.2.1). These joints were further analysed through EDX chemical analysis and microhardness traverses. Only the most relevant of these results will be considered within the bounds of this discussion but all data is presented in full in Appendix 1 and Appendix 2.

Table 6.2.1: Selected experiments to describe IN718 to Ti-6-4 joints.

Test No.	Coating	Powder Interlayer	Conditions			Comments
			Time (Min)	Temperature (°C)	Force (KN)	
1	Ta on IN718	Ti-6-4	37	925	1.25	Cracked
2	None	None	37	925	0.5	Cracked
3	Ta on IN718	None	37	925	0.5	Not Cracked
19	Ta on IN718	BurTi	57	970	2	Poor Consolidation
24	None	Ti-6-4 6%Cu	57	925	1	Excellent Consolidation
22	Cu on Ti-6-4	None	57	925	1	Cracked
8b	Ta on IN718	None	120	920	100 (MPa) HIP	Cracked
16b	None	None	120	920	100 (MPa) HIP	Not Cracked

### **6.2.1 Effects of interlayers / brazes**

EDX traverses were performed to establish reaction zone size. Whilst the use of EDX analysis for mapping light elements (C,O,B etc.) is acknowledged to be difficult it can map very accurately local fluctuations in both the most significant alloying elements across the bond lines. Traverses were conducted on the representative bonds highlighted in Table 6.2.1, to elucidate trends in inter diffusion and to help isolate the deleterious phases that have caused compromised structural integrity.

#### **6.2.1.1 Tantalum interlayer**

Tantalum layers were employed during the investigation as a barrier coating, aiming to prevent the formation of deleterious brittle phases at the bond line. Considering the brittle nature of the fracture surfaces noted within this group of trials it is obvious that the tantalum has not performed satisfactorily in this regard. Nevertheless, it is important to ascertain whether this brittle fracture was as a result of, or in spite of, the presence of these layers. To do this it is necessary to assess the microstructure associated with these bonds without the complication of the powder interlayer. Hence Tests 2 and 3 (resistance bonded) and Tests 8b and 16b (HIPed) are selected here.

For clarity the EDX traverses for these bonds were separated into two plots; one for the minority and one for the majority elements. Full traverses are displayed in Appendix 1. The tantalum appears to have surprisingly little effect on the local trends in inter-diffusion at the interface, which remained fairly consistent across all four bonds. Reaction zone sizes are detailed in Table 6.2.2, which show that tantalum has in fact increased the mobility of nickel in titanium. Conversely, reaction zones in the nickel were all limited to within 40 $\mu$ m before returning to parent levels. Titanium solubility in Ni, Cr and Fe is notoriously poor which is the likely reason for this, coupled with the presence of Al in the IN718 resulting in a lower concentration gradient and subsequently a lower mobility.

Table 6.2.2: A summary of reaction zone size for Ta coated and uncoated Ti-6-4 to IN718 bonds.

Test Number	Diffusion of nickel into titanium ( $\mu\text{m}$ )	Majority element reaction zone ( $\mu\text{m}$ )	Minority element reaction zone ( $\mu\text{m}$ )
2	200	240	35
3	90	130	60
16b	275	315	70
8b	400	440	55

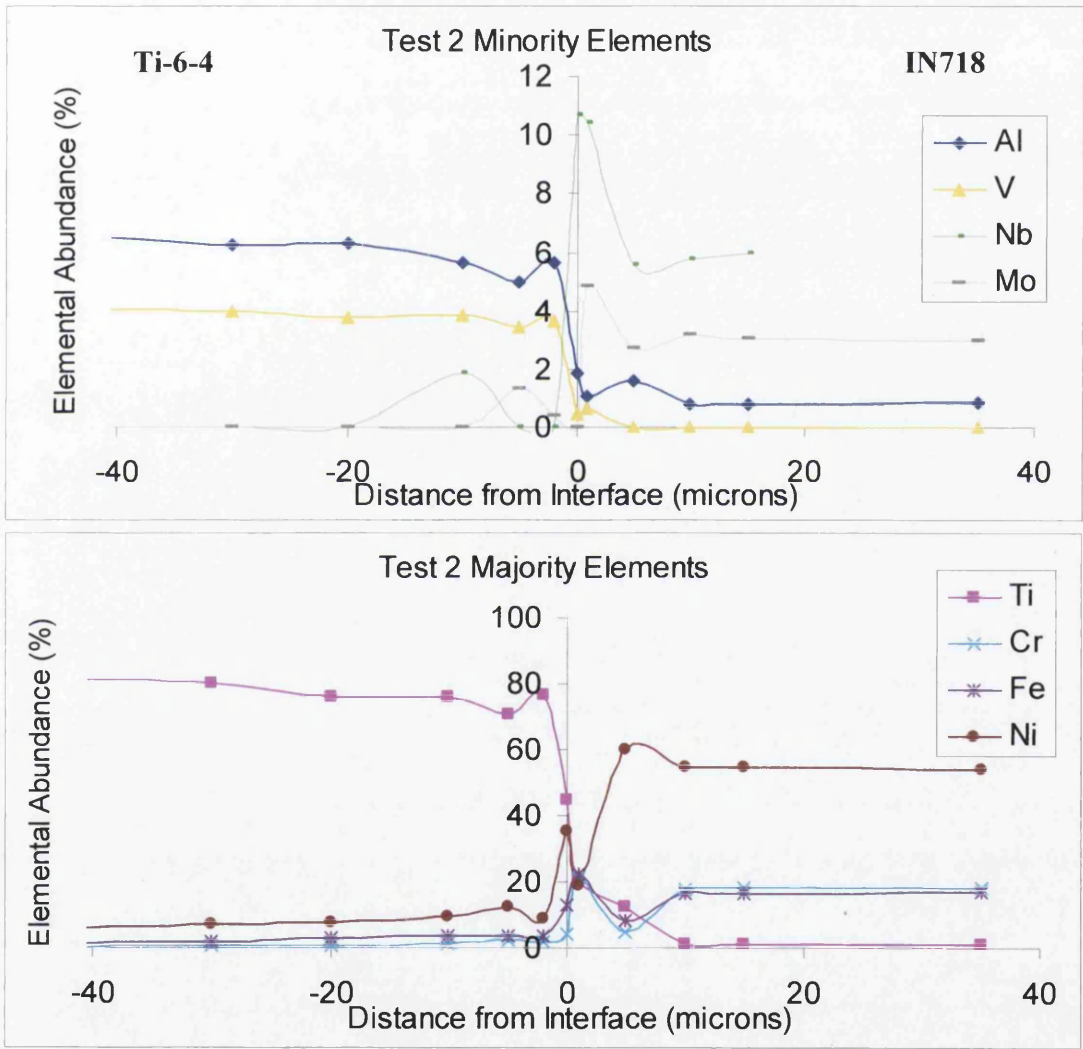


Figure 6.2.1: EDX traverses for minority and majority elements in Test 2.

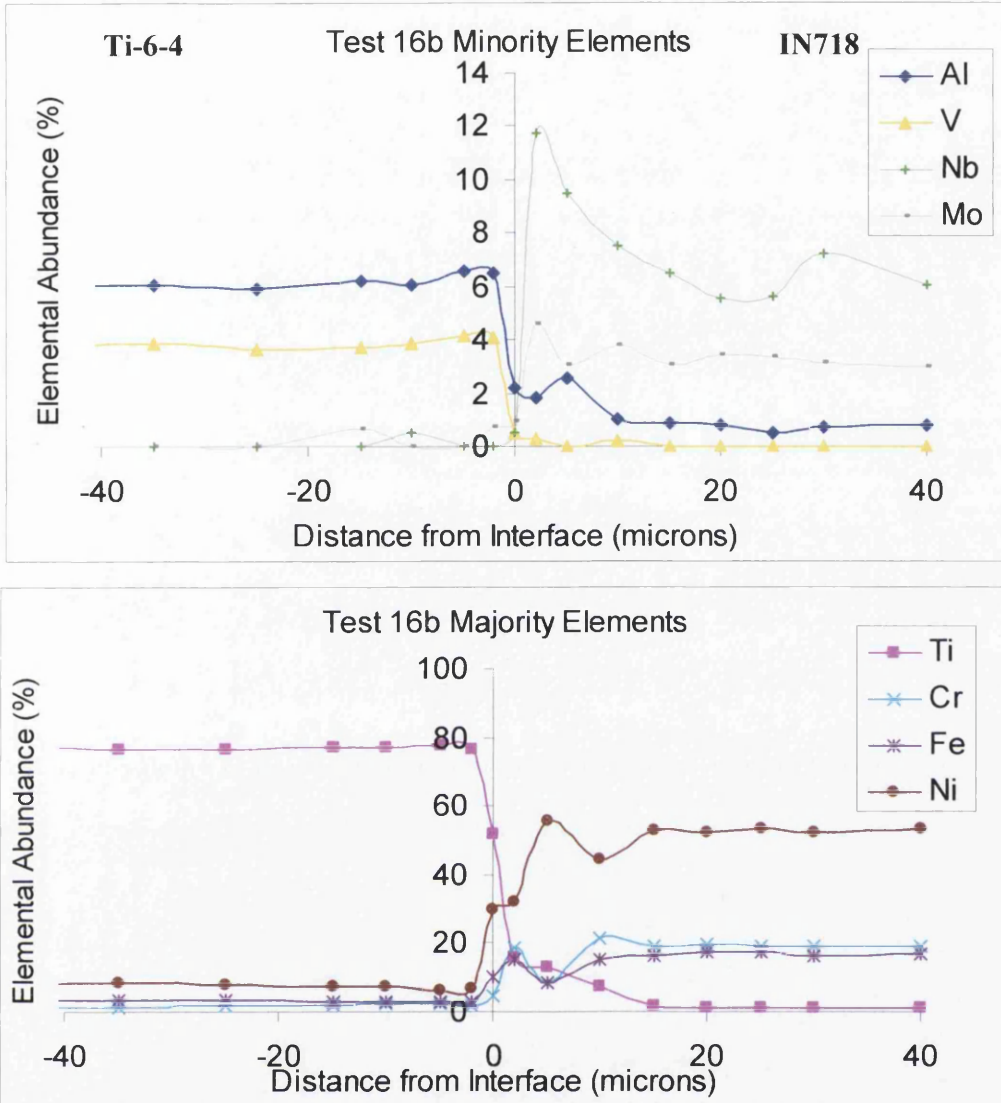


Figure 6.2.2: EDX traverses for minority and majority elements Test 16b.

Local inter-diffusion trends between the two uncoated trials 2 and 16b (Figure 6.2.1 and Figure 6.2.2) are remarkably similar. Both show high concentrations of niobium, molybdenum and chromium between 2 and 5  $\mu\text{m}$  into the nickel at the expense of nickel, followed by higher concentrations of aluminium. These profiles correlate well with the orientated precipitates observed in the micros in sections 5.1 and 4.2.2, suggesting the presence of Nb rich  $\delta$  phase. The relatively high and consistent levels of titanium observed up to 10 $\mu\text{m}$  into the nickel are also important given the microstructural sensitivity to titanium associated with IN718.

Finally trends were also noted in elemental concentrations of the intermetallic films at the interface, all of these concentrations are presented in Appendix 3. Two common profiles can be seen in Figure 6.2.3 and Figure 6.2.4 indicating the presence of NiTi and Ti<sub>2</sub>Ni intermetallics respectively. Microhardness traverses conducted on the bonds also highlight this effect with large increases in hardness at the interface. The hardness traverses for Test 16b can be seen in Figure 6.2.5.

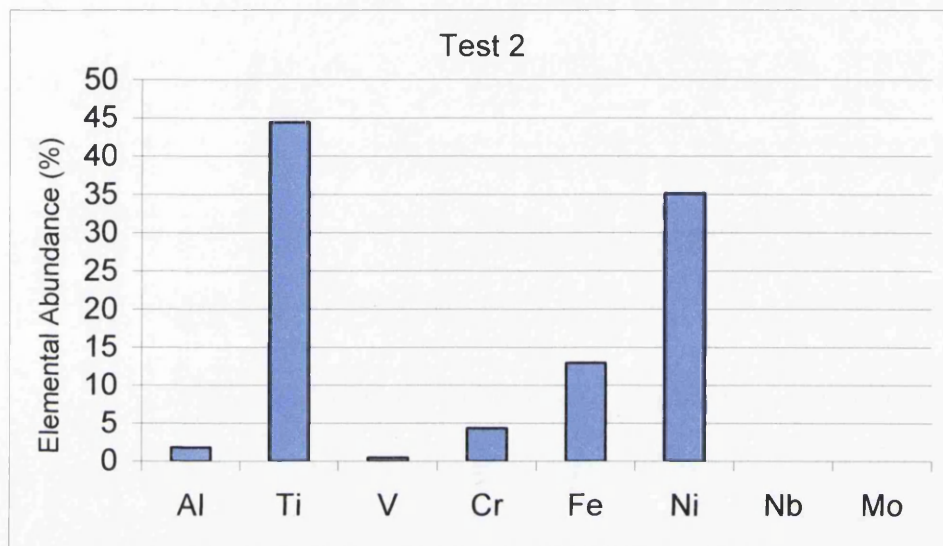


Figure 6.2.3: Spot EDX analysis on intermetallic films found in Test 2.

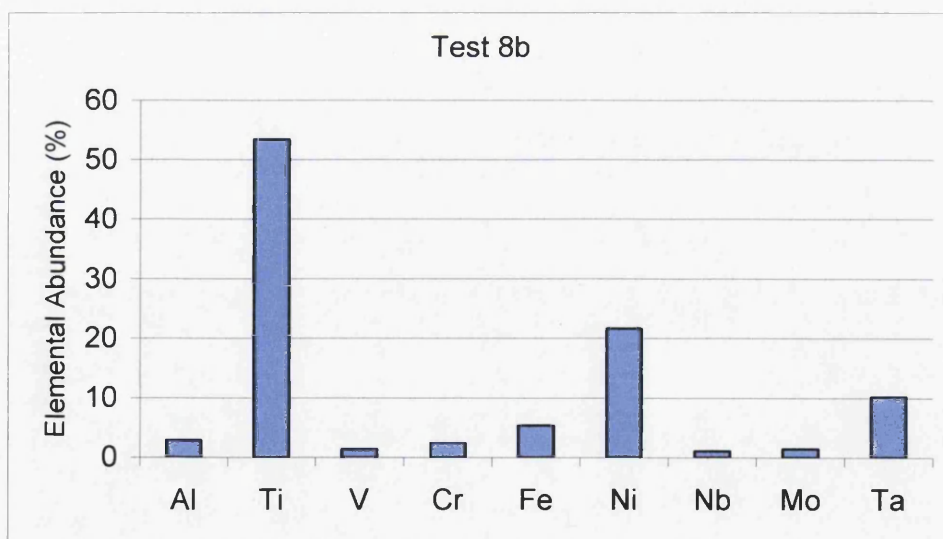


Figure 6.2.4: Spot EDX analysis on intermetallic films found in Test 8b.

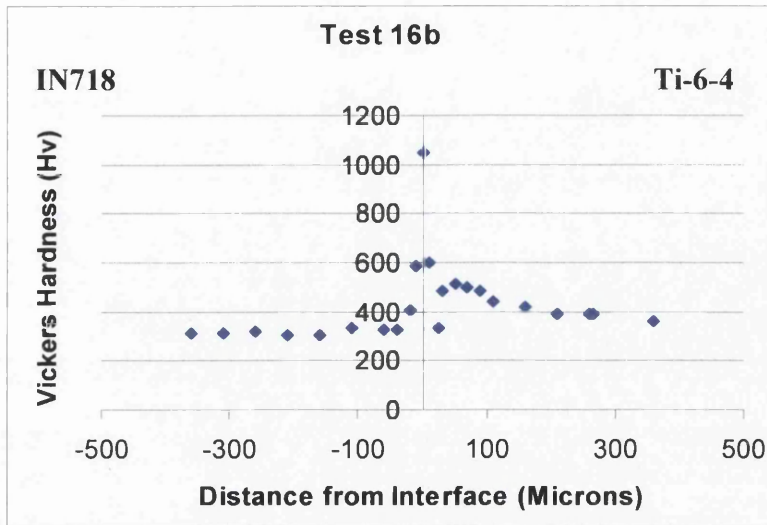


Figure 6.2.5: Microhardness traverse across the interface of Test 16b.

In summary the tantalum braze has not had a beneficial effect on bond quality and has in fact acted to increase the reaction zone size. The tantalum layer was also found to have very little effect on local inter-diffusion trends and did not restrict the formation of brittle intermetallics on the bond line.

### 6.2.1.2 Copper braze

As described in section 4.12 the Ti-6-4 to IN718 bonds incorporating a copper braze were wholly unsuccessful showing little or no adhesion on removal from the Gleeble apparatus and displaying brittle fracture characteristics. Intermetallic films are again believed to be the primary reason for these failures. Microstructural modification / growth of coarse acicular  $\alpha$  structures were also noted in the titanium. This was concentrated in a band roughly 50 microns wide adjacent to the interface. This specific area of modification is likely to be due to copper diffusion at the interface. Copper is known to be an effective  $\beta$  stabiliser in concentrations above 2% [150] and so is likely to have caused a local depression in the  $\beta$  transus, which on cooling allowed the growth of a coarse acicular structure from the local  $\beta$  solutioned region. Comparisons between the microstructures presented in section 4.12 and the results of the EDX traverse confirm this.



Comparisons between the EDX traverse of minority elements (Figure 6.2.6) and the microhardness traverse (Figure 6.2.7) elucidate the effect that copper diffusion can have on local mechanical properties. With the exception of anomalies at the interface the microhardness traverse shows a steady transformation in bond strength across the interface, a feature desirable in dissimilar bonds. Conversely, coupled with this is significant hardening of the titanium through the acicular region. The hardening is also observed beyond the acicular region and decreases to parent levels in partnership with copper concentration, suggesting that the hardness is affected by copper content directly and not just by its effect on the microstructure.

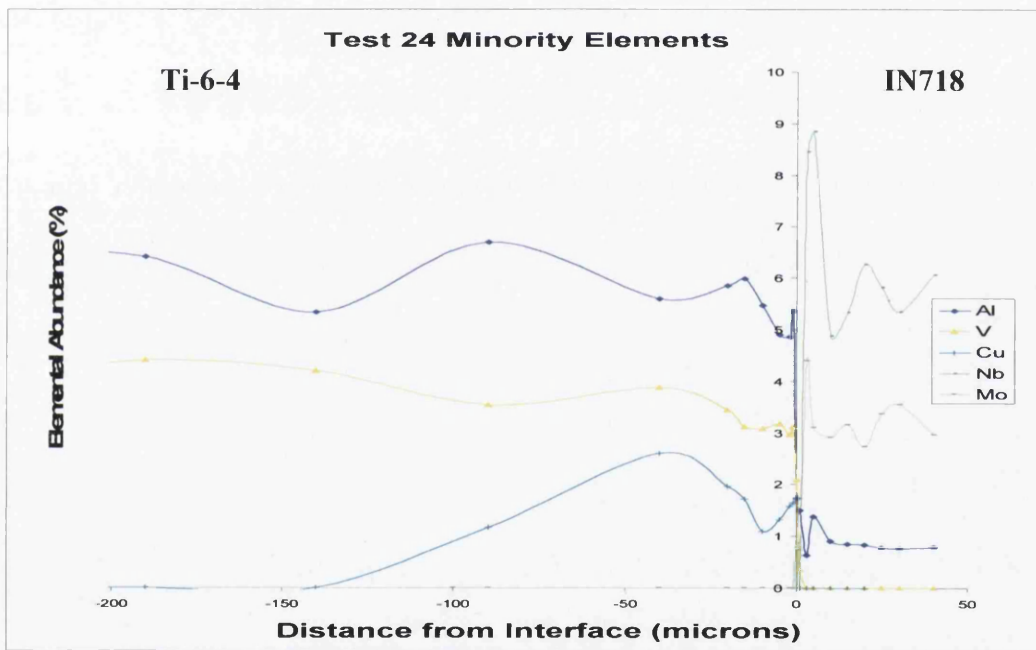


Figure 6.2.6: A minority element EDX traverse of Test 24.

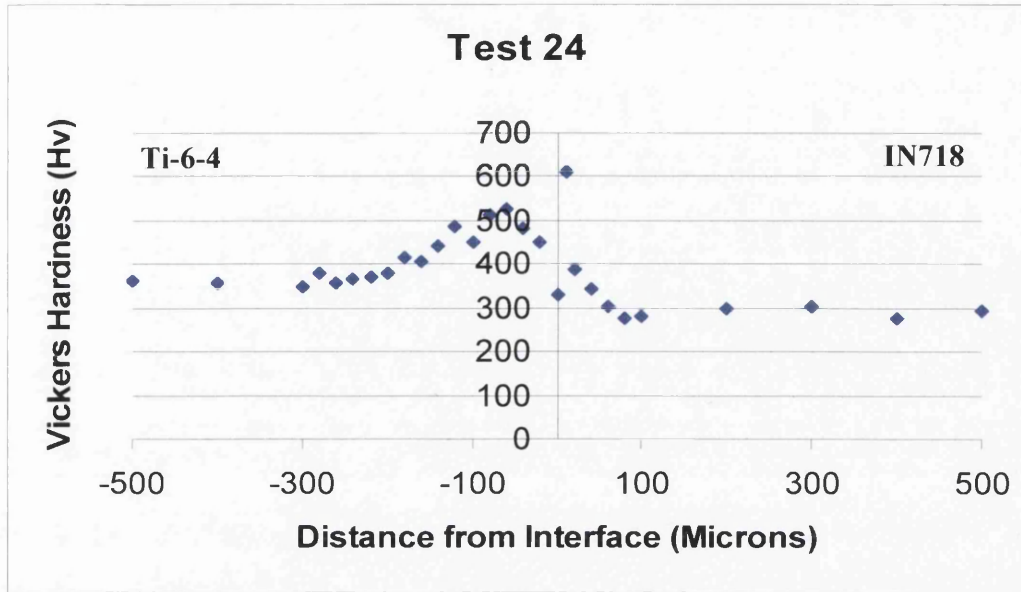


Figure 6.2.7: A microhardness traverse of Test 24.

Specific EDX analysis of the fractured films (Figure 6.2.8) suggested the formation of intermetallic NiTi compounds. This was reinforced by the high hardness noted near the interface in the IN718 on the microhardness traverse. So although the use of copper brazes certainly improves the transition between IN718 and Ti-6-4 it also cannot prevent the formation of deleterious phases at the interface.

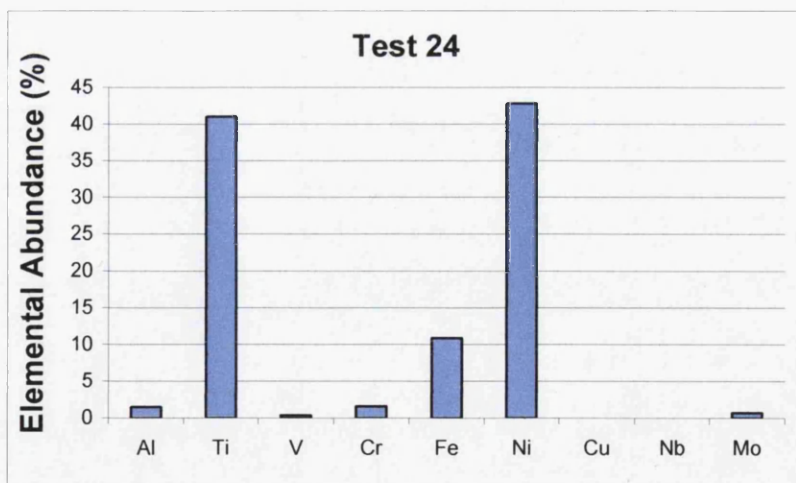


Figure 6.2.8: EDX spot analysis of fractured intermetallic films in Test 24.

## 6.2.2 Powder consolidation and chemistry

### 6.2.2.1 Ti-6Al-4V and BurTi powder interlayers

In terms of physical consolidation Test 1 proved to be the best powder interlayer trial performed between IN718 and Ti-6-4. The results showed levels of consolidation which would have been considered adequate for some degree of adhesion between the specimens. Detailed inspection of the fracture surfaces showed that interfacial contact area between the powder and the IN718 substrate had improved significantly. However, the fracture surfaces of the powder particles displayed a characteristic brittle fracture, and the EDX data presented in section 4.3.1 and high resolution SEM (Appendix 4) strongly suggests the presence of a  $Ti_2Ni$  intermetallic on the particle / substrate surfaces.

Whilst the formation of intermetallics can explain the poor bond strength, the incomplete consolidation of the powder was also a concern. Transverse sections of the powder interlayer showed that consolidation worsened closer to the IN718 substrate. Also when conducting the microhardness traverses it was noted that indenting particles that had bonded to IN718 substrate resulted in their fracture with little or no sign of deformation. No hardness data could be taken at these points such was the fragility of these particles. This indicates that a particle hardening effect may have occurred, which prevented those particles from deforming sufficiently to allow complete consolidation. EDX and microhardness traverses of the powder compact revealed a reaction zone size of  $140\mu m$ . This is lower than that observed for Tests 2 and 16b indicating that a powder interlayer is beneficial in reducing reaction zone size.

The BurTi interlayer trial displayed only minor consolidation, considering the extreme bond parameters. When compared to the consolidation of Ti-6-4 in Test 1, the explanation for this may be attributed to the particle size, and most importantly the particle size distribution. Valverde *et al* [151] have shown that for small loads, particle size plays a key role in developing inter-particle adhesive forces. At low forces inter-particle contact is extremely important as diffusional mass transport accounts for a

great deal of the consolidation within the compact. The figures in section 4.10 clearly show some areas of good consolidation, however very few small particles are present in the less consolidated areas. This is crucial as large particles result in larger inter-particle gaps relative to interlayer thickness, meaning that the effective contact area is reduced, diminishing the interlayers ability to conduct electrical current and heat; reducing the likelihood that it will consolidate effectively. Test 14b employed the same bond chemistry but was produced by HIP. Consolidation in the BurTi powder interlayer was much better but the clear prior particle boundaries (Figure 5.4.1, section 5.4) revealed a similar lack of small particles. This indicates that consolidation in this test relied much more on significant deformation of pre-existing particles, rather than diffusional mass transport.

#### **6.2.2.2 Copper Impregnated Ti-6Al-4V powder**

Of all the interlayers employed in the investigation the transient liquid phase bonded, copper impregnated powder interlayer displayed the best consolidation. However, this consolidation came at the expense of microstructural stability. As seen in Test 21 (Figure 4.11.2) the  $\beta$  stabilising effect of copper can be considerable in titanium and this was displayed in the micrographs presented in section 2.11. Here a mixture of coarse widmanstatten  $\alpha$  and equiaxed primary  $\alpha$  can be clearly seen. Microhardness traverses (Figure 6.2.9) showed that this resulted in a greater variation in hardness in the powder interlayer compared to that displayed by the parent microstructure. Also a gradual increase in hardness was observed leading up to the bond line. This correlated well with copper concentration, reinforcing the link noted in the analysis of Test 21. The general degree of disruption was certainly greater than that observed for Test 21 and EDX analysis (Appendix 7) confirmed that concentrations of copper remained consistent in the powder interlayer at about 2.5%.

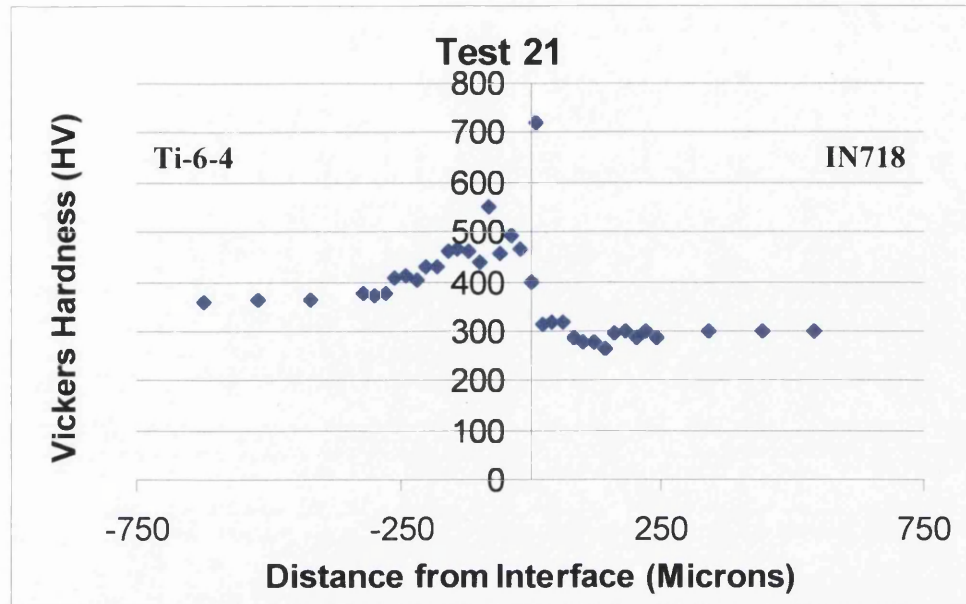


Figure 6.2.9: A microhardness traverse of Test 21.

Whilst powder consolidation was effective, the overall joint strength was poor. Brittle failures at the interface were again found to have propagated along intermetallic films that EDX spot analysis resolved as a  $Ti_2-Ni-Ta$  composition profile.

### 6.3 Ti-6Al-4V to Super CMV steel

Bond integrity was notably varied in these joints compared to that of the IN718 to Ti-6-4 pair, particularly in relation to powder consolidation. Three coatings were trialled; nickel, tantalum and triple coated Ni-Cr-V transition interlayers. As well as the Ti-6-4 powder interlayer, BurTi interlayers were also trialled as it was believed that they would provide closer, intermediate chemistry and thermo-physical properties between the steel and titanium (transition joining). A crucial factor controlling bond quality was found to be the inherent electric and thermal properties of the materials under investigation, which resulted in differential heating. All bonds were found to have failed along brittle phases evolved at the interface. The bonds identified for further consideration in respect of these general trends are detailed below in Table 6.3.1.

Table 6.3.1: Selected experiments to describe SCMV to Ti-6-4 joints.

Test No.	Coating	Powder Interlayer	Conditions			Comments
			Time (Min)	Temperature (°C)	Force (KN)	
4	Ta on SCMV	Ti-6-4	37	925	0.5	Good consolidation. Failed during Met-Prep
9	Ni on SCMV	Ti-6-4	57	925	1	'Hot jaws' employed. Cracked
16	Ni-Cr-V on SCMV	BurTi	57	970	1	'Hot jaws' employed. Cracked
7b	Ta on SCMV	None	120	920	100 (MPa)	Cracked

### 6.3.1 Thermo-physical effects – Differential heating

The differential heating effect presents unique problems for the resistance bonding process when applied to dissimilar materials. Whilst crude design modifications to the Gleeble wedge grips were employed to counteract this effect which improved powder consolidation and interfacial area, they resulted in substantial heat affected zones in the substrate materials (section 4.14). A small or non-existent heat affected zones associated with diffusion bonding presents one of the primary advantages of the process, and for this reason should be avoided at all costs.

Given adequate time it may have been possible to construct a system of heat sinks that could have produced a uniform temperature profile across each test piece. However, transferring this capability from simple cylindrical test pieces to more complex sections would prove very difficult. Applying conventional heat sinks to non-homogenously heated specimens may be relatively simple. Conversely, in tests pieces with a homogenously evolved heat source the effect of heat sink contact on local current density (and therefore heat) would have to be evaluated in addition to thermal conductivity. This twofold effect must be considered at every step of in the design process of dedicated bonding apparatus and would both influence grip and additional heat sink geometry and materials selection. Further to this, well designed macro circuitry would be required to enable good control of heat generation. Industrial scale

equipment design has yet to be considered, and it is suggested that the factors described above would require further research before such designs are attempted.

### **6.3.2 Effects of interlayers / brazes for Ti-6-4 powder interlayer joints**

Three separate interface structures were investigated for the Ti-6-4 to SCMV pairing. Early reports on the HIPed bonds produced at Birmingham university had suggested that Ta coatings had resulted in poor joint quality. To further understand this, Test 7b has been chosen as an example for further investigation. Work was concentrated on nickel coatings following the research by Chatterjee *et al* [120-122]. These trials were complicated by the differential heating, so for clarity both Test 4 (conducted with copper jaws) and Test 9 (conducted with hot jaws) have been considered in detail. Following the poor performance of these trials attention was focused on the production of transition joints following evidence of their benefits in dissimilar joining metals highlighted in the literature [119]. As the use of hot jaws had been shown to be beneficial to powder consolidation in previous tests they were employed for these trials and Test 16 will be discussed as an example.

#### **6.3.2.1 Tantalum interlayer**

Comparisons between microhardness and EDX traverses of Test 7b are presented in Figure 6.3. In contrast to its role in the IN718 to Ti-6-4 bonds the presence of tantalum at the interface in this system successfully prevented significant inter-diffusion of the base elements iron and titanium. In this respect it has certainly prevented the formation of the deleterious Ti-Fe type intermetallics ( $\text{FeTi}$ ,  $\text{Fe}_2\text{Ti}$ ,  $\sigma$ ) that have been associated with previous attempts to join the materials [120]. Furthermore microstructures of the specimens suggest that interfacial  $\beta$  titanium stabilization has also been retarded. Unfortunately this has not prevented embrittlement at the bond line. As indicated in Figure 6.3.1 it appears that the tantalum itself has formed intermetallics with the two base metals, namely  $\text{FeTa}$  and  $\text{Ti}_2\text{Ta}$  phases. The inability of these phases to

accommodate strains associated with thermal contraction during cooling is considered to be the likely cause of the fracture observed in the tantalum coated bonds.

Also of interest was the peak in microhardness noted in the bond approximately 2 mm from the interface in the SCMV substrate indicated at 1 in Figure 6.3.1. EDX analysis revealed no discrepancies in composition at this point so the peak must be attributed to microstructural variation. This provides interesting comparison to the HAZ banding effects discussed in detail later in section 6.5, especially considering the uniform test piece temperatures associated with the ambient heating employed for the HIPed bonds.



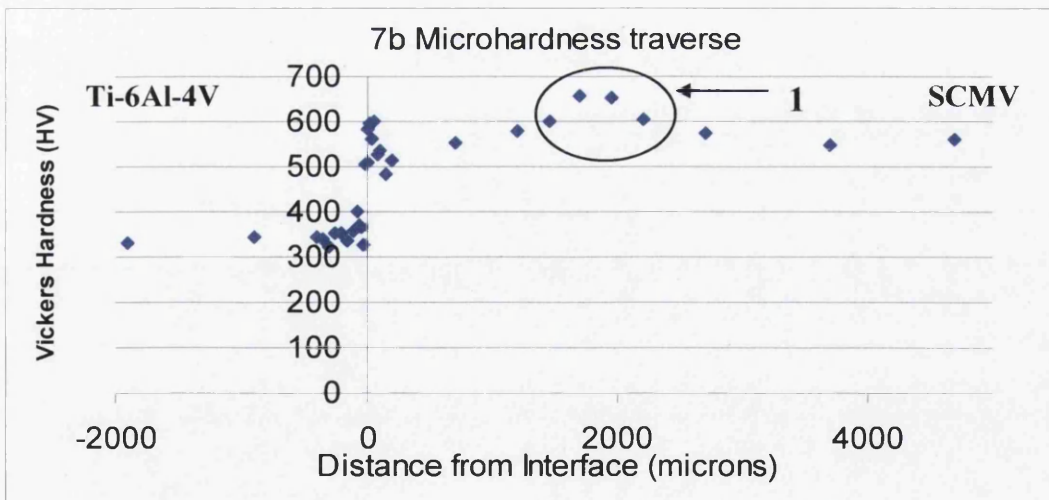
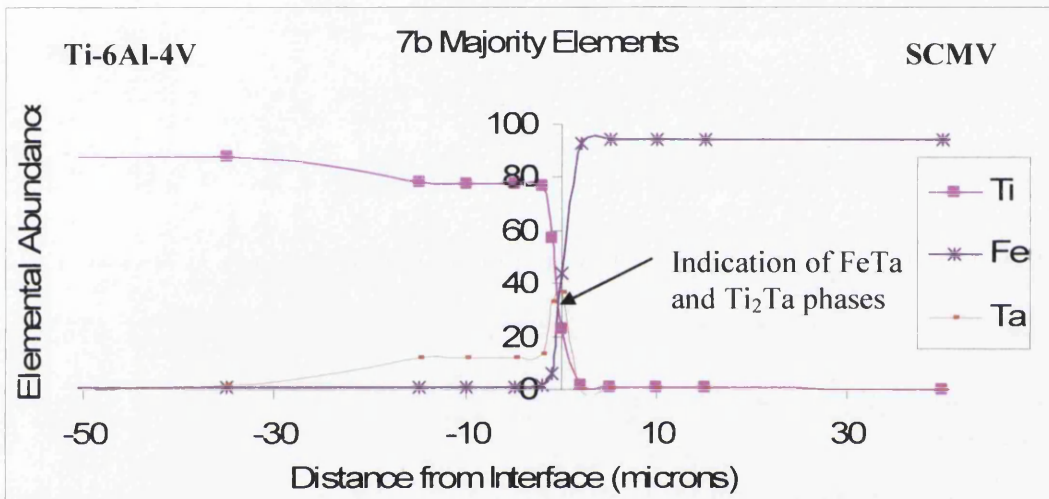
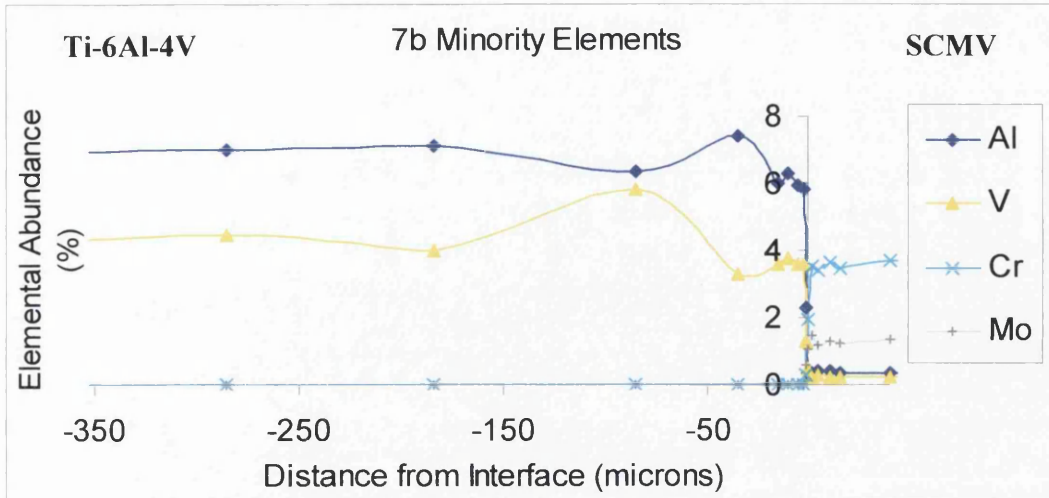


Figure 6.3.1: A comparison between an EDX traverses for minority and majority elements and an EDX traverse for Test 7b.

### 6.3.2.2 Nickel interlayer

As mentioned previously, Tests 4 and 9 provide an interesting comparison both in terms of powder consolidation (sections 4.3.2 and 4.5) and microstructural evolution. This is because of the very different temperature regimes they experienced on account of the differential heating effect. Direct comparisons between the chemical and hardness profiles of the two bonds reveal definite trends in phase evolution and powder consolidation that highlight the inherent difficulties in balancing the two considerations. The comparisons for Test 4 and 9 can be seen in Figure 6.3.4 and Figure 6.3.5 respectively.

The majority element traverse for Test 4 shows how the nickel coating diffuses primarily into the SCMV at the expense of aluminium and iron. Reaction zone size in the titanium is comparably limited, possibly as a result of the poorly consolidated powder interlayer Figure 4.3.5, providing an inadequate diffusion path. The microhardness traverse also shows little evidence of a well developed interfacial microstructure with no transition between the hardness values of the substrate materials. The poor powder consolidation and interface structure appear as a result of the differential heating effect.

Comparisons between these conditions and the significantly higher temperatures observed in Test 9 allow an assessment of the continually evolving microstructure. The first point of interest on the elemental traverses in Figure 6.3.5 is the reduction in size of the reaction zone in the titanium powder despite its significantly improved consolidation. This is due to the extensive inter-diffusion of nickel and iron occurring in the SCMV substrate. Chemical trends elucidate a migrating band of  $\text{Ni}_2\text{FeCr}$  that has progressed into the SCMV substrate over the course of the bonding time. The nickel enrichment and iron depletion in front of the advancing band (Figure 6.3.2 zone 1) indicate that at longer bonding times this migration may continue. Surprisingly the elemental composition of the material in zone 2 shows near parent SCMV composition. Even more interesting is that the microstructure in zone 2 shows remarkable similarities to parent microstructure. Fracture can clearly be seen to have occurred within the

SCMV substrate away from the interface. In contrast to the microhardness traverse of Test 4, a smooth transition in hardness across the bond is noted in Test 9 suggesting the development of a more accommodating interfacial microstructure.

To understand more about the reason for the fracture in the Ni-Fe-Cr band further information is required on its properties. Due to its prevalence in steels and nickel base alloys the system has received much attention in dedicated supplementary research. Reference to the Ni-Fe-Cr ternary phase diagram shows the composition lies in an area of mutually soluble  $\gamma$  phase field (point A on Figure 6.3.3) close to bond temperature. However, on cooling the  $\gamma$  phase is known to decompose to peritectoid  $\gamma + \text{Cr rich BCC } \alpha'$  resulting in subsequent embrittlement of the material [152]. This embrittlement appears to have led directly to the fracture of the bond.

The comparison of these two tests highlights the inherent difficulty in matching materials for powder interlayer bonds. Here it has been shown that differential heating can result in poor powder consolidation and interfacial contact, but negating differential heating whilst resulting in improved powder consolidation results in complex brittle phase evolution within the reaction zone. Hence deducing optimum bonding parameters for this alloy pair would require further dedicated research and new apparatus designs that build on these initial findings.

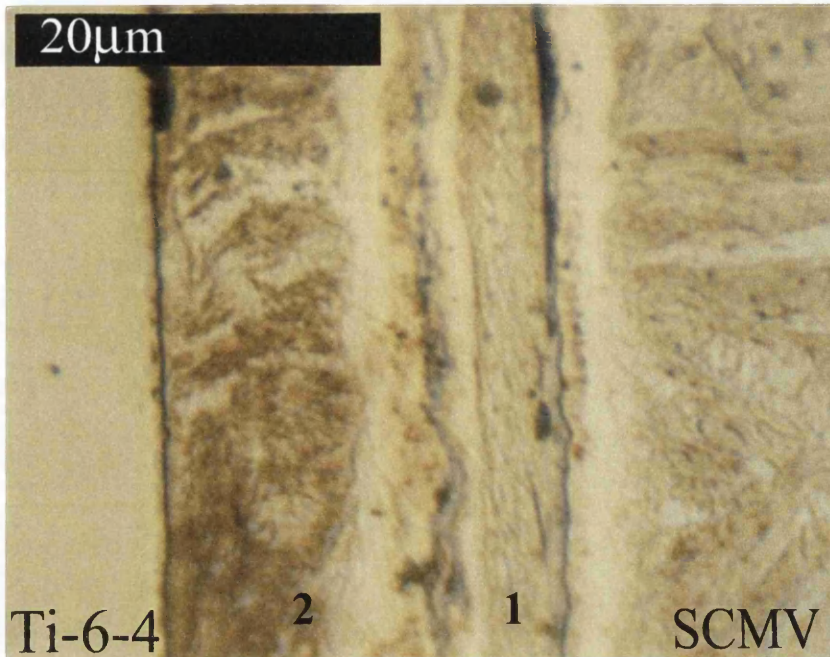


Figure 6.3.2: The interfacial microstructure of Test 9.

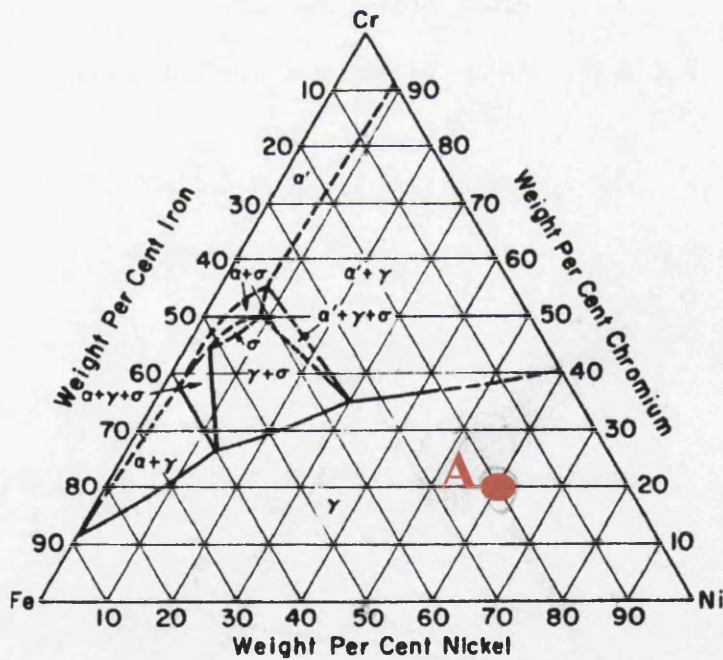


Figure 6.3.3: The ternary phase diagram for the Ni-Fe-Cr system at 900°C [153].

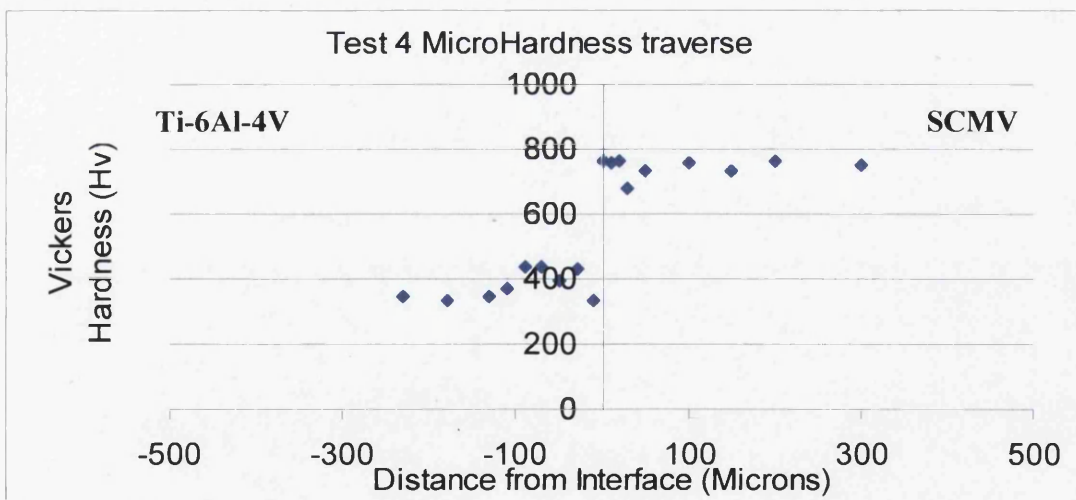
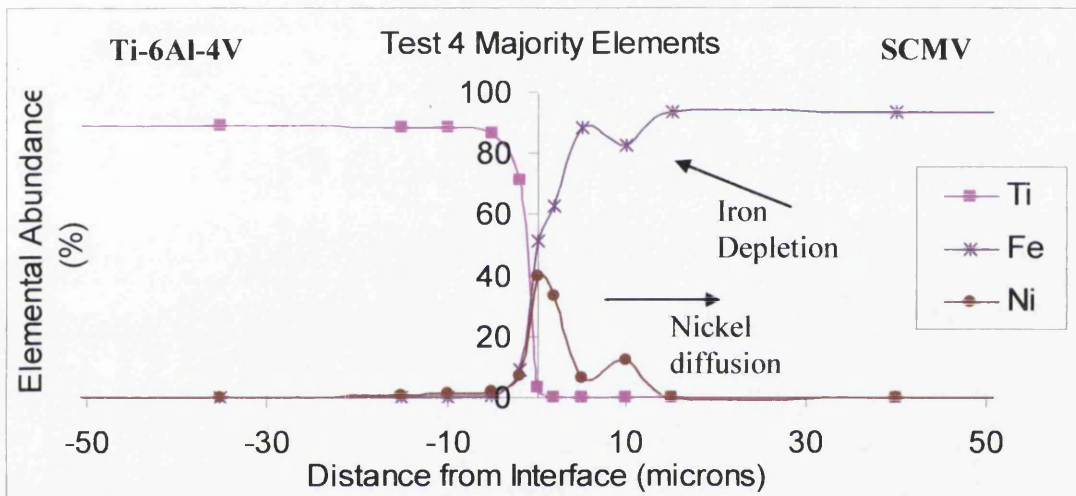
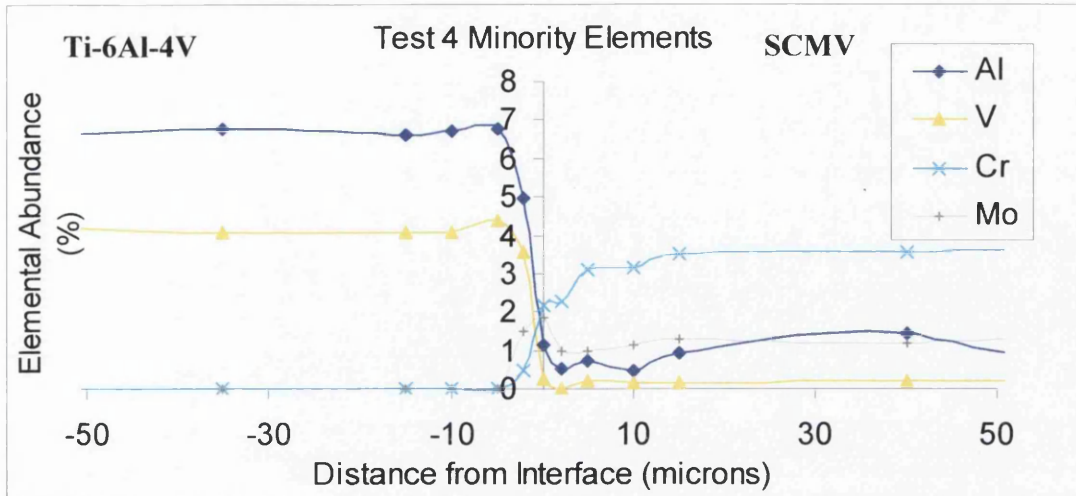


Figure 6.3.4: A comparison between an EDX traverses for minority and majority elements and an EDX traverse for Test 4.

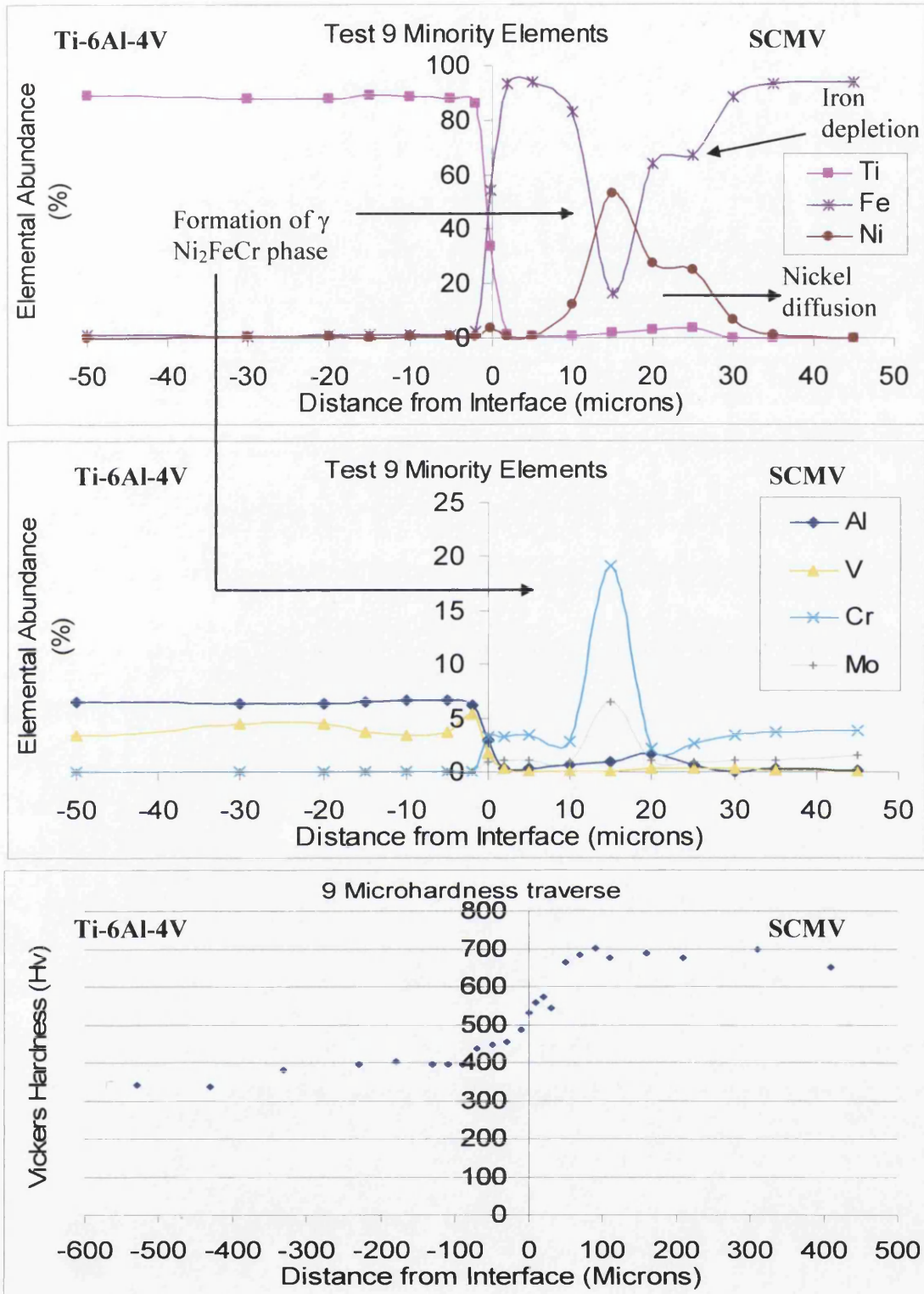


Figure 6.3.5: A comparison between EDX traverses for minority and majority elements and an EDX traverse for Test 9.

### **6.3.3 Triple layer transition joints employing a BurTi powder interlayer**

Following the poor results of the tantalum and mixed performance of nickel interlayers triple layer transition joints were performed that also employed the new hot jaw configuration. It was hoped that the intermediate properties and composition of the BurTi alloy powder together with the triple braze of intermediate composition with the SCMV substrate (Ni-Cr-V) would improve bond quality. The idea being to allow sound joints to form at the two separate interfaces Ti-6-4 : BurTi and BurTi: (V-Cr-Ni coated) SCMV without the formation of deleterious phases associated with the more direct joining techniques that had been previously attempted. Unfortunately, this technique again proved to be unsuccessful though some promising indications for improvements in future bond quality can be highlighted.

Initial analysis of the bond (presented in section 4.7) showed that relatively good consolidation had occurred in the BurTi powder close to the Ti-6-4 substrate but that this worsened on approaching the SCMV substrate. This mirrors the findings presented for the BurTi interlayers employed in IN718 to Ti-6-4 bonds that are discussed in section 6.2.2.1. However, Test 16 displayed markedly better powder consolidation than Test 19. The difference is again likely to be due to differential heating, as a result of their greater compatibility in respect of thermal physical properties (Table 4.4.1) on Ti-6-4 to IN718 bonds but which is not significant enough to warrant employing the hot jaws configuration. Further to this, evidence of a wider particle size distribution was noted on the fractured surface of the BurTi interlayer which will have contributed to its improved consolidation. This improved consolidation has come at the cost of severe microstructural modification in both the Ti-6-4 and SCMV substrate materials and these effects will be discussed further in section 6.5.

Comparisons of chemical and micromechanical features are presented below in Figure 6.3.6. Encouragingly, the interface between the BurTi powder and the Ti-6-4 substrate appears to be of high integrity. Elemental diffusion across the interface appears to be even with no evidence of deleterious phase formation. Whilst the corresponding microhardness traverse shows some fluctuations, these are most likely due to

microstructural features. Acicular  $\alpha$  growth that has so far been associated with high  $\beta$  stabiliser concentrations (vanadium in this case), noted in other BurTi interlayer trials (Figure 4.10.3) is the likely reason for the hardening in the Ti-6-4 substrate. The cause for the softening effect is not so easy to isolate but may be due to a relaxation of residual strains at the interface. Other than these minor fluctuations no evidence of embrittlement was noted at the powder substrate interface.

Fracture of the bond occurred at the interface between the BurTi powder and the vanadium coating on the SCMV. EDX measurements taken directly from the fracture surface (Figure 4.7.3) showed an inverse relationship in titanium and vanadium concentrations indicating the presence of a distinct interface at the point of fracture. This data indicated poor inter-diffusion between the vanadium layer and the BurTi powder resulting in poor local bond strength. This coupled with the reduced interfacial area on account of the poor consolidation is the likely reason for the failure. Although the microhardness traverse indicated spikes at the bond line these appear to be due to the pre-existing triple layer as opposed to brittle intermetallic phase formation. Aside from this fracture, the chromium and nickel layers appear to have performed reasonably well. The nickel has inter-diffused with iron without the formation of  $\text{Ni}_2\text{FeCr}$  bands observed in Test 9. Although the chromium coating has remained fairly distinct it has prevented large scale inter-diffusion of iron to the interface and showed some intermixing with the nickel which is likely to have improved adhesion between the coatings.

In general, these transition joints have shown many positive aspects despite the poor interfacial strength in this case. This suggests that modifications in joint design may yield dissimilar powder interlayer joints between Ti-6-4 and SCMV with improved properties. Nevertheless, it is important to reiterate that none of the Ti-6-4 to SCMV bonds produced under the conditions imposed in this investigation matched the mechanical integrity of the best substrate/substrate joints presented in the literature [124,125].



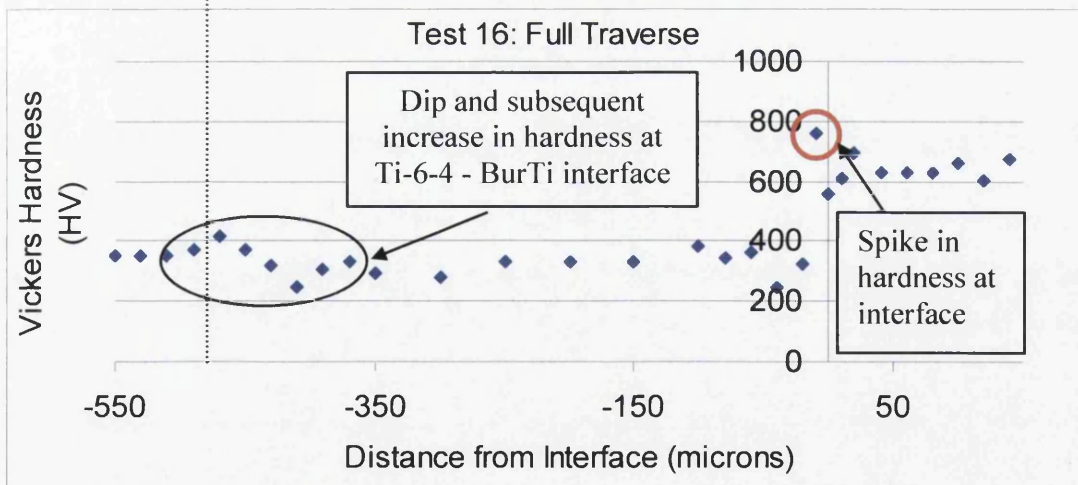
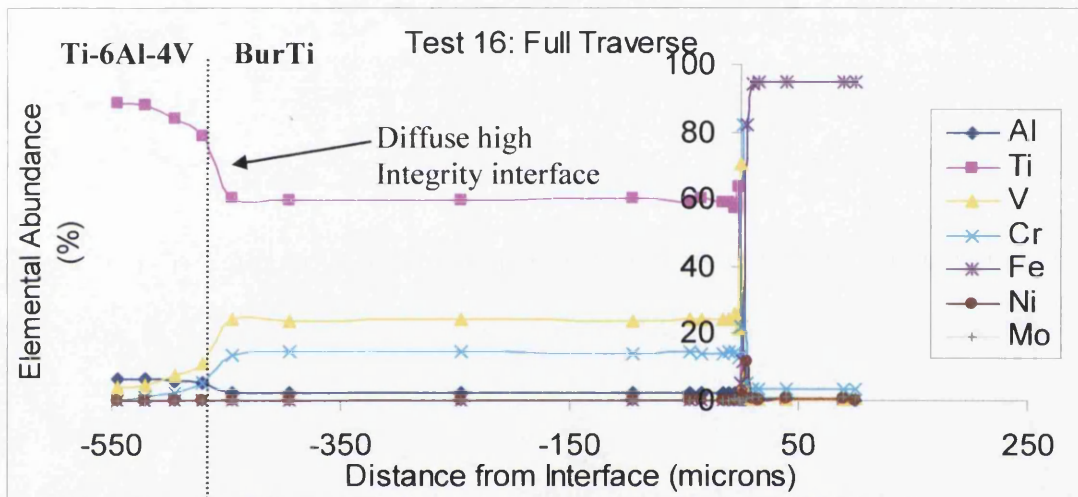
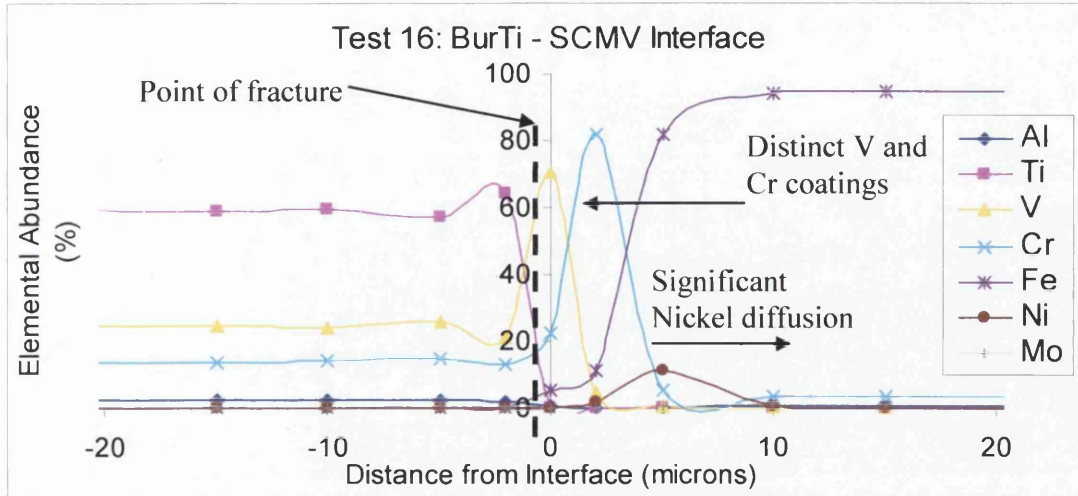


Figure 6.3.6: A comparison between EDX traverses for both the BurTi powder – SCMV substrate and Ti-6-4 substrate – BurTi powder interfaces and the full microhardness traverse for Test 16.

#### 6.4 Inconel 718 to Super CMV steel

Of the three alloy system pairs investigated, IN718 to SCMV proved to be the most successful. This success is reflected in the considerable attention that steel - nickel based joints have received in the literature. Bonding two alloys that maintain their strength at temperature also allowed for more freedom in applied force and temperature; this no doubt contributed to the quality of the bonds produced. Initially, problems with powder consolidation (Test 17) resulted in trials of a novel quasi-isostatic powder interlayer bonding technique that showed early signs of success in terms of powder consolidation and subsequent interfacial contact. Despite these improvements bonds were still found to fail at powder substrate interfaces as a result of trialling the tantalum interlayer. Bonds produced using the conventional HIP technique mimicked this behaviour. Unfortunately, it was not possible within the scope of the project to develop the technique. Finally, study of the literature had elucidated the benefits of boron and silicon rich brazes in improving joint quality which resulted in the use of the Walcomanoly developed Nicrobraz LM braze for both substrate - substrate and powder interlayer joints. These proved to be the most successful of the joints produced in the entire investigation and had a mechanical integrity sufficient enough to permit non-standard mechanical evaluation to be performed.

The trials picked for detailed consideration in respect of these trends are outlined below in Table 6.4.1.

Table 6.4.1: Selected experiments to describe SCMV to IN718 joints.

Test No.	Coating	Powder Interlayer	Conditions			Comments
			Time (Min)	Temperature (°C)	Force (KN) (MPa)	
19b	Ta on IN718	IN718	120	920	100 (MPa)	Cracked*
18	Ta on IN718	IN718	57	925	3	Good consolidation. Poor interface strength.
Ni5	Nicrobraz on IN718	None	60	990	5	Good adhesion. UTS = 350MPa
Ni5	Nicrobraz on IN718	None	N/A	1050 *	5	Melted: Control system failure. UTS = 639MPa
30	Nicrobraz on IN718	IN718	60	990	5	Good consolidation. UTS = 360MPa

#### 6.4.1 Quasi-isostatic powder interlayer bonding (QUIP) and continuing development

The results of the QUIP trials are presented in section 4.9 with corresponding HIP trial analysis in section 5.3. During Tests 17-20 a new IN718 interlayer material with a sub 50 micron mean particle size was employed with an aim to improving large scale consolidation. It was also felt that the in situ debinding stages had benefited the procedure as a whole and these were subsequently used in these tests.

Initial results for the IN718 - IN718- Ta coated SCMV pairing (Test 17) were disappointing. Fractography of the faying surfaces revealed poor inter particle assimilation, poor large scale consolidation, low effective interfacial area and low interface strength. Little or no adhesion of the powder compact to the uncommon substrate (SCMV in this case) was noted, something that was apparent to a limited degree in all tests performed up to this point. It appeared that the very fine particle size had not helped to aid consolidation. Insufficient temperatures and pressures are the

most plausible explanations for this anomalous behaviour. Nevertheless, this result suggested that the process window for joints with Ti-6-4 would be noticeably separate from that of the SCMV to IN718.

Tests 18 and 20 were perhaps the most promising of the bonds conducted in the investigation up to that point. Powder consolidation was excellent in comparison to all other tests, and Tests 18 was the only test in the investigation at that point to show substantial powder adhesion to the uncommon substrate material (SCMV). These results come in contrast to those of the conventionally formed bond in Test 17. The most obvious reason for this would be the higher pressure conditions imposed during bonding, but the absence of a binder was also important. EDX traverses for the test can be seen in Figure 6.4.1. Direct comparisons between the HIP and QUIP techniques were complicated by misplacement of the tantalum layer in the HIP bond, away from the interface. However, comparisons between the compact microstructures and porosity were favourable; indicating that in terms of powder consolidation the QUIP trial had performed well even under a reduced stress. Parallels can also be drawn between microstructures at the IN718 powder – SCMV substrate interface (Figure 4.9.6 and Figure 5.3.1). A significant degree of coarse precipitation was noted in both tests (though to a greater degree in the HIP bond) which has highlighted PPBs within the compact. Carbide precipitation is the likely explanation given both the high carbon content non-equilibrium SCMV microstructure and the high affinity of IN718 for carbide precipitation. The greater degree of precipitation in the HIP bonds is possibly due to absence of a tantalum coating on the SCMV substrate preventing excessive inter-diffusion. This precipitation was coupled with increased niobium concentrations (Figure 6.4.3) suggesting secondary NbC formation which is common at grain boundaries and PPBs in IN718 [154]. Other research has indicated that oxidation of NbC grain boundary precipitates results in complex brittle niobium oxide formation, which has been linked to a degradation of mechanical properties at high temperature [155]. This behaviour is certainly worth taking into account for future investigations. Also of note is the apparent presence of a film at the interface in the HIP bond. Local EDX analysis of the film was inconclusive due to its very fine nature, but the EDX

traverse presented in Figure 6.4.1 shows a very small reaction zone at this interface which is likely to be linked to this film formation.

Problems with frictional effects during Test 20 were noted and both a redesign of the constraint sleeve (to incorporate a refractive ceramic layer) would be suggested for continuing trials in this area.

## **6.4.2 Effects of interlayers / brazes with IN718 powder**

### **6.4.2.1 Tantalum interlayer**

The placement of the tantalum interlayer in Test 19b still produced results which further highlight its deleterious role when combined with IN718. Continuous fracture of the bond was observed along a distinct intermetallic film at this interface. With reference to the Ni-Ta-Ti ternary phase diagram (Figure 6.4.2); EDX data (Figure 6.4.1) clearly indicates the presence of a body centred tetragonal NiTa intermetallic phase. These brittle phases are known to have a negative effect on mechanical properties in nickel base superalloys [156].

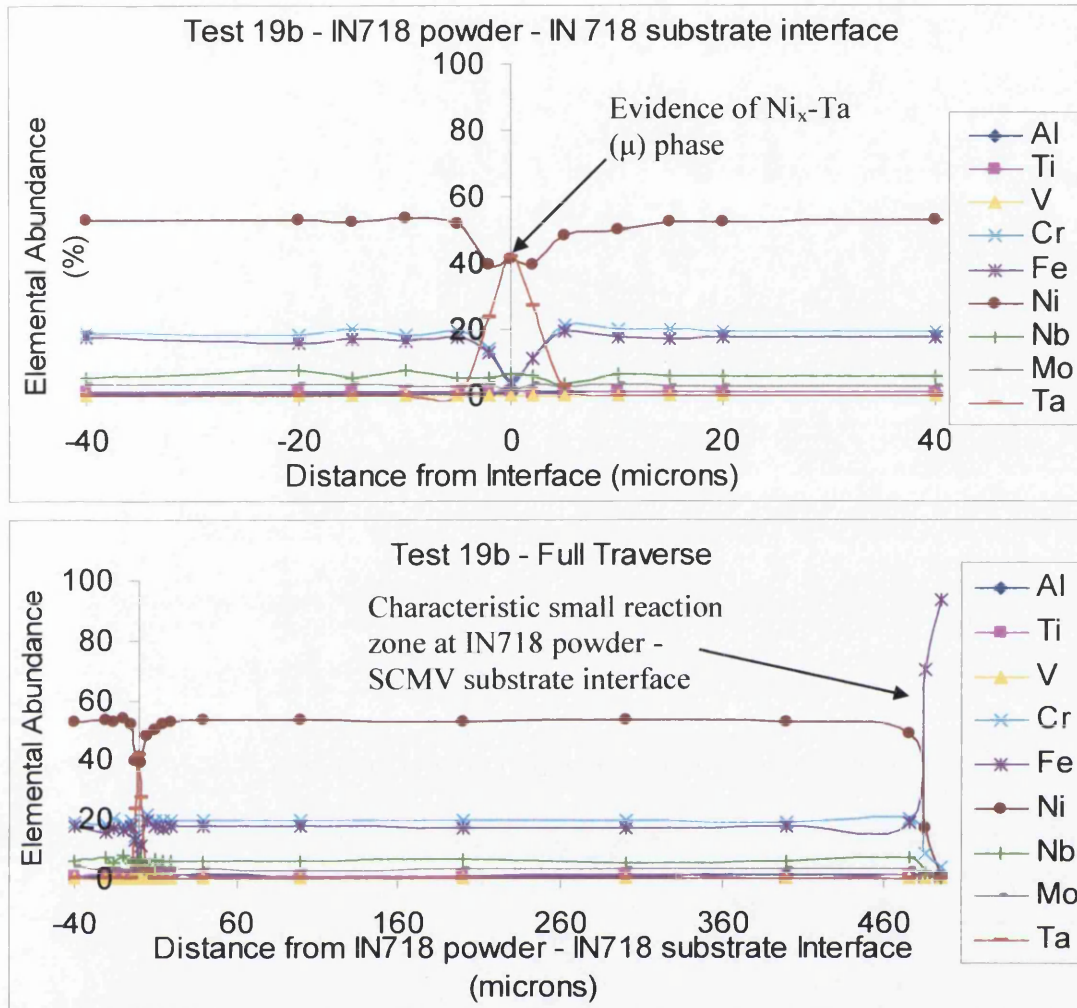


Figure 6.4.1: EDX traverses for Test 19b detailing compositions both at the IN718 powder – IN718 substrate and IN718 powder – SCMV substrate interfaces.

The role of tantalum in Test 18 showed similarities to the behaviour discussed for nickel coatings in Tests 4 and 9. The compositions at the IN718 – tantalum coated SCMV substrate interface presented in Figure 6.4.3 show a tantalum rich migrating zone that has diffused away from the SCMV surface. As in Test 9 the composition of the material immediately adjacent to this tantalum rich zone displays near parent metal properties. Compositions observed in this band suggest that hexagonal C14 laves phase may be present, which is often associated with poor mechanical properties in joints involving IN718 [157].

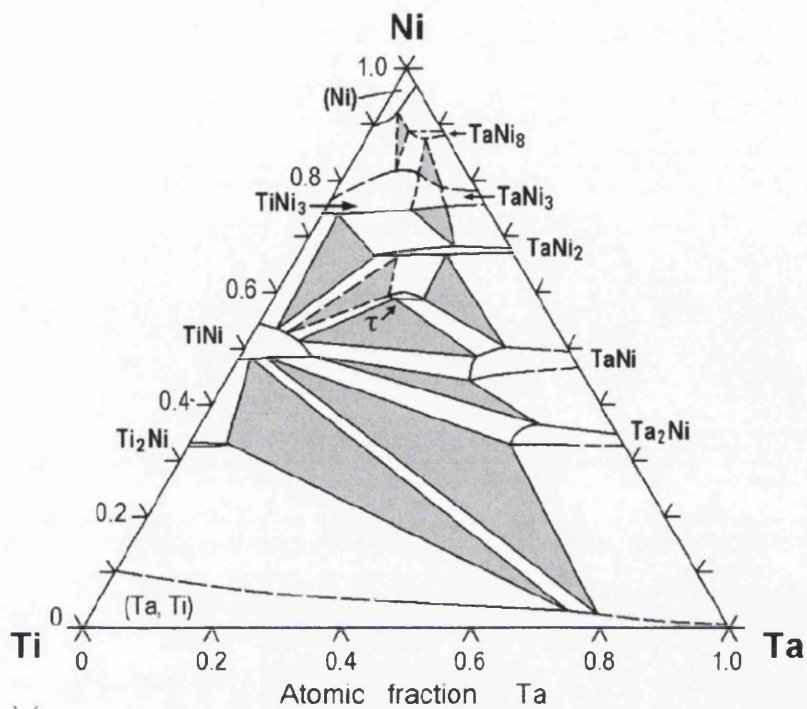


Figure 6.4.2: Isothermal section of the Ni–Ta–Ti system at 927 °C, derived from experimental data [156].

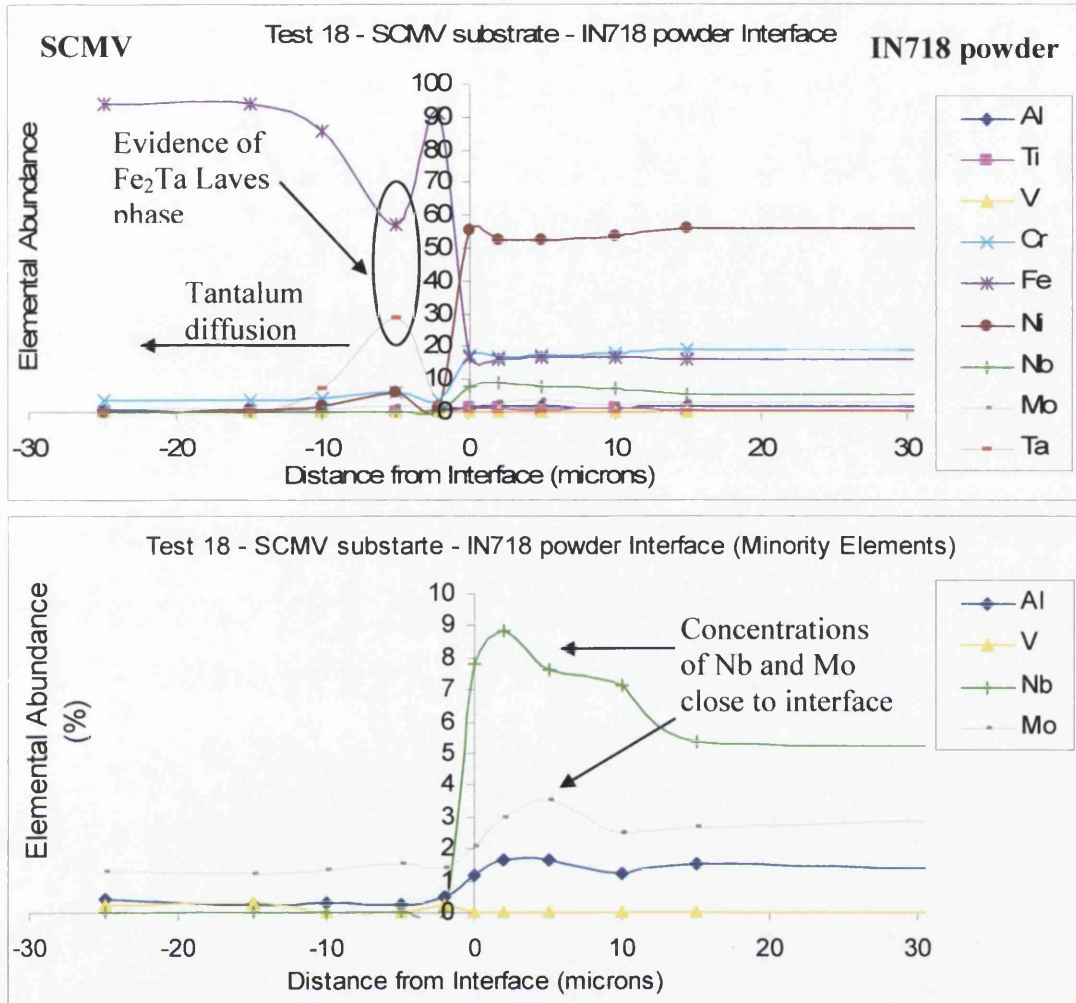


Figure 6.4.3: EDX traverses across the IN718 powder SCMV substrate interface for Test 18.

### 6.4.2.2 Microbraz LM braze

The poor integrity of Tests 18, 20 and 19b coupled with evidence of laves phase formation reinforced concerns raised in the literature as to its negative effect on as welded mechanical properties. Some papers had noted that the use of boron and silicon based brazes had successfully retarded laves phase formation and improved mechanical properties [133, 143]. Microbraz LM was chosen as a coating for IN718 – SCMV bonds because it fulfilled these criteria. Following the trends established for other nickel –



steel joints in the literature, a substantial improvement in joint quality was noted for this group of bonds.

Examples of interface structure and microstructural features are presented in section 2.13. With reference to figure 2.13.2 and 2.13.3 the most prevalent feature of the microstructure was the highly precipitated band occurring within the reaction zone of the IN718 substrate as defined by the EDX traverses Figure 6.4.4. Comparison to the minority EDX traverse reveals that this precipitated zone correlates to increases in local niobium concentrations. This is similar to the precipitation observed at the powder interface of Tests 18 and 19b. However, in Test 28 intragranular rather than grain boundary precipitation predominates. This suggests  $\gamma''$  formation as opposed to Nb carbides. This precipitation provides a plausible explanation for some areas of non-fusion identified at the interface, in that the continuing hardening of the material at temperature prevent the deformation necessary to close these voids.

Evidence of an increased degree of twinning at the interface was also noted in the microstructures. Twinning is common in strained IN718 due to its high stacking fault energies so it would be expected that the highly strained areas of the bond would show more twinning. This has encouraged growth of deleterious  $\sigma$  phase which forms preferentially at the twin boundaries. Increased  $\sigma$  precipitation has also been promoted by the high local concentrations of iron in the reaction zone.

As with most of the trials performed in the investigation the reaction zone in the SCMV is much smaller, with the nickel diffusion zone limited to 40 $\mu$ m. Importantly, though peaks in nickel concentration immediate to the interface are apparent, the high nickel content of the braze layer has not resulted in the bulk nickel diffusion and intermetallic formation noted in the nickel coating trials (Tests 4 and 16). This is likely due to silicon diffusion from the braze layer which was noted in the SCMV. Silicon diffusion was seen to correlate with a local reduction in hardness within the SCMV reaction zone as highlighted on the microhardness traverse presented in Figure 6.4.4. However, this softening was not seen to be significant in subsequent mechanical assessment.

Continual hardening of the SCMV substrate was noted away from the reaction zone which fits well with the HAZ banding effects described in section 4.14. Nevertheless, both the EDX and hardness traverses indicate a much smoother transition between the materials when compared to their tantalum coated counterparts. Finally, none of the analysis conducted on the bonds noted the presence of continuous intermetallic films or deleterious phase evolution, which is one of the primary reasons for the relative success of this specific dissimilar pairing.

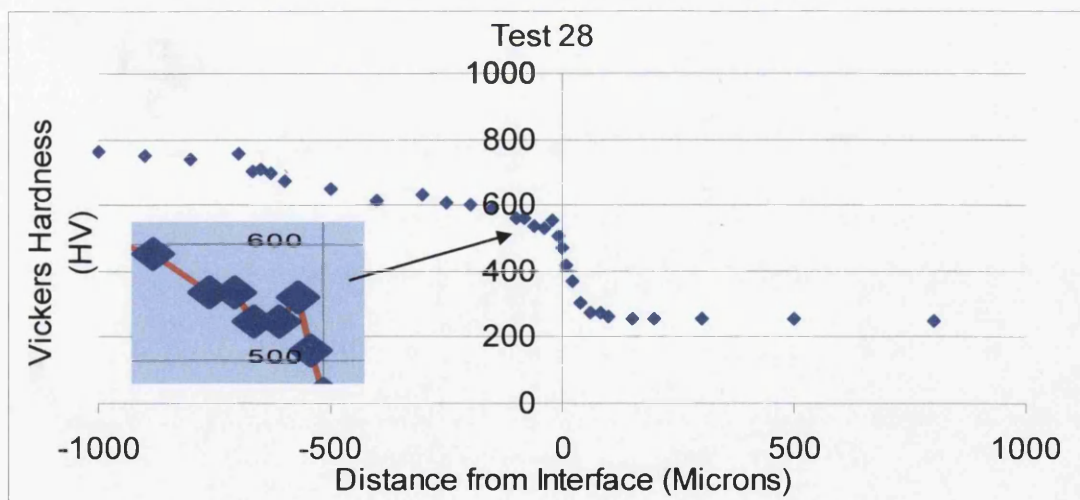
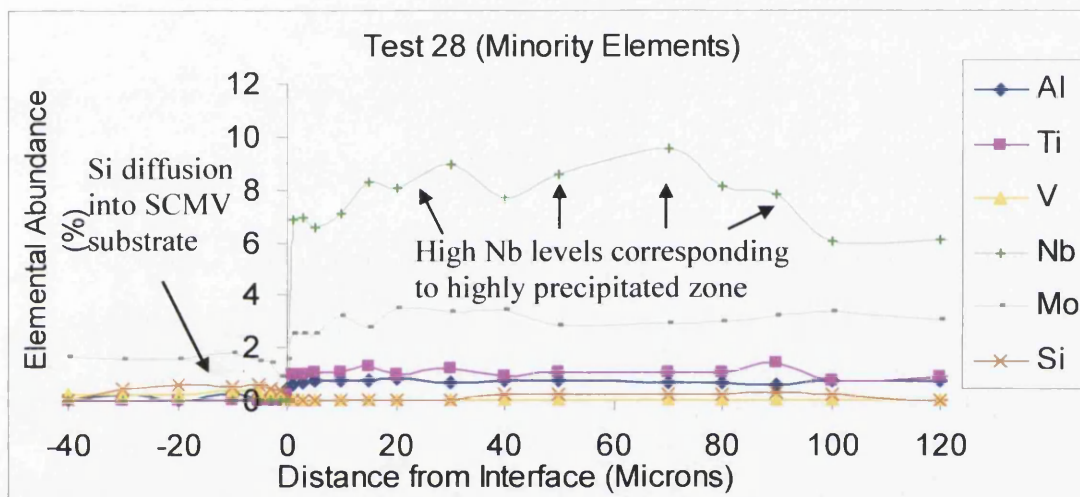
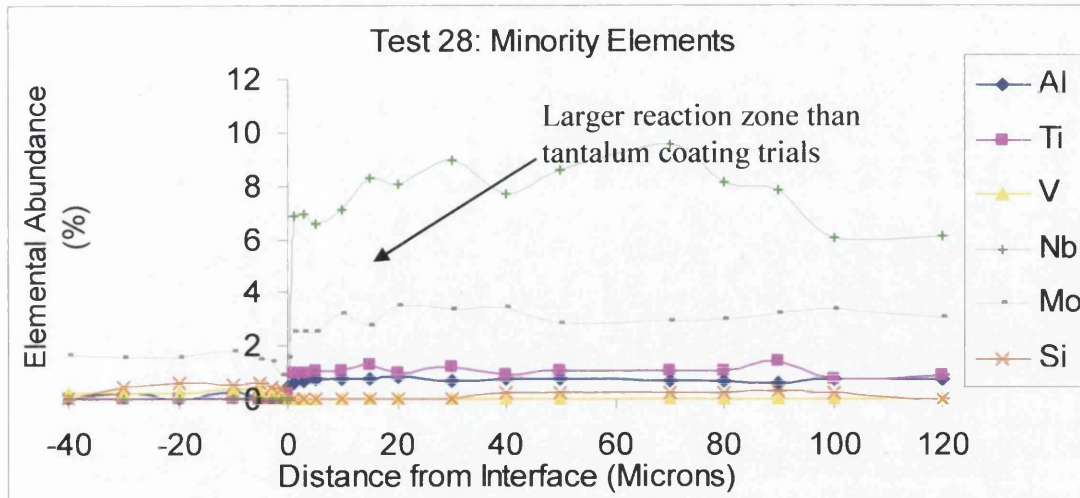


Figure 6.4.4: A comparison between EDX traverses for minority and majority elements and an EDX traverse for Test 28.

Comparative EDX and microhardness traverses for the IN718 powder SCMV substrate interface are presented below in Figure 6.4.5. As observed in Test 18, IN718 compositions remain fairly constant over the IN718 powder – IN718 substrate interface. Iron concentration in the powder compact fluctuates much more, peaking mid way between the two interfaces. These iron levels may account for the increased hardness values some distance away from the compact compared to the parent IN718. Iron diffusion was encouraged by the more diffuse nature of the IN718 powder – SCMV substrate interface compared to that observed in Test 28. The interface composition suggests a  $(\text{Fe-Ni})_2\text{Cr}$  type structure on the boundary of the  $\gamma$  phase field as defined by the ternary phase diagram (Figure 6.3.3), indicating that some peritectoid  $\gamma > \gamma + \alpha'$  decomposition may have occurred on cooling. However, the microhardness traverse across the bond line does not suggest significant evolution of hard, brittle deleterious phases with a similarly smooth transition to that noted in Test 28 (Figure 6.4.4). Furthermore, comparisons between the mechanical performance of this bond and bonds containing no interlayer suggest that this has not degraded mechanical properties.

The more diffuse nature of the powder interlayer bond compared to its non-interlayer counterpart comes in contrast to the results noted previously where reaction zones in powder interlayer bonds were retarded (Table 6.2.2). The three most plausible reasons for this are:

- Increased powder consolidation (improving diffusion paths)
- Increased temperature (increasing atomic mobility)
- The presence of silicon spanning the interface which was found to aid iron mobility in Test 28.

Aside from these differences, there are common features between the interlayer / non-interlayer tests. Dense precipitation coupled with high local niobium concentrations were noted at the powder interface, though encouragingly a lesser degree of twinning and  $\sigma$  precipitation was noted.

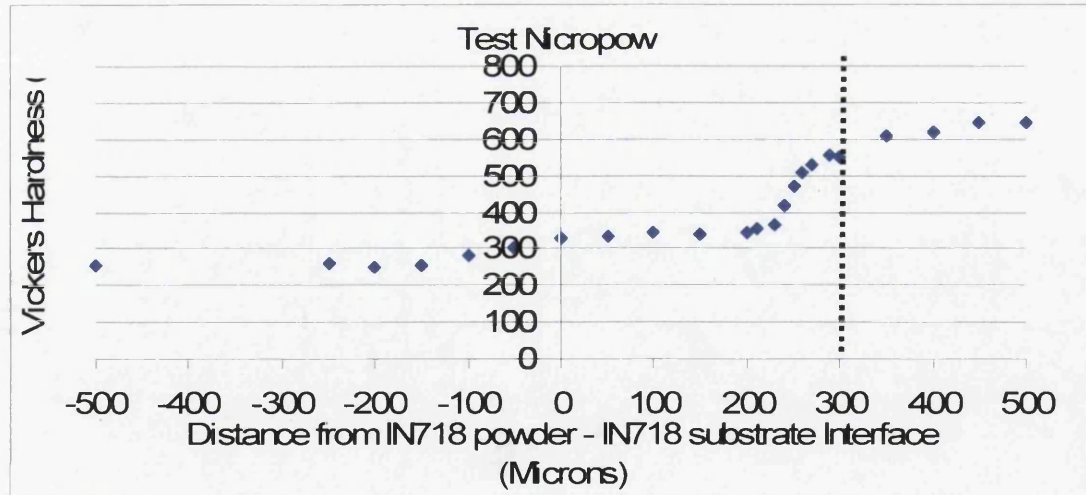
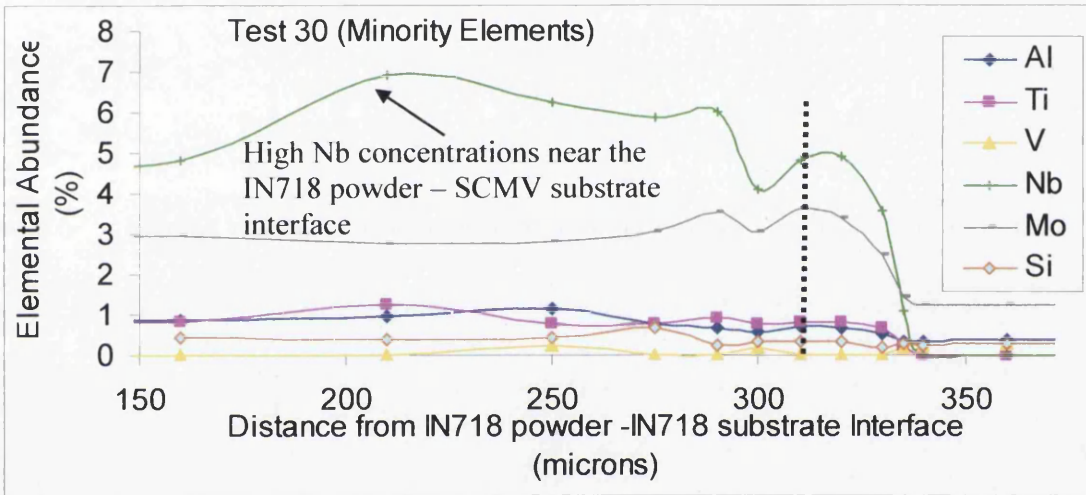
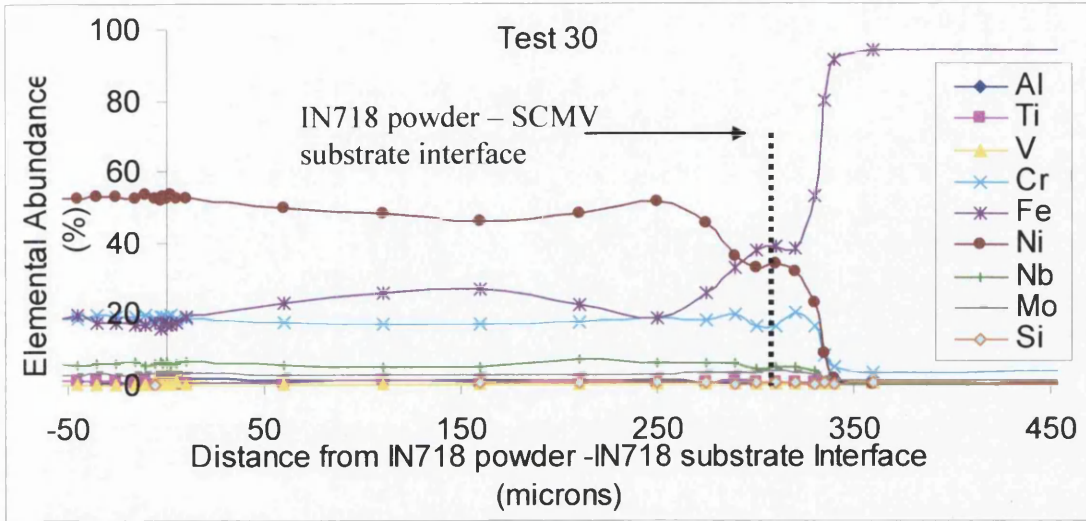


Figure 6.4.5: A comparison between EDX traverses for minority and majority elements and an EDX traverse for Test 30.

### 6.4.3 Mechanical integrity

The improved performance of the Microbraz LM bonds allowed non-standard specimens to be extracted for mechanical characterisation. The results of tensile tests performed on the bonds (Figure 4.14.9 and Table 4.13.5) showed that UTS increased proportionally with increasing bond time and temperature. Aside from one test, modulus values remained consistent over all process conditions. However all bonds exhibited exceptionally poor ductility.

Results from a previous investigation by Chandel *et al* [142] had produced tensile strengths in uniaxially pressed diffusion bonds of up to 720 MPa between IN718 and a martensitic stainless steel. Bonding temperature, time and pressure were 1000°C, 60mins and 40MPa respectively. Due to the non-standard nature of the specimens produced, no valid comparisons can be made between the quoted mechanical properties. Nevertheless, observations made between the data show interesting trends. Solid state bonds produced under comparable conditions in this investigation presented approximately 50% of the properties in [142] in respect of both mechanical strength and ductility. Comparison between this data and the semisolid flash butt weld test is much more favourable, showing very similar bond integrity. SEM analysis of the fracture surfaces revealed some of the areas of non fusion that had also been evident in the microscopy (Figure 4.13.9 and Figure 4.13.10). Whilst the reduction in effective joint area will have had a small effect on tensile strength it is unlikely to have resulted in the 50% relative properties that occurred. Typically, such areas of non fusion are associated with variation in ductility, but do not have the same considerable negative effect on tensile mechanical properties as they do in low cycle fatigue loading regimes [2].

Fundamentally, the only difference between the two investigations was the heating method employed (ambient/ furnace heating vs. localised resistance heating). Considering that the purely solid state bonds produced such poor comparative properties under similar conditions it seems that the heating method must have a significant effect on this outcome. It is significant that the properties of the semisolid

test were much more comparable to that of diffusion bonds produced in [142], despite vastly different process conditions (much shorter time, much higher temperature). This improved performance coupled with its similarity to joints produced by a conventional flash butt welding process imply that resistance heating is much more suited to rapid and intense joining processes for dissimilar materials.

## 6.5 HAZ and macro scale microstructural effects

The microstructural banding apparent on the specimens can be clearly linked to the parabolic heating effect associated with the joining technique. The presence of the bands raises the question as to whether these bands were formed through macro-scale diffusion to up to a point of low mobility. The EDX traverses presented in previous sections show that this is unlikely, with reaction zone size limited to 550 $\mu\text{m}$ . Despite this, localised EDX data was acquired in the banded region of a range of specimens to determine whether there were any local peaks in elemental concentrations. This revealed parent metal compositions in all cases (Appendix 8). Therefore the microstructural changes must have occurred isothermally during the course of the bonding. To better understand these effects the TTT and CCT diagrams, as well as heat treatment and processing principles will be considered in an attempt to both make recommendations for future work, and predict the possible effect of such banding in a successful bonding scenario (e.g. similar resistance bonds).

The band noted in the IN718 substrate materials was found to be caused by dense intragranular precipitation, but little or no coarsening of the intergranular precipitates was noted. The reasons for this can be better appreciated with reference to the IN718 TTT diagram presented in Figure 6.5.1. Though the temperature evolved in the material at the point of the band cannot be accurately quoted, it can be assumed that it is significantly below that measured at the interface (925-990°C). The diagram shows that grain boundary  $\delta$  formation occurs primarily at these interfacial temperatures along with the laves phase that was also formed in the interfacial microstructures. At the lower temperatures experienced away from this interface the TTT diagram shows both  $\gamma''$  and  $\gamma'$  to be the predominant phases evolved. This behaviour is reinforced with

reference to Figure 6.5.2, where the effects of both solution heat treatments and aging are described. The microstructural differences between the more solutioned  $\gamma + \delta$  microstructure noted in the area between the band and the interface (fig 4.14.1) and highly precipitated band at lower temperature conform well to the behaviour described in the diagram. The gradual increase in the density of  $\gamma''$  precipitation followed by its rapid disappearance can be accounted for by the parabolic heating effect which results in increasing thermal gradients with increasing distance from the bond line, but may also be explained by the distinct phase fields associated with material.

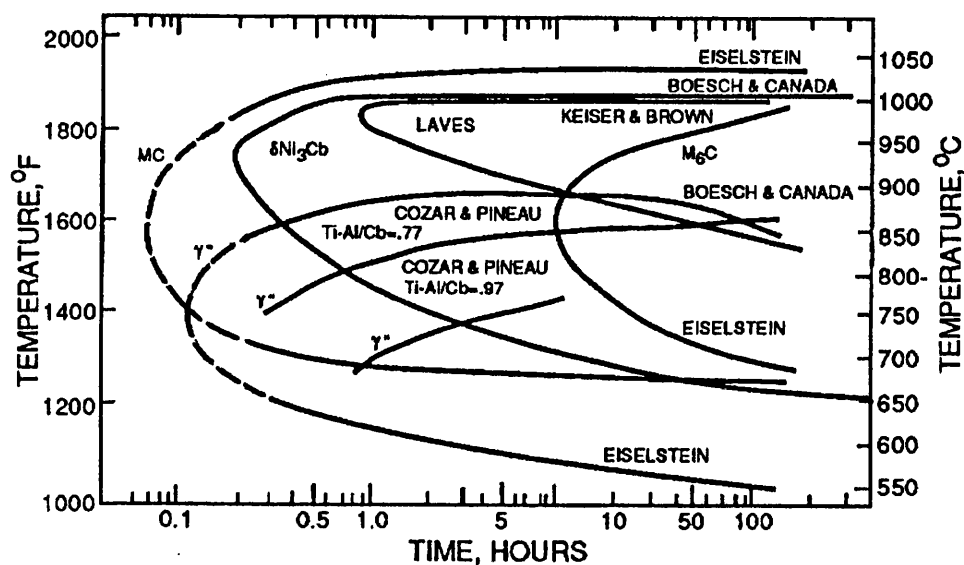


Figure 6.5.1: A TTT diagram for hot rolled IN718 bar [158].



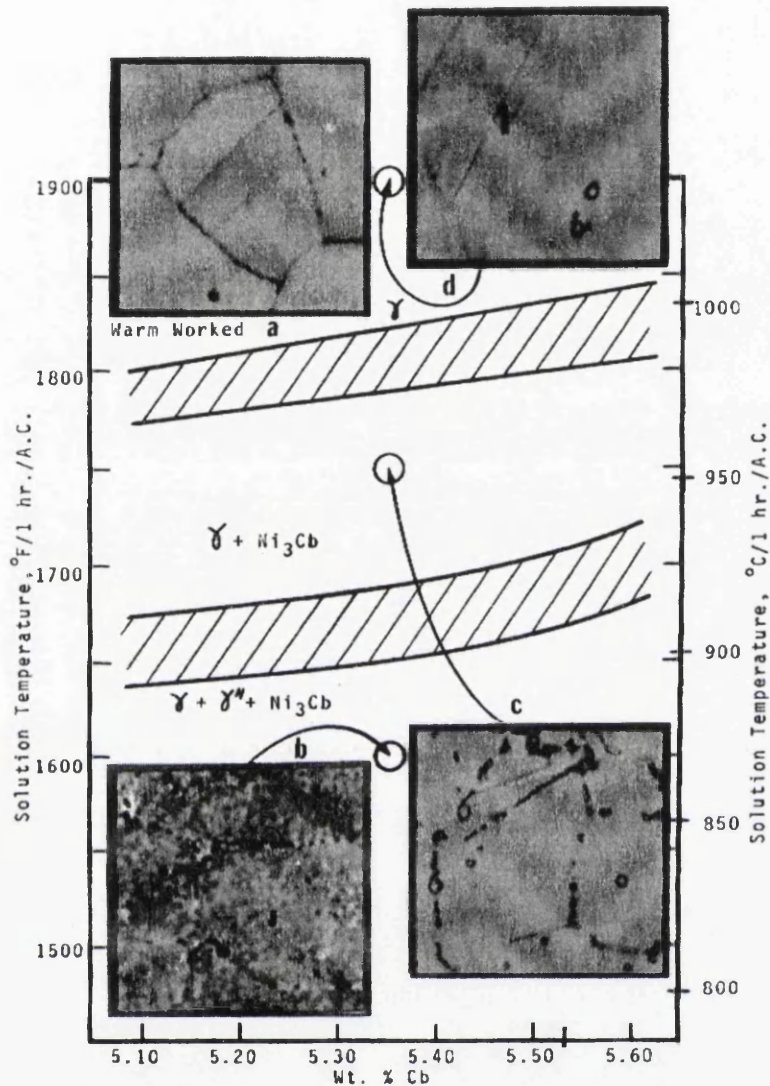


Figure 6.5.2: Phase relationships and the effect of heat treatments in IN718 [158].

With reference to figures 4.14.2 and 4.14.1, the radical changes in the SCMV microstructure and properties are more drastic and less concentrated in nature. All bonds in the SCMV exhibited similar microstructural trends. The fully martensitic lath structure close to the interface briefly gives way to a tempered structure similar to the parent (this microstructural change is mirrored in the microhardness values), before the banded region of what appears to be acicular ferrite dominates the microstructure. This more damage tolerant structure results in the large reduction in local Vickers hardness measured in the band. This softening is likely to be due to the reduced local

temperatures remote of the bond line that were high enough to drive diffusion based growth of the ferrite phase, but not so high as to harden as a result of cooling through  $A_3$ . The microhardness values then recovered to near parent properties further from the bondline as the local temperature drops below levels sufficient to induce microstructural modifications.

Analysis of the rapid semisolid test (29) provided an interesting comparison to the more extended solid state trials. Further analysis of the bond revealed that unlike the other IN718 – SCMV bonds no banding was noted in the IN718 material, but that the HAZ structure in the SCMV was very similar to that of bonds produced at much longer times. This is exemplified by the microhardness traverse of the semi-solid bond presented in Figure 6.5.3. The hardened zone adjacent to the interface shows slightly increased Vickers hardness levels compared to the longer tests, probably a result of the increased temperatures and cooling rates. The expected dip in hardness did occur, but not to the extent observed in the longer tests (where hardness dropped to 250Hv). The non-equilibrium martensitic microstructure maybe driving the rapid transformation close to the interface, however, the lesser degree of softening indicates that slower diffusion based processes are dominating this effect.

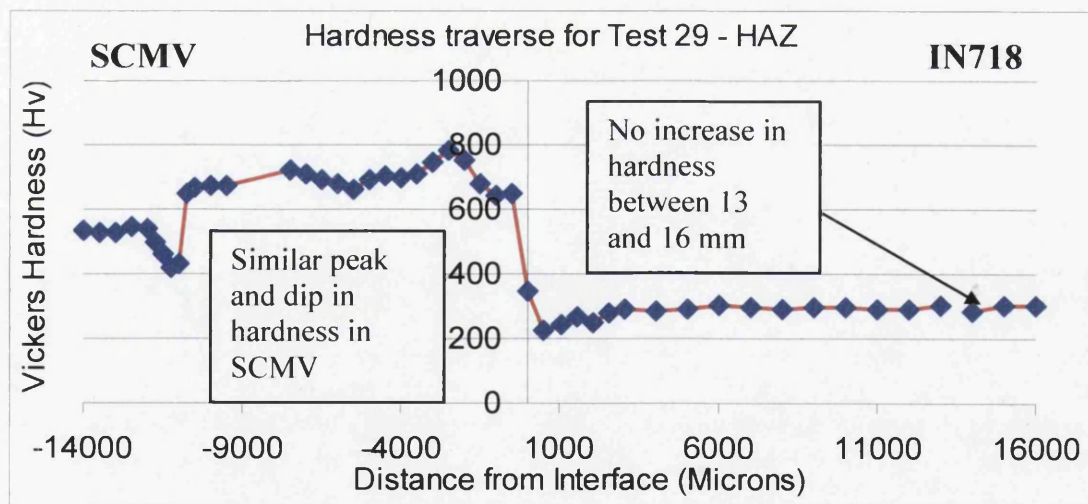


Figure 6.5.3: A hardness traverse the HAZ of Test 29 (rapid, semi – solid condition).

Compared to the heat affected zone in the IN718 and SCMV materials the microstructure of the titanium substrate is considerably more diffuse. Moving from a  $\beta$  annealed structure at the interface, gradually through a recrystallised annealed section and on to a primary  $\alpha$  dominated elongated (unaffected) parent microstructure. The gradual nature of the transition can be accounted for by the wider  $\alpha+\beta$  phase field associated with the alloy, allowing various degrees of  $\alpha$  growth during the isothermal condition. Differing cooling rates would also be experienced during the cooling of the bond with material closer to the copper heat sinks cooling more efficiently than material at the interface. However, specific cooling rates at all positions are hard to gauge on account of the interaction between exponential Newtonian cooling and the proximity of an area on the specimen to the heat sink.

## 6.6 Recommendations for Industrial Employment

Finally, comment should be made concerning the industrial application of the dissimilar alloy bonded pairs characterized during the present investigation.

During the course of this investigation it had come to light that the experimental processes adopted in this investigation were shown to produce bonds of exceptional quality in similar Ti-6246 bonds. These bonds were shown to consolidated fully employing bonding parameters that fell significantly below those required for conventional HIP processes in respect of time, temperature and pressure. This suggests that the process of resistance heated powder interlayer bonding has considerable scope for future industrial employment / commissioning studies for use with similar bonding pairs.

However, based on the results of this investigation, it is difficult to envisage the employment of either Ti-6-4 to SCMV or Ti-6-4 to IN718 joints, whether processed via resistance heating or HIP techniques, for any application where structural integrity is a

design requirement. Furthermore, given the chemical incompatibility demonstrated by the diffusion profiles it appears highly unlikely that process optimisation alone could circumvent these problems in the joint chemistries trialled here.

In the case of resistance heating this is partly due to the vastly different thermo-physical properties between the substrate materials. Under laboratory conditions these problems may be circumvented by the use of current and heat sinks as discussed previously. However, in an industrial scenario, when applied to real components of complex cross section, these techniques are likely to encounter considerable difficulty. These issues represent a fundamental restriction for resistance heating of dissimilar metal pairs in the industrial sector.

IN718 to SCMV bonds performed more encouragingly, both in respect of joint chemistry and thermo-physical properties, and whilst joints conducted via solid state resistance heated powder interlayer bonding are not advised, joining these alloys through more conventional processes (flash butt welding) provides scope for further research and possible future industrial employment.

## 7 CONCLUSIONS

- A viable experimental bonding procedure based on the Gleeble 1500 thermo-mechanical simulator that facilitates resistance heated powder interlayer trials and further process optimisation has been established.
- Refinements to the procedure have been developed allowing close control of new process variables such as interlayer thickness and contamination.
- Bonding trials have been conducted between Inconel 718, Ti-6Al-4V and super CMV steel with tantalum, nickel and Ni-Cr-V diffusion barriers employing Ti-6Al-4V, Inconel 718 and BurTi powder interlayers.
- Bond quality has been shown to be adversely effected by increasing powder particle size.
- Preliminary findings have indicated that in situ debinding procedures can have deliver improvements in bond quality with certain vulnerable material pairings.
- The use of copper impregnated interlayer powders substantially improved powder consolidation characteristics, but resulted in considerable microstructural modification of the Ti-6-4 compact microstructure.
- Inconel 718 – Ti-6Al-4V bond quality was poor in all tests conducted, attributed to NiTi and Ti<sub>2</sub>Ni intermetallic formation at the interface.
- Ti-6Al-4V – SCMV bond quality was poor in all tests conducted, with intermetallic phase formation identified at the interface.
- Transition joints employing BurTi powder interlayer joints and triple layer Ni-Cr-V brazes were found to substantially retard intermetallic phase formation

and reduce reaction zone size in Ti-6Al-4V – SCMV bonds. However, these bonds were still found to fail in a brittle manner.

- Difficulties in bonding dissimilar materials (in particular Ti-6Al-4V to SCMV) in relation to their thermo-physical / electrical properties have been highlighted. The effect has been termed differential heating.
- Materials more similarly matched in these respects have shown the most potential for resistance bonding processes, eg. IN718 to SCMV and IN718 to Ti-6-4.
- Nickel coatings were shown to reduce reaction zone sizes in Ti-6Al-4V – SCMV bonds, but preferentially formed intermetallics that progressively diffuse into the SCMV substrate creating a secondary interface.
- Tantalum coatings severely degrade bond integrity in all alloy combinations leading to the formation brittle intermetallics at the bond interface.
- Brazing trials employing copper coatings between IN718 and Ti-6Al-4V were unsuccessful as a result of intermetallic formation at the interface.
- Bonds employing a Microbraz braze layer have proved the most successful. However bond strengths indicated that better results may be possible using standard welding techniques such as flash butt welding.
- HAZ banding effects related to the parabolic nature of the resistance heating effect have been observed in all resistance bonded specimens. It has been shown that these have a direct effect on mechanical properties and deformation behaviour. However, these can be removed by standard post weld heat treatment techniques.

- Limited use of a novel quasi isostatic bonding technique, indicates substantially improve bond quality. This technique is now being adopted in ongoing investigations into powder interlayer joining of similar titanium aluminide material.

## 8 RECOMMENDATIONS

### 8.1 Further Experimental design and process optimisation

During the course of this investigation it was suggested that a concise, robust experimental design be employed in the case of further experimentation on more successful alloy pairings. It was proposed that further experimentation should be focussed on process optimisation. The factors under investigation should be the three fundamental variables of bonding; time, temperature and force/pressure. It was recommended that bond integrity for each of these preliminary bonds should be assessed by means of low cycle fatigue testing, due to its ability to elucidate defects through fatigue crack initiation. Subsequent to this a full array of mechanical tests (tensile, fatigue, torsion and Charpy impact testing) could be performed on bonds produced using the optimised process variables. This design could then be employed with an aim to producing statistically comparable, representative results.

A factorial experimental design was prepared at the beginning of the investigation; however, the poor quality of the bonds produced meant the matrix was soon abandoned. It was envisaged that it would enable a full statistical approach to the optimisation process. The design requires each variable to be tested at four different levels. This allows for the occurrence of non-linear interactions between the parameters. Finally the test order is randomised to avoid any false interactions that might occur by performing similar tests sequentially. Table 2.4.1.1 shows the detail of the design. The coded values have been included because they most clearly represent the design as a whole. A, B and C represent the variables of time, temperature and force respectively. The appearance of their lower case counterparts in the far left column indicates that their levels are set high.



Table 8.1.1: The full statistically based testing matrix for optimisation of all bonding pairs.

	Actual Values			Coded values			Test Order
	Time (min)	Temperature (°C)	Force (KN)	A	B	C	
-	24	910	0.84	-1	-1	-1	7
A	51	910	0.84	1	-1	-1	12
B	24	940	0.84	-1	1	-1	14
Ab	51	940	0.84	1	1	-1	2
C	24	910	1.7	-1	-1	1	1
Ac	51	910	1.7	1	-1	1	3
Bc	24	940	1.7	-1	1	1	8
Abc	51	940	1.7	1	1	1	13
0	37	925	1.25	0	0	0	4
ap1	15	925	1.25	-1.68	0	0	9
ap2	60	925	1.25	1.68	0	0	5
bp1	37	900	1.25	0	-1.68	0	11
bp2	37	950	1.25	0	1.68	0	15
cp1	37	925	0.5	0	0	-1.68	10
cp2	37	925	2	0	0	1.68	6

The envelope for the range of values for each variable has been established with reference to previous research conducted by Pleydell-Pearce [4] and Tuppen [3]. Neither the effect of powder interlayer thickness nor atmospheric pressure was meant to be studied at the preliminary stage of the investigation, since powder interlayer thickness was envisaged constant at 500µm and all tests were carried out under hard vacuum ( $10^{-5}$  mbar).

A modified variant of this experimental design is now being implemented in an investigation of similar Ti-6246 powder interlayer bonds, following on from the work by Forsdike [149]. Early signs are that the optimised bonds produced match parent metal mechanical properties in both monotonic and cyclic loading regimes.

## **8.2 Further dissimilar bonding trials**

It is recommended that further investigation into powder interlayer bonding between Ti-6Al-4V and SCMV or IN718 should not be attempted under resistance heating conditions without considerable modifications to the experimental technique (see section 7.3). This is primarily on account of the differential heating effect, which has been shown to adversely affect powder consolidation and effect interfacial contact area. Indications that electromagnetic fields may promote intermetallic phase formation in alloy combinations known to be prone to their formation also detracts from the possibility of using resistance heating. Nevertheless, it must be acknowledged that it was not possible to explore all avenues in respect of intermediate joint chemistry and further work examining a wider range of chemistries may yield more promising results. It is recommended that interlayers with significant mutual solubility of both parent base elements are prioritised if this work is to be initiated.

In contrast, the scope for development of IN718 to SCMV is slightly more optimistic. Early trials have shown that bonds of moderate strength can be produced in conventional diffusion bonds and powder interlayer bonds between the two alloys. However, the most successful parameters for bonding more closely resemble a flash butt welding technique, which should be prioritised for any further assessment.

## **8.3 Revisions for the resistance heating technique**

Resistance heating has been shown to provide exceptional solid state bond quality with relative ease compared to conventional processes in both the standard diffusion bonding and the powder interlayer variants. However, these successful trials have been conducted on similar material pairs or dissimilar alloys within a particular group. This investigation has highlighted that this is not the case for vastly dissimilar metal systems, where differential heating leads to poor joint quality and non-uniform heat affected zones. These factors must be taken into account when considering resistance heated solid state bonding for industrial applications, as overcoming them would

involve adding considerable complexity and cost to the process (two primary factors which have generated much of the industrial interest in this technique to date).

#### **8.4 Quasi isostatic powder interlayer bonding**

Whilst only simplified trials of this technique were conducted during the investigation the technique showed scope for further development. It was shown to substantially improve powder consolidation and overall bond quality in material pairs shown to be incompatible under other resistance heated techniques. For this reason it was suggested during the course of the investigation that the process could be developed further by its application to more compatible bonding pairs. Subsequently the technique has been adopted as part of an investigation into similar powder interlayer joints in  $\gamma$  titanium aluminide alloy Ti-45 -2 -2, which is ongoing and remains unpublished at present.

## 9 REFERENCES

1. J.M.Khoury, J.P.K. *Recent Experience in Dissimilar Metal Weld Failures*. in *International Conference on Boiler Tube Failures in Fossil Plants*. 1997. Nashville, Tennessee: EPRI.
2. Pleydell-Pearce, C., *Resistance Bonding of the Dissimilar Titanium Alloys Ti-6-4 and Ti-6246*, in *Materials Engineering*. 2005, Swansea University.
3. Tuppen, S.J., *Resistance Bonding of Titanium Based Areospace Alloys*, in *Materials Research Centre*. 2004, Swansea University: Swansea.
4. Broede, J., *Titanium Rotors in Military Aero Engines - Designed to Weight and Life*, in *Presented to the AVT Specialists Meeting 7 - 11 May 2001*, MTU Aero Engines: Loen, Norway. p. 12 Available at <http://www.enginemonitoring.org/publications/loenbde.pdf>
5. Y. Ikeda, H.Y., Y. Tanaka. *Production and Properties of SuperClean MonoBlock LP Turbine Rotor Forgings*. in *Clean Steel: Superclean Steel* 1996. London, UK: IOM.
6. *MatWeb Online Materials Database* [www.matweb.com](http://www.matweb.com).
7. [cited 2006; Data Sheets Courtesy of Timet Plc]. Available from: [www.timet.com](http://www.timet.com).
8. Evans, W.J., *Gas Turbine Materials*, in *Swansea University IRC Information Booklets*. 2006.
9. N. Stanford, P.S.B., *Crystallographic Variant Selection in Ti-6Al-4V*. *Acta Mater*, 2004. **52**: p. 5215-5224.
10. D. Bhattacharyya, G.B.V., S.C. Vogel, D.J. Williams, *A study of the Mechanism of Alpha to Beta Phase Transformation by Tracking Texture Evolution with Temperature in Ti-6Al-4V using Neutron Diffraction*. *Scripta Mat*, 2006. **54**: p. 231-236.
11. O.M. Ivanshishin, S.L.S., P.E. Markovsky, *Grain Growth and Texture Evolution in Ti-6Al-4V during Beta Annealing under Continuous Heating Conditions*. *Mat Sci and Eng*, 2002. **A377**: p. 88-96.
12. Lutjering, G., *Influence of Processing on Microstructure and Mechanical Properties of (alpha +beta) Titanium Alloys*. *Mat Sci and Eng*, 1998. **A243**: p. 32-45.
13. Albrect, J., *Comparing Fatigue Behaviour of Titanium and Nickel-Based Alloys*. *Mat Sci and Eng A*, 1999. **A263**: p. 176-186.
14. C.T. Sims, W.C.H., *The Superalloys*. 1972: John Wiley & Sons. 15-20.
15. Duranand-Charre, M., *The Microstructure of Superalloys*. 1997: Gordon and Breach Science.
16. Sims, C.T., ASME Technical Publication No. 70-GT-24, May 1970.
17. Orowan, E. *Symposium on Internal Stress in Metals and Alloys in The Institute of Metals*. 1948. London, United Kingdom.
18. Cone, F.P., *Observations on the Development of Delta Phase in IN718 Alloy, in Superalloys 718, 625, 706 and Various Derivatives*, E.A. Loria, Editor. 2001, TMS. p. 323 - 332.
19. *Vacuum Induction Melting Technology*. TechCommentary (Centre for Metals Processing), 1987. 3(3).

20. Haynes, W.S.a.A.G., *The Temperature of formation of martensite and bainite in low alloy steel*. JISI, 1965. **203**: p. 721-727.
21. Libsch, G.K.a.J.F., *Phase Diagrams in Ceramic, Glass and Metal technology*, ed. A. Alper. 1970, New York: Academic Press.
22. S. Morito, X.H., T. Furuhashi, *The Morphology and Crystallography of Lath mArtsite in Alloy Steels*. Acta Mater, 2006. **54**: p. 5323-5331.
23. Bain, M.A.G.a.E.C., *Principles of Heat Treatment*. 5th ed. 1964: American Society for Metals
24. M.Atkins, *Atlas of Continuous Cooling Transformation Diagrams for Engineering Steels*. Rev US ed. British Steels Corp. 1980: American Society for Metals.
25. R.A. Grange, C.R.H.a.L.F.P., *Hardness of Tempered Martensite in Carbon and Low-Alloy Steels*. Met Trans A, 1977. **8A**: p. 1775-1785.
26. P. Bocquet, A.C.a.R.D. *Recent Developments in High Pressure Vessles for the Petrochemical Industry: Materials and Products*. in *Clean Steel: Superclean Steel*. 1995. London, UK: IOM.
27. Tomita, Y., *Improved Fracture Toughness of Ultrahigh Strength Steel through Control of Non-Metallic Inclusions*. Journal of Materials Science, 2004. **28**(4): p. 853-859.
28. A.D. Batte, J.M.B., S.R. Holdsworth, J. Myers and P.E. Reynolds, *The Effects of Residual Elements and Deoxidation Practice on the Mechanical Properties and Stress Relief Cracking Susceptibility of 1/2%CrMoV Turbine Castings*. Phil, Trans. R. Soc. Lond, 1980. **A 295**: p. 253-264.
29. Kiessling, R. *Clean Steel - A debatable concept*. in *Clean Steel*. 1981: The Metals Society.
30. Ford, T., *Mainshafts for the Trent*. Aircraft Engineering and Aerospace Technology, 1997. **69**(6): p. 555-560.
31. W. Betz, B.B., W. Track. *Comparative Assessment of PM Materials for Turbine Disks*. in *Superalloys 1980 - Proc. 4th Int. Conf. on Superalloys*. 1980. Seven Springs. Pasadena. US: ASM.
32. Mitchell, R.J., *Development of a New Powder Processed Ni-Base Superalloy for Rotor Disc Application*, in *Materials Engineering*. 2004, Cambridge University: UK. p. 210.
33. Eksi, A., *Effects of Powder Hardness and Particle Size on the Densification of Cold Isostatically Pressed Powders*. Turk J. Eng. Env. Sci, 2002. **26**: p. 377-384.
34. J. Ma, L.C.L., *Effect of Particle Size Distribution on Sintering of Agglomerate-free Submicron Alumina Powder Compacts*. Journal of the European Ceramics Society, 2002. **22**: p. 2197-2208.
35. T. Hartwig, G.V., F. Petzoldt, H. Kunze, *Powders for Metal Injection Molding*. Journal of the European Ceramics Society, 1998. **18**: p. 1211-1216.
36. Lawley, A., *Atomization: The Production of Metal Powders*. 1 ed. 1992: Metal Powder Industries Federation. 11-34.
37. Hausner, H.H., *Handbook of Powder Metallurgy*. 1st ed. 1973, New York: Chemical Publishing Inc. 144-271.

38. J.R. Groza, A.Z., *Sintering Activation by External Electrical Field*. Mat Sci and Eng, 2000. **A287**: p. 171-177.
39. R. Kalyanaraman, S.Y., R.J. Dowding, *Synthesis and Consolidation of Iron Nanopowders*. Nanostructured Materials, 1998. **10(8)**: p. 1379-1392.
40. Kornysushin, Y.V., *Influence of EXternal Magnetic and Electric Fields on Sintering Structure and Properties*. Journal of Materials Science, 1980. **15(3)**: p. 799-801.
41. J.R. Groza, R.J.D., *Nanoparticulate Materials Densification*. Nanostructured Materials, 1996. **7(7)**: p. 749-768.
42. V.Y. Kodash, J.R.G., G. Aldica, *Field-activated Sintering of Skutterudites*. Scripta Mat, 2007. **57**: p. 509-511.
43. J.M. Montes, J.A.R., E.J. Herrera, *Thermal and Electrical Conductivities of Sintered Powder Compacts*. Powder Metallurgy and Metal Ceramics, 2003. **46(3)**: p. 251-257.
44. A. Zavaliangos, J.Z., M. Krammer, *Temperature Evolution during Field Activated Sintering*. Mat Sci and Eng, 2004. **A379**: p. 218-228.
45. K.R. Anderson, J.R.G., M. Fendorf, *Surface Oxide Debonding in Field Assisted Powder Sintering*. Mat Sci and Eng, 1999. **A270**: p. 278-282.
46. J.E. Garay, Z.A.M., *Enhanced Growth of Intermetallic Phases in the Ni-Ti System by Current Effects*. Acta Mater, 2003. **51**: p. 4487-4495.
47. W. Chen, J.E.G., Z.A. Munir, *Fundamental Investigations on the Spark Plasma Sintering/Synthesis Process 1. Effect of DC pulsing on Reactivity*. Mat Sci and Eng, 2005. **A394**: p. 132-138.
48. Conrad, H., *Thermally Activated Plastic Flow of Metals and Ceramics with an Electric Field or Current*. Mat Sci and Eng, 2002. **A322**: p. 100-107.
49. Various, *Powder Metallurgy*. 9th ed. Metals Handbook, ed. E. Klar. Vol. 7. 1984, Ohio USA: ASM. 897.
50. J. Alcock, D.S. (1996) *The Powder Injection Moulding Process*. Materials World **Volume**, 629-630 (<http://www.azom.com/details.asp?ArticleID=1080>)
51. Froes, F.H., *Advances in Titanium Metal Injection Moulding*. Powder Metallurgy and Metal Ceramics, 2007. **46(5-6)**: p. 303-310.
52. [www.sparta.co.uk/casting.htm](http://www.sparta.co.uk/casting.htm). SPARTA Casting Ltd 2006 [cited 2006 November].
53. Kent, J.D.G.S.a.J.S., *Prediction of Ship Brittle Fracture Casualty Rates by a Probabilistic Method* Marine Structures, 2004. **17**: p. 575 - 589.
54. Szekeres, W.F.S.E.F.N.a.E.F., *A Study of Weld Interface Phenomena in Low Alloy Steel*. Welding Journal, 1976. **Sept**: p. 260 - 268.
55. Kirkendall, E.O., *Diffusion of Zinc in Alpha Brass*. Trans. AIME, 1942. **147**.
56. Bhadeshia, S.Y.Y.a.H.K.D.H. *M<sub>4</sub>C<sub>3</sub> Precipitation in Fe-C-Mo-V Steels and its Relationship to Hydrogen Trapping*. in Proc. R. Soc A. 2006.
57. Mathew, S.L.M.a.M.D., *Creep of Austenitic Stainless Steel Welds*. Bulletin of Materials Science, 1995. **19(6)**: p. 985-1007.
58. T. Mohandas, G.M.R., *A Comparative Evaluation of Gas Tungsten and Shielded Metal Arc Welds of Ferritic Stainless Steel*. Materials Processing Technology, 1999. **94**: p. 133-140.

59. S.D. Meshram, T.M., G. Madhusudhan Reddy, *Friction Welding of Dissimilar Pure Metals*. Materials Processing Technology, 2007. **184**: p. 330-337.
60. N.C. Sekhar, R.C.R., *Power Beam Welding of Thick Section Nickel Base Superalloys*. Science and Technology of Welding & Joining, 2002. **7**: p. 77-87.
61. Q. Yunlian, D.J., H.Quan, *Electron Beam Welding, Laser Beam Welding and Gas Tungsten Arc Welding of Titanium Sheet*. Mat Sci and Eng A, 2000. **A280**: p. 177-181.
62. R. Rogeon, P.C., J. Costa,, *Characterization of Electrical Contact Conditions in Spot Welding Assemblies*. Journal of Materials Processing Technology, 2008. **195**: p. 117-124.
63. S. Aslanlar, A.O., U. Ozsarac, *Welding time effect on mechanical properties of Automotive Steel in Electrical Resistance Spot Welding* Materials & Design 2008. **29**: p. 1427-1431.
64. Kahraman, N., *The Influence of Welding Parameters on the Joint Strength of Resistance Spot-Welded Titanium Sheets*. Materials & Design, 2007. **28**: p. 420-427.
65. M. Mavromihales, J.M., W. Weston, *A Case of Reverse Engineering for the Manufacture of Wide Chord Fan Blades (WCFB) used in Rolls Royce Aero Engines*. Materials Processing Technology, 2003. **134**: p. 279-286.
66. B. Derby, E.R.W., *A Theoretical Model of Diffusion Bonding*. Metal Sci, 1982. **16**: p. 42.
67. A. Hill, E.R.W., *Modelling Solid State Diffusion Bonding*. Acta Metall, 1989. **37**: p. 2425-2437.
68. Ashworthy, M.A., *Basic Mechanisms and Interface Reactions in HIP Diffusion Bonding*. Materials & Design, 2000. **21**: p. 351-358.
69. Pilling, J., *The Kinetics of Isostatic Diffusion Bonding in Superplastic Materials*. Mat Sci and Eng 1988. **100**(1-2): p. 137-144.
70. Y. Takahashi, M.T., *Effect of Surface Asperity on Interfacial Contact Process Control by Power Law Creep-Numerical Study of Viscoplastic Adhereing Process*. J.Eng Mater. Tech ASME, 1995. **117**(3): p. 330-335.
71. Y. Takahashi, M.T., *Experimental Study Of Interfacial Contacting Processes Controlled By Power Law Creep*. J.Eng Mater. Tech ASME, 1995. **117**(3): p. 336-340.
72. M.J. Cox, R.W.C., M.J. Kim, *Interface Nanochemistry effects on Stainless Steel Diffusion*. Met Trans A, 2002. **33**(2): p. 437-442.
73. H. Somekawa, H.W., T. Mukai, *Low Temperature Diffusion Bonding of Superplastic AZ31 Magnesium Alloy* Scripta Mat, 2003. **48**(9): p. 1249-1254.
74. Y. Takahashi, T.N., K., Nishiguchi, *Dissolution Process of Surface Oxide Film during Diffusion Bonding of Metals*. Journal of Materials Science, 1992. **27**: p. 485-498.
75. A.A. Shirzadi, H.A., E.R. Wallach, *Interface Evolution and Bond Strength when Diffusion Bonding Materials with Stable Oxide Films*. Surface and Interface Analysis, 2001. **31**: p. 609-618.
76. Gale, W.F., *Applying TLP Bonding to the Joining of Structural Intermetallic Compounds*. Journal of Minerals, Metals and Materials Society, 1999. **51**(2): p. 49-52.

77. A.A. Shirzadi, E.R.W. *A New Method to Diffusion Bond Superalloys*. in *The Microstructure & Performance of Joints in High Temperature Alloys*. 2002. London: Institute Of Materials, Minerals and Mining.
78. A.A. Shirzadi, E.R.W. *Diffusion Bonding*. 2007 [cited; Available from: <http://www.msm.cam.ac.uk/phase-trans/2005/Amir/bond.html>].
79. Schwartz, M.M., *Modern Metal Joining Techniques*. 1969: John Wiley and Sons. 370-401.
80. Callister, W.D., *Fundamentals of Materials Science and Engineering*. 5th ed, ed. W. Anderson. 2001: John Wiley and Sons. p. 216.
81. J. Jellison, F.Z., *Solid State Welding*, in *Metals Handbook*, J.R. Davies, Editor. 1983, ASM. p. 673 - 691.
82. Jr, R.W.M., *Joining of Materials and Structures - From Pragmatic Process to Enabling Technology*. 1st ed. 2004: Elsevier - Butterworth Heinemann. p.332 - 336.
83. T. Kuroda, K.I., H. Ikeda, *Flash Butt Resistance Welding for Duplex Stainless Steels*. Vacuum - Surface Engineering, Surface Instrumentation and Vacuum Technology, 2006. **80**: p. 1331-1335.
84. Goldsberry, C., *Resistance Welding Technology Advances*, in *Penton's Welding Magazine*. 2007.
85. Kanne, W.R. *Solid-State Resistance Upset Welding: A Process with Unique Advantages for Advanced Materials*. in *2nd Advanced Joining Technologies for New Materials*. 1994. Florida: AWS.
86. Kanne, W.R., *Resistance Upset Welding For Vessel Fabrication*, J.D. Meeting, Editor. 1992: Aldermarston, UK.
87. Kanne, W.R., *Solid-State Resistance Welding of Cylinders and Spheres*. Welding Journal, 1986. **65**(5): p. 33-38.
88. M.B.D. Ellis, T.G.G., *Bonding of SiC Fibre Reinforced Ti-6Al-4V MMC Sheet by Resistance Heating*. TWI Journal, 1998. **7**(4): p. 685-719.
89. S. Ukai, M.F., *Perspective of ODS Alloys Application in Nuclear Environments* Journal of Nuclear Materials, 2002. **307 - 311**: p. 749-757.
90. B.J. Eberhard, J.W.K., *High Current Resistance Welding of Nuclear Waste containers*. Welding Journal, 1982. **61**(6): p. 15-19.
91. M. Koizumi, M.N., *Isostatic Pressing Technology and Applications*. 1991: Elsevier Applied Science. p.259-263.
92. E. Rigal, G.L.M., T. lechler, G. Reimann, *Development of FM Steels Diffusion Bonding TEchnologies for Blanket Manufacturing Applications*. Fusion Engineering and Design, 2000. **49 - 50**: p. 651-656.
93. K. Bhanumurth, R.S.-F., *Solid-State Reaction Bonding of Silicon Carbide below 1000C*. Mat Sci and Eng A, 1996. **A220**: p. 35-40.
94. M. Holmquist, V.R., B. Pettersson, *Tensile and Creep Properties of Diffusion Bonded Titanium Alloy IMI 834 to Gamma Titanium Aluminide IHI alloy 01A*. Acta Mater, 1999. **47**(6): p. 1791-1799.
95. Kurt, B., *The interface Morphology of Diffusion Bonded Dissimilar Stainless Steel and Medium Carbon Steel Couples*. Journal of Materials Processing Technology, 2007. **190**: p. 138-141.



96. L. Jianguo, L.H., R. Soremark, *Joining Ceramics of Different Biofunction by Hot Isostatic Pressing*. Journal of the American Ceramics Society, 1993. 76(10): p. 2685-2686.
97. Y. Zhang, D.F., X. Chen, *Progress in Joining Ceramics*. Journal of Iron and Steel Research, International, 2006. 13(2): p. 01-05.
98. A.D. Ivanov, S.S., G. Le Marois, *Evaluation of Hot Isostatic Pressing for Joining Fusion Reactor Structural Components*. Journal of Nuclear Materials, 2000. 35-42: p. 283-287.
99. B.R. Garret, G.F.B., A.J. Ranadive, *Broad Applications of Diffusion Bonding*, in *Available from [www.ntrs.nasa.gov](http://www.ntrs.nasa.gov)*. 1966, NASA.
100. B. Vamsi Hrishna, P.V., K. Prasad Rao, *Solid State Joining of Steel-Cu P/M Preform Tubes: Use of Interlayer and Post Joining Heat Treatments*. Journal of Materials Science, 2006. 41: p. 1175-1185.
101. J.Fan, C.L., X. Shi, *Joining of Mo to CoSB<sub>3</sub> by Spark Plasma Sintering by Inserting a Ti Interlayer*. Materials Letters, 2004. 58: p. 3876-3878.
102. B. Vamsi Krishna, K.P., K. Prasad Rao, *Improved Weld Strength of P/M Bimetallic Tubes and Transition Joints by Means of Nano-Interlayer Particles*. Mat Sci and Eng, 2005. A394: p. 277-284.
103. S.F. Gnyusovin, S.N.K.K., *Low-Temperature Diffusion Bonding of Plastically Deformed Molybdenum*. Welding International, 2004. 18: p. 557-561.
104. Fedyanin, V.S., *Using Powder Interlayers in Pressure Welding*. Welding International, 2003. 17(4): p. 324-327.
105. T. Matsubara, T.S., K. Uenishi, K.F. Kobayashi, *Fabrication of a Thick Surface Layer of Al<sub>3</sub>Ti on Ti Substrate by Reactive-Pulsed Electric Current Sintering*. Intermetallics, 2000. 8: p. 815-822.
106. Z. Tatli, D.P.T., *Joining of Silicon Nitride using Coating Technology*. Surface and Coatings Technology, 2005. **In press**.
107. Matsoura, K., *Joining of Nickel Aluminate to Steel by Reactive Sintering*. Metal Powder Report, 1999. 54(2): p. 41.
108. Lenel, F.V., *Liquid Phase Sintering*, in *Metals Handbook*, J.R. Davies, Editor. 1984, ASM. p. 316-321.
109. W.D. Macdonald, T.W.E., *Transient Liquid Phase Bonding*. Annu, Rev. Mater. Sci, 1992. 22: p. 23-46.
110. Randall, G., *Supersolidus Liquid-Phase Sintering of Prealloyed Powders*. Met Trans A, 1997. 28(7): p. 1553-1567.
111. T.W. Eagar, W.D.Z., *Transient Liquid-Phase Bonding Using Coated Metal Powders* Welding Supplement: p. 157-162.
112. C.S. Musso, T.W.E., *Methods for Forming Articles having very Small Channels Therethrough, and such Articles, and Methods of Using Such Articles*, in [www.freepatentsonline.com](http://www.freepatentsonline.com), U.P. Office, Editor. 2005, MIT (Cambridge, Ma, US): US.
113. T.W. Eagar, W.D.Z., *Liquid Infiltrated Powder Interlayer Bonding: A Process for Large Gap Joining*. Science and Technology of Welding & Joining, 2000. 5(3): p. 125-134.
114. H. Zhuang, J.C., E. Lugschider, *Wide Gap Brazing of Stainless Steel with Nickel-base Brazing Alloys*. Welding in the World, 2000. 24(9/10): p. 200-208.

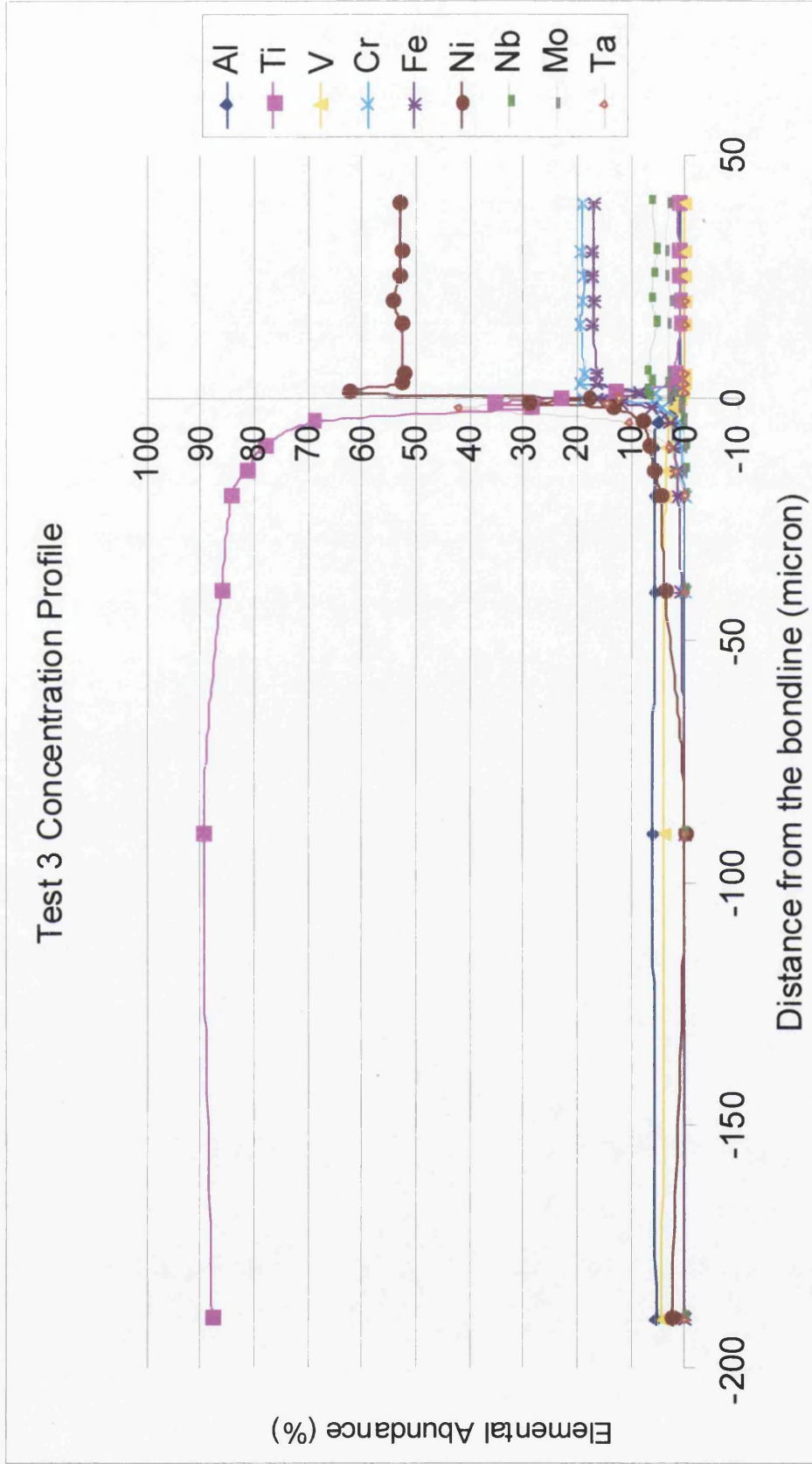
115. D.F. Neal, P.A.B., *Internal Fatigue Origins in Alpha - Beta Titanium Alloys*. Acta Metall, 1976. **24**(1): p. 59-63.
116. L.S. Kireev and V.N, Z., *Fusion Welding of Titanium to Steel (Review)*. The Paton Welding Journal, 2002. **8**: p. 28 - 30.
117. U. Kamachi Mudali, B.M.A.R., K. Shanmugan, *Corrosion and Microstructural aspects of Dissimilar Joints of Titanium and type 304L Stainless Steel*. Journal of Nuclear Materials, 2003. **2003**: p. 40-48.
118. N. Kahraman, B.G.a.F.F., *Joining of titanium / stainless steel by explosive welding and effect on interface*. Materials Processing Technology 2005. **169**: p. 127 - 133.
119. Chatterjee, M.G.a.S., *Diffusion Bonded Transition Joints of Titanium to Stainless Steels with Improved Properties*. Mat Sci and Eng A, 2003. **A358**( ): p. 152 -158.
120. Chatterjee, M.G.a.S., *Effect of Interface Microstructure on the Bond Strength of the Diffusion Welded Joints Between Titanium and Stainless Steel*. Materials Characterization, 2005. **54**: p. 327-337.
121. Chatterjee, M.G.a.S., *Variation in the Reaction Zone and its effects on the Strength of Diffusion Bonded Titanium-Stainless Steel Couple*. Mat Sci and Eng A, 2005. **A390**: p. 217-226.
122. Chatterjee, M.G.a.S., *Diffusion Bonding of Titanium to 304 Stainless Steel*. Journal of Nuclear Materials, 2003. **322**: p. 235 - 241.
123. S. Kundu, S.C., *Diffusion Bonding between Compercially Pure Titanium and Micro-Duplex Stainless Steel*. Mat Sci and Eng A, 2008. **A480**: p. 316-322.
124. S. Kundu, S.C., *Interfacial Microstructure and Mechanical Properties of Diffusion-Bonded Titnaium-Stainless Steel Joints using a Nickel Interlayer*. Mat Sci and Eng A, 2006. **(In Press)**.
125. s. Kundu, S.C., A. Laik, *Diffusion Bonding of Comerercially Pure Titanium to 304 Stainless Steel Using a Copper Interlayer*. Mat Sci and Eng A, 2005. **A407**: p. 154-160.
126. N. Orhan, T.I.K., M. Eroglu, *Diffusion Bonding of MicroDuplex Stainless Steel to Ti-6Al-4V*. Scripta Mat, 2001. **45**: p. 441-446.
127. P. He, J.Z., R. Zhou and X. Li, *Diffusion Bonding Technology of a Titanium Alloy to Stainless Steel Web With Ni Interlayer*. Materials Characterization, 1999. **43**: p. 287-292.
128. A. Mugarra, K.O., J.L. Alcaraz, *Validation of IN718 SPF and DB Processes for the Design of Aircraft Engine Parts*. Journal of Materials Processing Technology, 2002. **125-126**: p. 549-554.
129. G.D. Janaki Ram, A.V.R., K. Prasad Rao, *Microstructure and Tenilse Properties of Inconel 718 Pulsed Nd-YAG Laser welds*. Journal of Materials Processing Technology, 2005. **167**: p. 73-82.
130. G. Zhang, R.S.C., H.P. Seow, *Solid State Diffusion Bonding of Inconel 718*. Science and Technology of Welding & Joining, 2001. **6**(4): p. 235-239.
131. M.B. Henderson, D.A., M. Heobel, R. Larrson, *Nickel-Based Superalloy Welding Practices for Industrial Gas Turbine Application*, Cambridge University Private Communication for ALSTOM.

132. C.A. Blue, R.Y.I., J-F. Lei, W.D. Williams, *Joining of Hastelloy X to Inconel 718 using an Infrared Process*. Journal of Materials Processing Technology, 1996. **58**: p. 32-38.
133. X. Wu, R.S.C., H. Li, H.P. Seow, *Induction Brazing of Inconel 718 to Inconel X-750 using Ni-Cr-Si-B Amorphous Foil* Journal of Materials Processing Technology, 2000. **104**: p. 34-43.
134. M. Preuss, P.J.W., G.J. Baxter, *A Comparison of Interia Friction Welds in THree Nickel Base Superalloys*. Mat Sci and Eng, 2006. **A437**: p. 38-45.
135. J.J. Kim, J.-W.P., T.W. Eagar, *Interfacial Microstructure of Partial Transient Liquid Phase Bonded Si<sub>3</sub>N<sub>4</sub>-to-Inconel 718 Joints*. Mat Sci and Eng, 2003. **A344**: p. 240-244.
136. M.S. Domack, J.M.B., *Development of Nickel-Titanium Graded Composition Components*. Rapid Prototyping Journal, 2005. **11**(1): p. 41-51.
137. Zhang, P., *Joining Enabled by High Velocity Deformation*, in *Materials Science and Engineering*. 2003, Ohio State University. p. 271.
138. I.E. Locci, J.A.N., F.J. Ritzert, *Reaction Zones Associated with Joining Ni-Based Superalloys to Refractory Metals Studied*. Research and Technology, 2005. **3**: p. 146-148.
139. J. Krishnamoorthi, B.R., P.C. Angelo. *Diffusion Bonding of Ti-6Al-4V with Inconel 718*. in *45th National Metallurgists' Day*. 2007. Mumbai, India.
140. J.N. Dupont, S.W.B., A.R. Marder, *Microstructural Evolution and Weldability of Dissimilar Welds between a Super Austenitic Stainless Steel and Nickel-Based Alloys*. Welding Research in Welding Journal, 2003. **82**(6): p. 125s-135s.
141. H.T. Lee, S.L.J., C.H. Yen, T.Y. Kuo, *Dissimilar Welding of Nickel-Based Alloy 690 to SUS 304L with Ti Addition*. Journal of Nuclear Materials, 2004. **335**: p. 59-69.
142. Z. Guoge, R.S.C., H.P.Seow, *Solid-State Diffusion Bonding of Inconel Alloy 718 to 17-4 PH Stainless Steel*. Materials and Manufacturing Processes, 2001. **16**(2): p. 265-279.
143. R.S. Chandel, S.H.P., Hang Li, *Brazing of Inconel X-750 to Stainless Steel 304 using Induction Process*. Mat Sci and Eng, 2000. **A288**: p. 84-90.
144. X. Wu, R.S.C., H. Li, H.P. Seow, *Wide Gap Brazing of Stainless Steel to Nickel-Based Superalloy*. Journal of Materials Processing Technology, 2001. **113**: p. 215-221.
145. Tuppen, S.J., *Mechanical Integrity of Diffusion Bonds between Dissimilar Titanium Alloys Ti-6-4 and T-550*, in *Materials Reseach Centre 2003*, Swansea University: Swansea
146. S.G.R. Brown, J.D.J., J.A. Spittle, *A 3D Numerical Model of the Temperature-Time Characteristics of Specimens Tested on a Gleeble Thermo-mechanical Simulator*. Modelling and Simulation in Materials Science and Engineering, 1997. **5**: p. 539-548.
147. North, P.N., *Avoiding Dissimilar Metal Weld Failure with Graded Transition Joints*. Lehig Energy Update, 2007. **25**(1): p. 1-3.
148. Foes, F.H., *Advances in Titanium Metal Injection Molding Powder Metallurgy and Metal Ceramics*, 2007. **46**(5-6): p. 303-310.

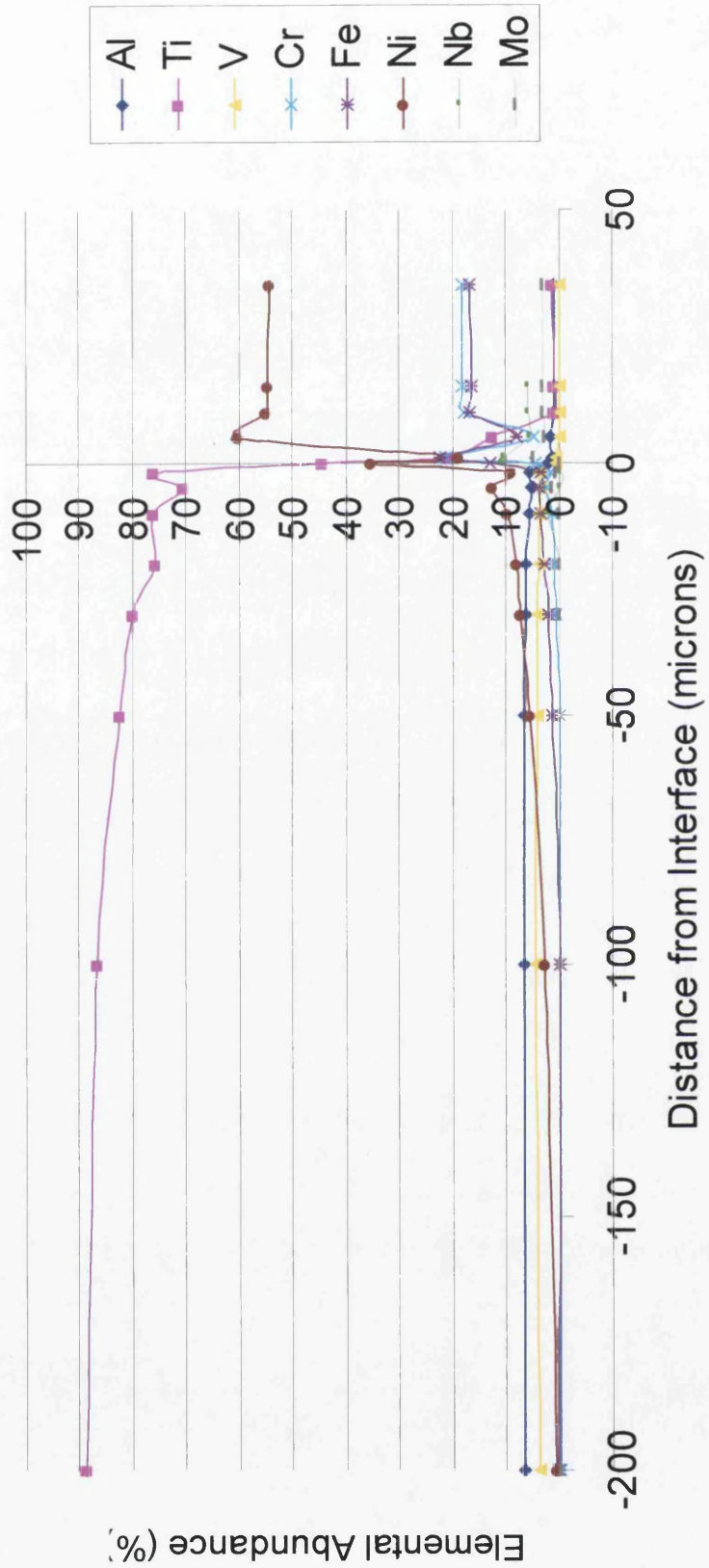
149. Forsdike, J., *A Novel Joining Technique for Blisc Repair*, in *Materials Research Centre*. 2006, Swansea University.
150. Donachie, M.J., *Titanium A Technical Guide*. 2nd Edition ed. 2000: ASM International. 381.
151. J.M. Valverde, A.C., P.K. Watson, *The Effect of Particle Size on Interparticle Adhesive Forces for Small Loads*. Powder Technology, 2001. **118**: p. 236-241.
152. Marucco, A., *Phase Transformations during Long-term Ageing of Ni-Fe-Cr Alloys in the Temperature Range 450 - 600°C*. Mat Sci and Eng, 1995. **A194**: p. 225-233.
153. E.L. Kamen, P.A.B. 1953, NACA Technical Report 1122.
154. M. Gao, R.P.W., *Grain Boundary Niobium Carbides in Inconel 718*. Scripta Mat, 1997. **37**: p. 1843-1849.
155. U. Krupp, W.K., X. liu *Oxygen-induced Intergranular Fracture of Nickel-base Alloy IN718 during Mechanical Loading at High Temperature* Materials Research, 2004. **7**(1).
156. Y. Du, H.X., Y. Zhou, *Phase equilibria of the Ni-Ti-Ta system at 927 °C*. Mat Sci and Eng, 2007. **A448**: p. 210-215.
157. C. Radhakrishna, K.P.R., *The Formation and Control of Laves Phase in Superalloy 718 Welds*. Journal of Materials Science, 1997. **32**: p. 1977-1984.
158. Muzyka, D.R., *Metallurgy of Nickel-Iron Alloys*. The Superalloys. 1972: John Wiley & Sons. 3-144.

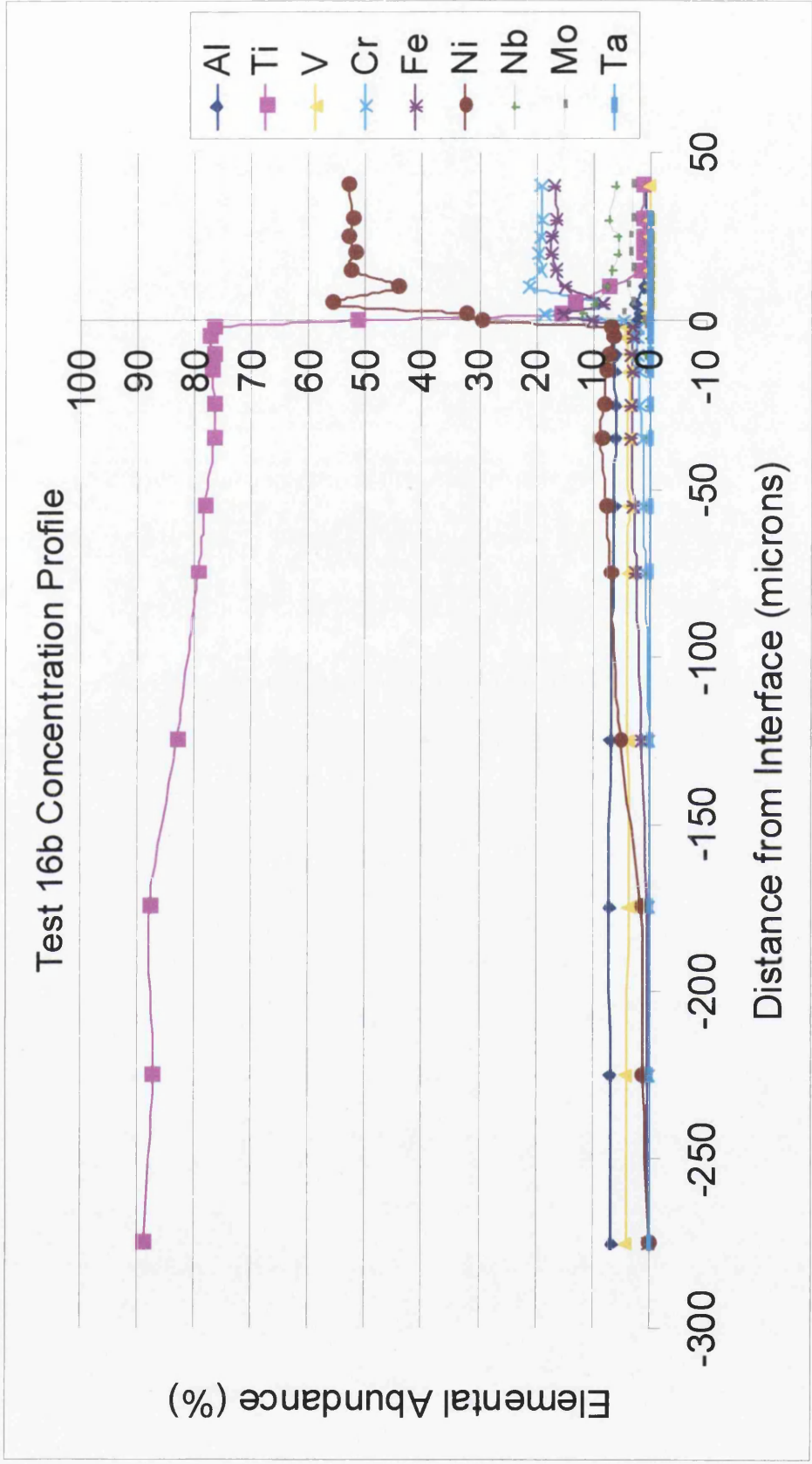
10 APPENDICES

Appendix 1: Full concentration profiles for selected IN718 to Ti-6-4 joints.

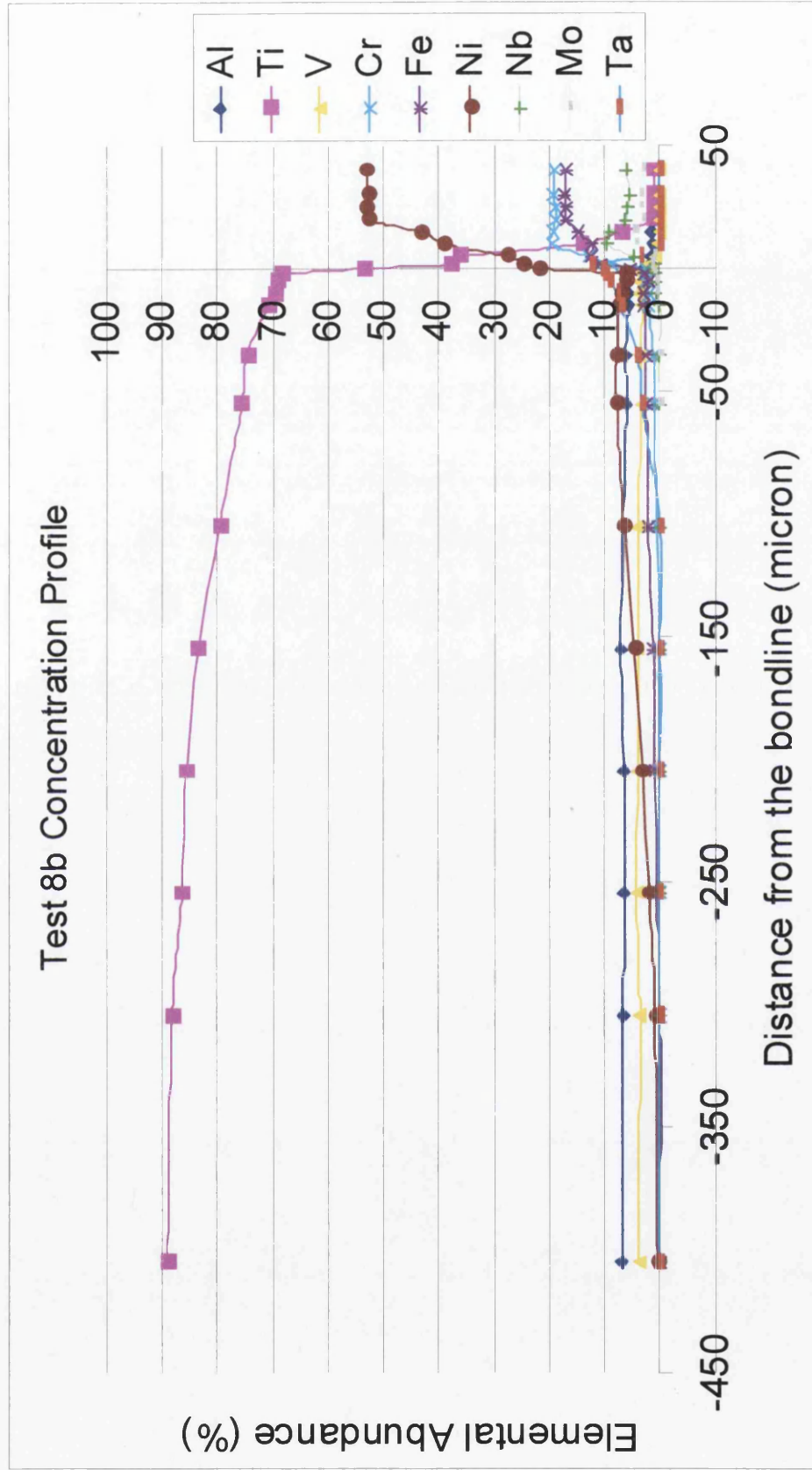


Test 2 Concentration Profile



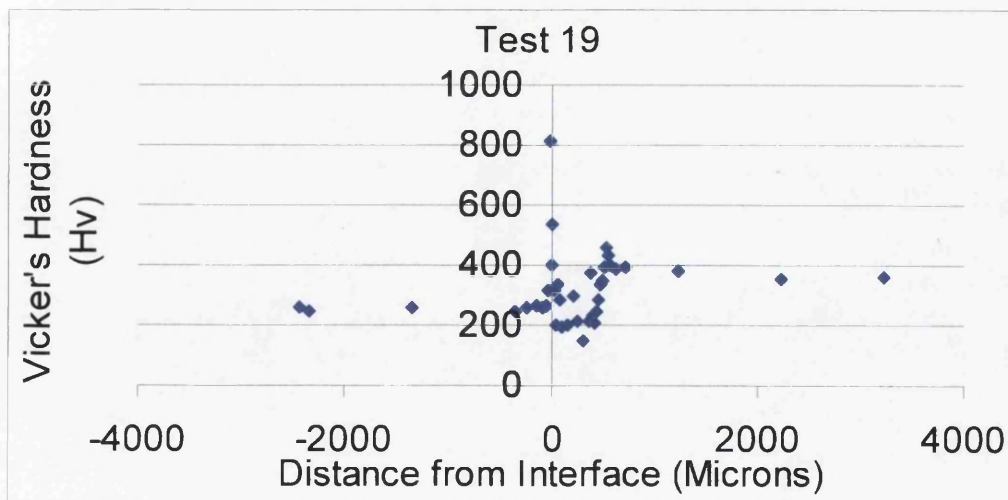
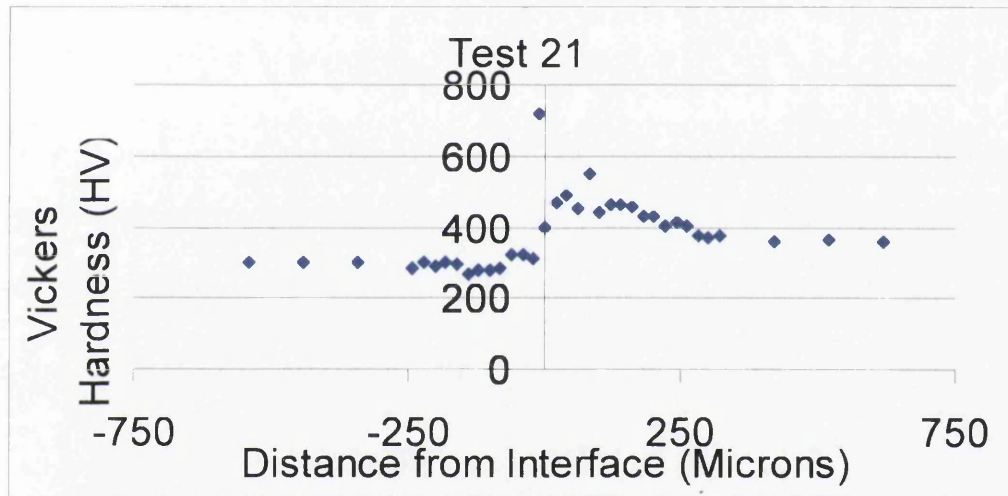
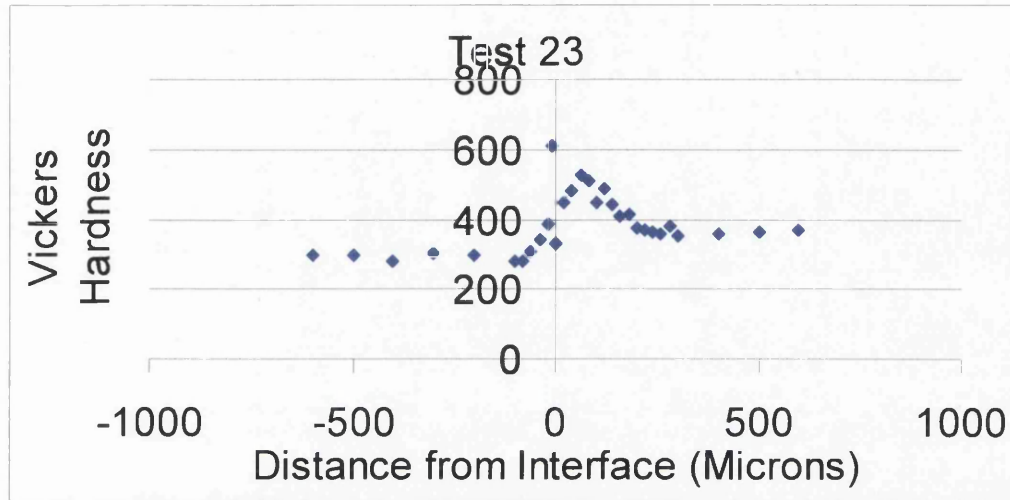


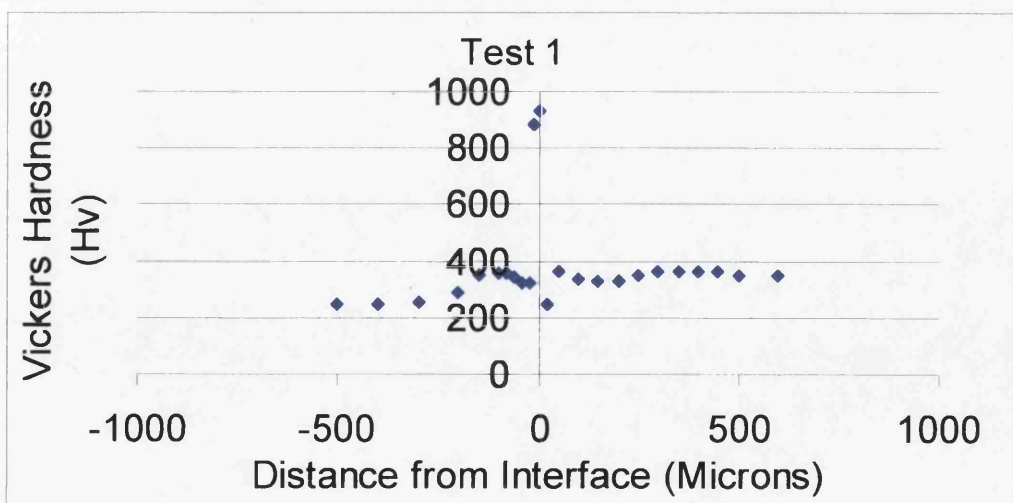
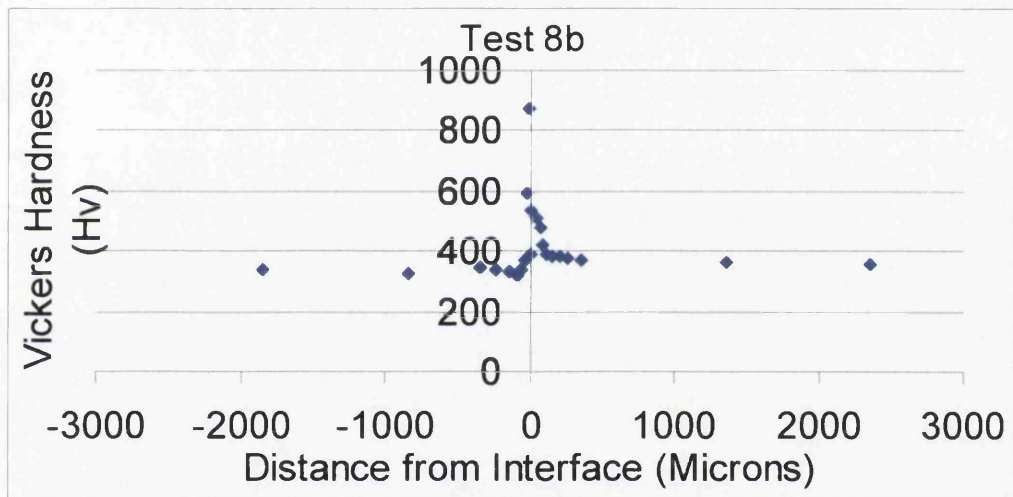
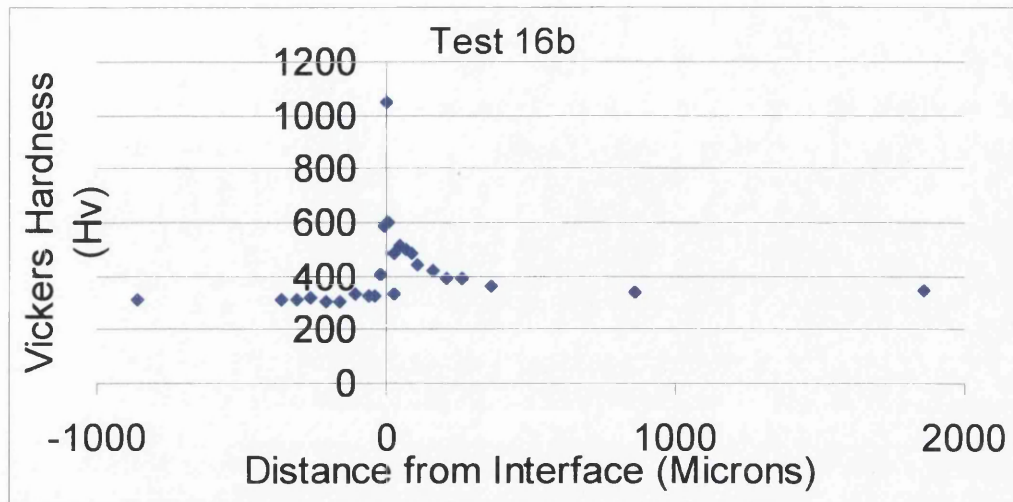
Test 8b Concentration Profile



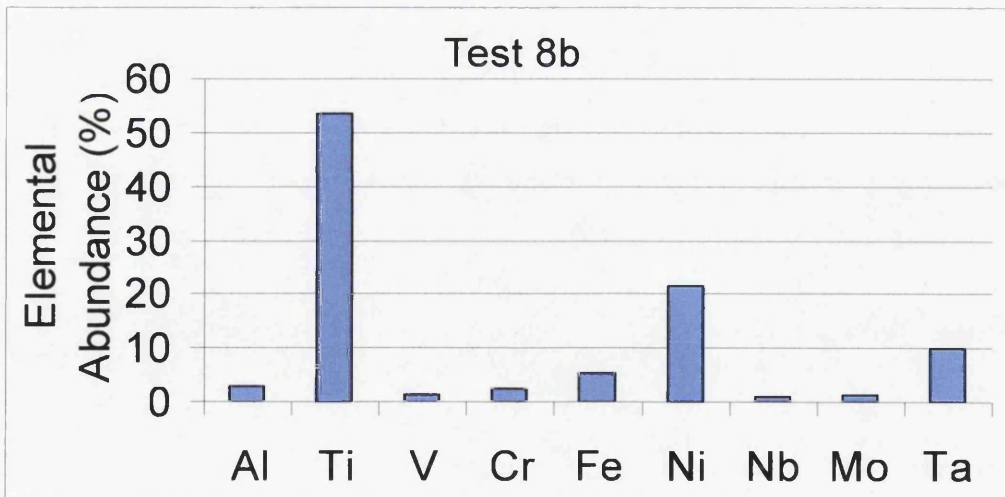
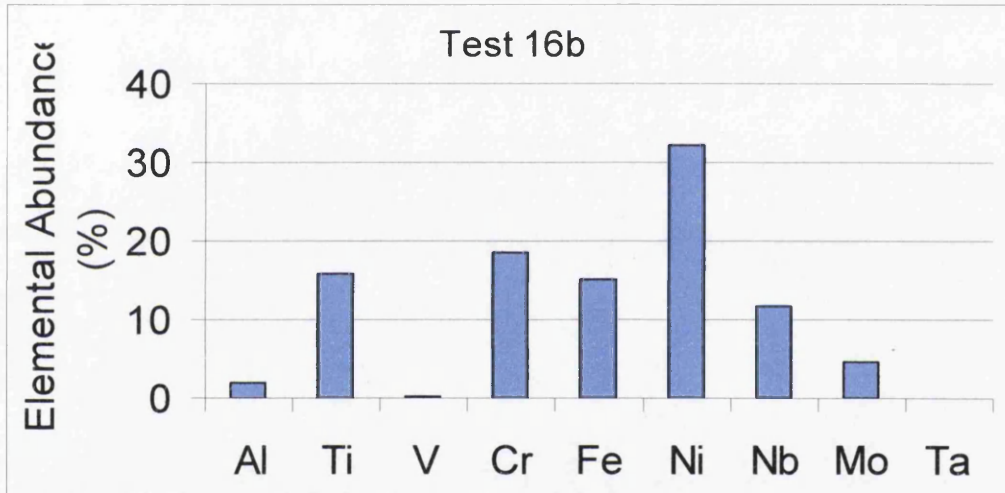
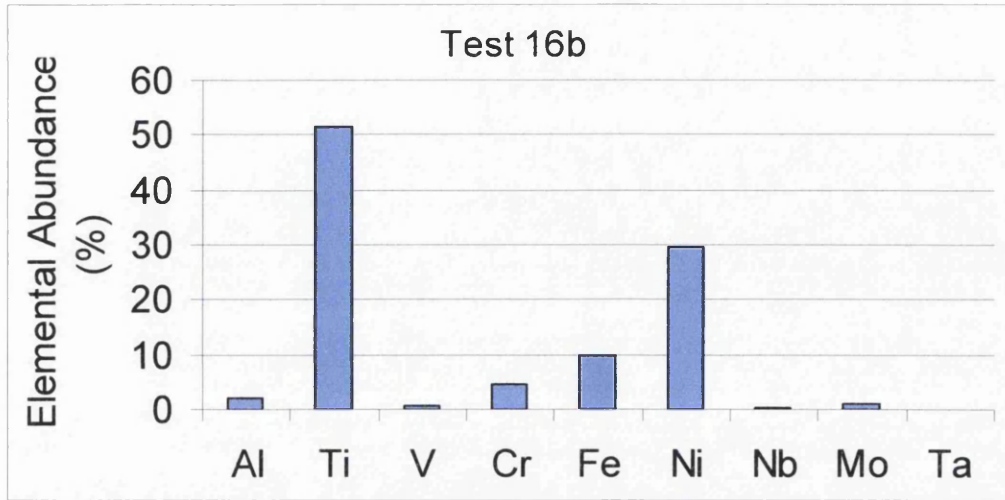


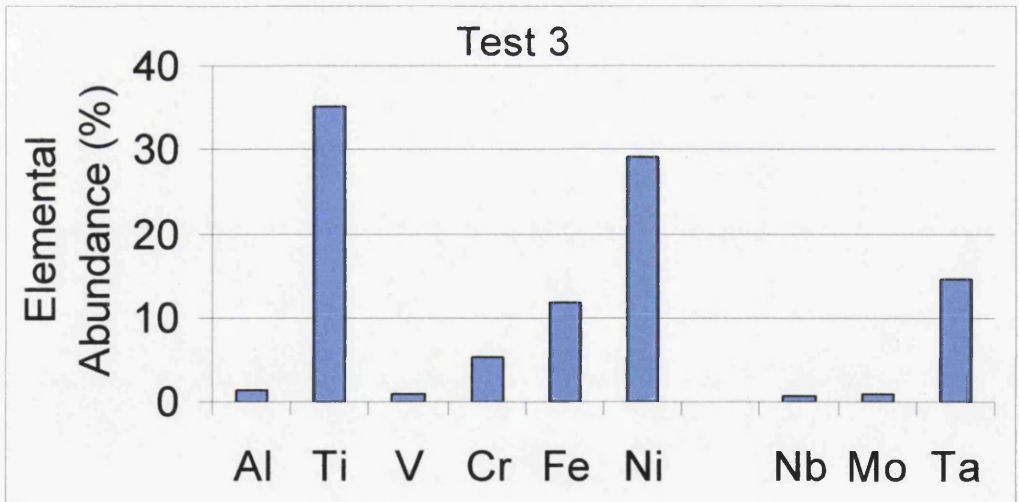
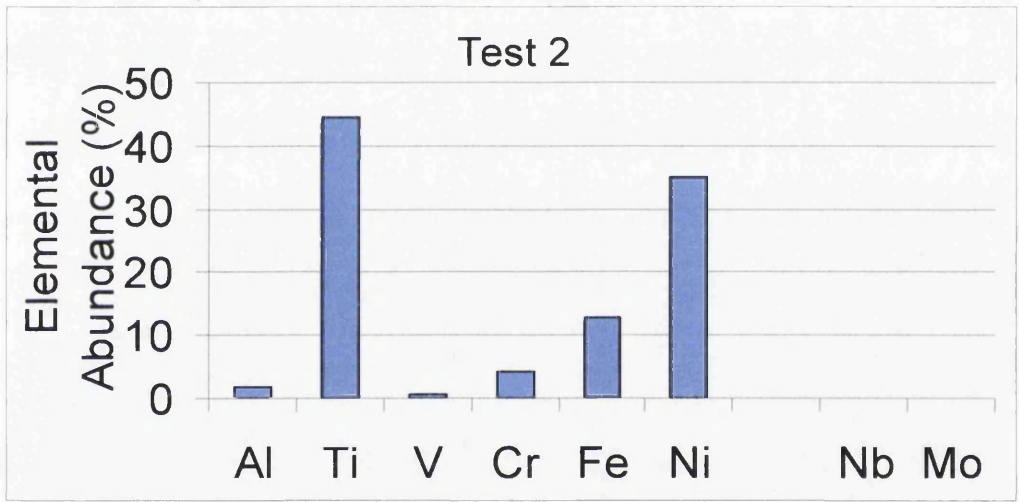
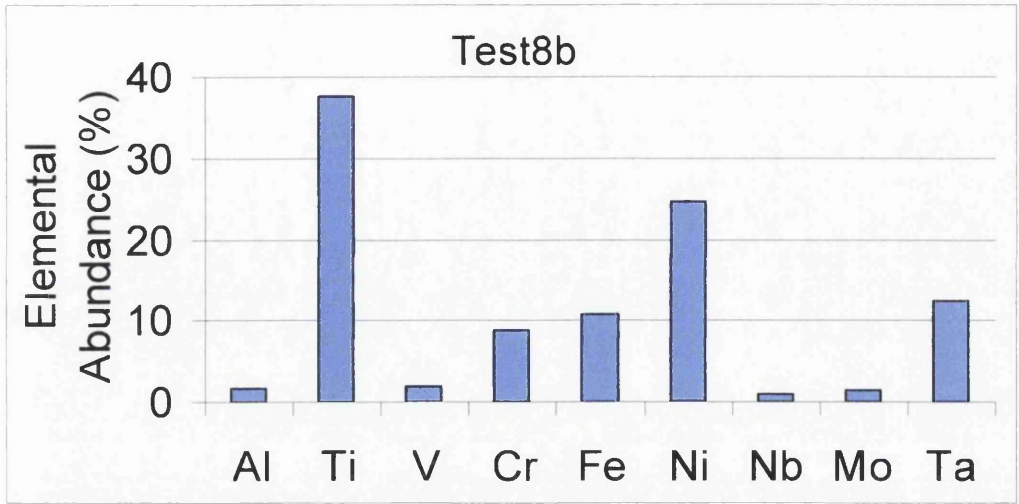
Appendix 2: Microhardness Data for selected IN718 to Ti-6-4 bonds



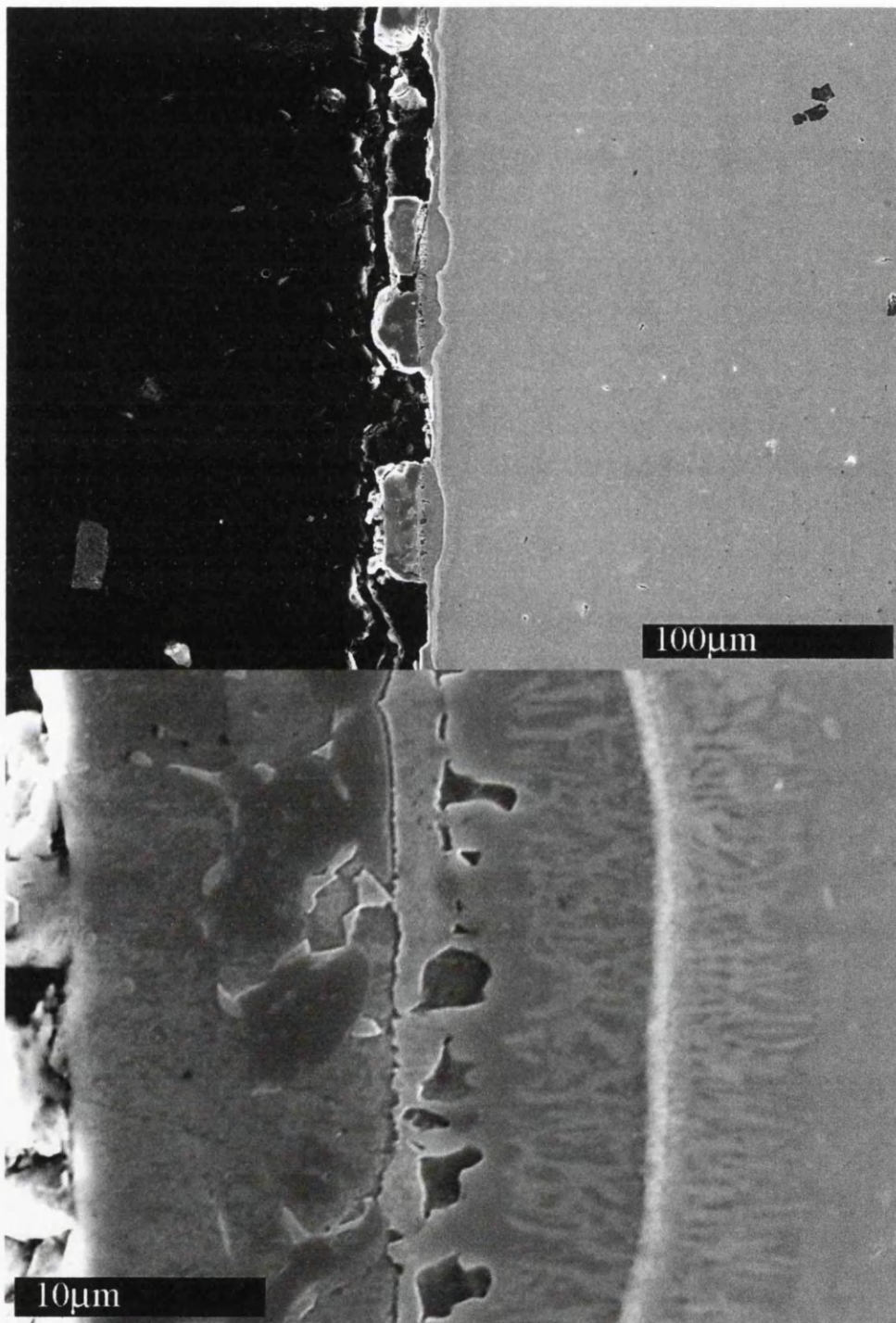


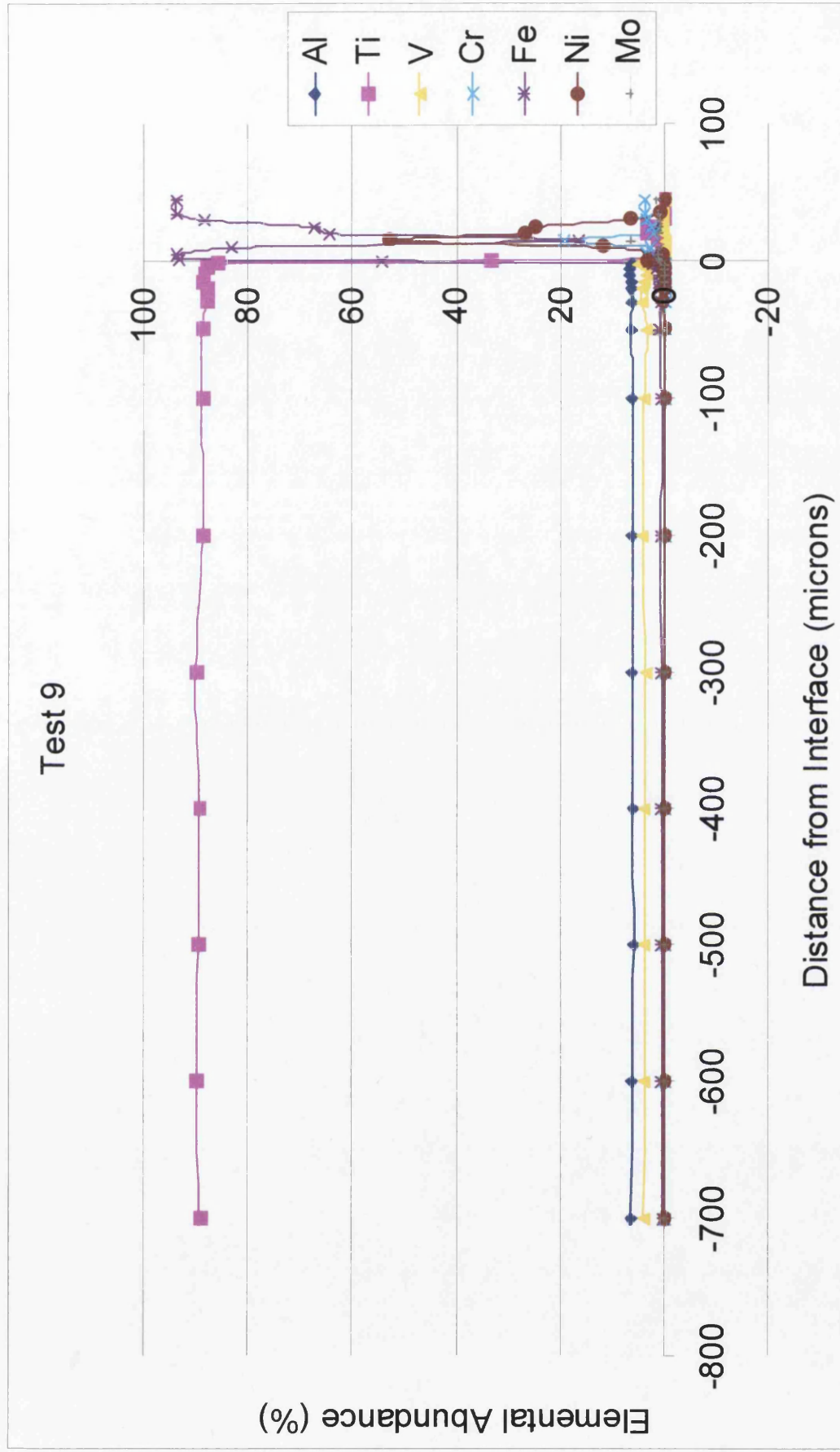
Appendix 3 Concentration Profiles for Intermetallic phases found in IN718 to Ti-6-4 joints.



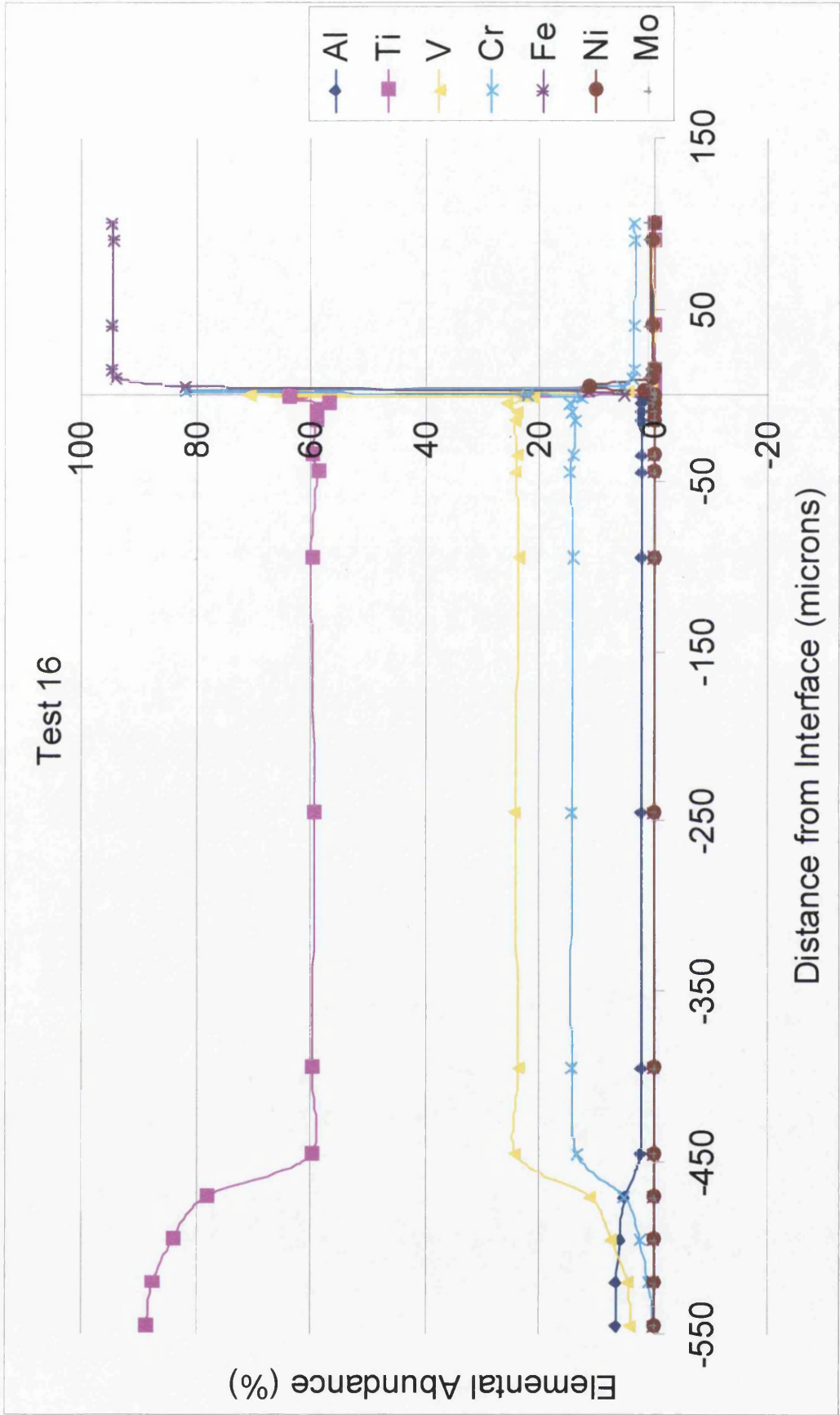


Appendix 4: Examples of interdiffusion zones between Ti-6-4 powder particles bonded to IN718 substrate.

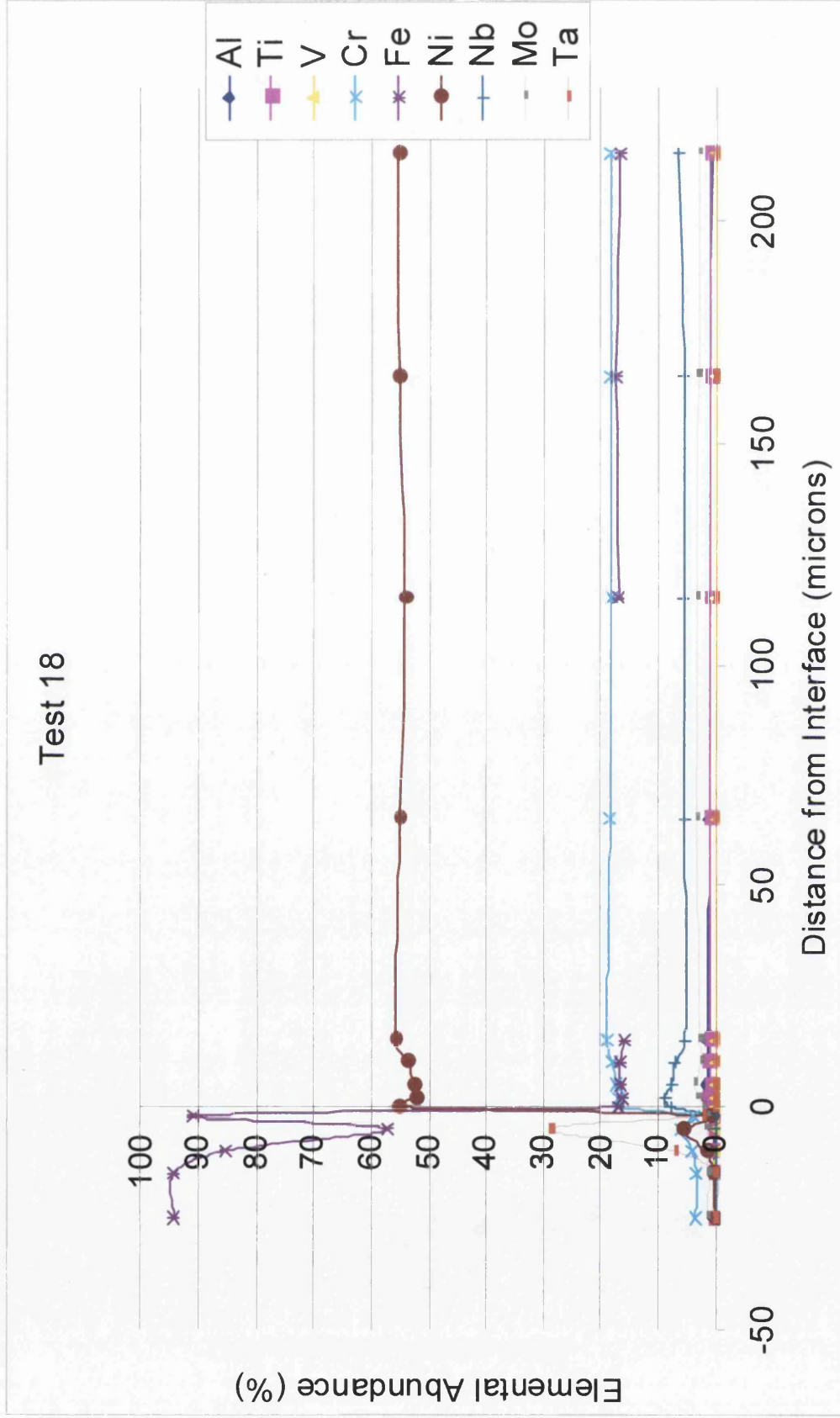




Test 16

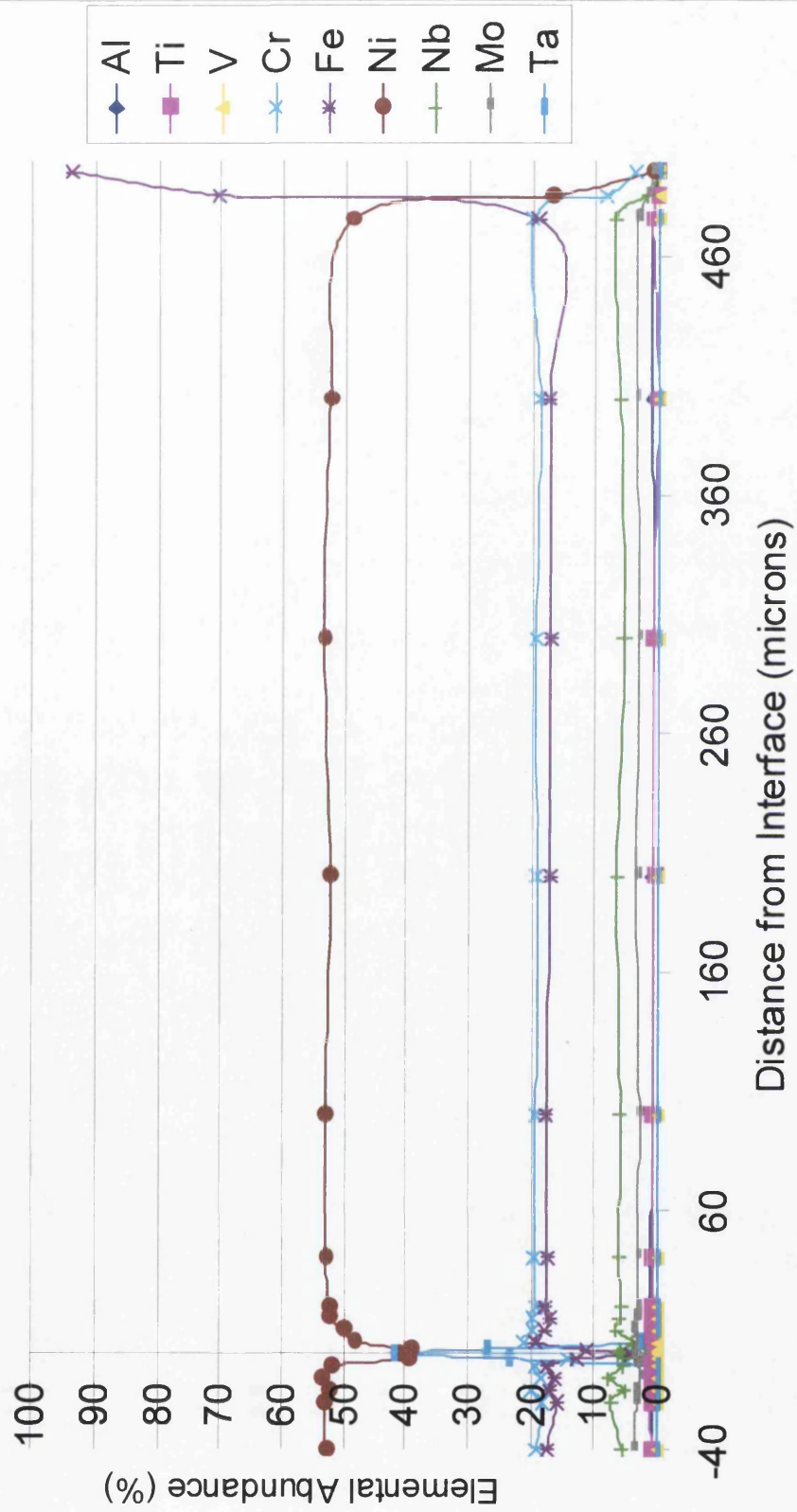


Appendix 6: Full EDX traverses for Tests 18 and 19b (QUIP trial Comparison).

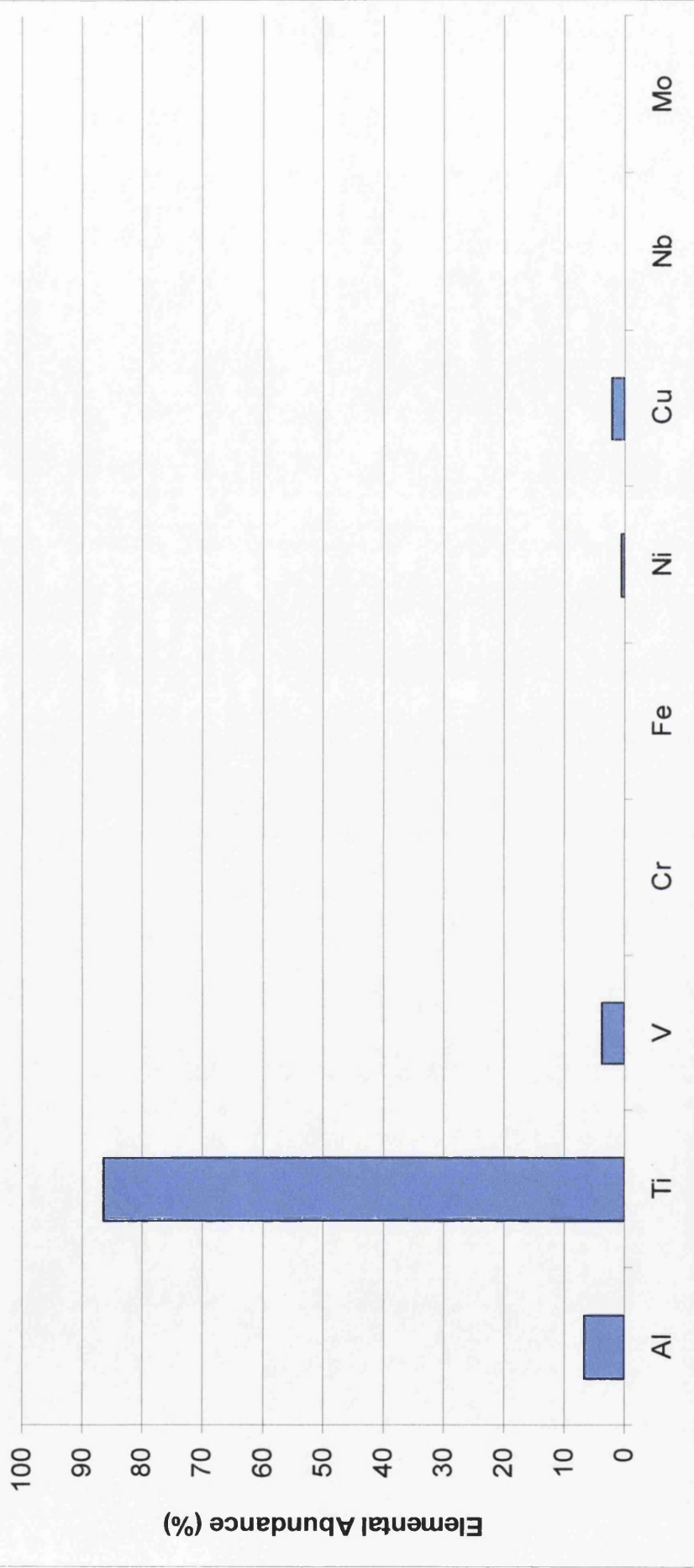




# Test 19b



### Average Powder interlayer concentration profile for test 24



Appendix 8: A comparison between microstructure, microhardness and local chemical fluctuations in Test 30.

